Investigation of efficient and stable nanostructured Mo based chalcogenides electrocatalysts for Hydrogen Evolution Reaction

Thesis

Submitted in Partial Fulfilment of the Requirements

for the Award of Degree of

DOCTOR OF PHILOSOPHY

in

NANOSCIENCE & TECHNOLOGY

by

Jyoti Gupta

(Reg. No. 18ENPH03)

Under the supervision of

Dr. Dibakar Das

Professor & Dean

School of engineering Science and Technology (SEST), University of Hyderabad (UOH), Hyderabad, Telangana State, India

Dr. B. V. Sarada

Scientist 'F',

Center for Nanomaterials, International Advanced Research Center for Powder Metallurgy & New Materials (ARCI), Hyderabad, Telangana State, India

SCHOOL OF ENGINEERING SCIENCES AND TECHNOLOGY, UNIVERSITY OF HYDERABAD, HYDERABAD – 500046, TELANGANA, INDIA

JUNE – 2023

CERTIFICATE

This is to certify that the thesis entitled, **"Investigation of Efficient and Stable Nanostructured Mo based Chalcogenides Electrocatalysts for Hydrogen Evolution Reaction"** submitted by **Jyoti Gupta**, bearing registration number **18ENPH03** in partial fulfilment of the requirements for the award of **Doctor of Philosophy in Nanoscience and Technology, School of Engineering Sciences and Technology**, is a bonafide work carried out by her under my supervision and guidance.

This thesis is free from plagiarism and has not been submitted previously in part or in full to this or any other University or Institute for the award of any degree or diploma.

Parts of this thesis have been:

A. Published in the following publications:

1. **Jyoti Gupta**, Dibakar Das, Pramod H. Borse, "Nanosheets Decorated MoS_2 Micro Balls: Effect of 1T/2H Composition", Chemistry Select 5 (2020) 11764– 11768.
2. **Jyoti Gupta**, Dibakar Das, Anirudha Karati, Joydip Joardar, Pramod H. Borse, "Nanostructure MoS_2 electrocatalyst modified large area carbon electrode for efficient hydrogen evolution", Physica Scripta 97 (2022) 095003.
3. Alka Pareek, Rekha Dom, **Jyoti Gupta**, Jyothi Chandran, Vivek Adepu, Pramod H. Borse, "Insights into renewable hydrogen energy: Recent advances and prospects," Materials Science for Energy Technologies 3 (2020) 319–327.

B. Presented at the following conferences:

1. Poster presentation on "**Nanosheets decorated spherical MoS_2 electrocatalyst for water splitting application**", Jyoti Gupta, Dibakar Das, Pramod H. Borse, ACS publications symposium: The Power of Chemical Transformations (Virtual event) held on 20th-21st May, 2021.
2. Oral presentation on "**Noble metal doped MoS_2 electrocatalyst: A comparative study for hydrogen evolution reaction**", Jyoti Gupta, Dibakar

Das, Pramod H. Borse, International Conference of Condensed Matter and Device Physics (ICCMDP)-2021 held on 9th Sept – 11th Sept, 2021.

3. Poster presentation on "**Heteroatom doping of V into MoS_2 for efficient Hydrogen Evolution Reaction**", Jyoti Gupta, Dibakar Das, B. V. Sarada, International conference on H_2 & CO_2 (virtual event) held on 17th – 19th November, 2022.

The student has passed the following courses towards fulfilment of the course work requirement for Ph. D.

Course Code	Title of the Course	Credits	Results
PD801	Research Methodology	4	Pass
PD802	Advanced Materials processing and Characterization	4	Pass
PD803	Advanced Engineering Mathematics	2	Pass
PD805	Materials Characterization - I	4	Pass

.....

Supervisor

Dr. Dibakar Das

Professor & Dean,

School of Engineering Sciences and Technology (SEST), University of Hyderabad, Hyderabad, T.S. India

Prof. Dibakar Das
DEAN
School of Engineering Sciences and Technology
University of Hyderabad, Hyderabad 500 046.

.....

Dean of the School

Dr. Dibakar Das

Professor & Dean,

School of Engineering Sciences and Technology (SEST), University of Hyderabad, Hyderabad, T.S. India

Prof. Dibakar Das
DEAN
School of Engineering Sciences and Technology
University of Hyderabad, Hyderabad 500 046.

CERTIFICATE

This is to certify that the thesis entitled, **"Investigation of Efficient and Stable Nanostructured Mo based Chalcogenides Electrocatalysts for Hydrogen Evolution Reaction"** submitted by **Jyoti Gupta**, bearing registration number **18ENPH03** in partial fulfilment of the requirements for the award of Doctor of Philosophy in Nanoscience and Technology **School of Engineering Sciences and Technology**, is a bonafide work carried out by her under my supervision and guidance.

This thesis is free from plagiarism and has not been submitted previously in part or in full to this or any other University or Institute for the award of any degree or diploma.

B. V. Sarada.

Dr. B. V. Sarada
Thesis External Supervisor
Sc. 'F,' Centre for Nanomaterials (CNM)
International Advanced Research Centre for
Powder Metallurgy and New Materials (ARCI)
Hyderabad, T.S. India

Thesis Approval for Ph.D.

This Thesis entitled "**Investigation of Efficient and Stable Mo based Chalcogenides electrocatalysts for Hydrogen Evolution Reaction**," by **Jyoti Gupta (Reg. No. 18ENPH03)**, is approved for the degree of Doctor of Philosophy.

Examiners

_____

_____

_____

Internal Supervisor

_____

_____

_____

External Supervisor

_____

_____

_____

Date: _____

Author's declaration

I, **Jyoti Gupta**, declare that this thesis entitled with "**Investigation of Efficient and Stable Nanostructured Mo based Chalcogenides Electrocatalysts for Hydrogen Evolution Reaction**," has been composed solely by myself under the supervision of **Dr. Dibakar Das, Prof., UOH** and **Dr. B. V. Sarada, Sc. 'F', ARCI** and it has not been submitted, in whole or in part, in any previous application for the award of any degree. To the best of my knowledge, this thesis contains no material previously published by any other person and appropriate references/citations are made for results and literature obtained from different authors for comparison purposes. I also declare that I have been adhere to all principles of academic honesty and integrity and have not misprinted or fabricated falsified any idea/ data/ fact/ source in my thesis submission. I understand that any violation of the above will be a cause for disciplinary action by the Institute and can also evoke penal action from the sources which have not been properly cited or from whom proper permission has not been taken when needed.

Jyoti Gupta
(signature)

Jyoti Gupta

Reg. No.: 18ENPH03

Date: 5th June, 2023

Acknowledgements

Ph.D. tenure has been bit challenging experience in many ways. I would not have been able to complete this dissertation without help and support from many wonderful mentors, colleagues, friends, and family members.

First and foremost, I would like to extend my sincere gratitude to Dr. Tata N. Rao, Director, ARCI, for giving me an excellent opportunity as well as extraordinary facilities, assistance, and advises throughout my research journey in ARCI.

I am extremely grateful to my supervisor Dr. Dibakar Das, Prof., Dean, School of Engineering Sciences and Technology (SEST), University of Hyderabad (UOH) for his invaluable advice, continuous support, and patience during my PhD study. His immense knowledge and plentiful experience have encouraged me in all the time of my academic research.

I am truly indebted and express my earnest gratitude to my co-supervisor Dr. B. V. Sarada, Scientist 'F', Centre for Nanomaterials (CNM), ARCI, Hyderabad for her immense support and guidance without which I could not have been completed my work successfully. Her unabated enthusiasm, which stems from his absolute command over the subject, has been a constant source of inspiration for me to work hard and the outcome is expressed in the form of this thesis.

I express my heartiest regards to Dr. R. Vijay, Scientist 'G', Team Leader, Centre for Nanomaterials (CNM), ARCI, for his support to me in research related issues. A debt of gratitude also owed to Dr. Neha Hebalkar, Sc. 'F', Centre for Nanomaterials (CNM), ARCI, who acted my unofficial mentor during Ph. D. journey. The completion of this study could not have been possible without her continuous support, beloved advices, and suggestions.

I also express my sincere gratitude to Dr. Swati Goshacharya, Ass. Prof., SEST, UOH, Doctoral Review Committee member, for the detailed review, constructive suggestions, and excellent advice during the progress of this research work. I am thankful to Dr. Pramod H. Borse, Sc. 'F', CSEM, ARCI for arousing my interest in electrocatalysts and its utilization in hydrogen generation and technical guidance to operate various instruments. I am also grateful to scientists Dr. Joydeep Joardar, Scientist 'F', Dr. Anirudha Karati, post-doctoral Fellow for extending their cooperation.

Much of research that I completed at ARCI was performed at shared user facilities, which are truly remarkable resources, not only due to the state-of-the-art equipment they contain, but also because of the dedicated staff members that provide support to users. I would like to thank Dr. Ravi Chandra Gundakaram (Scientist 'G' & Team leader, CMCT), Mr. M. Ramakrishna (Scientist 'E', CMCT), Mr. G. Janaki Rao (Technician A), Mr. K. Ramesh Reddy (Technical officer B, CMCT) for their tremendous support on many characterization tools that were critical to my work.

I would like to thank my friends Jyothi Chandran, Dr. S. Mamatha, Vivek Adepu, Mr. G. Shreenu, Mr. Kumar S. Reddy, Mr. P. Rahul, Ms. K. Shireesha, Ms. G. Nivetha, Mr. Krishna, Ms. P.N. Lakshmi devi without whom Ph.D. journey would not have been exciting. I take this opportunity to thank all my co-scholars in University of Hyderabad and ARCI as well, for their help and encouragement. I also express my thanks to technical staff Mr. I. Prabhu, Technician-B, Mr. Shridhar, Technician who helped me in this endeavour as and when required.

At last, I would be remiss in not mentioning my family, especially my mother, husband, sister and both brothers. My family has helped me achieve everything I have accomplished in my life. My mother has always been extremely supportive, encouraging, and loving. All my wonderful childhood experiences provided me with the self-confidence, sense of adventure, and openness to new experiences that have helped me overcome all the challenges I have faced in during Ph.D. journey. My sister and my both brothers have been wonderful companions and friends through the years. I genuinely enjoy spending time with all of them.

Finally, I thank with lots of love to Ashish, my husband. Understanding me best as a Ph.D. himself. Ashish has been my best friend and great companion, loved, supported, encouraged, entertained, and helped me get through this agonizing period in the most positive way.

I would never have made it to ARCI let alone completed this dissertation without my family!

Jyoti Gupta
5/06/2023
Jyoti Gupta

Abstract

Fossil fuels are the primary energy source to generate power to the world. But depletion of these energy sources and large contribution to global warming due to the emission of CO_2 is a subject of deep concern. Therefore, alternative clean energy source is very much required to develop sustainable environment and green society. Hydrogen has been considered as a promising energy carrier with highest energy density compared to other traditional fossil fuels with zero emission of CO_2, thus provides a clean and green energy. But the process and quantitative production of green hydrogen is still bottleneck for hydrogen economy. Electrocatalytic water splitting/water electrolysis using renewable energy sources such as solar, wind energy has recently gained much attention as one of the eco-friendly routes for green hydrogen production. However, water electrolysis requires highly active electrocatalyst, capable to split water into hydrogen and oxygen. Currently, state of the art electrocatalyst for hydrogen evolution reaction (HER) are Pt and others, well known as noble metals. However, their scarcity, poor long-term durability limits their application at commercial level. Therefore, development of efficient, cost effective, stable, and scalable electrocatalyst for HER application is need of time.

This Ph.D. thesis mainly focuses on developing Molybdenum sulfide (MoS_2) as an economic, robust, stable, and cost-effective electrocatalysts for hydrogen evolution reaction (HER) application. The work describes several attempts to improve the HER performance of MoS_2 by its nanostructuring and heteroatom doping. Hence, this thesis has been divided into two parts.

The thesis first focuses on nanostructuring of MoS_2 for improved electrochemical hydrogen evolution reaction (HER) performance. In the first part, powder synthesis as well as *in-situ* deposition of MoS_2 film over a conducting substrate have been attempted using simple and economic one-step hydrothermal method. Several characterization techniques have been utilized to understand physico-chemical and electro-chemical properties and how it differs from bulk MoS_2. Synthesized nanostructured MoS_2 powder and film show improved electrocatalytic performance towards HER application.

The thesis also includes the development of an efficient and cost-effective electrocatalyst by heteroatom doping in MoS_2, which tend to improve further electrocatalytic HER activity of MoS_2. Heteroatom doping in MoS_2 is performed using single step hydrothermal method which make synthesis of efficient electrocatalyst very simple and

scalable. Excellent electrocatalytic performance arising from the heteroatom doped MoS_2 as well as its single step synthesis highly contributes efforts in finding the alternative of noble materials for HER application. Ultimately, developed highly active MoS_2 based electrocatalyst is utilized for electrocatalytic water splitting and quantifying the H_2 evolution.

Finally, this thesis mainly attempts for the nanostructuring of MoS_2, noble metal and non-noble metal doping in MoS_2 using single step hydrothermal route and their utilization as an electrocatalyst for HER application. These adopted strategies are found to be one of best approaches which lead to enhances the MoS_2's performance towards HER application and make MoS_2 as an efficient, stable, earth abundant and cost-effective electrocatalyst. This thesis also represents the important advancements towards large-scale renewable H_2 production using electrocatalytic water splitting.

Table of Contents

LIST OF FIGURES

LIST OF TABLES

LIST OF ACRONYMS

CHAPTER 1

INTRODUCTION

1.1: Traditional energy: resources and crises

The huge population of the world mainly depends on consumption of fossil fuels like coal, petroleum, natural gas etc. to fulfil their energy requirements. It has been theoretically calculated that coal will be available only for the next 156 years, natural gas for the next 60 years and petroleum for the next 40 years [1]. After estimating energy consumption data, it is suggested that price of fossil fuels will be continued with price hike and it also may be out of stock if it's consumption will not be taken care [2,3]. In addition, climate change is also a major issue in today's world due to the emission of greenhouse gases in large amount [4,5]. Energy production from fossil fuels results in carbon dioxide (CO_2) main *by-product*, which contributes approximately 75% to greenhouse gases which is curse for the earth and is non-acceptable for mankind [6]. Therefore, it is indeed an urgency to replace the traditional fuels for energy production with sustainable and eco-friendly energy resources [7]. Green energy production and its utilization has become the primary focus of researchers as well as government of majority of countries. Vision for the production of green energy contains following priorities [8]:

- ✓ Sustainable and secured energy resources which are eco-friendly and cost-effective.
- ✓ Reduction in greenhouse gases, especially carbon dioxide (CO_2).
- ✓ Considerable improvement in local air quality.
- ✓ Development of new technological and industrial base which is necessary for future economy.

Considering above points, renewable energy sources have been found as the best option to alternate the consumption of traditional fossil fuels. As per International Energy Agency (IEA) consideration, renewable energy sources can reduce up to 32% of CO_2 emission with efficiency improvement up to 40% [9]. It can be seen from Figure 1.1, energy consumption based on renewable energy sources is gradually increasing but it is still far from traditional fossil fuels. Nowadays, various renewable energy resources like solar energy, biomass energy, wind energy and geothermal energy are being exploited as the options for renewable energy and are

available for large-scale energy generation for example hydropower [10], solar energy [11], wind power [12] etc.

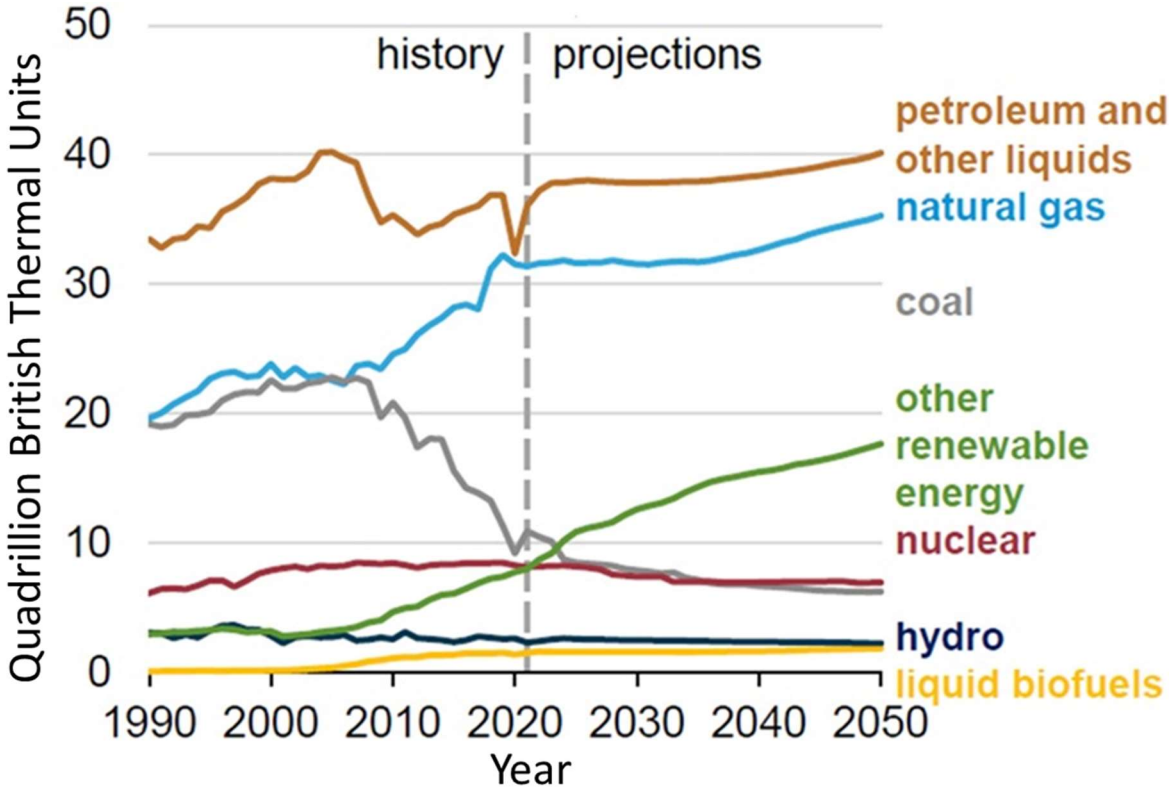

Figure 1. 1: Worldwide energy consumption per year of various energy resources and future projections [13].

However, these kinds of energies suffers from intermittent availability due to geographical or technological factors [14]. Therefore, it is required to explore new ways in the direction of maximum possible energy extraction from sustainable energy resources.

1.2: Hydrogen: a green energy source

Hydrogen energy is an emerging option since it is sustainable, non-toxic, offers low emission of CO_2 and contains highest gravimetric energy density (relevant term to compare energy efficiency) compared to other hydrocarbon fuels [14]. Hydrogen contains three times more energy (141 $MJ.Kg^{-1}$) than natural gas (52 $MJ.Kg^{-1}$) (Figure 1.2). However, unlike coal and petroleum, hydrogen is not the primary source of energy, its role is mostly close to electricity like an 'energy carrier' [15]. When hydrogen molecules are combined with oxygen molecules to react together, useful energy is released, and form water as the main by-product, which is harmless to environment. However, unlike fossil fuels, hydrogen itself is not a naturally existing energy resource but it has capability to support sustainable development of

green energy [15]. Hydrogen is produced from either of the energy sources such as renewable sources (water, solar, wind etc.) or non-renewable sources (coal, methane, natural gas etc.) and then it is transported or stored for further energy utilization [16]. H_2 is an important intermediate due to its highest energy density and clean & sustainable combustion [17].

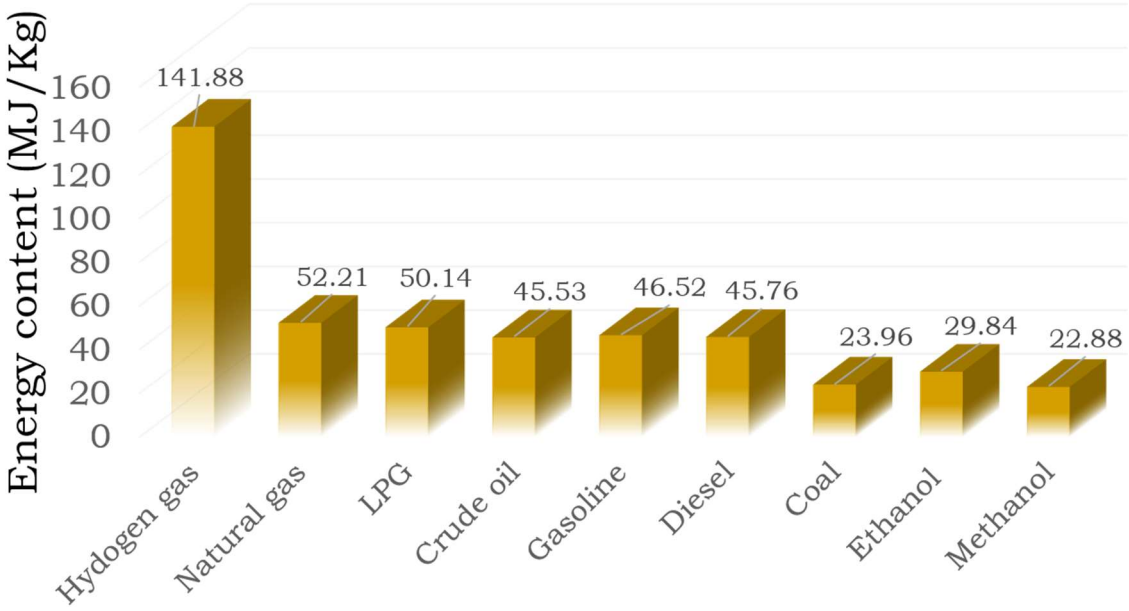

Figure 1. 2: Comparison among some selected fuels w.r.t. energy content [18]**.**

Figure 1.3 displays the various methods for hydrogen production including steam reforming, water electrolysis, photocatalysis etc. and it is utilized in different areas like fuel cells, ammonia synthesis, methanol synthesis etc.

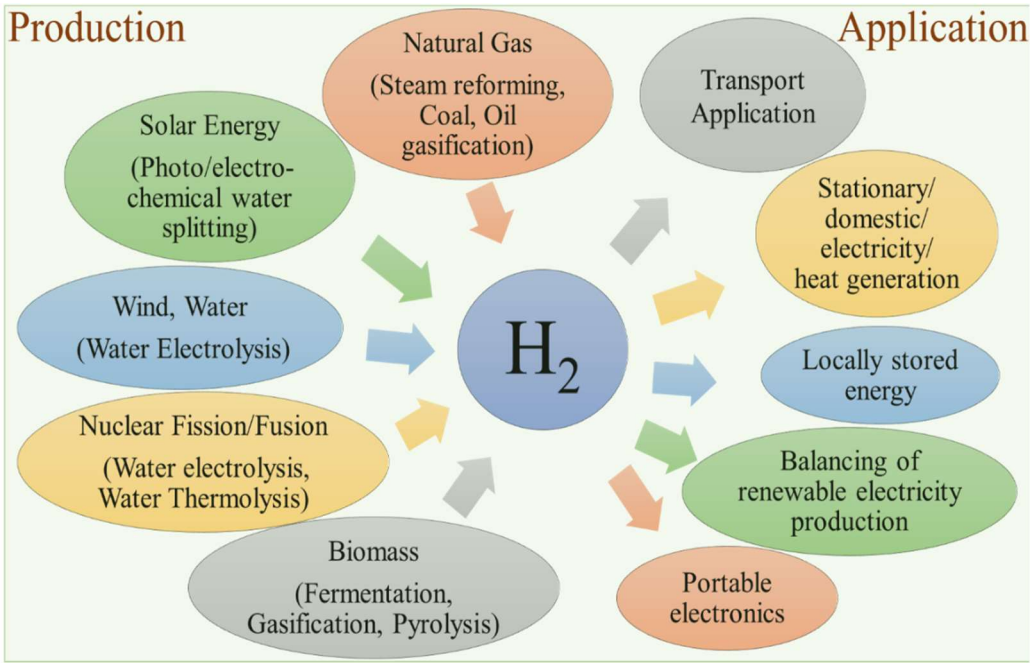

Figure 1.3: Various methods for hydrogen (H_2) production and its different applications.

Large portion of hydrogen (96%) is being generated from steam reforming of natural gases and coal gasification methods [19–21]. However, these methods mainly depend on consumption of fossil fuels and produce blue hydrogen (Hydrogen production with CO_2 emission). Therefore, these methods are not acceptable for sustainable and green hydrogen production in long term due to limited storage of fossil fuels and emission of CO_2. High-temperature pyrolysis of hydrocarbons, biomass, and solid waste is a promising route for hydrogen generation with zero CO_2 emission but, much costlier than steam reforming and gasification [22–24]. Therefore, for sustainable and green hydrogen production, abundantly available renewable energy source is required with no CO_2 emission. Among the available renewable energy sources, water is abundant in quantity (around 70% of earth) and water electrolysis is a sustainable way for green hydrogen production (H_2 with no CO_2), shown in eq. 1.1.

$$2H_2O \rightarrow 2H_2 + O_2 \qquad \ldots 1.1$$

1.3: Water electrolysis/ water splitting

During water electrolysis, water molecules are forced to decompose into its primary contents i.e., Hydrogen (H_2) and Oxygen (O_2) using externally applied electricity [25]. Even though, water electrolysis is cost effective and eco-friendly, ways to produce green hydrogen among other methods, is still a very small portion (~ 4%) of hydrogen that is being produced [26]. As a result, developing this technology for large-scale hydrogen generation is critical in the concept of a green energy economy.

Water electrolyzer is a device, where water electrolysis takes place. It contains two electrodes, filled with conductive electrolyte or water, as shown in Figure 1.4. Negative charged electrode is known as cathode whereas anode is positive charged electrode. Water splits into hydrogen (H_2) and oxygen (O_2) at a potential of +1.23 V (eq. 1.2) and can be performed in acidic or alkaline electrolyte (eq. 1.3 to eq. 1.6) [30].

$$\textit{Overall Water Splitting}: 2H_2O \rightarrow 2H_2 + O_2; \quad E^0 = +1.23\ V \qquad \ldots 1.2$$

In acidic electrolyte:

$$\textit{At cathode}\ (HER): 2H^+ + 2e^- \rightarrow H_2; \quad E^0 = 0\ V \qquad \ldots 1.3$$

$$\textit{At anode}\ (OER): 2H_2O \rightarrow O_2 + 4H^+ + 4e^-; \quad E^0 = +1.23\ V \qquad \ldots 1.4$$

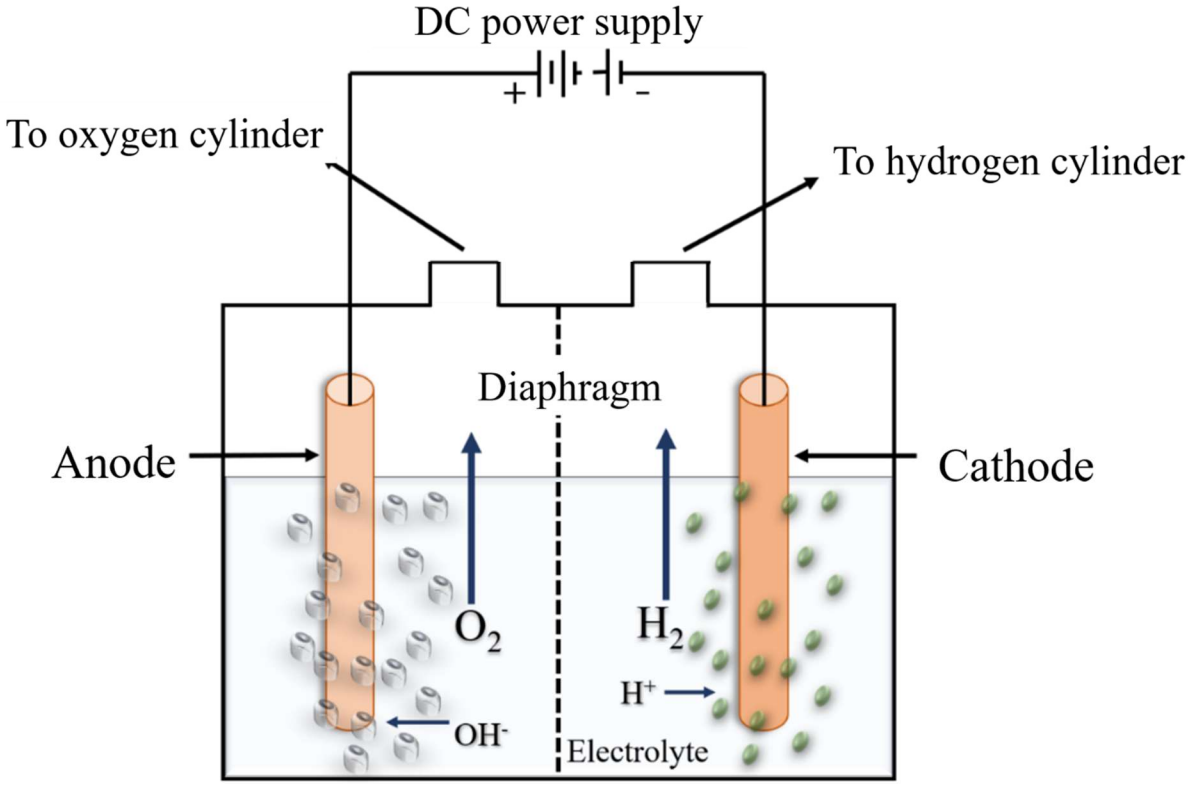

Figure 1.4: Schematic represents for electrolysis of water.

In alkaline electrolyte

$$\textbf{At cathode } (\textbf{HER}): 2H_2O + 2e^- \rightarrow H_2 + 2OH^-; \quad E^0 = +0.83V \qquad \textbf{...1.5}$$

$$\textbf{At Anode } (\textbf{OER}): 4OH^- \rightarrow O_2 + 2H_2O + 4e^-; \quad E^0 = +0.4V \qquad \textbf{...1.6}$$

During the water electrolysis process, the cathode evolves hydrogen gas from its surface and this electrochemical reaction is known Hydrogen Evolution Reaction (HER), whereas anode evolves oxygen gas from its surface and this electrochemical reaction is known as Oxygen Evolution Reaction (OER) [27].

1.4: Hydrogen Evolution Reaction (HER)

HER is being often studied [28] and simplest electrochemical reaction as it contains only two electrons transfer process (eq. 1.3 & 1.5) [29]. As mentioned above, HER is a half-cell reaction which takes place at cathode during water electrolysis. Nowadays, numerous efforts are made for the development of green hydrogen technology by designing advanced electrocatalysts like nanomaterials, metal alloys etc. [30–32]. Prior to discussing the advancement in electrocatalysts, fundamentals of HER are important since the role of electrocatalyst and its efficiency towards HER can be understood better.

1.4.1: Fundamentals of HER

1.4.1.1: Mechanism of HER

The mechanism of HER involves several steps for hydrogen evolution from the electrocatalyst's (cathode) surface [33]. It depends on physico-chemical properties of electrocatalysts (cathode's materials). The HER mechanism starts from an electrochemical adsorption of water molecules on the electrocatalyst's surface and is completed *via.* electrochemical desorption or chemical desorption of H_2 molecule from the surface [34]. Figure 1.5 displays the steps involved in HER mechanism in acidic as well as alkaline water and the electrochemical reactions that take place, have been described from eq. 1.7 to eq. 1.12. The first step of HER mechanism (Figure 1.5), referred as Volmer step creates the adsorbed hydrogen species (eq. 1.7 and 1.10) on the catalyst's surface [35]. Hydrogen evolution from electrocatalyst's surface is further followed by step 2, Heyrovsky step (electrochemical desorption of H_{ads}, eq. 1.8 & 1.11) or step 3, Tafel step (chemical recombination of H_{ads}, eq. 1.9 & 1.12).

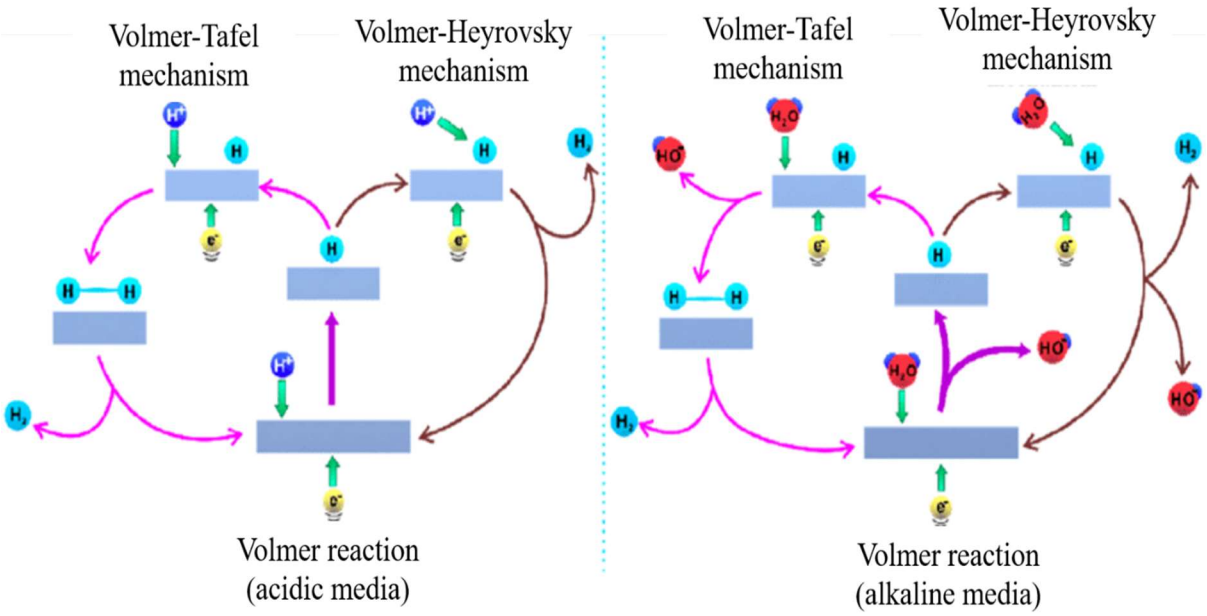

Figure 1.5: Three steps mechanism involved in HER process when electrode is immersed into acidic solution (left side) or alkaline solution (right side) **[36].**

Acidic electrolyte:

$$\boldsymbol{Volmer\ step - H^+ + e^- \rightarrow H_{ads}} \quad \textbf{...1.7}$$

$$\boldsymbol{Heyrovsky\ step - H^+ + H_{ads} + e^- \rightarrow H_2} \quad \textbf{...1.8}$$

$$\boldsymbol{Tafel\ step - 2H_{ads} \rightarrow H_2} \quad \textbf{...1.9}$$

Alkaline electrolyte

$$\boldsymbol{Volmer\ step - H_2O + e^- \rightarrow H_{ads} + OH^-} \quad \textbf{...1.10}$$

$$\boldsymbol{Heyrovsky\ step - H_2O + H_{ads} + e^- \rightarrow H_2 + OH^-} \quad \textbf{...1.11}$$

$$\boldsymbol{Tafel\ step - 2H_{ads} \rightarrow H_2} \quad \textbf{...1.12}$$

1.4.1.2: Kinetics of HER

Kinetics of HER are crucial for both evaluating the efficiency of the electrocatalysts towards HER and providing insightful knowledge about the HER mechanism. It can be well described by Butler-Volmer equation [37].

$$\boldsymbol{j = j_0\left[-e^{\frac{\alpha nF\eta}{RT}} + e^{\frac{(1-\alpha)nF\eta}{RT}}\right]} \quad \textbf{...1.13}$$

Where, j_0: current density (A/cm^2) at zero overpotential (η), j: cathodic current density (A/cm^2), η: overpotential (V), α: charge transfer coefficient, F: Faraday constant (96485 C/mol), R: Gas constant (8.314 J.K^{-1}.mol^{-1}), n: number of charges transferred, and T: Temperature (K).

1.4.1.2.1: Overpotential (η)

Overpotential is a kinetic parameter which decides the efficiency of electrocatalysts. It is a difference between the experimental and the thermodynamic potential, necessary to achieve chemical reaction at a fix rate. The overpotential is calculated at a current density of 10 mA/cm^2 [38]. The lower possible value of the overpotential for an electrocatalyst reflects its efficiency towards HER [39].

1.4.1.2.2: Exchange current density (j_0)

Exchange current density (j_0) is the measure of number of the electrons transferred between the electrode and solution under reversible condition per unit time at zero overpotential [37]. Exchange current density is one of the important kinetic parameters that decides the electrocatalyst's intrinsic activity and it differs for each material. The higher value of j_0 favours the HER.

1.4.1.2.3: Tafel slope (b)

Butler-Volmer equation (eq. 1.14) can also be expressed in logarithmic form.

$$\boldsymbol{\eta = a + blogj = \frac{-2.3RT}{\alpha nF} logj_0 + \frac{2.3RT}{\alpha nF} logj} \quad \textbf{...1.14}$$

Eq. 1.14 represents the correlation between the overpotential (η) and cathodic current density (j) [40,41]. The slope of eq. (xiv) is known as Tafel slope. Tafel slope determines the required η to raise j over one decade and identifies the possible HER mechanism at the electrocatalyst's surface. Experimentally, Tafel slope can be evaluated directly from the recorded linear polarization curves using equation (xiv). Lower value of b is desirable for an efficient electrocatalyst towards HER process.

1.4.1.2.4: Gibb's free energy for hydrogen adsorption/desorption (ΔG_{H^*})

ΔG_{H^*} is an one of the important theoretical descriptors for efficiency of any materials towards HER [42]. Parson *et.al.*, [43] explained the relationship between ΔG_{H^*} and j_0 and further it was plotted by Norskov *et. al.*, [44] for different transition metals. When the exchange current density of various transition metals is plotted against the Gibb's free energy for hydrogen adsorption, a volcano shape is obtained for which apex appeared very close to $\Delta G_{H^*} = 0$ eV. This plot is well known as volcano graph and shown in Figure 1.6.

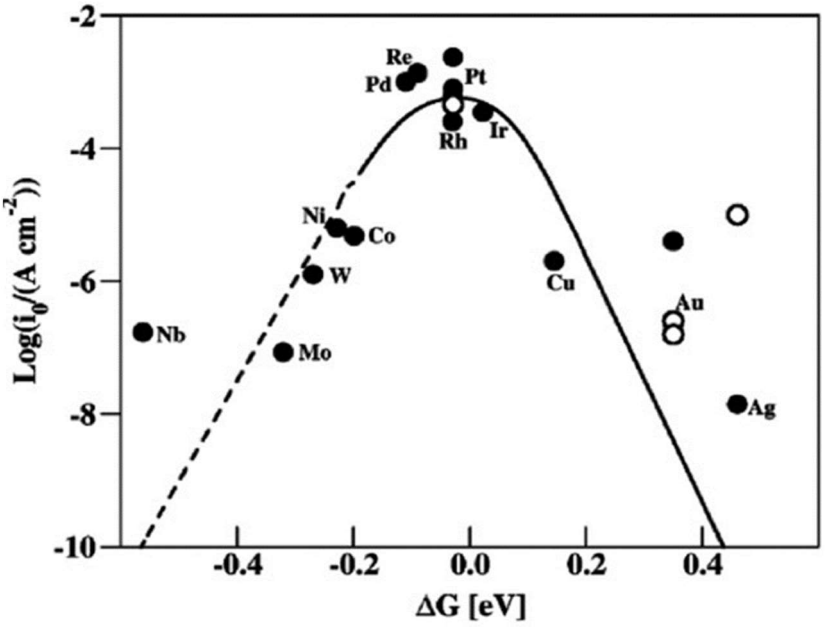

Figure 1.6: Volcano plot of calculated j_0 as a function of the DFT-calculated ΔG_{H^*} on pure metals [45].

Positive value of ΔG_{H^*} favours the hydrogen atom adsorption on electrode surface but it slows the hydrogen desorption from electrode's surface area and *vice versa*. A material, to be an efficient electrocatalyst for HER application, should possess ΔG_{H^*} values close to zero.

1.4.1.2.5: Electrocatalytic active surface area (ECSA)

ECSA plays a critical role in describing, analysing, and comparing the efficiency of an electrocatalyst for HER applications [42,43]. Estimation of ECSA is directly attributed to mass activity of electrocatalyst which is affected by porosity and surface roughness of the catalyst. ECSA is the ratio of double-layer capacitance (C_{dl} is the slope of linear curve drawn between anodic & cathodic current density *vs.* scan rates of CV graphs recorded at non-faradaic zone) and specific capacitance of material (C_s).

1.4.1.2.6: Stability/Durability

Electrochemical stability is a crucial kinetic parameter because materials are usually operated under extreme pH (acidic (pH = 0) or alkaline (pH = 14)) conditions and the material also suffers excess bubble formation on its surface during high hydrogen evolution [46]. Stability of an electrocatalyst can be characterized using different analytical techniques including chronoamperometry (CA), Chronopotentiometry (CP) and cyclic voltammetry (CV).

1.5: Electrocatalysts

Catalysts are known to enhance the reaction rate of any system and they can be in form of solid or fluid. Electrocatalyst participates in the electrochemical reaction and increases the rate of reaction by transferring or accepting charge, without itself being consumed [47].

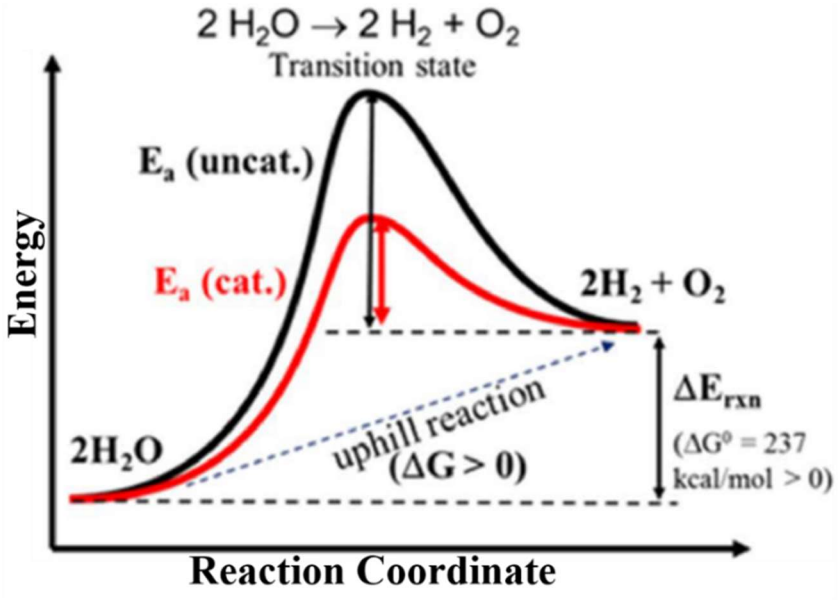

Figure 1.7: Energy diagram for an electrochemical reaction with and without electrocatalyst. This image shows that electrocatalyst increases the rate of reaction by reducing the activation energy during water splitting.

Electrocatalysts help to narrow the energy barrier, results in reduction the electric potential at which electrochemical reaction occurs (Figure 1.7). In other words, an electrocatalyst can be consider as a mediator which accelerates a particular chemical interaction at an electrode's surface.

1.5.1: Electrocatalysts for HER

For HER application, noble metals (Pt, Pd, Ir etc.) are known to be the best electrocatalysts [48], as they exhibit near zero ΔG_{H^*} (Figure 1.6), zero overpotential (η), lower Tafel slope (b) and excellent stability. For example, Pt, Pd are being used as cathode materials for H_2 generation in commercially available PEM electrolyzers [49]. Despite such excellent properties, low abundancy as well as poor anti-poisoning ability limit the path of noble metals from being commercialized. Therefore, to improve the efficiency and make the system cost effective for HER, there are two popular ways. First, alloying or loading the noble metals on a cost effective system [50–55], second, utilization of earth abundant materials as alternative to noble metals.

Being earth abundant and economic systems, transition metals and their compounds are widely used and being modified for HER application [56]. Due to the arrangement of electrons in 3d orbitals, transition metals exhibit different oxidation states resulting in variation of their intrinsic properties[49, 57, 58] etc.

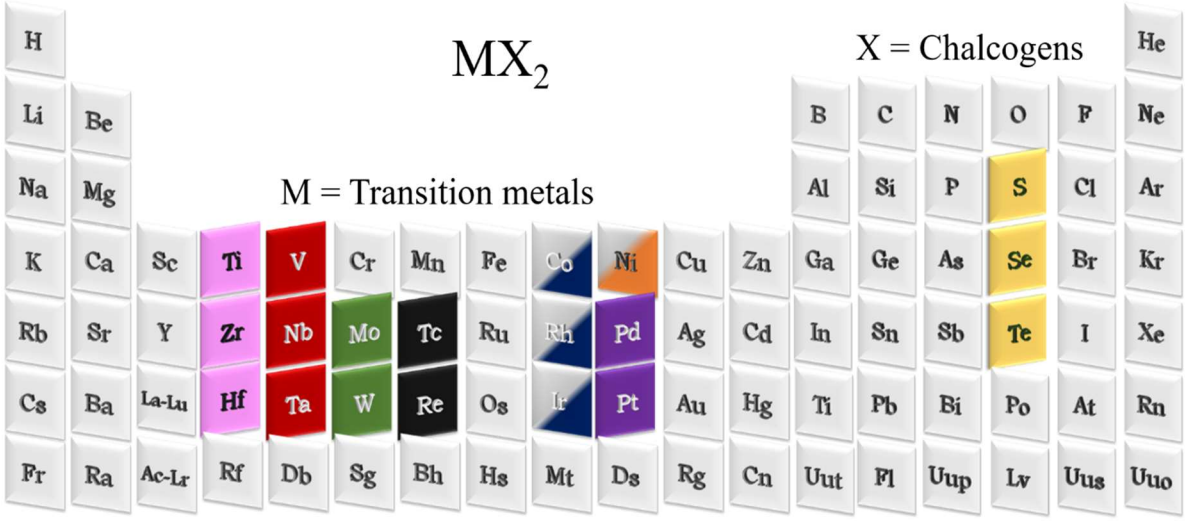

Figure 1.8: Possible layered TMCs has been shown in periodic table, highlighted block shows transition metals and three chalcogens that can form layered crystal structure. Gradient blocks for Co, Ni, Rh, Ir indicate that only some of oxidation states with dichalcogenides form layered structures.

Among transition metal based systems, 2-dimensional (2D) transition metal dichalcogenides (TMCs) have gained more attraction towards HER application [59] since they exhibit graphene like layered structure and tremendous structure based chemical and electronic properties [60]. 2D TMCs are family of elements having a specific molecular formula M_nX_2, where M stands for the transition metals like Titanium (Ti), Zirconium (Zr), Hafnium (Hf), Molybdenum (Mo), Tungsten (W), Nickel (Ni), Platinum (Pt), Palladium (Pd), Tantalum (Ta), Rhenium (Re), & Niobium (Nb) etc. and X represents a chalcogenide elements such as sulfur (S), selenium (Se), & Tellurium (Te) [61] (Figure 1.8).

Among known 2D TMCs, Molybdenum disulfide (MoS_2) has attracted many researchers of various research areas due to its extraordinary physico-chemical and electronical properties and being utilized in the various fields like tribology, electronics, hydrodesulfurization, photo/electrochemical hydrogen evolution etc. As an electrocatalyst, MoS_2 has been elected as possible alternative of noble metals for HER due to its low price, earth abundancy and excellent stability [62].

1.6: Molybdenum Disulfide (MoS_2)

MoS_2 possesses an analogous structure to graphene[62], (Figure 1.9a). MoS_2 is well known for its multi-functionality due to its varying properties like band gap conversion to direct (1.8 eV) from indirect (1.2 eV) as it changes from bulk structure to nanoscale (Figure 1.9b & c). MoS_2 crystal structure consists of Mo (+4 oxidation state) at the middle of a triangular prism coupled to six S atoms, whereas each S atom connected to three Mo centres, forming a monolayer with a thickness of 3.17 Å. Monolayers of MoS_2 are connected to each other by weak Vander Waal's force along z-axis to form layered structure. Distance between two consecutive monolayers is 6.5 Å (Figure 1.9a) [63]. MoS_2 exhibits mainly three polymorphs: 2H, 3R, and 1T. Where H, R, and T represent hexagonal, rhombohedral, and trigonal crystal structure respectively and numeric before the alphabets represents number of repeated layers per unit cell (Figure 1.9 d to f). Naturally occurred and thermodynamically stable MoS_2 consists mainly of 2H phase along with 3% of 3R while 1T phase of MoS_2 does not occur naturally, it is being converted from 2H phase of MoS_2 using physical/chemical methods. Moreover, to achieve thermodynamic stability of 1T-MoS_2, 2H-phase MoS_2 is being mixed along with 1T-MoS_2 [64]. Table 1.1 gives details of lattice parameters, stacking order, space groups and characteristics of MoS_2's polymorphs. In 2H phase of MoS_2, six S atoms surround the Mo atom in trigonal prismatic coordination, resulting in Mo 4d orbital splitting into three sub orbitals

i.e., $d_{xy,x^2-y^2}, d_{yz,xz}$ and d_{z^2} while in case of 1T phase of MoS_2, Mo atom is packed by six S atoms with octahedral geometry, which splits the 4d orbital into two sub orbitals $d_{xy,xz,yz}$ and d_{z^2,x^2-y^2}, Figure 1.9 (g & h).

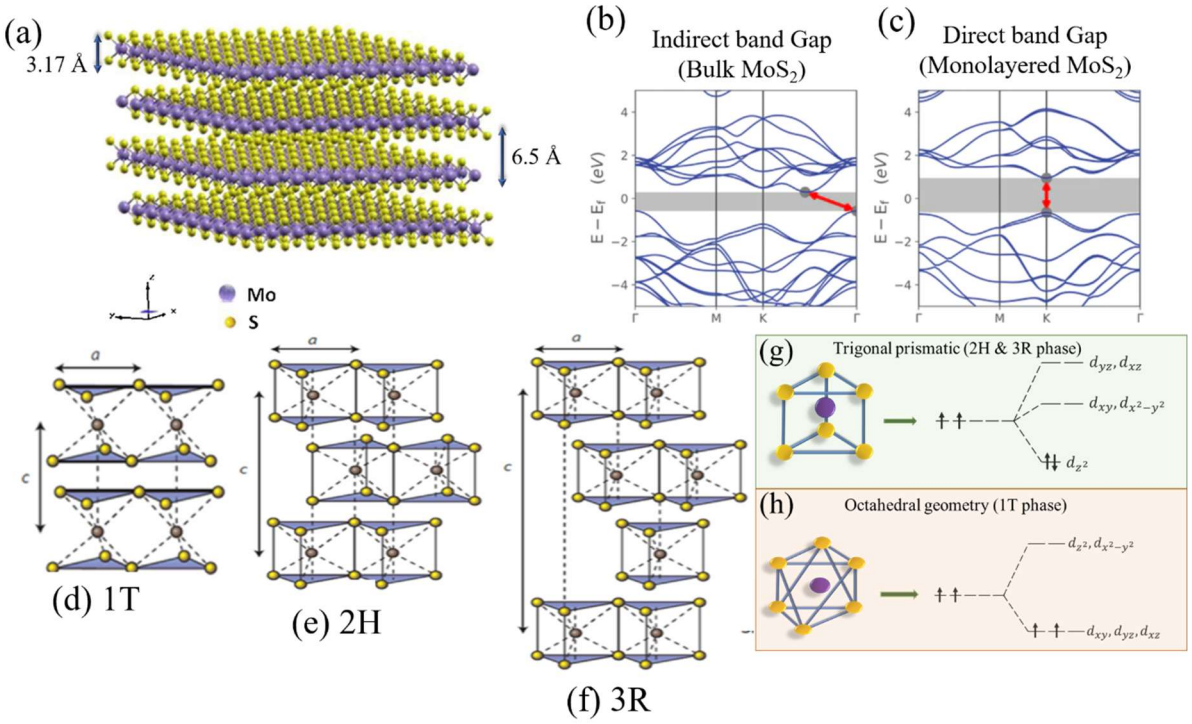

Figure 1.9: Layered structure of MoS_2 (a), Indirect and direct band diagram of bulk (b) & monolayered MoS_2 (c), polymorphs of MoS_2 (d, e, f), Mo and S atoms coordination and d orbital splitting in 2H (g) and 1T (h) phase of MoS_2.

The complete filling of electrons with opposite spin in the d_{z^2} orbital of 2H phase of MoS_2 tends to semiconducting nature and excellent stability. Whereas the incomplete filling of $d_{xy,xz,yz}$ sub orbitals is cause of the metallic behaviour and instability in 1T-MoS_2 [68].

Table 1.1: Crystal structure and nature of MoS_2's polymorphs [65–67].

Polymorphs	**Stacking order**	**Lattice parameters**	**Space group**	**Properties and remarks**
2H	AbA BaB	a = 3.15 Å and c = 12.30 Å	$P6_3/mmc$	Diamagnetic, semiconductor, Chemically stable
3R	AbA BcB CaC	a = 3.17 Å and c = 18.38 Å	R_3m	Diamagnetic, properties like 2H phase of MoS_2

1T	AbC	a = 5.60 Å and c = 5.99 Å	P_3m_1	Paramagnetic, Metallic, Metastable structure

1T-MoS_2 exhibits ~10^5 times higher electronic conductivity than 2H phase. Hence, 1T phase is an excellent material for electronic application as well as for energy conversion and storge application.

1.7 MoS_2: An efficient electrocatalyst for HER

In early reports, it was revealed that bulk MoS_2 (BMS) can't be utilized as electrocatalyst as it is not very active for HER [69]. Interestingly, in 2005, J. K. Norskov and his group reported that nanoparticulated MoS_2 is catalytically active for HER application. They had plotted graph between the Gibb's free energy of hydrogen adsorption *vs.* exchange current densities for MoS_2 and compared with other metals [70]. According to theoretical research, the edges of 2H-MoS_2 have a ΔG_{H^*} of ~0.08 eV, which is substantially closer to that of noble metals., (Figure 1.10). Therefore, MoS_2 has been considered as a potential candidate to replace the noble metals for HER studies.

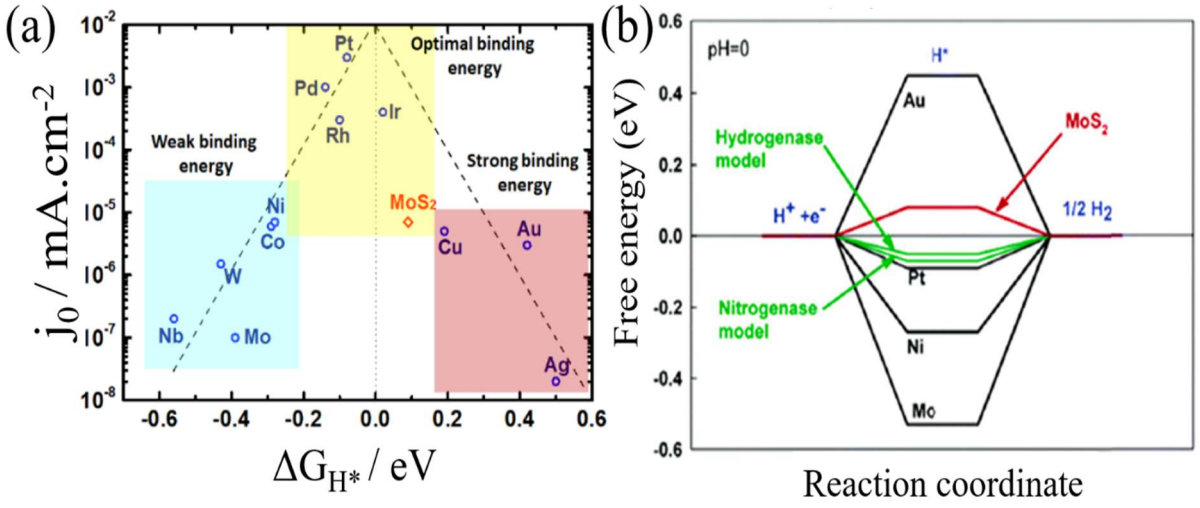

Figure 1.10: (a) The Sabatier plot also known as 'Volcano curve' for HER electrocatalysts (b) calculated free energy diagram for hydrogen evolution relative to the standard hydrogen electrode (SHE) at zero pH for metals and MoS_2 [71,72].

However, semiconducting behaviour of 2H MoS_2 hampers the smooth flow of electrons to the active area while high population of catalytically inert basal plane makes it low rated HER electrocatalyst. In contrast, metallic phase of MoS_2 *i.e.*, 1T phase is known to be active

for HER since its edges as well as basal planes are catalytically active and its high electronic conductivity boosts the charge transfer. Utilization of 1T MoS_2 as electrocatalyst for HER application was firstly reported by M. A. Lukowski *et.al.*, in 2013 [73]. They converted 2H MoS_2 into 1T MoS_2 *via.* chemical exfoliation using n-butyllithium solution. This material demonstrated an increased electrocatalytic activity, with an overpotential of 195 mV *vs. RHE* at a cathodic current density of 10 $mA.cm^{-2}$ current, whereas the 2H phase of MoS_2 needed an overpotential of 300 mV *vs. RHE* to generate the same cathodic current density. In spite of such excellent performance, it was found that 1T phase is not electrochemically stable and gradually converts into 2H phase of MoS_2 [74]. In conclusion, poor electrical conductivity, inert basal planes, stability during electrolysis are the bottlenecks for MoS_2 to be commercialized for HER application.

As discussed in above section, MoS_2 edges are catalytically active than its basal planes while metallic phase (1T) of MoS_2 is found to be more efficient than semiconducting (2H) phase towards HER application. Numerous attempts have been applied to increase the electrocatalytic activity of MoS_2 like increasing the number the catalytic edges sites, conversion of 2H (semiconducting) phase of MoS_2 into the 1T (metallic) phase of MoS_2. These efforts are mainly classified into nanostructuring, heteroatom doping, heterostructures formation, metal loading, support of carbon materials etc. which led the edge orientation, defects in crystal structure, vacancies creation, enhancement in intrinsic conductivity of MoS_2 system as well as crystal structure transformation from 2H to 1T-MoS_2, which are desirable conditions to improve MoS_2's HER activity. To have insightful knowledge of these approaches, we have discussed briefly about the adopted strategies and efforts to improve efficiency of MoS_2 for HER application in further sections.

1.8: Strategies to improve MoS_2's efficiency towards HER

To improve the electrocatalytic efficiency of MoS_2 and making it industrially available for HER application, several approaches are being adopted [62,63,75]. Among the various strategies, nanostructuring of MoS_2, substitutional heteroatom doping in Mo or S sties in MoS_2 lattice, defects formation in crystal structure of MoS_2 by creating Mo or S vacancies, phase change into 1T-MoS_2 from 2H-MoS_2, heterostructures formation using metal-based compounds, carbon-based materials *etc.*, are the most preferred routes to improve the HER efficiency of MoS_2. Figure 1.11 presents the classification of the adopted strategies for MoS_2's

efficiency enhancement. To understand the state of art of MoS_2 for HER application, we have discussed each section, presented in Figure 1.11, briefly in further sections.

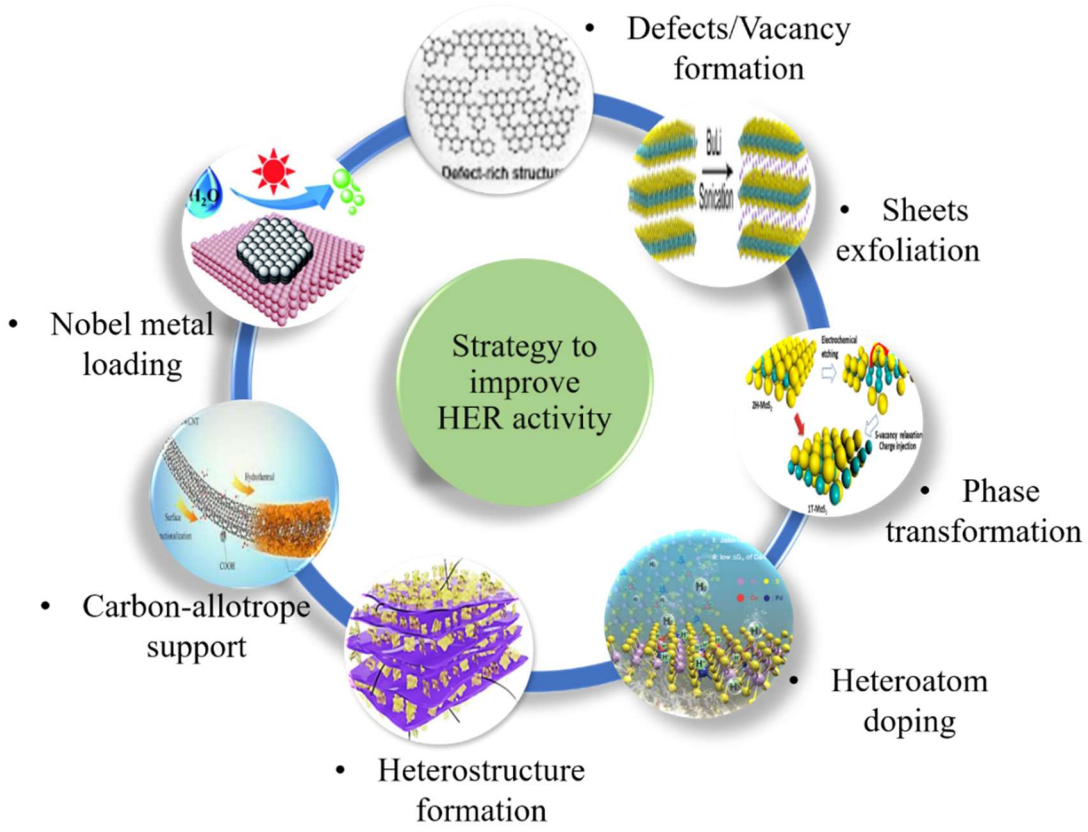

Figure 1.11: Several strategies to improve electrocatalytic HER activity of MoS_2.

1.8.1: Nanostructuring of MoS_2

Basal planes of 2H MoS_2 are known to be catalytically inert whereas its edges are active towards HER application. Therefore, to enhance the HER activity of MoS_2, there is requirement to increase the ration of catalytic sites to basal planes and the catalytically active edges formation with maximum possible exposure. Nanostructuring of MoS_2 leads to maximize the density of active sites with higher exposure of catalytically active edges of MoS_2 as compared to its basal planes by creating edge oriented nanosheets (Figure 1.12).

In 2007, it was the first time, T. F. Jaramillo [76] and his research group experimentally identified that edges of MoS_2 are catalytically active for electrochemical hydrogen evolution. They have deposited MoS_2 on Au (111) substrate using Physical Vapor Deposition (PVD) method. Appearance of bright rim for MoS_2 edges in Scanning Tunnelling Microscope (STM), revealed the metallic nature, resulting in more catalytically active nature as compared to basal plane of MoS_2. Moreover, electrochemical characterization also confirmed the catalytic

activity towards edges and established a linear relationship between MoS_2 edges and catalytically active sites.

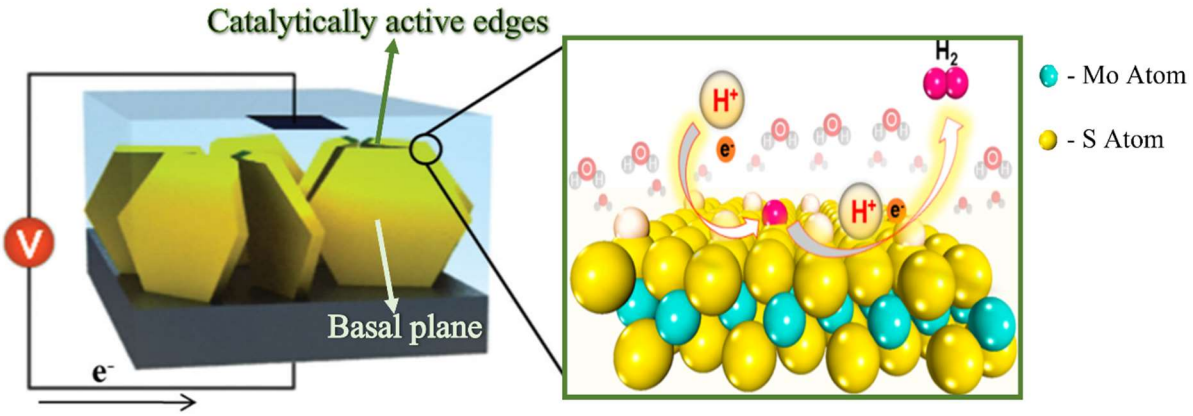

Figure 1.12: Nanostructuring of MoS_2 by creating vertically exposed catalytic sites to improve HER activity.

Therefore, after experimental validation of better catalytic activity of edges over basal planes, D. Kong *et.al.*,[77] have grown vertically oriented MoS_2 layers on Si substrate by Chemical Vapor Deposition (CVD) to optimize the exposure of catalytically active edges over the substrate. This edge terminated film grown using CVD method exhibited 400 mV overpotential under the negative current density of 8 $mA.cm^{-2}$ and proved itself catalytically active for HER application. This film also possessed 105 $mV.dec^{-1}$ Tafel slope and outstanding durability up to 10000 CV cycles. To explore other synthesis methods towards higher exposure of active edges, Z. Wu *et.al.*, [78] developed MoS_2 nanosheets by microdomain reaction method and optimized the annealing temperature to achieve maximum edge/basal plane ratio. This optimized MoS_2 nanosheets showed efficient catalytic activity towards HER application. MoS_2 nanosheets achieved 4.56 $mA.cm^{-2}$ current density at only 150 mV *vs. RHE* overpotential and exhibited Tafel slope of 68 $mV.dec^{-1}$, electrochemical durability up to 1000 CV cycles. However, to develop an efficient, stable, and cost-effective electrocatalyst, S. Murugesan [79] *et.al.*, reported an economic method by using electrodeposition of MoS_2 thin films using ionic liquids as electrolyte. Flower like morphology of electrodeposited MoS_2 thin film maximized the exposure of active sites and reflecting in higher HER catalytic activity. This few layered MoS_2 required only 600 mV *vs. RHE* of overpotential at cathodic current density of 22 $mA.cm^{-2}$ and yielded 106 $mV.dec^{-1}$ Tafel slope. Nanostructuring of MoS_2 was also done by using top-down synthesis route [80]. By using ball milling method, distorted MoS_2 with abundant exposed active edges was prepared. This distorted MoS_2 exhibited only -0.9 $mA.cm^{-2}$ current density at 200 mV *vs. RHE* of overpotential which was not found to be much active for HER

as compared to earlier reports, based on bottom-up synthesis route. To develop simple and facile synthesis route for the nanostructuring of MoS_2, hydrothermal synthesis method has been approached to synthesize MoS_2 nanoflowers with nanosheets as petals [81]. This hydrothermally synthesized MoS_2 nanoflowers exhibited large exposure of catalytically active sites and relatively higher electronic conductivity. MoS_2 nanoflower synthesized at 220 ^{0}C exhibited improved HER performance with 13.8 mA.cm^{-2} at an overpotential of 300 mV *vs. RHE* and lower value of Tafel slope (52 mV.dec^{-1}). In order to boost the electrocatalytic activity of MoS_2, J. Benson *et.al.*, [82] synthesized MoS_2 nanodots (7 layers thick and less than 20 nm in size) *via.* ionic liquid assisted exfoliation method from bulk counterpart and characterized it for HER application. The smaller number of MoS_2 layers and smaller lateral size providing smooth flow of charges with higher active sites density, lead to better HER activity. To produce the cathodic current density of 10 mA.cm^{-2}, synthesised MoS_2 nanodots had a modest Tafel slope of 61 mV.dec^{-1} and a reduced overpotential of 248 mV *vs. RHE*, which is equivalent to the efficient values achieved for pure 2H-MoS_2. A. Ambrosi *et.al.*, [83] again approached the top down synthesis route for the synthesis of MoS_2 nanosheets *via.* ball milling method. They have improved the electrocatalytic behaviour of MoS_2 through ball milling procedure and enhanced 20% current as compared to BMS. This ball milled MoS_2 exhibited 480 mV *vs. RHE* overpotential at HER current density of 3 mA.cm^{-2} with 138 mV.dec^{-1} of Tafel slope. To reduce the formation off impurities in MoS_2, S. Muralikrishna *et.al.*, [84] used MoO_3 instead of ammonium heptamolybdate tetrahydrate. They first synthesized MoO_3 powder by annealing Ammonium heptamolybdate tetrahydrate at 450 ^{0}C for 2 h in atmospheric air, followed by sulfurization using hydrothermal method. The synthesized MoS_2 nanosheets by a two-step process required 280 mV *vs. RHE* overpotential to achieve 25 mA.cm^{-2} cathodic current with 90 mV.dec^{-1} Tafel slope and showed long-term stability. To develop rich in-plane edges, hierarchically nanostructured MoS_2 was synthesized by solvothermal method [85]. This hierarchically developed MoS_2 nanosheets featured nanostructures with small size and an unconventionally rich edge-oriented structure of MoS_2 nanoflakes. Edge rich structured MoS_2 nanosheets shows remarkable HER activity and required 290 mV *vs. RHE* potential to generate higher cathodic current of 326 mA.cm^{-2}, 42 mV.dec^{-1} Tafel slope with excellent durability up to 3000 CV cycles and continuous run for 12 hours in acidic water. Moreover, the HER activity of 2D MoS_2 nanosheets was also compared in acidic and alkaline water. It was found that 2D MoS_2 nanosheets have better HER performance in acidic water and exhibited 385 mA.cm^{-2} ECSA specific current density at only 220 mV *vs. RHE* overpotential whereas, MoS_2 nanosheets required lower overpotential of 300 mV *vs. RHE* to achieve 385 mA.cm^{-2} specific

current density (current/ECSA) in alkaline water [86]. To synthesize nanostructured MoS_2 with maximum possible exposure of active edges, X. Shang *et.al.*, [87] developed the different morphology by synthesizing nanocolumns using solvothermal method. Electrochemical surface area of these MoS_2 nanocolumns, stacked with vertically oriented (002) planes with maximum exposed active sites, was increased by 25 times than BMS and required an overpotential of 258 mV *vs. RHE* drive 10 $mA.cm^{-2}$ HER current with 57 $mV.dec^{-1}$ of Tafel slope. To explore different cost-effective and simple methods for nanostructuring of MoS_2, Z. Wang *et.al.*, [88] used controllable steam etching method to converted MoS_2 basal plane into active edge sites. It was proved that large number of the created catalytically active edges on MoS_2's basal plane effectively reduces its surface energy barrier, resulting in improved HER activity. Further, Tafel slope was reduced by 49% for etched MoS_2 basal plane, results in improved HER activity. Orientation of edges as well as exposure in nanostructured MoS_2 resulted in more efficient system compared to BMS, however, basal planes of MoS_2 does not participate in the construction of active sites due to presence of saturated coordinative atoms in the MoS_2's basal planes. Thus, to make MoS_2's basal planes catalytically active and further enhancement in HER performance, defect engineering, surface modification, vacancies creations, phase transformation have been proposed to optimize MoS_2's HER efficiencies, which will be discussed in following section.

1.8.2: Defects/ Vacancy creation/Phase transformation

Defect formation, unsaturated S/Mo atoms near to Mo or S vacancies in MoS_2 lattices lead to abrupt enhancement in density of active sites in basal planes of nanostructured MoS_2. Moreover, phase transformation from semiconducting to metallic phase leads to increase the catalytically active sites density and electrical conductivity of MoS_2 simultaneously (Figure 1.13) which results dramatic improvement in HER performance. Therefore, several research groups have utilized phase transformation, defect formation or Mo/S vacancies creations by using chemical exfoliation, foreign atom incorporation *via.* hydrothermal/solvothermal route etc. To convert 2H phase of MoS_2 into 1T phase, M. A. Lukowski *et.al.*, [73] used chemical exfoliation *via.* Li ion intercalation of 2H MoS_2 nanosheets which was grown directly on graphite substrate using CVD method, and prepared metallic 1T phase of MoS_2 which showed dramatical enhancement in HER activity by exhibiting lower overpotential of 180 mV *vs. RHE* to generate 10 $mA.cm^{-2}$ of cathodic current density with small Tafel slope of 43 $mV.dec^{-1}$. Exfoliated 1T MoS_2 led to smooth flow of charges, formation of edge exposed active sites which favoured the kinetics towards HER. Similarly, multi-step exfoliation method using Li

ion intercalation has also been utilized to prepare monolayered MoS_2 QDs from its bulk counterpart [89].

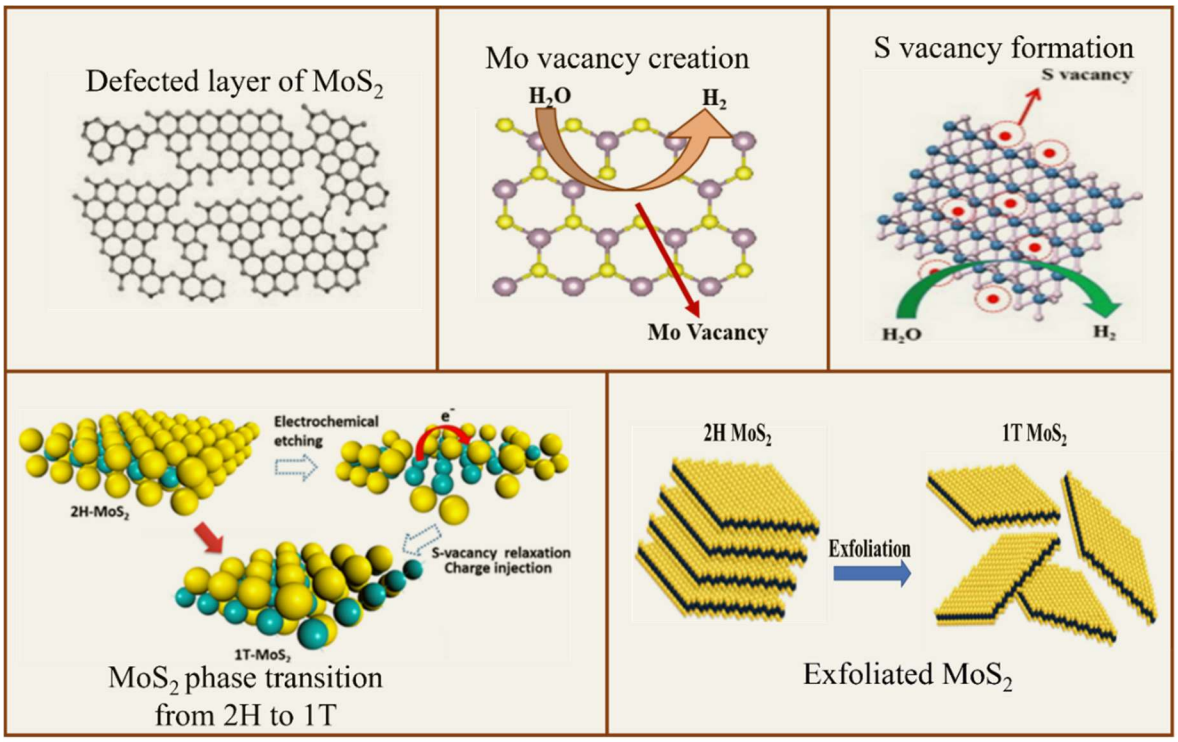

Figure 1.13: Schematic of defected MoS_2 layer, Mo/ S vacancies formation in MoS_2 lattices, phase transition and exfoliation of bulk MoS_2.

Multi-step exfoliated monolayered MoS_2 QDs displayed improved HER activity and exhibited overpotential of 300 mV *vs. RHE* for 35 $mA.cm^{-2}$ cathodic current density and 69 $mV.dec^{-1}$ of Tafel slope. Apart from HER activity, it also showed the excellent durability up to 2000 CV cycles. It was found that multi-step exfoliation of MoS_2 does not improve much efficiency than single step exfoliation. However, Y. Wang *et. al.*, [90] used simulated sun assisted Li intercalation which led to the smaller sized nanoflakes and phase transformation of 2H phase of MoS_2 into 1T phase of MoS_2 simultaneously. 1T-MoS_2 synthesized by Li-intercalation method exhibited 150 mV overpotential under 10 $mA.cm^{-2}$ negative current density and displayed corresponding Tafel slope of 58 $mV.dec^{-1}$. Li-ion intercalation in 2H phase of MoS_2 has been exploited to achieve 1T MoS_2. However, such lithium intercalation technique leads to an unwanted impurity of Li_2S which is hazardous to environment as well [91]. To avoid Li ion intercalation, vertically oriented 1T-MoS_2 was synthesized by using liquid phase exfoliation of 2H-MoS_2 [92]. This liquid phase exfoliation of MoS_2 not only provided higher exposure of active sites but improved the charge transfer due to close packing of porosity as well. This mixed phase (1T/2H) MoS_2 displayed superior catalytic activity for HER and exhibited lower overpotential of 203 mV *vs. RHE* to obtain10 $mA.cm^{-2}$ current density, 60

$mV.dec^{-1}$ of Tafel slope and excellent cyclic stability. However, liquid phase exfoliation was not found as efficient as Li-ion intercalation. Moreover, F. Z. Wang *et.al.*, [93] approached simple and facile method for the intercalation of 2H MoS_2 and develop vertically oriented ultrathin 1T MoS_2 nanosheets using ammonia intercalation *via.* hydrothermal method. Ammonia intercalation led the expansion in interlayer spacing and phase transfer from 2H to 1T of MoS_2 which dramatically enhanced the HER activity and possessed 10 $mA.cm^{-2}$ cathodic current density at only an overpotential of 200 mV *vs. RHE*. In addition, mixed phase *i.e.*, 1T/2H MoS_2 was synthesized *via.* hydrothermal method and fraction of 1T phase was controlled by reaction temperature. The presence of 1T phase displayed Tafel slope of 46 $mV.dec^{-1}$ and demonstrated exceptional HER activity with increased intrinsic conductivity whereas phase formation of 2H-MoS_2 helped to electrochemical stability during water electrolysis procedure [94]. To investigate the synergistic effect of sulfur vacancies, metallic phase conversion and edges exposure of nanostructured MoS_2 towards HER application, C. Tsai *et.al.*, [95] studied theoretical as well as experimental aspects and formed sulfur atom vacancies on the MoS_2's basal planes using electrochemical desulfurization. Created sulfur vacancies with 12.5% exhibited lowest Gibb's free energy to adsorb hydrogen molecules and was also responsible to form new catalytically active sites. These 2H MoS_2 nanosheets with sulfur vacancies showed better HER performance and required 170 mV *vs. RHE* of overpotential at 10 $mA.cm^{-2}$ current and Tafel slope of 60 $mV.dec^{-1}$ [96]. Whereas, sulfur vacant 1T MoS_2 with rich edges was found higher HER active than its conventional counterpart as well as sulfur vacant 2H MoS_2 by exhibiting only an overpotential of 153 mV *vs. RHE* to achieve 10 $mA.cm^{-2}$ HER current density and 43 $mV.dec^{-1}$ Tafel slope [97]. In order to eliminate to create sulfur vacancies at the basal planes of MoS_2 and turn into active sites, D. Kiriya *et.al.*, [98] proposed a general thermal texturization process. The main purpose of this process was to remove bonded sulfur from MoS_2 basal plane by passing hydrogen gas and convert same location as an active edge. This sulfur vacant MoS_2 showed enhanced HER activity by reduced overpotential of 170 mV *vs. RHE* to afford HER current density of 10 $mA.cm^{-2}$.

Although, plenty of work have been reported on nanostructuring, defects formation, Mo/S vacancies creations, phase transformation for the increment in electrocatalytic activity of MoS_2 towards HER application, efficiency of MoS_2 for HER application can be further improved by heteroatom doping. The following section discusses the influence of heteroatom

doping on the physicochemical and electrochemical characteristics, as well as the electronic structure of MoS_2.

1.8.3: Heteroatom doping

Heteroatom doping has been considered as one of the important approaches for utilizing MoS_2 as an efficient, sustainable, and environmentally acceptable electrocatalyst for HER application. It is observed that heteroatom doping narrows the band gap by modulating electronic structure, increases intrinsic conductivity, lowers the ΔG_H* values, induces strain and defects in lattice. Moreover, heteroatom doping also responsible for phase transformation of 2H into 1T phase of MoS_2. Above said modifications are preferred for efficient electrocatalytic HER. Therefore, heteroatom doping in MoS_2 lattices has attracted many researchers to develop MoS_2 as an efficient, sustainable, and cost-effective electrocatalyst.

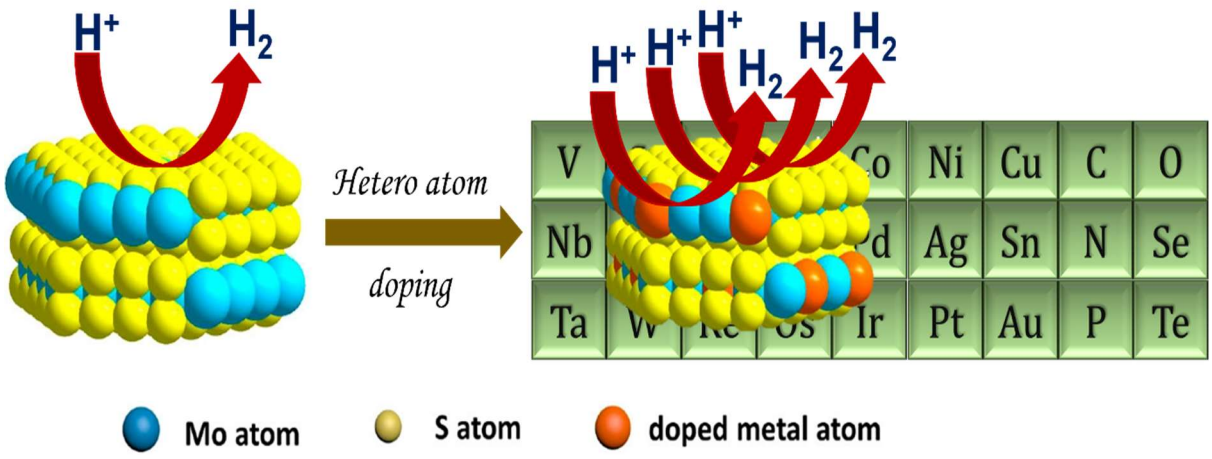

Figure 1.14: Schematic of heteroatom doping into MoS_2 lattice for higher hydrogen evolution.

Noble metals are known as best electrocatalyst for HER application. Therefore, for the synthesis of efficient and cost-effective system, a small amount of noble metal doping in MoS_2 lattices, has been approached. J. Deng *et.al.*, [99] reported Pt doping in MoS_2 to enhanced the electrocatalytic activity of pristine 2D MoS_2. Pt doped few layered MoS_2 (Pt-MoS_2) was found superior over pure 2D MoS_2 due to better hydrogen adsorption behaviour, resulting in enhanced HER performance. Pt-MoS_2 reduced overpotential by 60 mV *vs. RHE* to afford 10 $mA.cm^{-2}$ cathodic current density and exhibited corresponding Tafel slope of 96 $mV.dec^{-1}$. Pt-MoS_2 showed slight decay in HER activity over 5000 CV cycles. To further improve the HER activity of MoS_2, C. H. An *et.al.*, [100] approached dual metal doping by using Pt and Te in order to enhance the electrocatalytic hydrogen evolution of MoS_2 ultrathin nanosheets in acidic as well as alkaline solution. Pt - Te co-doped MoS_2 ultrathin nanosheets showed superior HER activity

over Pt doped MoS_2, Te doped MoS_2 and undoped MoS_2. Pt and Te co-doped MoS_2 required an overpotential of 52 mV *vs. RHE* and 79 mV *vs. RHE* overpotential to generate 10 $mA.cm^{-2}$ HER current density in alkaline and acidic electrolyte, respectively. In continuation to noble metal doping, Z. Luo *et.al.*, [101] chemically activated inert basal planes of 2H MoS_2 *via.* Palladium (Pd) interfacial doping to synthesize an efficient and electrochemically stable electrocatalyst for HER application. Substitutional Pd doping at Mo sites created sulfur vacancies and induced the phase transformation in 1T-MoS_2 from 2H-MoS_2. DFT calculation also revealed that sulfur atom next to substituted Pd exhibited only Gibb's free energy of -0.02 eV for hydrogen adsorption, which responsible for faster HER kinetics. The optimized MoS_2 with 1wt% of Pd showed requirement of 76 mV *vs. RHE* overpotential to afford 10 $mA.cm^{-2}$ cathodic current density with 62 $mv.dec^{-1}$ Tafel slope and excellent electrochemical durability up to 5000 CV cycles with negligible loss in HER activity. Whereas, D. Han *et.al*., [102] developed dual doped *i.e.*, Cu and Pd doped MoS_2 *via.* two step synthesis procedure to increase the electrocatalytic efficiency of MoS_2 towards HER. Presence of Cu in the system improved electrical conductivity which eased the charge transfer and Pd dopant was responsible for phase transformation in 1T-MoS_2 from 2H-MoS_2 and as Pd-S bond provided stability to the system. At a current density of 10 $mA.cm^{-2}$, this synthesised electrocatalyst had a lower overpotential of 93 mV *vs. RHE*, a corresponding Tafel slope of 74 $mV.dec^{-1}$, and notable electrochemical stability over 5000 CV cycles and 50 hours of continuous operation. In case of metal/non-metal doping into MoS_2, Y. Zhan *et.al.* [103] developed Pd and O co-doped MoS_x *via.* sacrificial counter electrode method to boost electrocatalytic efficiency towards HER application. Small sized MoSx clusters on CNTs co-doped with Pd and O, glycine (Gly) as a complexing agent, possessed ultrasmall overpotential of only 23 mV *vs. RHE* at 10 $mA.cm^{-2}$ cathodic current density and corresponding Tafel slope of 18 $mV.dec^{-1}$ with excellent electrocatalytic activity.

Even though, noble metal doping makes MoS_2 more efficient towards HER application but in search of cost-effective electrocatalysts, noble doping does not fit well as its precursors are comparatively expensive. Whereas, substitutional doping of various earth abundant transition metals into MoS_2 has also been found as efficient as noble metal doped MoS_2. In order to study the effect of different earth abundant transition metal doping into MoS_2 system, L. Ma *et.al.*, [104] synthesized Sn doped MoS_2/graphene hybrids using hydrothermal method. It was reported that doping of Sn supressed the stacking of layers of MoS_2 to form few layers and increased its active sites density which robust synthesized system's HER performance by lowering overpotential of 300 mV *vs. RHE* at large HER current density of 27.98 $mA.cm^{-2}$ with

Tafel slope of 54 mV.dec^{-1}. Further, J. Pan *et.al.*, [105] enabled intermediate band in MoS_2 by cobalt (Co) doping to increase the HER activity of MoS_2. Co-MoS_2 was synthesized using solid reaction method which was further followed by rapid heating and quenching. DFT calculation revealed that half-filled intermediate band in Co doped MoS_2 helped to increase the electrical conductivity and accelerated charge transfer which was reflected in HER performance increment. Co doped MoS_2 exhibited 357 mV *vs. RHE* overpotential to achieve current density of 10 mA.cm^{-2} and displayed corresponding Tafel slope of 120 mV.dec^{-1}. To investigate how metal doping affects the HER efficiency of MoS_2 in alkaline water, X. Kong *et.al.*, [106] synthesized Ni doped MoS_2. Ni doping helped to create new active site in MoS_2 lattices and accelerated charge transfer from surface to electrolyte, resulted improved HER performance. Ni-MoS_2 exhibited an overpotential of 207 mV *vs. RHE* at current density of 10 mA.cm^{-2} and corresponding Tafel slope of 60.5 mV.dec^{-1} with excellent stability while maintaining Faradaic efficiency 96 %. Effect of transition metal doping in 1T MoS_2 has also been studied by optimizing the tungsten (W) doping concentration for efficient hydrogen evolution [107]. It was observed that W doping reconstruct the electronic structure *via.* electrons redistribution, optimized energy level, reduced Gibb's free energy and lowered the energy barrier for Volmer reaction and Heyrovsky reaction. Therefore, W doped 1T MoS_2 possessed better catalytic activity than undoped MoS_2 and required 292 mV *vs. RHE* overpotential to generate the current density of 10 mA.cm^{-2} current density and possessed 55.7 mV.dec^{-1} Tafel slope. This system also showed high term stability up to continuous run of 16 hours. T. Liu *et.al.*, [108] reported defects rich Vanadium (V) doped MoS_2 nanosheets with increase interlayer spacing to boost the HER activity. V doping benefited the electronic structure of MoS_2 by narrowing band gap, lowering the Gibb's free energy and increment in the electronic conductivity. With V doping concentration of 10%, Optimized V doped MoS_2 exhibited only 146 mV *vs. RHE* overpotential to afford 10 mA.cm^{-2} cathodic current density and displayed the corresponding Tafel slope of only 48 mV.dec^{-1} with long hours operation stability up to 80 hours. Based on results reported in literatures, Pd metal (noble metal) doping and V (non-noble metal) metal doping were found much efficient as an electrocatalyst for HER application than other heteroatoms doped MoS_2, therefore, these systems can be deeply studied as doping in MoS_2 to synthesize efficient electrocatalyst for HER application. Aside from heteroatom doping, metal loading/alloying with the pure MoS_2 system has been found to be an efficient and cost-effective method for increasing the HER activity of MoS_2.

1.8.4: MoS_2/ Metal loading/ Metal alloying

Before discussing metal loading and its effects on MoS_2 system, it is necessary to understand differences between the terms 'doping' and 'loading/alloying' in materials science aspects. Heteroatom doping is referred an intentional incorporation of small amount of foreign atom into host material to improve the intrinsic properties without changing its crystal structure whereas, alloying/loading/mixing of metals or metal systems are combined form of their solid solutions [109,110]. Alloying led formation of new materials with new properties [111]. Therefore, loading of few metal atoms or nanoparticles or single metal atoms on to MoS_2 is also one of effective and efficient approaches to enhance the HER performance of MoS_2, Figure 1.15. These alloys with MoS_2 system are attributed to increase active sites, enhances the electrical conductivity, lower the resistance during reaction, which favours the higher hydrogen evolution. Here, we will be discussing how these metals loading help to increase electrocatalytic efficiency of MoS_2 for HER application based on reported work. X. Y. Xu *et.al.*, [112] decorated Pt nanoparticles on MoS_2 nanosheets deposited over carbon cloth to enhanced HER activity. Results revealed that Pt insertion made MoS_2 inert basal plane active for charge transfer.

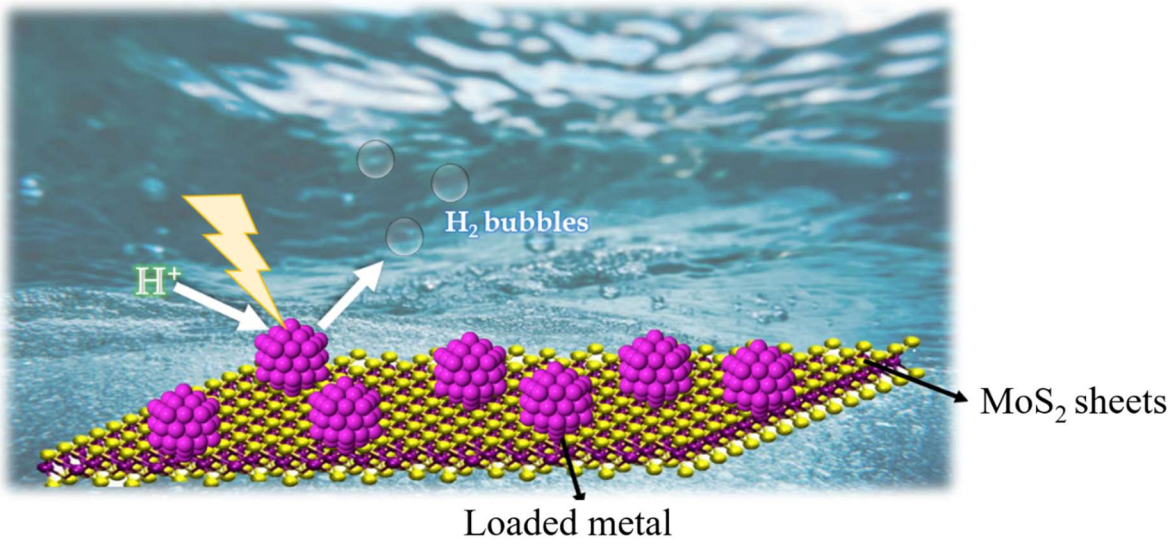

Figure 1.15: Loading of metal atoms/ nanoparticles/ nanocluster onto MoS_2 sheets for higher hydrogen evolution.

Pt@MoS_2/carbon cloth exhibited 70 mV *vs. RHE* overpotential for 10 mA.cm^{-2} cathodic current density and corresponding Tafel slope of only 36 mV.dec^{-1}. With significant HER activity, Pt@MoS_2/carbon cloth displayed electrochemical stability up to 500 min at potential of 300 mV *vs. SAE* (Saturated Ag/AgCl electrode). S. Zhao *et.al.*, [113] publishes an approach

to improve HER performance of MoS_2 *via.* incorporating Gold (Au) nanocluster as co-catalyst. Improved HER activity of Au/MoS_2 are mainly due to electronic bonding between composite and faster electron transfer. The Au/MoS_2 nanocomposite displayed improved electro-catalytic performance, requiring an overpotential of 400 mV *vs. RHE* to reach 59.3 $mA.cm^{-2}$ cathodic current density and retaining almost the same current density after 1000 CV cycles, demonstrating the nanocomposite's outstanding durability. Whereas, D. Y. Hwang *et.al.*, [114] investigated the HER activity of strain and phase engineered MoS_2 by Pt loading. The unique structure of Pt@MoS_2 displayed exceptional HER performance and had an overpotential of 125 mV *vs. RHE* to afford 10 $mA.cm^{-2}$ current density, corresponding Tafel slope of 39 $mV.dec^{-1}$ with a unique combination of 8.3 wt% loading of Pt nanoparticles, induced strain, and 1T phase. To design dual metal loaded MoS_2 systems, Y. Du *et.al.*, [115] developed atomically precise Au-Pd nanocluster on MoS_2 for robust electrocatalytic hydrogen evolution through multi step synthesis route. Improved HER catalytic activity and long-term stability up to 5000 CV cycles of system was attributed to modified electronic interaction between MoS_2 and Au_2Pd_6 nanocluster and optimized adsorption of H* on Au_2Pd_6/MoS_2 (ΔG_{H^*} min. = -0.01 eV). Au_2Pd_6/MoS_2 generated 91 $mA.cm^{-2}$ HER current at an overpotential of 400 mV *vs. RHE*, corresponding Tafel slope of 67 $mV.dec^{-1}$. This Au_2Pd_6/MoS_2 nanocluster also possessed remarkable electrocatalytic stability with almost no change in HER performance after 5000 CV cycles. Similarly, J. Wang *et.al.*, [116] investigated HER efficiency of Ag/Au nanoparticles decorated 1T/2H and 1T phase of few layered MoS_2. 1T MoS_2 decorated with Ag/Au nanoparticles displayed higher electrochemical activity in acidic electrolyte (aqueous solution of 0.5 M H_2SO_4) and exhibited higher electrochemical active surface area of 1048.6 cm^2, low charge transfer resistance of only 36 **Ω**, 201 mV *vs. RHE* overpotential at 10 $mA.cm^{-2}$ cathodic current density, corresponding Tafel slope of 53 $mV.dec^{-1}$ and an electrochemical durability up to 5000 CV cycles and slight decay after 10 hours.

Until now, pure MoS_2 system has been studied and modified to benchmark the MoS_2's efficiency as an electrocatalyst for HER application. It has been found that combination of other metal sulphide/phosphide/nitrides with MoS_2 can significantly improve the properties of matrix of MoS_2 and can lead to higher electrical conductivity and catalytic efficiency than pure MoS_2 systems [117,118].

1.8.5: Nanocomposites

Combination of MoS_2 with heterosystems is known as nanocomposite. These heterosystems benefit the efficiency of MoS_2 towards HER. Figure 1.16 shows the schematic representation of the other systems which provide a template to grow nanostructured MoS_2, tend to the surface area increment, provide large number of catalytic active edges and a clear path for charge transportation.

To synthesize the efficient nanocomposites for HER application, S. Xu *et.al.*, [119] studied the Mo metal based different chalcogenides and prepared a 3D network of $MoS_2/MoSe_2$ nanosheets with graphene using multi-step process. This nanocomposite had higher number of catalytically active sites and a smooth charge transfer. $MoS_2/MoSe_2$ nanocomposite demonstrated outstanding HER activity with an onset potential of 70 mV *vs. RHE*, 61 $mV.dec^{-1}$ corresponding Tafel slope, and long-term electrochemical durability for 1000 CV cycles.

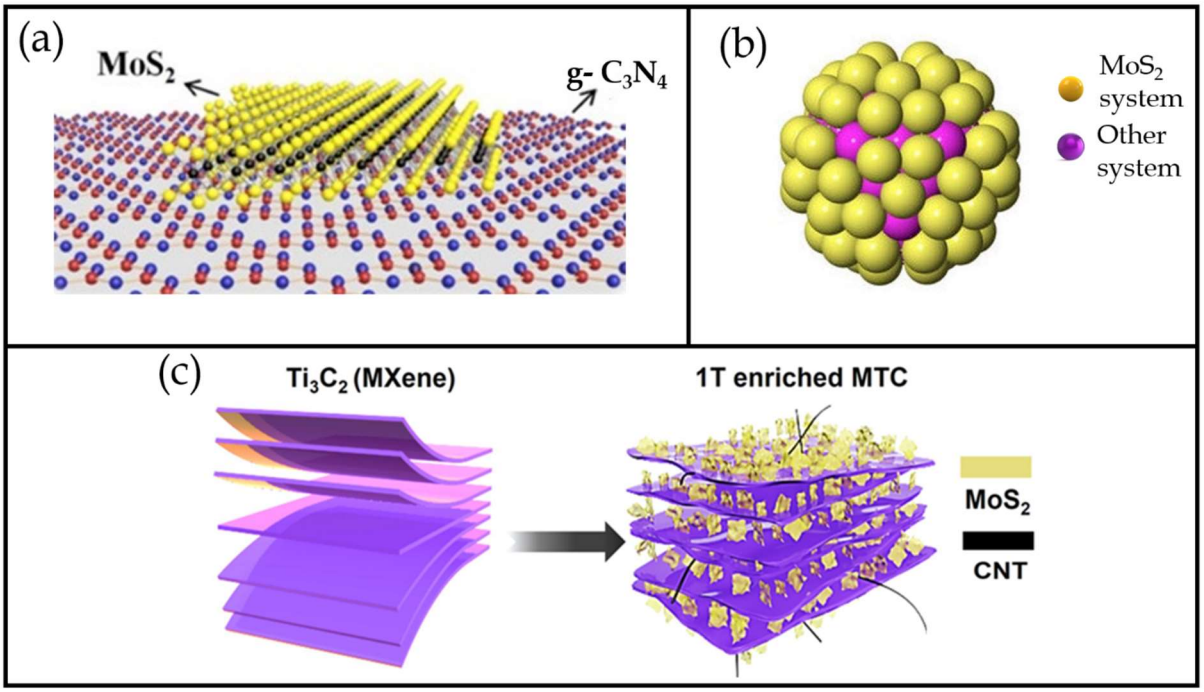

Figure 1.16: Schematic for MoS_2 nanocomposite. (a) g-C_3N_4 provides 2D large area for incorporation of MoS_2, (b) represents the formation of core shell structure with other systems, (c) MXene provides multi 2D layers for incorporation of MoS_2.

N. Zhang *et. al.* [120] created a 3D hierarchical heterostructure of MoS_2/Ni_3S_2@Ni foam that was used as a bifunctional electrocatalyst for alkaline water splitting to explore the capabilities of various metal-based chalcogenides as nanocomposite. The optimised MoS_2/Ni_3S_2 demonstrated good electrochemical activity for HER, requiring

overpotentials of 187 mV *vs. RHE* and 274 mV *vs. RHE*, respectively, to obtain 10 $mA.cm^{-2}$ and 100 $mA.cm^{-2}$. Furthermore, Y. Zhou *et. al.* [126] demonstrated improved electrocatalytic efficiency of a MoS_2/WTe_2 heterostructure for HER application. It was proved that enhanced efficiency was attributed to large-area MoS_2/WTe_2 interface which provided efficient charge injection into MoS_2. This heterostructure exhibited 140 mV *vs. RHE* overpotential to drive 10 $mA.cm^{-2}$ current density during electrochemical characterization, corresponding Tafel slope of 40 $mV.dec^{-1}$ with long-term electrochemical durability up to 3000 CV cycles. Since, MoS_2/ Metal oxides nanostructures has been reported for exhibiting excellent electrical and catalytical properties [122,123], J. Liu *et.al.*, [124] designed Co_3O_4/MoS_2 heterostructure through two step hydrothermal method and investigated its performance towards overall water splitting. Improved catalytic activity of heterostructure was attributed to optimized adsorption of intermediates and accelerated water dissociation. Co_3O_4/MoS_2 heterostructure demonstrated an overpotential of 90 mV *vs. RHE* to obtain10 $mA.cm^{-2}$ and Tafel slope of 59.5 $mV.dec^{-1}$ in 1 M KOH electrolyte. Moreover, Y. Wang *et.al.*, [121] approached metal oxide/phosphide/ chalcogenides and synthesize a unique heterostructure of Ni_2P nanoparticles decorated on the surface of MoO_2/MoS_2 sub-microwires on titanium (Ti) foil through temperature programmed sulfurization-phosphorization process. Presence of metallic MoO_2 core benefited the easy charge transfer and MoS_2/Ni_2P interface provided enhanced electrocatalytic activity to system for HER and OER application. J. Liu *et.al.*, [127] developed heterostructure of metal chalcogenide (MoS_2) and MXene ($Ti_3C_2T_x$) using liquid nitrogen freezing and annealing technique and developed nanoroll like unique morphology which provided more active sites and facilitated electron transfer. This one-of-a-kind heterostructure demonstrated improved HER performance, requiring just 30 mV *vs. RHE* onset overpotential and 152 mV *vs. RHE* overpotential to create a current density of 10 $mA.cm^{-2}$ and a Tafel slope of 70 $mV.dec^{-1}$.

In order of nanocomposites synthesis and development for efficient electrocatalyst for HER application, carbon and its allotropes have also been attracted since they are easy to synthesize. Possesses higher surface area, electrical conductivity, cost- effective and eco-friendly. The effect on MoS_2's electrocatalytic properties after composite with carbon-based materials based on literatures, have been discussed in following section.

1.8.6: MoS_2/ Carbon and its allotropes

Carbon and its allotropes are well known for their excellent electrical conductivity and higher surface area. Many researchers prefer the formation of MoS_2/Carbon materials such as

graphene, reduced graphene oxide (rGO), carbon nanotubes with single and multiple walls (SWCNTs, MWCNTs), carbon cloth, and carbon paper to increase the efficiency of MoS_2 towards HER and make it electrochemically stable.

As shown in Figure 1.17, carbon materials provide higher surface area to grow the MoS_2 nanosheets which increases the electro-catalytically active sites density in systems as well as provides higher electrical conductivity which accelerates electron transfer from material to electrolyte and results higher hydrogen evolution. We have thoroughly discussed importance of carbon materials with MoS_2 and its progress towards HER application.

Y. Li *et.al.*, [128] have grown MoS_2 nanoparticles on graphene *via.* solvothermal synthesis method and studied its catalytic efficiency towards HER. MoS_2/rGO hybrid possessed abundant exposure active edges and high electrical conductivity due to MoS_2 & rGO. This hybrid showed improved HER performance by exhibiting 100 mV *vs. RHE* onset overpotential and corresponding Tafel slope of 41 $mV.dec^{-1}$ with remarkable stability up to 1000 CV cycles. Similarly, C. B. Ma *et.al.*, [129] developed MoS_2 nanoflower embedded with rGO *via.* solvothermal method for the HER application.

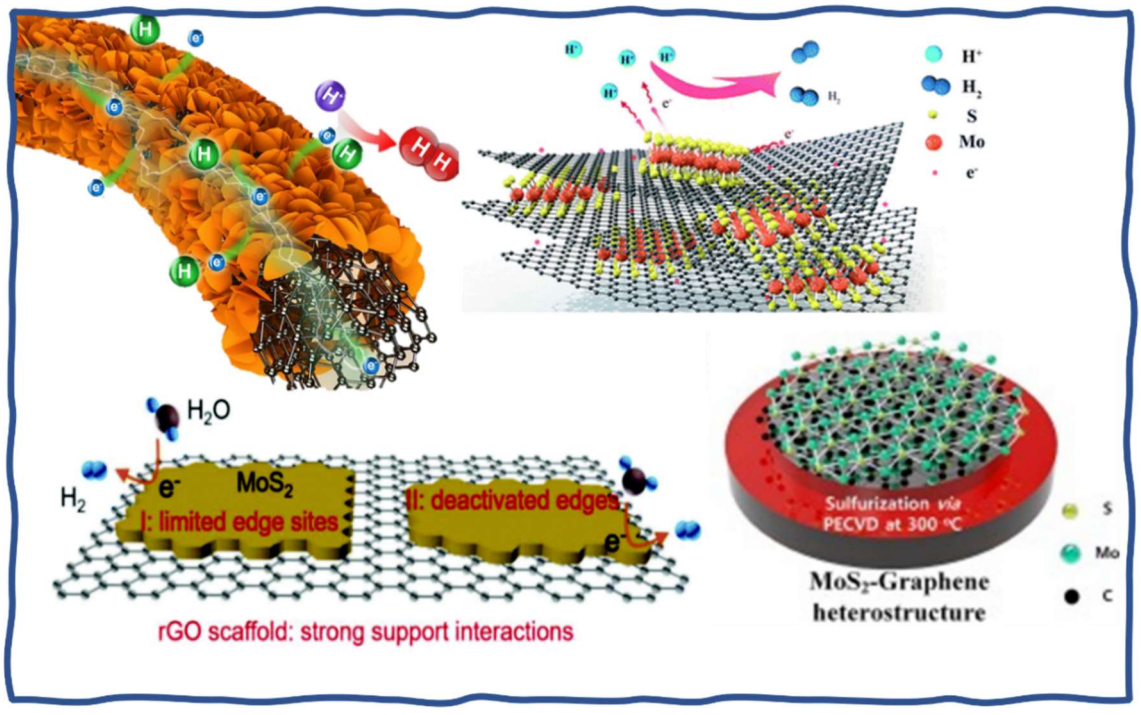

Figure 1.17: MoS_2 modified carbon allotropes for development of an efficient electrocatalyst for HER application.

The freestanding, flexible and durable MoS_2 nanoflower decorated on rGO paper exhibited efficient catalytic activity for HER by delivering 10 $mA.cm^{-2}$ current at 190 mV *vs. RHE* overpotential with 95 $mV.dec^{-1}$ Tafel slope and negligible loss in current density for 300

CV cycles. For further HER activity improvement and investigate the effect of different morphologies on MoS_2's HER efficiency, 3D hierarchical MoS_2 nanotubes supported over rGO [131], 1D graphene nanoribbon on MoS_2 nanosheets [132], have also been synthesized by different methods. In case of the carbon based materials, nanostructured MoS_2 system has been supported over N doped carbon nanofibers [133], graphene [134] [135], single walled carbon nano tubes (SWCNTs) [136], Fullerene (C_{60}) [137] etc. by using various synthesis methods like CVD, electro-spinning, hydrothermal route etc.

After the detail investigation of efforts to make MoS_2 as an efficient HER electrocatalyst, it was found that nanostructuring, defect formation, phase transformation, heteroatom doping are significantly efficient approaches of enhancing the electrocatalytic activity of MoS_2. Still, there is lot of scope to study the MoS_2 system and for the modification of its electrocatalytic properties for HER application.

1.9: Scope of work

The gradual increment in research work and related publications per year can be in Figure 1.18 which clearly displays the interest of researchers to improve the efficiency of MoS_2 as an electrocatalyst towards HER application.

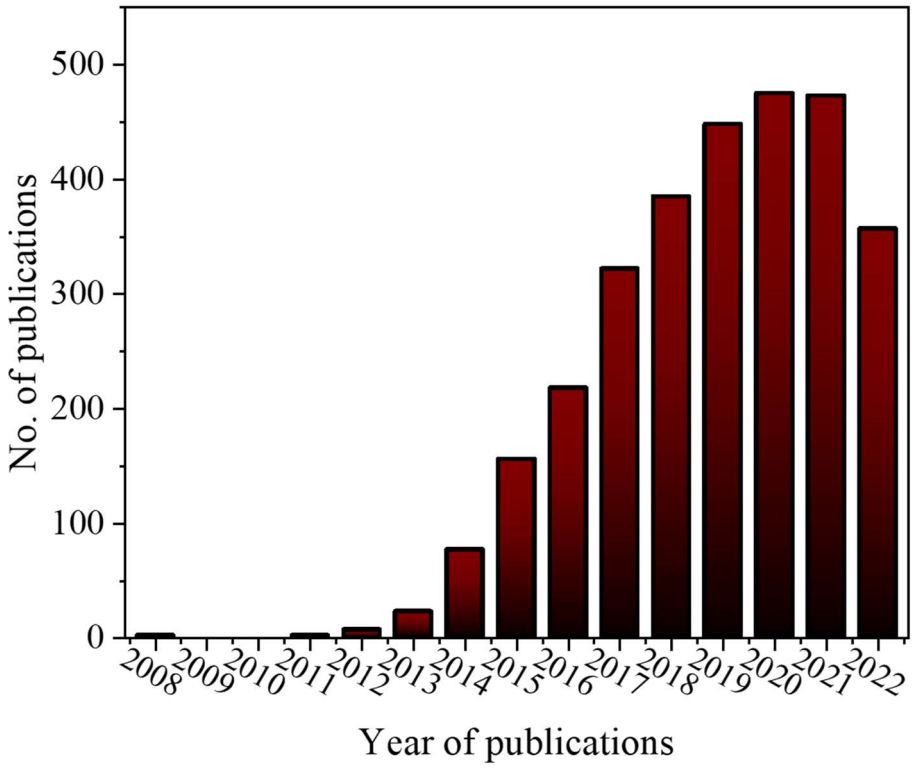

Figure 1.18: Number of published papers per year for MoS_2 as an electrocatalyst for HER application (source: 'Web of Science').

Even though MoS_2 is being researched since several years, its efficiency is yet to be accepted at industrial scale. We have discussed about various approaches to improve the efficiency of MoS_2 by tuning its intrinsic conductivity, increment in active sites population, phase transition, formation of heterostructures, incorporation of foreign elements etc.

It is evident from extensive literature survey, that electrocatalytic hydrogen evolution using MoS_2 as an electrocatalyst is an emerging area for green energy generation as it has the potential to replace Pt & its group materials. In addition, MoS_2 is an economic and cost-effective material which is acceptable at commercial level. Owing to extraordinary properties of metallic (1T)-MoS_2, the major focus of researchers is to develop a stable metallic phase (1T) of nanostructured MoS_2 by use cost-effective techniques. Synthesis of 1T-MoS_2 by intercalation method is not being accepted since it is not cost-effective method, produces hazardous compound and 1T MoS_2 synthesized by this method is also not electrochemically stable.

In case of CVD method, it is the oldest method for the development of one or few layered MoS_2 thin film with uniform thickness over the substrates. But this method requires uses flammable, toxic precursor gases as well as sophisticated experimental arrangement like reactor, vacuum system make this method non-scalable and not acceptable for the development of cost-effective and economic electrocatalyst. Additionally, both processes *i.e.*, intercalation and CVD require two or several steps for the synthesis of MoS_2. Since, this thesis focuses the development of nanostructured MoS_2 with single step and minimum possible experimental efforts, solvothermal and hydrothermal processes meet the criteria among the available synthesis methods. Solvothermal method has been found one of the simple routes to synthesize nanostructured MoS_2 but the choice of suitable organic solvents limits it to be accepted for scalable production. Whereas, hydrothermal synthesis route is found as simple, facile, scalable, and cost-effective route for synthesis of nanostructured MoS_2 and it does not require costly precursors/solvent, any special environment arrangement like high temperature, pressure. Therefore, present thesis approached single step hydrothermal route for synthesis of nanostructured and heteroatom doped MoS_2.

1.10: Objectives of present work

As discussed in previous sections, nanostructuring and heteroatom doping are the effective ways to increase the HER efficiency of MoS_2, as they provide the new active sites, defects, sulfur vacancies, phase transformation of MoS_2 from 2H into 1T and stability to MoS2

system. Therefore, attempts for nanostructuring and heteroatom doping of MoS_2 and investigation of electrocatalytic efficiency of modified MoS_2 system towards HER application will be studied. As shown in Figure 1.19, objectives of the study are containing two main sections which are as follows:

1. Nanostructuring of MoS_2: Nanostructuring of MoS_2 is discussed in two sub-sections including the nanostructured powder synthesis followed by preparation of electrodes and MoS_2 film preparation by *in-situ* deposition.

a. **MoS_2 electrocatalyst synthesis**: Synthesis of nanostructured MoS_2 electrocatalyst using single step hydrothermal technique and optimization of synthesis parameters to develop MoS_2 and film preparation as an efficient, stable, and environmentally benign electrocatalyst for HER use.

b. **MoS_2 film deposition**: *In-situ* deposition of MoS_2 film over large area conducting substrate using hydrothermal method and physico-chemical & electrochemical properties investigations of *in-situ* deposited MoS_2 film. This sub-part also includes the stability measurements and rate estimation of electrocatalytically evolved hydrogen gas during HER process.

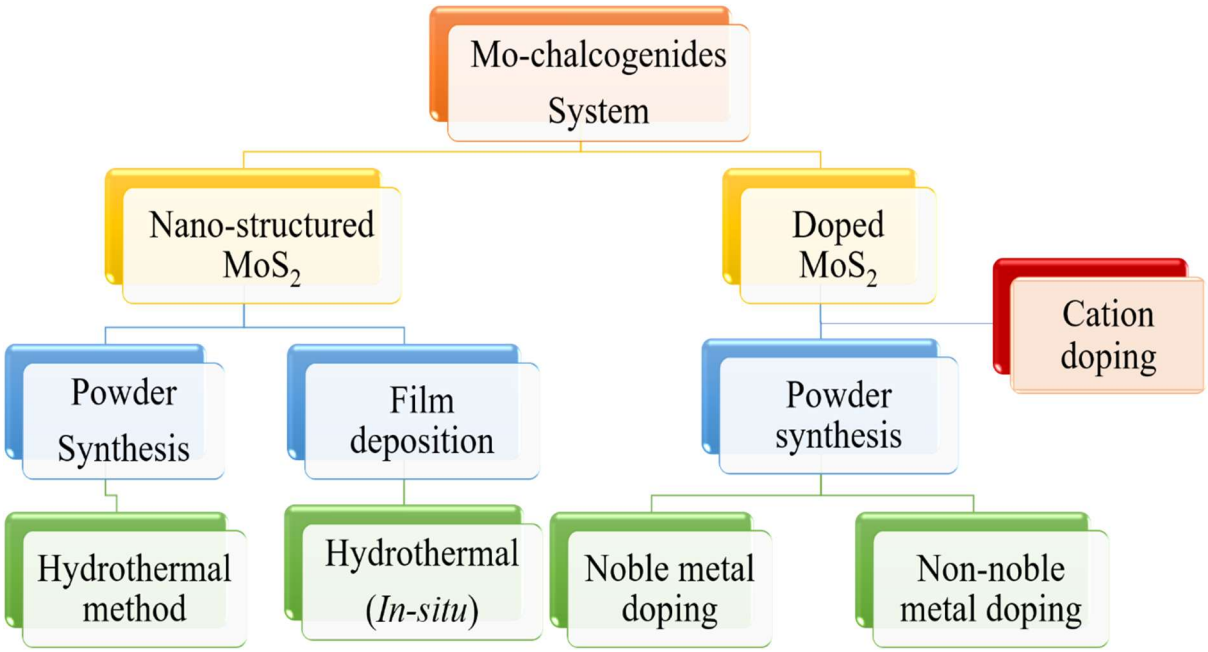

Figure 1.19: Objectives of Ph.D. research work.

2. Noble metal [Palladium (Pd)] doped MoS_2: Synthesis of Pd doped MoS_2 using one-step hydrothermal method and optimization of Pd dopant concentration for higher performance

HER application. This section also includes the electrocatalytic water splitting by utilizing Pd doped MoS_2 as HER cathode/ bare C.P. as OER anode and rate estimation of real -time electrocatalytically evolved hydrogen and oxygen.

3. Transition metal [Vanadium (V)] doped MoS_2: Single-step hydrothermal synthesis of V doped nanostructured MoS_2 electrocatalyst and optimization content of V as dopant in MoS_2 for efficient electrocatalytic performance during HER process. This section also contains the overall water splitting by utilizing V doped MoS_2 as HER cathode/ bare C.P. as OER anode and rate estimation of real -time evolved hydrogen and oxygen.

1.11: References

1. A. Midilli, M. Ay, I. Dincer, and M. A. Rosen, Renew. Sustain. Energy Rev. **9**, 255 (2005).

2. T. N. Veziroglu, Energy Procedia **29**, 654 (2012).

3. T. N. Veziroğlu and S. Şahi˙n, Energy Convers. Manag. **49**, 1820 (2008).

4. D. A. J. Rand, J. Solid State Electrochem. **15**, 1579 (2011).

5. L. Chiari and A. Zecca, Energy Policy **39**, 5026 (2011).

6. J. G. J. and P. J. A. H. . Olivier, PBL Netherlands Environ. Assess. Agency 1 (2020).

7. N. P. Brandon and Z. Kurban, Philos. Trans. R. Soc. A Math. Phys. Eng. Sci. **375**, 20160400 (2017).

8. D. J. Durbin and C. Malardier-Jugroot, Int. J. Hydrogen Energy **38**, 14595 (2013).

9. M. Götz, J. Lefebvre, F. Mörs, A. McDaniel Koch, F. Graf, S. Bajohr, R. Reimert, and T. Kolb, Renew. Energy **85**, 1371 (2016).

10. I. Yüksel, Renew. Sustain. Energy Rev. **14**, 462 (2010).

11. W. T. Xie, Y. J. Dai, R. Z. Wang, and K. Sumathy, Renew. Sustain. Energy Rev. **15**, 2588 (2011).

12. C. Bueno and J. A. Carta, Sol. Energy **78**, 396 (2005).

13. Global Primary Energy Consumption by Source, IE02021 Reference Case (2010-2050) Source: U.S. Energy Information Administration, International Energy Outlook 2021.

14. Neha and R. Joon, J. Phys. Conf. Ser. **1979**, 12023 (2021).

15. Y. Dou, L. Sun, J. Ren, and L. Dong, in edited by A. Scipioni, A. Manzardo, and J. B. T.-H. E. Ren (Academic Press, 2017), pp. 277–305.

16. A. Kovač, M. Paranos, and D. Marciuš, Int. J. Hydrogen Energy **46**, 10016 (2021).

17. K. T. Møller, T. R. Jensen, E. Akiba, and H. Li, Prog. Nat. Sci. Mater. Int. **27**, 34 (2017).

18. J. P. Rodrigue, The Geography of Transport Systems. 5th Edition (2020).

19. M. Balat, Energy Sources, Part A Recover. Util. Environ. Eff. **31**, 39 (2008).

20. K. Yamashita and L. Barreto, Energy **30**, 2453 (2005).

21. C. Song, Q. Liu, N. Ji, Y. Kansha, and A. Tsutsumi, Appl. Energy **154**, 392 (2015).

22. B. Zhao, X. Zhang, L. Sun, G. Meng, L. Chen, and Y. Xiaolu, Int. J. Hydrogen Energy **35**, 2606 (2010).

23. N. Sánchez-Bastardo, R. Schlögl, and H. Ruland, Ind. Eng. Chem. Res. **60**, 11855 (2021).

24. B. Zhang, Q. Lu, W. Huang, Y. Chen, W. Yan, B. Yu, X. Yang, and J. Zhang, Int. J. Hydrogen Energy **47**, 6605 (2022).

25. K. Zeng and D. Zhang, Prog. Energy Combust. Sci. **36**, 307 (2010).

26. K. Mazloomi, N. B. Sulaiman, and H. Moayedi, Int. J. Electrochem. Sci. **7**, 3314 (2012).

27. A. Pareek, R. Dom, J. Gupta, J. Chandran, V. Adepu, and P. H. Borse, Mater. Sci. Energy Technol. **3**, 319 (2020).

28. H. A. M. Snelders, Ambix **26**, 116 (1979).

29. J. Janata, Angew. Chemie Int. Ed. **50**, 9538 (2011).

30. H. Jin, C. Guo, X. Liu, J. Liu, A. Vasileff, Y. Jiao, Y. Zheng, and S.-Z. Qiao, Chem. Rev. **118**, 6337 (2018).

31. J. Hou, Y. Wu, B. Zhang, S. Cao, Z. Li, and L. Sun, Adv. Funct. Mater. **29**, 1808367 (2019).

32. Q. Gao, W. Zhang, Z. Shi, L. Yang, and Y. Tang, Adv. Mater. **31**, 1802880 (2019).

33. M. Fang, G. Dong, R. Wei, and J. C. Ho, Adv. Energy Mater. **7**, 1700559 (2017).

34. B. E. Conway and B. V Tilak, Electrochim. Acta **47**, 3571 (2002).

35. Q. Lei, B. Wang, P. Wang, and S. Liu, J. Energy Chem. **38**, 162 (2019).

36. J. Zhu, L. Hu, P. Zhao, L. Y. S. Lee, and K.-Y. Wong, Chem. Rev. **120**, 851 (2020).

37. M. Zeng and Y. Li, J. Mater. Chem. A **3**, 14942 (2015).

38. C. C. L. McCrory, S. Jung, J. C. Peters, and T. F. Jaramillo, J. Am. Chem. Soc. **135**, 16977 (2013).

39. J. Lu, S. Yin, and P. K. Shen, Electrochem. Energy Rev. **2**, 105 (2019).

40. W. Feng, W. Pang, Y. Xu, A. Guo, X. Gao, X. Qiu, and W. Chen, ChemElectroChem **7**, 31 (2020).

41. R. D. L. Smith, M. S. Prévot, R. D. Fagan, S. Trudel, and C. P. Berlinguette, J. Am. Chem. Soc. **135**, 11580 (2013).

42. P. Sabatier, Berichte Der Dtsch. Chem. Gesellschaft **44**, 1984 (1911).

43. R. Parsons, Trans. Faraday Soc. **54**, 1053 (1958).

44. J. K. Nørskov, T. Bligaard, A. Logadottir, J. R. Kitchin, J. G. Chen, S. Pandelov, and U. Stimming, J. Electrochem. Soc. **152**, J23 (2005).

45. E. Skúlason, V. Tripkovic, M. E. Björketun, S. Gudmundsdóttir, G. Karlberg, J. Rossmeisl, T. Bligaard, H. Jónsson, and J. K. Nørskov, J. Phys. Chem. C **114**, 18182 (2010).

46. S. Wang, A. Lu, and C.-J. Zhong, Nano Converg. **8**, 4 (2021).

47. N. Dyantyi, J. C. Calderón Gómez, L. Mekuto, P. Bujlo, and G. Pattrick, in edited by G. B. T.-P. E. M. F. C. Kaur (Elsevier, 2022), pp. 55–70.

48. C. Li and J.-B. Baek, ACS Omega **5**, 31 (2020).

49. D. Bessarabov, H. Wang, H. Li, and N. Zhao, *PEM Electrolysis for Hydrogen Production: Principles and Applications* (CRC press, 2016).

50. Z. Zhao, H. Liu, W. Gao, W. Xue, Z. Liu, J. Huang, X. Pan, and Y. Huang, J. Am. Chem. Soc. **140**, 9046 (2018).

51. Y. Xie, J. Cai, Y. Wu, Y. Zang, X. Zheng, J. Ye, P. Cui, S. Niu, Y. Liu, J. Zhu, X. Liu, G. Wang, and Y. Qian, Adv. Mater. **31**, e1807780 (2019).

52. C. Li and J. B. Baek, ACS Omega **5**, 31 (2020).

53. J. Cai, R. Javed, D. Ye, H. Zhao, and J. Zhang, J. Mater. Chem. A **8**, 22467 (2020).

54. S. Yang and X. Luo, Nanoscale **6**, 4438 (2014).

55. T. Chao, Y. Hu, X. Hong, and Y. Li, ChemElectroChem **6**, 289 (2019).

56. S. Mansingh, K. K. Das, and K. Parida, Sustain. Energy Fuels **5**, 1952 (2021).

57. Y. Zhu, Q. Lin, Y. Zhong, H. A. Tahini, Z. Shao, and H. Wang, Energy Environ. Sci. **13**, 3361 (2020).

58. D. Balaji, K. Premnath, and M. Jagannathan, in edited by P. Arunachalam, J. Theerthagiri, A. M. Al-Mayouf, M. Y. Choi, and M. B. T.-O. F. N. for E. S. and C. A. Jagannathan (Elsevier, 2022), pp. 451–466.

59. S. Rani, M. Sharma, D. Verma, A. Ghanghass, R. Bhatia, and I. Sameera, Mater. Sci. Semicond. Process. **139**, 106313 (2022).

60. M.-H. Kang, D. Lee, J. Sung, J. Kim, B. H. Kim, and J. Park, in edited by D. L. Andrews, R. H. Lipson, and T. B. T.-C. N. and N. (Second E. Nann (Academic Press, Oxford, 2019), pp. 55–90.

61. Q. Fu, J. Han, X. Wang, P. Xu, T. Yao, J. Zhong, W. Zhong, S. Liu, T. Gao, Z. Zhang, L. Xu, and B. Song, Adv. Mater. **33**, 1907818 (2021).

62. D. Gupta, V. Chauhan, and R. Kumar, Inorg. Chem. Commun. **121**, 108200 (2020).

63. O. Samy, S. Zeng, M. D. Birowosuto, and A. El Moutaouakil, Crystals **11**, (2021).

64. H. Eidsvåg, M. Rasukkannu, D. Velauthapillai, and P. Vajeeston, RSC Adv. **11**, 3759 (2021).

65. B. Schönfeld, J. J. Huang, and S. C. Moss, Acta Crystallogr. Sect. B **39**, 404 (1983).

66. W. S. Yun, S. W. Han, S. C. Hong, I. G. Kim, and J. D. Lee, Phys. Rev. B **85**, 33305 (2012).

67. K. Kobayashi and J. Yamauchi, Phys. Rev. B **51**, 17085 (1995).

68. S. Jayabal, J. Wu, J. Chen, D. Geng, and X. Meng, Mater. Today Energy **10**, 264 (2018).

69. H. Tributsch and J. C. Bennett, J. Electroanal. Chem. Interfacial Electrochem. **81**, 97 (1977).

70. B. Hinnemann, P. G. Moses, J. Bonde, K. P. Jørgensen, J. H. Nielsen, S. Horch, I. Chorkendorff, and J. K. Nørskov, J. Am. Chem. Soc. **127**, 5308 (2005).

71. X. Zou and Y. Zhang, Chem. Soc. Rev. **44**, 5148 (2015).

72. C. A. C.-R. and N. Alonso-Vante, J. Mex. Chem. Soc. **63**, 28 (2019).

73. M. A. Lukowski, A. S. Daniel, F. Meng, A. Forticaux, L. Li, and S. Jin, J. Am. Chem. Soc. **135**, 10274 (2013).

74. S. Jiménez Sandoval, D. Yang, R. F. Frindt, and J. C. Irwin, Phys. Rev. B **44**, 3955 (1991).

75. V. P. Kumar and D. K. Panda, ECS J. Solid State Sci. Technol. **11**, 33012 (2022).

76. T. F. Jaramillo, K. P. Jørgensen, J. Bonde, J. H. Nielsen, S. Horch, and I. Chorkendorff, Science (80-.). **317**, 100 (2007).

77. D. Kong, H. Wang, J. J. Cha, M. Pasta, K. J. Koski, J. Yao, and Y. Cui, Nano Lett. **13**, 1341 (2013).

78. Z. Wu, B. Fang, Z. Wang, C. Wang, Z. Liu, F. Liu, W. Wang, A. Alfantazi, D. Wang, and D. P. Wilkinson, ACS Catal. **3**, 2101 (2013).

79. S. Murugesan, A. Akkineni, B. P. Chou, M. S. Glaz, D. A. Vanden Bout, and K. J. Stevenson, ACS Nano **7**, 8199 (2013).

80. D. Wang, Z. Wang, C. Wang, P. Zhou, Z. Wu, and Z. Liu, Electrochem. Commun. **34**, 219 (2013).

81. D. Wang, Z. Pan, Z. Wu, Z. Wang, and Z. Liu, J. Power Sources **264**, 229 (2014).

82. J. Benson, M. Li, S. Wang, P. Wang, and P. Papakonstantinou, ACS Appl. Mater. Interfaces **7**, 14113 (2015).

83. A. Ambrosi, X. Chia, Z. Sofer, and M. Pumera, Electrochem. Commun. **54**, 36 (2015).

84. S. Muralikrishna, K. Manjunath, D. Samrat, V. Reddy, T. Ramakrishnappa, and D. H. Nagaraju, RSC Adv. **5**, 89389 (2015).

85. H. Huang, L. Chen, C. Liu, X. Liu, S. Fang, W. Liu, and Y. Liu, J. Mater. Chem. A **4**, 14577 (2016).

86. X. Kong, X. Shen, C. Zhang, S. N. Oliaee, and Z. Peng, Inorg. Chem. Front. **3**, 1376 (2016).

87. X. Shang, W.-H. Hu, X. Li, B. Dong, Y.-R. Liu, G.-Q. Han, Y.-M. Chai, and C.-G. Liu, Electrochim. Acta **224**, 25 (2017).

88. Z. Wang, Q. Li, H. Xu, C. Dahl-Petersen, Q. Yang, D. Cheng, D. Cao, F. Besenbacher, J. V Lauritsen, S. Helveg, and M. Dong, Nano Energy **49**, 634 (2018).

89. W. Qiao, S. Yan, X. Song, X. Zhang, Y. Sun, X. Chen, W. Zhong, and Y. Du, RSC Adv. **5**, 97696 (2015).

90. Y. Wang, B. J. Carey, W. Zhang, A. F. Chrimes, L. Chen, K. Kalantar-zadeh, J. Z. Ou, and T. Daeneke, J. Phys. Chem. C **120**, 2447 (2016).

91. Z. Guo, Q. Ma, Z. Xuan, F. Du, and Y. Zhong, RSC Adv. **6**, 16730 (2016).

92. J. Yang, K. Wang, J. Zhu, C. Zhang, and T. Liu, ACS Appl. Mater. Interfaces **8**, 31702 (2016).

93. F. Z. Wang, M. J. Zheng, B. Zhang, C. Q. Zhu, Q. Li, L. Ma, and W. Z. Shen, Sci. Rep. **6**, 31092 (2016).

94. D. Wang, X. Zhang, S. Bao, Z. Zhang, H. Fei, and Z. Wu, J. Mater. Chem. A **5**, 2681 (2017).

95. C. Tsai, H. Li, S. Park, J. Park, H. S. Han, J. K. Nørskov, X. Zheng, and F. Abild-Pedersen, Nat. Commun. **8**, 15113 (2017).

96. H. Li, C. Tsai, A. L. Koh, L. Cai, A. W. Contryman, A. H. Fragapane, J. Zhao, H. S. Han, H. C. Manoharan, F. Abild-Pedersen, J. K. Nørskov, and X. Zheng, Nat. Mater. **15**, 48 (2016).

97. Y. Yin, J. Han, Y. Zhang, X. Zhang, P. Xu, Q. Yuan, L. Samad, X. Wang, Y. Wang, Z. Zhang, P. Zhang, X. Cao, B. Song, and S. Jin, J. Am. Chem. Soc. **138**, 7965 (2016).

98. D. Kiriya, P. Lobaccaro, H. Y. Y. Nyein, P. Taheri, M. Hettick, H. Shiraki, C. M. Sutter-Fella, P. Zhao, W. Gao, R. Maboudian, J. W. Ager, and A. Javey, Nano Lett. **16**, 4047 (2016).

99. J. Deng, H. Li, J. Xiao, Y. Tu, D. Deng, H. Yang, H. Tian, J. Li, P. Ren, and X. Bao, Energy Environ. Sci. **8**, 1594 (2015).

100. C.-H. An, W. Kang, Q.-B. Deng, and N. Hu, Rare Met. **41**, 378 (2022).

101. Z. Luo, Y. Ouyang, H. Zhang, M. Xiao, J. Ge, Z. Jiang, J. Wang, D. Tang, X. Cao, C. Liu, and W. Xing, Nat. Commun. **9**, 1 (2018).

102. D. Han, Z. Luo, Y. Li, N. Gao, J. Ge, C. Liu, and W. Xing, Appl. Surf. Sci. **529**, 147117 (2020).

103. Y. Zhan, X. Zhou, H. Nie, X. Xu, X. Zheng, J. Hou, H. Duan, S. Huang, and Z. Yang, J. Mater. Chem. A **7**, 15599 (2019).

104. L. Ma, L. Xu, X. Zhou, X. Xu, J. Luo, and L. Zhang, Colloids Surfaces A Physicochem. Eng. Asp. **509**, 140 (2016).

105. J. Pan, C. Song, X. Wang, X. Yuan, Y. Fang, C. Guo, W. Zhao, and F. Huang, Inorg. Chem. Front. **4**, 1895 (2017).

106. X. Kong, N. Wang, Q. Zhang, J. Liang, M. Wang, C. Wei, X. Chen, Y. Zhao, and X. Zhang, ChemistrySelect **3**, 9493 (2018).

107. J. Rong, Y. Ye, J. Cao, X. Liu, H. Fan, S. Yang, M. Wei, L. Yang, J. Yang, and Y. Chen, Appl. Surf. Sci. **579**, 152216 (2022).

108. T. Liu, C. Fang, B. Yu, Y. You, H. Niu, R. Zhou, J. Zhang, and J. Xu, Inorg. Chem. Front. **7**, 2497 (2020).

109. W. D. Callister Jr and D. G. Rethwisch, *Materials Science and Engineering - An Introduction* (2015).

110. Y. Zhou, Z. Zhou, M. Chen, Y. Zong, J. Huang, S. Pang, and N. P. Padture, J. Mater. Chem. A **4**, 17623 (2016).

111. J. Suh, T. Sarkar, H. S. Choe, J. Park, T. Venkatesan, and J. Wu, Appl. Phys. Lett. **113**, 22103 (2018).

112. X. Y. Xu, X. F. Dong, Z. J. Bao, R. Wang, J. G. Hu, and H. B. Zeng, J. Mater. Chem. A **5**, 22654 (2017).

113. S. Zhao, R. Jin, Y. Song, H. Zhang, S. D. House, J. C. Yang, and R. Jin, Small **13**, 1701519 (2017).

114. D. Y. Hwang, K. H. Choi, J. E. Park, and D. H. Suh, Phys. Chem. Chem. Phys. **19**, 18356 (2017).

115. Y. Du, J. Xiang, K. Ni, Y. Yun, G. Sun, X. Yuan, H. Sheng, Y. Zhu, and M. Zhu, Inorg. Chem. Front. **5**, 2948 (2018).

116. J. Wang, W. Fang, Y. Hu, Y. Zhang, J. Dang, Y. Wu, H. Zhao, and Z. Li, Catal. Sci. Technol. **10**, 154 (2020).

117. N. Mphuthi, L. Sikhwivhilu, and S. S. Ray, Biosensors **12**, (2022).

118. T. Wang, S. Chen, H. Pang, H. Xue, and Y. Yu, Adv. Sci. **4**, 1600289 (2017).

119. S. Xu, Z. Lei, and P. Wu, J. Mater. Chem. A **3**, 16337 (2015).

120. N. Zhang, J. Lei, J. Xie, H. Huang, and Y. Yu, RSC Adv. **7**, 46286 (2017).

121. Y. Wang, T. Williams, T. Gengenbach, B. Kong, D. Zhao, H. Wang, and C. Selomulya, Nanoscale **9**, 17349 (2017).

122. A. Huang, Y. He, Y. Zhou, Y. Zhou, Y. Yang, J. Zhang, L. Luo, Q. Mao, D. Hou, and J. Yang, J. Mater. Sci. **54**, 949 (2019).

123. M. S. Chavali and M. P. Nikolova, SN Appl. Sci. **1**, 607 (2019).

124. J. Liu, J. Wang, B. Zhang, Y. Ruan, H. Wan, X. Ji, K. Xu, D. Zha, L. Miao, and J. Jiang, J. Mater. Chem. A **6**, 2067 (2018).

125. L. Zhang, Y. Guo, A. Iqbal, B. Li, D. Gong, W. Liu, K. Iqbal, W. Liu, and W. Qin, Int. J. Hydrogen Energy **43**, 1251 (2018).

126. Y. Zhou, J. V Pondick, J. L. Silva, J. M. Woods, D. J. Hynek, G. Matthews, X. Shen, Q. Feng, W. Liu, Z. Lu, Z. Liang, B. Brena, Z. Cai, M. Wu, L. Jiao, S. Hu, H. Wang, C. M. Araujo, and J. J. Cha, Small **15**, 1900078 (2019).

127. J. Liu, Y. Liu, D. Xu, Y. Zhu, W. Peng, Y. Li, F. Zhang, and X. Fan, Appl. Catal. B Environ. **241**, 89 (2019).

128. Y. Li, H. Wang, L. Xie, Y. Liang, G. Hong, and H. Dai, J. Am. Chem. Soc. **133**, 7296 (2011).

129. C.-B. Ma, X. Qi, B. Chen, S. Bao, Z. Yin, X.-J. Wu, Z. Luo, J. Wei, H.-L. Zhang, and H. Zhang, Nanoscale **6**, 5624 (2014).

130. K. Zhang, H.-J. Kim, J.-T. Lee, G.-W. Chang, X. Shi, W. Kim, M. Ma, K. Kong, J.-M. Choi, M.-S. Song, and J. H. Park, ChemSusChem **7**, 2489 (2014).

131. L. Song, M. Zhao, X. Li, Z. Zhang, and L. Qu, RSC Adv. **6**, 70740 (2016).

132. H. Gu, L. Zhang, Y. Huang, Y. Zhang, W. Fan, and T. Liu, RSC Adv. **6**, 13757 (2016).

133. H. Zhu, M. Du, M. Zhang, M. Zou, T. Yang, S. Wang, J. Yao, and B. Guo, Chem.

Commun. **50**, 15435 (2014).

134. H. Li, K. Yu, C. Li, Z. Tang, B. Guo, X. Lei, H. Fu, and Z. Zhu, Sci. Rep. **5**, 18730 (2015).

135. Z. H. Deng, L. Li, W. Ding, K. Xiong, and Z. D. Wei, Chem. Commun. **51**, 1893 (2015).

136. L. Chen, M. Zeng, W. Zhang, L. He, W. He, F. Yang, and X. Zhang, ChemCatChem **10**, 1128 (2018).

137. A. R. Puente Santiago, T. He, O. Eraso, M. A. Ahsan, A. N. Nair, V. S. N. Chava, T. Zheng, S. Pilla, O. Fernandez-Delgado, A. Du, S. T. Sreenivasan, and L. Echegoyen, J. Am. Chem. Soc. **142**, 17923 (2020).

CHAPTER 2

EXPERIMETNAL METHODOLOGY

&

CHARACTERIZATION TECHNIQUES

This chapter discusses about the specifications of materials/ precursors used for the synthesis of nanostructured and doped MoS_2. Brief introduction about hydrothermal synthesis method has been discussed. Steps followed during solution preparation for hydrothermal reaction to synthesize the nanostructured MoS_2, Pd doped MoS_2, V doped MoS_2 *via.* single step, details of synthesis parameters for each sample and working electrode preparation have also been detailed. This chapter also discusses the facilities used, their respective model and specifications for physico-chemical as well as electrochemical properties investigations for the synthesized systems.

2.1: Materials

The following are the details of the precursors, solvents, and chemicals utilized in the development of nanostructured and heteroatom doped MoS_2:

Ammonium Molybdate tetrahydrate [$(NH_4)_6Mo_7O_{24}.4H_2O$, M.W.: 1235.96, make: Qualigens]; Hydroxylamine Hydrochloride ($HO.NH_3CL$, M. W. 69.49, make: Fisher Scientific); Thiourea ($CH_4.N_2S$, M. W.: 76.12, make: Fisher Scientific); Palladium (II) Chloride with Pd content 59.5% ($PdCl_2$, M. W.: 177.31, make: Alfa Aesar); Chloroplatinic acid with Pt content 40% ($H_2PtCl_6.XH_2O$, M. W.: 409.81, make: Finar); Ammonium metavanadate (H4NO3V, M. W.: 116.98, make: Sigma Aldrich) Sodium hydroxide (NaOH, M. W., 40.00, make: Fisher Scientific); Nafion 117 solution ($C_9HF_{17}O_5S$, M. W.: 544.14, 5 wt. % in mixture of lower aliphatic alcohols and water, contains 45% water make: Sigma Aldrich); Platinized Carbon, 20 wt% Pt loading on carbon (Pt/C, M. W.: 195.08, make: Sigma Aldrich); Sulfuric acid (H_2SO_4, M. W.: 98.07, make: Fisher Scientific); Nitric acid (HNO_3, M. W.: 63.01, make: Fisher Scientific); Hydrochloric acid (HCl, M. W.: 36.45, make: Fisher Scientific); De-Ionised Water (D.I. Water, Resistivity: 18 MΩ-cm, make: Millipore); Ethanol 99.9%, Analytical Reagent ($CH_3.CH_2OH$, M.W.: 46.06, make: Changshu song sheng fine chemicals); Iso-propyl alcohol (IPA) [$(CH_3)_2CHOH$, M. W.: 60.10, make: Fisher Scientific].

2.2: Method of synthesis

For the single step synthesis of nanostructured MoS_2, *in situ* deposition of MoS_2 over large area conducting substrate and heteroatom doped nanostructured MoS_2 p, hydrothermal synthesis route has been adopted. Hydrothermal method is well known as a one of the simple, facile, eco-friendly, scalable, and cost-effective routes for nanomaterials production [1]. This synthesis method terms as hydrothermal (hydro + thermal) since it involves heterogeneous reaction in solvent (aqueous or non-aqueous) at pressure higher than the atmospheric pressure and higher temperature [2]. Figure 2.1 displays the steps followed during synthesis of nanostructured and doped MoS_2 systems.

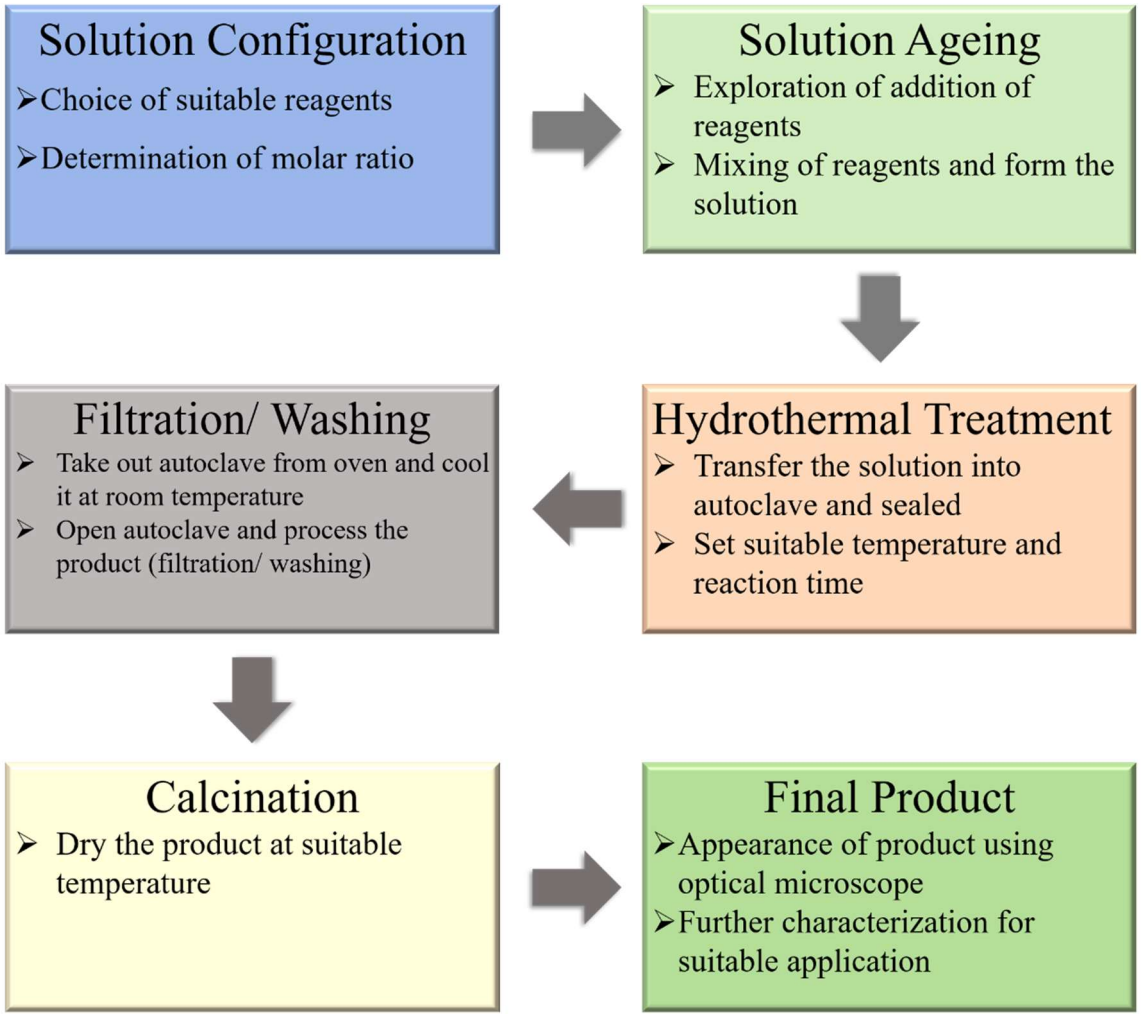

Figure 2.1: Schematic representation of step followed during synthesis of nanostructured and doped MoS_2.

Hydrothermal synthesis takes place in special type of closed vessel, called as 'Autoclave reactor.' Autoclave reactor made with stainless steel (S.S.) has been used for

hydrothermal process which was able to sustain at higher pressure and higher temperature without any compositional or structural change.

2.2.1: Hydrothermal synthesis of nanostructured MoS_2 electrocatalyst

Figure 2.2 displays schematic representation of the procedure followed for the synthesis of nanostructured MoS_2 using hydrothermal method. 4×10^{-3} M aqueous solution of ammonium molybdate tetrahydrate was prepared.

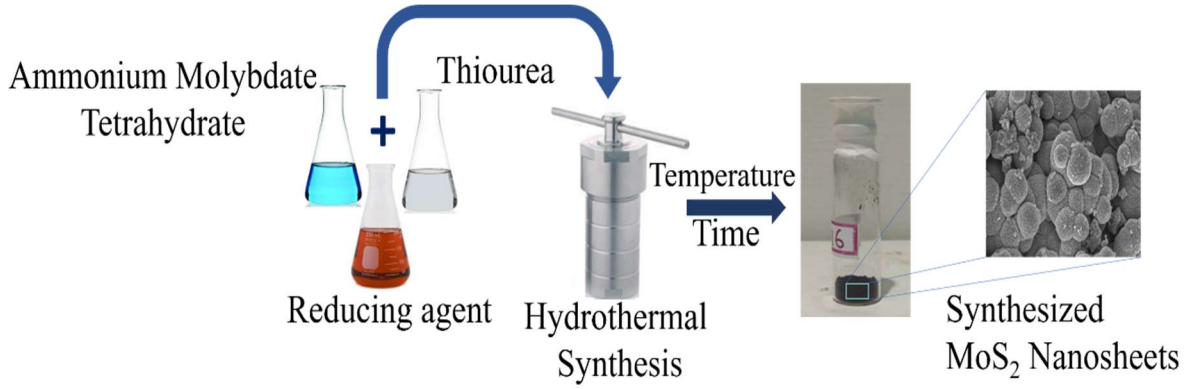

Figure 2.2: Hydrothermal synthesis procedure for nanostructured MoS_2.

Table 2.1. Synthesis parameters for respective nanostructured MoS_2.

Sample Name	Reaction temperature (^{0}C)	Reaction time (hours)	Molarity of Reducing agent *(Molar)*
MS24	180	24	7×10^{-2}
MS30	180	30	7×10^{-2}
MS36	180	36	7×10^{-2}
MS-R0	180	24	00
MS-R1	180	24	7×10^{-2}
MS-R2	180	24	14×10^{-2}
MS-R3	180	24	21×10^{-2}
MS-R4	180	24	28×10^{-2}
MS-R5	180	24	35×10^{-2}

After this, reducing agent (hydroxylamine hydrochloride) with varied concentration has been to aqueous solution of ammonium molybdate tetrahydrate. Aqueous solution of 36×10^{-2} M thiourea was prepared and both the solutions were mixed thoroughly. The pH of resulting solution was raised up to 6 by adding 1 M of sodium hydroxide. Final solution was transferred into teflon liner cup and the hydrothermal reactor was sealed. Initially, hydrothermal reaction parameters *i.e.,* reaction time as well as concentration of reducing agent were optimized for the synthesis of nanostructured MoS_2 as an efficient HER electrocatalyst. After the completion of hydrothermal reaction, reactor was allowed to cool down at room temperature. The black precipitate formed as final product was vacuum filtered, and washed further using D. I. water and ethanol, followed by drying at 60 ^{0}C for 2 hours.

Table 2.1 presents the sample name and their respective synthesis parameters. Name convention has been discussed the performance of the respective samples in Chapter 3A. Commercial bulk MoS_2 (BMS) has been used for the comparison study.

2.2.1.1: Immobilization of nanostructured MoS_2 electrocatalyst over conducting substrate

To immobilize the synthesized nanostructured MoS_2 sample on a conducting substrate, drop casting method has been used. Here, drop-casting is performed on carbon paper (C.P.) which was used as conducting substrate, (Figure 2.3). Homogenous ink was prepared for drop casting of nanostructured MoS_2 electrocatalyst.

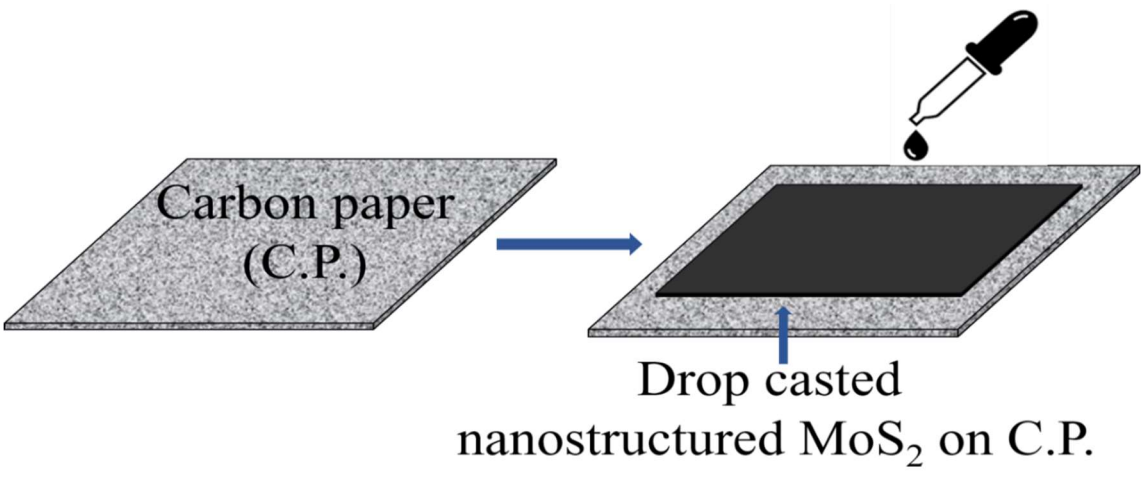

Figure 2.3: Pictorial presentation for drop casting of nanostructured MoS_2 on C.P.

For preparation of homogenous ink, 10 mg of hydrothermally synthesized MoS_2 powder, 0.7 ml of isopropyl alcohol (IPA) and 0.07 ml of Nafion 117 solution (10 vol% of IPA) were mixed thoroughly and ultrasonicated for 2 hours. A fixed volume of 40 µl of ink

was drop casted on the C.P. (*dimension 1×1 cm*^{2}) and allowed to dry at room temperature. Nanostructured MoS_2 modified C.P. by drop casting method has been used as working electrode during all electrochemical characterization studies.

2.2.2: Large area *in-situ* deposition of nanostructured MoS_2 on conductive substrate using one-step hydrothermal method

Figure 2.4 presents the schematic for the *in-situ* deposition of nanostructured MoS_2 on conductive substrate (Stain less steel, grade 316; S.S.) using hydrothermal method. To prepare the solution for hydrothermal reaction, first, different concentration of reducing agent was mixed with 4×10^{-3} M aqueous solution of ammonium molybdate tetra hydrate.

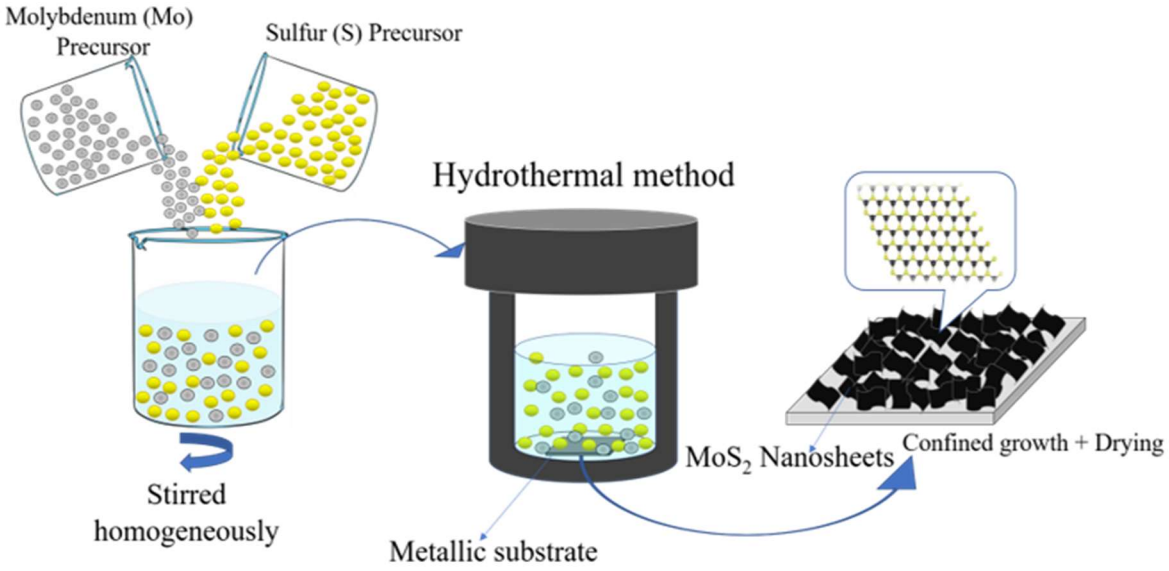

Figure 2.4: Schematic representation for in-situ deposition of MoS_2 nanosheets on metallic substrate (S.S.) using hydrothermal method.

Further, an aqueous solution of thiourea (36×10^{-2} M) was prepared and both the solutions were mixed thoroughly. The pH of resulting solution was raised to 6 by adding 1 M aqueous solution of sodium hydroxide. Sand blasted S.S. substrates (dimension: 2.5 × 2.5 cm^2) (Figure 2.5 a) were placed in the teflon cup.

Prior to hydrothermal reaction, all S.S. plates were ultrasonicated in water and ethanol for 2 to 3 time to remove impurities. The aqueous solution was transferred into teflon liner cup. The hydrothermal reactor was sealed, kept in oven, and heated at a temperature of 180 ^{0}C for 24 hours. After 24 hours of hydrothermal reaction, allowed autoclave reactor to cool down to room temperature.

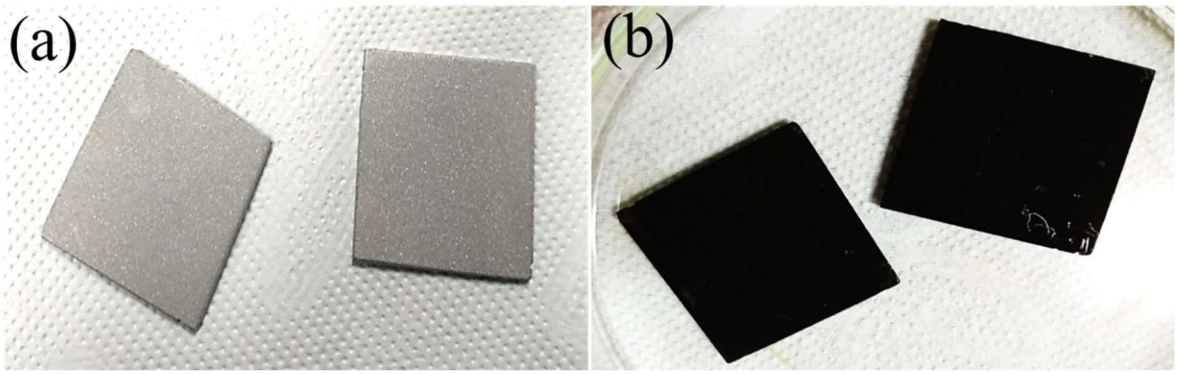

Figure 2.5: Digital images of S.S. substrates (a) before hydrothermal reaction and (b) after hydrothermal reaction.

The S.S. substrates on which MoS_2 was deposited, (Figure 2.5b) have been taken out carefully from the teflon cup, washed further using D. I. water and ethanol several times, followed by drying at 60 ^{0}C for 2 hours.

Table 2.2. Hydrothermal reaction parameters for the in-situ deposited nanostructured MoS_2 films.

Sample Name	**Reaction temperature (^{0}C)**	**Reaction time (hours)**	**Molarity of Reducing agent *(Molar)***
MS00	180	24	00
MS07	180	24	7×10^{-2}
MS14	180	24	14×10^{-2}
MS21	180	24	21×10^{-2}
MS28	180	24	28×10^{-2}
MS35	180	24	35×10^{-2}

Figure 2.5 shows the picture of S.S. plate before and after hydrothermal reaction which confirms deposition of MoS_2 over S.S. substrate after hydrothermal reaction. Sample name and related synthesis parameters has been tabulated in Table 2.2. This sample name convention has been used in Chapter 3B.

These *in-situ* deposited nanostructured MoS_2/S.S. large area films were used as working electrode during all electrochemical characterizations without any further modifications.

2.2.3: One-step synthesis of noble metal (Palladium; Pd) doped MoS_2 nanostructured electrocatalyst using hydrothermal method

Figure 2.6 represents the schematic for the synthesis of noble metal (Pd) doped MoS_2 electrocatalyst. Pd-MoS_2 sample has been synthesized using one-step hydrothermal method. Firstly, 0.274 g ammonium molybdate tetrahydrate and 0.972 g of hydroxylamine hydrochloride were mixed in 100 ml of D.I. water with magnetic stirring up to 30 min. Different weight% of palladium chloride has been added for optimization of Pd dopant concentration. To dissolve the Pd precursor in solution, 100 µl of 33% hydrochloric acid (HCl) was also added. Next, 1.40g of thiourea (NH_2CSNH_2) was mixed in the above solution and allowed stirring again up to 30 min. This homogeneous solution prepared was transferred in 200 ml volume of Teflon lined stainless steel autoclave reactor and subjected to thermal reaction at 180 ^{0}C for 24 hours. After the completion of hydrothermal reaction, the autoclave reactor was allowed to cool down to room temperature.

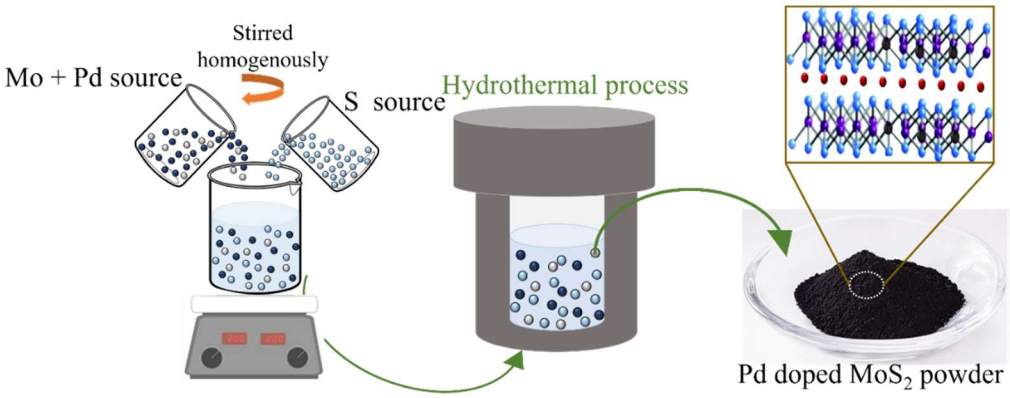

Figure 2.6: Schematic representation for one-step hydrothermal synthesis of Pd doped MoS_2.

The resulting solution was filtered using vacuum filtration setup. The precipitate obtained was washed multiple times, sequentially by using D.I. water and ethanol. This washed precipitate was annealed at 80 ^{0}C for 6 hours in an oven.

To compare and evaluate the HER activity of Pd doped MoS_2, the pristine MoS_2 was synthesized by using the same procedure as mentioned above without adding $PdCl_2$ and was denoted as pristine MoS_2. Samples, synthesized by adding 5, 10, 20, 30, 40 and 50 mg amount of $PdCl_2$ precursor have been named as Pd-MS1, Pd-MS2, Pd-MS3, Pd-MS4, Pd-MS-5 and Pd-MS6, respectively. These sample name conventions have been used during characterization to represents respective samples. As mentioned in section 2.2.1.1, same procedure has been followed to immobilize all the synthesized Pd-MoS_2 and pristine MoS_2 samples onto C.P. by

drop casting method. Pd-MoS_2 modified C.P. samples have been used as working electrode during all electrochemical characterizations.

2.2.4: Single-step synthesis of transition metal (Vanadium; V) doped MoS_2 nanostructured electrocatalyst using hydrothermal method

Figure 3.7 shows schematic representation for the synthesis of transition metal (Vanadium; V) doped MoS_2 (V-MoS_2). The V-MoS_2 electrocatalyst was synthesised in a one-step hydrothermal method with varying V doping concentrations. Pristine MoS_2 was also prepared following the same procedure. In first step, 50 ml homogeneous solution of 0.04 M of ammonium molybdate tetrahydrate was prepared. Further, different weight% of ammonium metavanadate was added for the optimization of V dopant concentration into MoS_2. After this, 0.28 M hydroxylamine hydrochloride was mixed into the solution. In a separate beaker, 50 ml homogeneous solution of 0.36 M of thiourea was made and both the solutions were mixed.

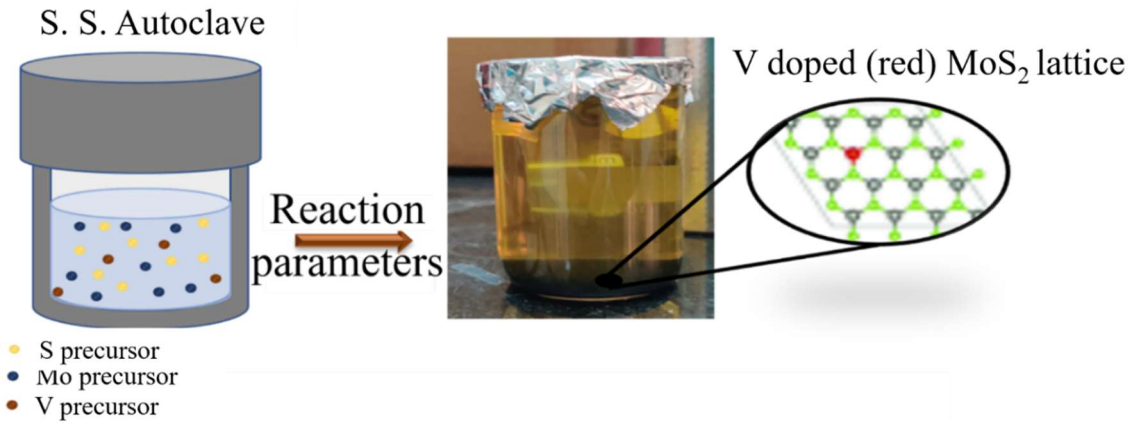

Figure 2.7: Schematic representation for single step synthesis of nanostructured V-MoS_2 electrocatalyst using hydrothermal route.

This homogeneous solution prepared, was transferred in 200 ml Teflon lined stainless steel autoclave reactor and heated up to temperature of 180 ^{0}C for time of 24 hours. Autoclave reactor was allowed to cool down at room temperature after the completion of hydrothermal reaction. Resulting solution was filtered using vacuum filtration. The precipitate obtained was washed 3-4 times using D.I. water and then ethanol and further kept for drying up to 6 hours at 80 ^{0}C in vacuum oven. For the comparative study with V doped MoS_2, the pristine MoS_2 was synthesized using the same procedure mentioned above without adding ammonium metavanadate, denoted as pristine MoS_2 throughout the study. Samples, synthesized by adding

6, 12, 24 and 36 mg amount of ammonium metavanadate precursor have been labelled as V-MS6, V-MS12, V-MS24 and V-MS36, respectively. These sample name conventions have been used during characterization to represents respective samples.

As mentioned in section 2.2.1.1, the same procedure has been followed to immobilize all synthesized V-MoS_2 and pristine MoS_2 samples on C.P. by drop casting method. V-MoS_2 and pristine MoS_2 modified C.P. samples have been used as working electrode during all electrochemical characterizations.

2.3: Materials characterization

Selection of precursors, synthesis method and reaction parameters play a significant role in development and synthesis of materials. Similarly, characterization of the synthesized materials in right direction gives necessary information about its potential towards desired application. Physico-chemical (surface morphology, elemental analysis, structure and phase detection) and electro-chemical properties (overpotential, Tafel slope, charge transfer resistance, electrochemically active surface area, stability) of the synthesized materials are the important parameters to prove material's capability towards HER application. Table 2.3 gives details about physico-chemical and electrochemical properties to determine and utilized respective technique.

2.3.1: Physico – chemical characterization

The very first step of physico-chemical characterization of the material is to study the surface morphology, particles distribution, particle size *etc.* for which electron microscopy is preferred always.

Table 2.3: Physico-chemical and electrochemical properties and their respective characterization tools/ techniques.

S. No.	**Characterization**		**Characterization Technique**
1.	Physico-chemical	Surface morphology	FESEM, TEM
2.		Element analysis	EDS/EDAX, XPS

3.		Structural investigations	XRD, SAED, Raman Spectrometer
4.		Specific surface area	BET theory
5.	Electro-chemical	HER parameters evaluation [Overpotential (η), Tafel slope (b), Charge Transfer Resistance (R_{ct}), Electro Chemically Active Surface Area (ECSA), Stability, Durability]	Electrochemical Work Station
6.		Electrocatalytic hydrogen evolution rate estimation	Gas Chromatography

Here, we have basically utilized two types of electron microscopies to investigate morphology of synthesized systems. No further treatment, modification or purification has been performed during physico-chemical characterization of synthesized samples.

2.3.1.1: Field Emission Scanning Electron Microscope (FESEM)

To investigate the surface morphology of the synthesized materials, FESEM (Model: ***Gemini 500, M/s Carl Zeiss***) equipped with Lanthanum Hexaboride (LaB_6) as hot cathode, has been used.

Figure 2.8: Digital image of ZEISS Gemini 500 FESEM.

The Ziess Gemini 500 provide high resolution for imaging with superb quality from 100 mm diameter wafers down to small samples at high as well as low voltage [166]. The

Gemini 500 FESEM exhibits highly efficient *in lens* secondary electrons detector for excellent resolution and high contrast surface imaging. In lens Energy Selective Back scatter (ESB) detector is also equipped with Gemini 500 to detect backscattered electrons at low accelerating voltages. This system is completely computer controlled. It provides high resolution up to 5 Å at 15 kV, 9 Å at 1 kV and 10 Å at 500 V and provides magnification from 50x to 2000kx. It can work with accelerating voltage range from 0.02 to 30 kV. The specimen stage is motorized and travels in 6 directions.

2.3.1.2: Transmission Electron Microscope (T.E.M.)

Transmission electron microscope (TEM) generates the digital pictures of nanomaterials at significantly higher resolution owing to smaller De-Broglie wavelength of electrons. TEM allows to magnify very thin samples down to atomic resolution and it can show finest details of internal structure as small as individual atom [3].

Figure 2.9: Digital image of JEM-F200, JEOL TEM.

It allows the chemical bonding analysis in Electron Energy Loss Spectrum (EELS), reduces the chromatic aberrations, and enables higher resolution imaging (TEM lattice image 1 Å; point to point-1.9 Å; STEM-HAADF images – 1.4 Å). This system provides higher magnification of 20x to 2 Mx in TEM mode and 200x to 150 Mx in STEM mode. The JEM-F200 incorporates Quad-Lens Condenser System, the 4-stage probe-forming optical system, to controls the number of electrons as well as the focusing of generated electron beam independently. Loading of a sample holder also brings a human error during imaging, therefore, this system is incorporated with 'SPECPORTER' which smoothen the loading and unloading of the sample holder. It automatically places a sample holder at a given location, and gets

activated by a single click ensures safe loading/unloading of the holder. TEM can be operated with accelerating potential range from to 20 V to 200 KV. This system is also equipped with Energy Dispersive X-ray Spectrometer (EDAX), Electron Energy Loss Spectrometer (EELS), Digital Camera as optional accessories.

2.3.1.3: Elemental Analysis

For elemental analysis of nanostructured MoS_2 as well as heteroatom doped nanostructured MoS_2, there are three two characterization techniques i.e., EDAX or EDS and XPS. Before elemental analysis, no sample preparation has been performed. Samples have been characterized directly (in powdered form).

2.3.1.3.1: Energy Dispersive X-Ray spectroscopy (EDAX or EDS)

EDAX or EDS is mainly known for qualitative investigation and sometimes for quantitative analysis for materials. In SEM, when electrons get reflected from the sample's surface it contains secondary electrons and back scattered electrons which are used to create images but reflected beam also includes characteristic X-Rays which help to detect and quantify presence of elements in the sample. The quality of EDS result depends completely on sample's surface characteristics. Concentration of the major (higher the 10 wt%) as well as minor (1 to 10 wt%) elements can be detected by using EDS but it is not useful to detect trace element concentration below 0.01 wt% [4]. This technique can produce area distribution maps for the elements. EDS detectors equipped with FESEM (***Gemini 500, M/s Carl Zeiss***) and TEM (JEM-F200, JEOL) have been utilized for the detection of the various elements present in the samples as well as the elemental area mapping.

2.3.1.3.2: X-Ray photoelectron Spectroscopy (XPS)

X-ray photoelectron spectroscopy (XPS) technique is one of the important tools which non-destructive and surface sensitive and can probe up to depth of 10 nm (30 atomic layers) of material. XPS's sensitivity to the surface and capability to detect the chemical state of element are main feature and make it an important tool for the sample analysis [5]. XPS (Omicron Nanotechnology, UK) has been used for the elemental analysis like composition, chemical state and their oxidation states present in synthesized samples. For the measurements, this XPS system use Omicron's DAR 400 dual Mg/Al X-ray source. Omicron's 124 mm mean radius electrostatic hemi spherical dispersive energy analyser with the 128-channel micro-channel plate Argus detector with 0.8 eV resolution may be used for electron analysis.

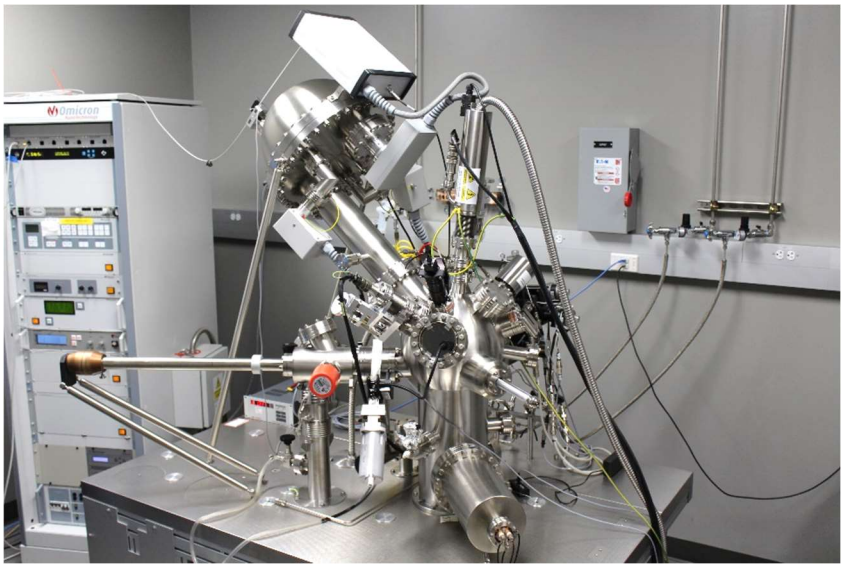

Figure 2.10: Digital image of Omicron Spectroscopy.

2.3.1.4: Structural Investigation

Following morphological studies and elemental analysis, structural investigation is critical in the physicochemical characterization of synthesised *materials*. The X-ray diffraction (XRD) technique, Electron Diffraction pattern, and Raman spectroscopy tool were used to investigate the structural properties of materials.

2.3.1.4.1: X-Ray Diffraction (X.R.D.)

Two advanced diffractometers have been used to identify the phase formation of synthesized samples.

First XRD tools is D8 advanced system (Model: Smart lab XRD system, Bruker AXS GMbH, Karlsruhe, Germany), shown in figure 3.10 (a). This system is equipped with rotating anode generator. It was used for X-ray diffraction pattern recording and has focus size of 0.04×1.2 cm line/point. Cu-Kα [wavelength (λ)=1.5418 Å] radiation was employed as a source and the LynxEyeTM silicon strip detector was utilized for investigation. Sample holder contains the powder need to be characterized, and this sample holder is inserted in the Bragg-Brentano diffractometer setup. The sample was scanned from angle (2θ) from 10^0 to 80^o. Second XRD tool, used for structural investigation of synthesized samples is Microfocus X-Ray diffractometer (Model: Rapid II D/Max, Rigaku, Japan, source: Cr – Kα, λ=2.29 Å), shown in figure 3.10 (b). This unique X-ray diffractometer system is equipped with Micromax TM – 007 high flux microfocus anode (Cu/Cr dual wavelength), exhibits a very high brilliance compared to conventional XRD unit.

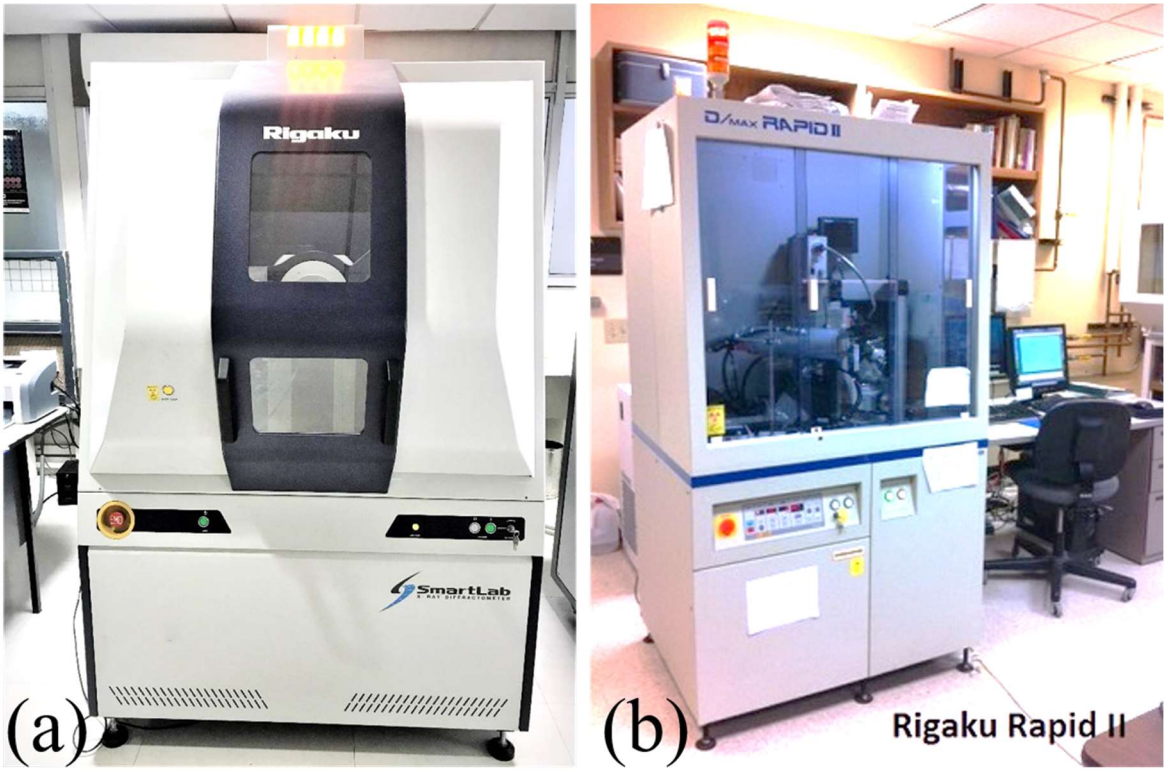

Figure 2.11: (a) Smart lab XRD system, (b) microfocus XRD system.

Unlike conventional XRD system (employs a line focus), this special unit employs a spot focus range of 10 µm - 800µm. It possesses a large size cylindrical two-dimensional image plate as detector with active area of 460x256 mm^2. XRD patterns were recorded using a Debye-Scherrer geometry with a fixed angle of incidence of 20°. Phase analysis was carried out using MATCH software with International Centre for Diffraction Data – Powder Diffraction file (ICDD-PDF4+) database.

2.3.1.4.2 Selected Area Electron Diffraction (SAED)

To record SAED pattern, TEM (Model: JEM-F200, JEOL) has been utilized. SAED, a crystallographic technique, is used to obtain quantitative data such as phase investigation, crystal defects, crystal orientation and lattice constants for the sample. In TEM, focused and highly energetic electron beam behaving as a wave with wavelength of few thousands of a nanometres is illuminated on very thin sample (less than 100 nm), and gets diffracted through the crystal lattice due to hundred times larger spacing between atoms in crystals than incident electron beam wavelength, therefore, act as a diffraction grating [6]. Only a part of the electrons gets diffracted at particular angles (provide SAED pattern) while remaining get transmitted through sample (provide TEM images). By analysing the electron diffraction pattern, crystallographic information can be identified for example amorphous, single

crystalline or polycrystalline nature. There are mainly three type of diffraction pattern which deepens on sample's condition.

- **Ring pattern**: Ring pattern rise due to ultrafine grains of polycrystalline materials.
- **Spot pattern**: Spot pattern rise due single crystalline nature of materials.
- **Kikuchi Pattern**: Kikuchi line pattern occurs when sample's thickness is more than normal or almost perfect. Inelastic scattering of electrons at small angles with less loss of energy is main reason of this pattern.

This gives SAED a spatial resolution up to several hundred times greater than conventional X-ray diffraction techniques.

2.3.1.4.3: Raman Spectroscopy

Raman Spectroscopy is also a non-destructive technique for chemical analysis which gives details about chemical structure, phase presence and polymorphs based on vibrational modes of molecules [7]. Raman spectrum is a generally a distinct fingerprint for a particular material or molecule and it can very quickly identify the chemical structure/ phase of material. Raman spectroscopy typically measures the vibrational spectra using laser radiation which can't be absorbed by the samples. Raman spectra of synthesized nanostructured electrocatalyst were recorded using ***Witech Alpha 300***, Oxford instruments, Germany, where He-Ne laser with an excitation wavelength of 532 nm as light source. This spectrometer is equipped with Charged Coupled Device (CCD) detector.

2.3.1.5: Specific surface area investigation

Specific surface area is the ratio of total surface area to material's mass given in $m^2.g^{-1}$, calculated using the Brunauer-Emmett-Teller (BET) adsorption technique. [8]. The assumptions of BET theory are (a) an infinite layer of gas molecules exist on the surface of the material, (b) negligible interactions occur between the adsorbed layers. For the investigation of specific surface area, powder was subjected to BET surface area measurement using BET surface area analyser (***Micromeritics Instruments Corp, ASAP 2020, Norcross GA, USA***). The system works on the concept of static volumetric. A known amount of adsorbate (nitrogen) is sequentially introduced to the sample holder, which is held at liquid nitrogen temperature (77K). The liquid nitrogen temperature is critical to facilitating the adsorption of injected gas on the sample surface, leading in a steady drop in pressure until

an equilibrium pressure is attained. In general, the BET measurement is performed by putting 0.08 g of powder which was degassed at temperature of 200 ^{0}C for 2 hours to eliminate any other adsorbed gas. The amount of nitrogen absorbed, relative pressure (p/p_0) and $\{1/ [\vartheta (p_0/p)-1]\}$ is calculated from BET analysis results, as well as the plot of $1/ [\vartheta (p_0/p-1)]$ against (p/p_0).

2.3.2: Electrochemical characterization

Electro-chemical characterization of the synthesized samples decides the sample's efficiency for HER application. It starts from the HER parameters evaluation to ultimately hydrogen evolution rate estimation using the synthesized samples. For the electrochemical characterization of samples, all electrodes were prepared as mentioned for the preparation of working electrode in section 2.2.1.1.

2.3.2.1: HER parameters evaluation

Overpotential (η), Tafel slope (b), charge transfer resistance (R_{ct}), electrochemically active surface area (ECSA), and electrochemical stability/durability are the important electrochemical parameters to investigate the electrocatalytic efficiency of synthesised material towards HER application.

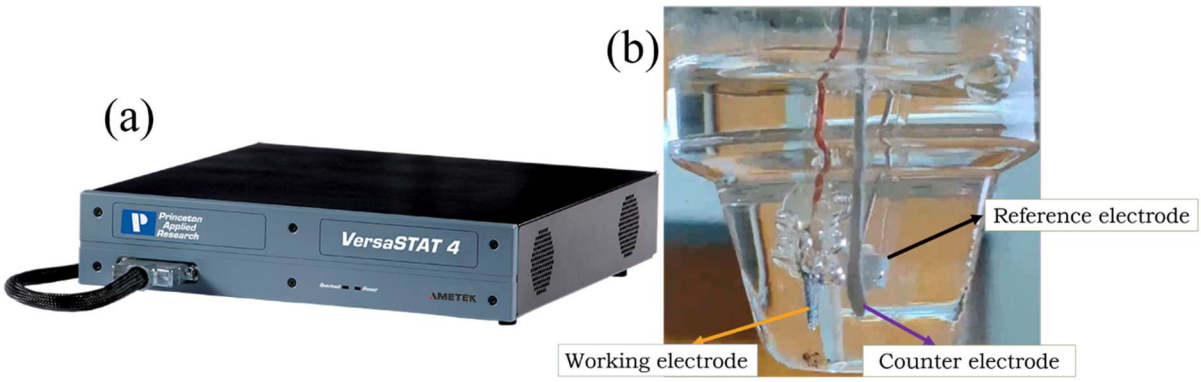

Figure 2.12: Digital image of VersaStudio 4 EWS, Ametek (a) and three electrode configuration microcell setup containing working, counter, and reference electrode with electrolyte (b).

These parameters must be recorded or calculated using LPR curve, Nyquist plot, and CV graphs. To record these graphs, Electrochemical Work Station (EWS) is a well-known device. These all approaches provide a good platform to study the reaction kinetics, trace level analysis, basic research, corrosion, energy conversion, and storage as well. An EWS works both as a potentiostat as well as galvanostat and relevant control software, and the

electrochemical cell setup. For the electrochemical characterization of synthesized samples, EWS (Model: ***VersaStudio 4, Ametek***, Figure 2.12 a) has been utilized with three electrode electrochemical cell configuration, consisting of working, reference, counter electrodes, and an electrolyte (Figure 2.12 b).

2.3.2.1.1: Linear Polarization Resistance (LPR) curve

LPR is non-destructive technique which is generally being used for corrosion studies and suited for ionically conductive liquid environment. LPR technique is used to characterize the kinetics between materials and medium *via.* scanning of current-potential domain [9]. LPR technique was used to determine the overpotential at a fixed value of the current density, Tafel slopes and durability. It was run with a negative potential window of 0 to -0.7 V vs. reference electrode (Saturated Calomel Electrode was used to characterized nanostructured MoS_2 based electrodes and Ag/AgCl in 3M KCl was used to characterized heteroatom doped MoS_2 based electrodes) with 5mV scan rate. For electrocatalytic water splitting performance of samples, LPR curve was recorded from 0 V to 2.5 V at a 5mV.sec^{-1} scan rate.

2.3.2.1.2: Cyclic Voltammogram (CV)

CV has already become widely used and important among others electrochemical technique in various areas of chemistry [10]. This technique has utilized to investigate ECSA as well as electrochemical durability which was done by running of hundreds of CV curve. To determine the ECSA, CV studies were performed between potential biasing of -0.015 V to 0.15 V *vs. reference electrode* with scan rate of 10 to 100 mV.sec^{-1} with step size of 10 mV/sec. In order to perform the electrochemical durability of the electrocatalysts, 1000 CV cycles were recorded with potential biasing from -0.2 V to -0.5 V vs. reference electrode, 100 mV/sec scan rate. LPR curve of electrocatalyst was recorded before and after performing the 1000 cycles of CV.

2.3.2.1.3: Chronoamperometry (CA)

CA is one of the useful techniques to determine the electrochemical activity/ stability of the electrocatalysts [11,12]. To investigate the electrochemical stability of samples, CA has been performed up to 20 hours at a fixed value of overpotential, depending upon the performance of system.

2.3.2.1.4: Electrochemical Impedance Spectroscopy (EIS)

EIS, a multifrequency AC electrochemical characterization technique, is used for determining the many electrochemical parameters of the working electrode such as coating layers, internal resistance, double layer capacitance, charge transfer resistance etc [13]. To evaluate the kinetics of electrode/electrolyte interface, EIS has been performed for all samples at a fixed AC amplitude (RMS) of 10 mV. EIS curves were recorded by applying 100 mHz to 100 KHz frequency at a potential of 0 V vs. reference electrode (Saturated Calomel Electrode was used to characterized nanostructured MoS_2 based electrodes and Ag/AgCl in 3M KCl was used to characterized heteroatom doped MoS_2 based electrodes).

2.3.2.1.5: Estimation of ESCA of Electrocatalyst

Electrochemical Surface Area (ESCA) of electrocatalyst is directly proportional to double layered capacitance (C_{dl}), which was calculated for electrocatalyst *via.* recording CV curves with different scan rates from 10 to 100 $mV.sec^{-1}$ with a step size of 10 $mV.sec^{-1}$ within the non–Faradic region of the electrode. The C_{dl} was estimated by calculating the of anodic/cathodic current densities' difference at potential of 100 mV *vs. SCE* with respect to the scan rate.

$$\boldsymbol{C_{dl} = \frac{d(\Delta J)}{dV_b}} \qquad \ldots \mathbf{2.1}$$

Where V_b is the scan rate.

The ECSA was calculated from the c_{dl} using the following relation –

$$\boldsymbol{ECSA = \frac{C_{dl}}{C_s}} \qquad \ldots \mathbf{2.2}$$

is the Specific capacitance (C_s) of material has been considered 60 μF, with 1 cm^2 of real surface area.

2.3.2.2: Rate estimation of electrocatalytically evolved hydrogen

After investigating the efficiency of the synthesized electrocatalyst towards HER application, rate estimation of the hydrogen evolution is also important part to characterize the material's potential as an electrocatalyst. The quantification of electrocatalytically evolved hydrogen (H_2) gas and oxygen (O_2) gas were completed by Gas chromatography (Model: GC 2010 plus, Schimazdu, Japan), equipped with 'splitless/split direct' injector,

capillary column (*internal diameter - 0.25 mm, made up of fused silica, length - 30 meter*) and thermal conductivity detector (TCD made by Tungsten Rhenium filament). This unit can be operated in the temperature range of 4 °C to 450 °C. Nitrogen gas (N_2; purity 99.999%) was used as carrier gas during the analysis. Evolved gas was extracted from the electrocatalytic cell with help of gas-tight micro syringe (SGE, 10µl), and injected in the GC port. GC solution software was used for data collection and analysis. Electrocatalytic cell was made air tight during electrolysis and before starting the water splitting procedure, Cell was flushed using nitrogen (N_2) gas continuously for 10 minutes to eject out other gaseous impurities from the cell.

Figure 2.13: Digital image of GC 2010 plus Gas chromatography.

2.4: Conclusion

In this chapter, we have briefly explained about synthesis of nanostructured, Pd doped and V doped MoS_2, utilized the respective techniques and equipment to investigate synthesized sample's physico-chemical, electrochemical characterizations and rate estimation of electrocatalytically evolved gases as shown in the Figure 2.14.

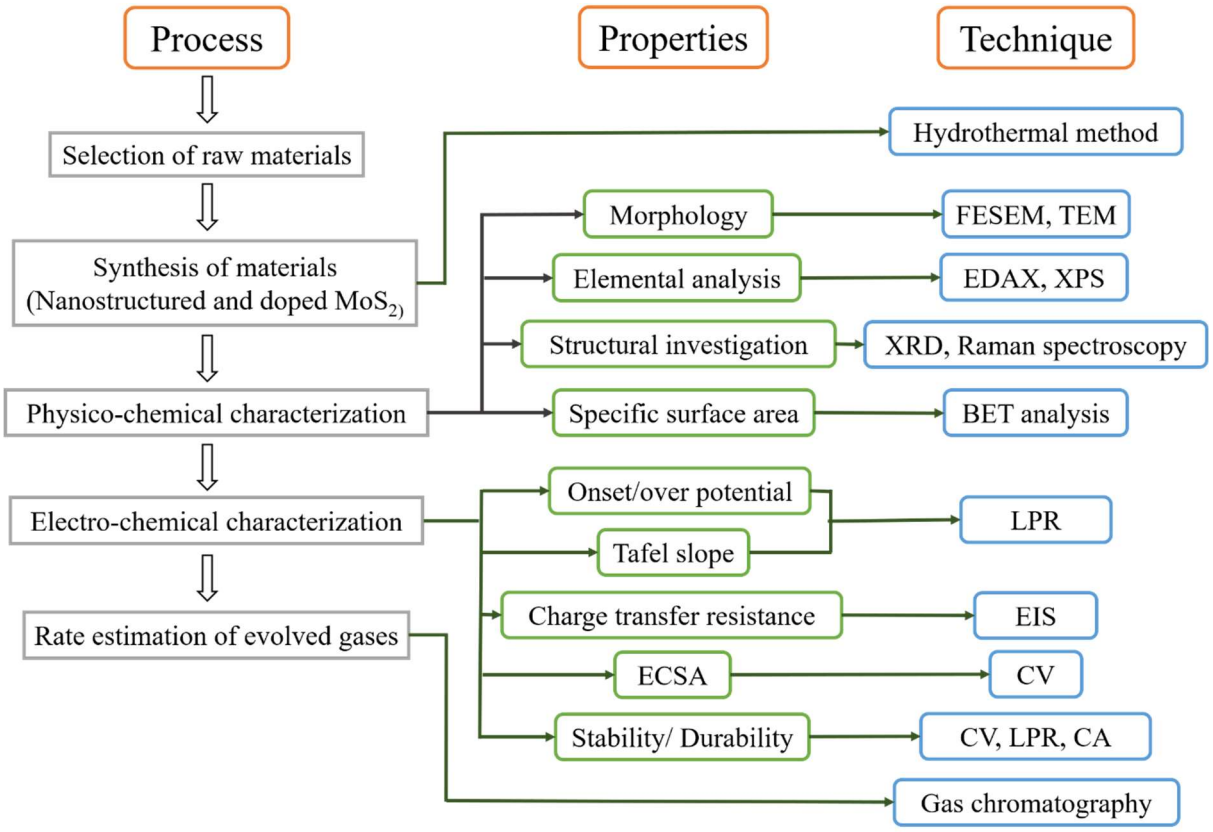

Figure 2.14: Flow chart for synthesis and characterization for nanostructured and doped MoS_2.

2.5: References

1. Y. X. Gan, A. H. Jayatissa, Z. Yu, X. Chen, and M. Li, J. Nanomater. **2020**, 8917013 (2020).

2. G. Yang and S.-J. Park, Mater. (Basel, Switzerland) **12**, (2019).

3. C. Y. Tang and Z. Yang, in edited by N. Hilal, A. F. Ismail, T. Matsuura, and D. B. T.-M. C. Oatley-Radcliffe (Elsevier, 2017), pp. 145–159.

4. M. Scimeca, S. Bischetti, H. K. Lamsira, R. Bonfiglio, and E. Bonanno, Eur. J. Histochem. **62**, 2841 (2018).

5. F. A. Stevie and C. L. Donley, J. Vac. Sci. Technol. A **38**, 63204 (2020).

6. H. Janik and M. Wrona, in edited by P. Worsfold, C. Poole, A. Townshend, and M. B. T.-E. of A. S. (Third E. Miró (Academic Press, Oxford, 2019), pp. 107–116.

7. U. A. Jayasooriya and R. D. Jenkins, in edited by D. L. Andrews and A. A. Demidov (Springer US, Boston, MA, 2002), pp. 77–104.

8. M. Naderi, in edited by S. B. T.-P. in F. and S. Tarleton (Academic Press, Oxford, 2015),

pp. 585–608.

9. J. G. Speight, in edited by J. G. B. T.-S. and D. O. and G. S. and T. Speight (Gulf Professional Publishing, Boston, 2015), pp. 213–256.

10. G. Bontempelli, N. Dossi, and R. B. T.-R. M. in C. Toniolo Molecular Sciences and Chemical Engineering, in (Elsevier, 2016).

11. O. J. Guy and K.-A. D. Walker, in edited by S. E. B. T.-S. C. B. (Second E. Saddow (Elsevier, 2016), pp. 85–141.

12. R. J. Mortimer, in edited by J. C. Lindon, G. E. Tranter, and D. W. B. T.-E. of S. and S. (Third E. Koppenaal (Academic Press, Oxford, 2017), pp. 172–177.

13. H. S. Magar, R. Y. A. Hassan, and A. Mulchandani, Sensors (Basel). **21**, (2021).

CHAPTER 3

NANOSTRUCTURING OF MoS_2 FOR EFFICEINT HYDROGEN EVOLUTION REACTION (HER) APPLICATION

The very first strategy adopted to boost the HER performance of MoS_2, is nanostructuring. Nanostructuring increases the density of catalytically active edges, which helps to improve MoS_2's electrocatalytic activity. The processes utilized for the one step hydrothermal synthesis and *in-situ* deposition of nanostructured MoS_2 have been mentioned in the previous chapter (section 2.2.1 & 2.2.2). In this chapter, we have discussed the physico-chemical and electrochemical characterization of hydrothermally synthesized nanostructured MoS_2 electrocatalysts as well as *in situ* deposited MoS_2 film on a conducting substrate of large area (2.5 × 2.5 cm^2) and their electrocatalytic efficiency of the nanostructured MoS_2 for HER application by engineering the surface is studied.

For a better comprehension of the outcomes, the chapter is separated into two sections:

(I) Investigation of the nanostructured MoS_2 powder-based electrodes as an efficient electrocatalyst towards HER application.

(II) *In situ* deposition of MoS_2 film on large area conducting substrate *via.* hydrothermal method and its electrocatalytic efficiency for HER application.

CHAPTER 3A

INVESTIGATION OF THE NANOSTRUCUTRED MoS_2 AS AN EFFICNET ELECTROCATALYST TOWARDS HER APPLICATION

In chapter 3A, synthesis of nanostructured MoS_2 electrocatalyst has been attempted using bottom-up method *i.e.*, hydrothermal method (the procedure followed for preparation of nanostructured MoS_2 has been mentioned in section 2.2.1, Chapter 2) and investigated MoS_2's electrocatalytic efficiency towards HER application. We have discussed the results obtained for the nanostructured MoS_2 in the present chapter and concluded by demonstrating its electrocatalytic efficiency towards HER application.

3A.1: Results and discussion

3A.1.1: Morphological studies of nanostructured MoS_2 electrocatalyst

To synthesize the efficient nanostructured MoS_2 as an electrocatalyst for HER application, firstly, we have optimized hydrothermal reaction time by varying from 24 to 36 hours. Figure 3A.1 shows the morphology of the synthesized nanostructured MoS_2 at a hydrothermal reaction time of 24 hours, 30 hours and 36 hours and hydrothermal reaction temperature of 180 ^{0}C. Formation of nanosheets is clearly visible and distinct at reaction time of 24 hours, while agglomerated structures were observed with increase in reaction time (Figure 3A.1). We have not found any particles precipitation in less than 24 hours hydrothermal reaction time. For the sake of comparison, FESEM image of bulk MoS_2 (Figure 3A.1d) has also been included. From the figure 3A.1 (a-c) and 3A.1 (d), there is obvious difference in the morphologies of hydrothermally synthesized nanostructured MoS_2 and bulk MoS_2 (commercial). Hydrothermally synthesized nanostructured MoS_2 exhibited higher exposure of catalytically active edges whereas in case of bulk MoS_2, the ration of inert basal planes to active edges is high, therefore, the electrocatalytic efficiency of hydrothermally synthesized nanostructured MoS_2 for HER application is much more than bulk MoS_2. To further optimize the efficiency of nanostructured MoS_2 for HER application, concentration of reducing agent, used during synthesis, has also been varied from 0.07 M to 0.35 M (*details related to synthesis parameters and respective sample name has been mentioned in table 2.1*).

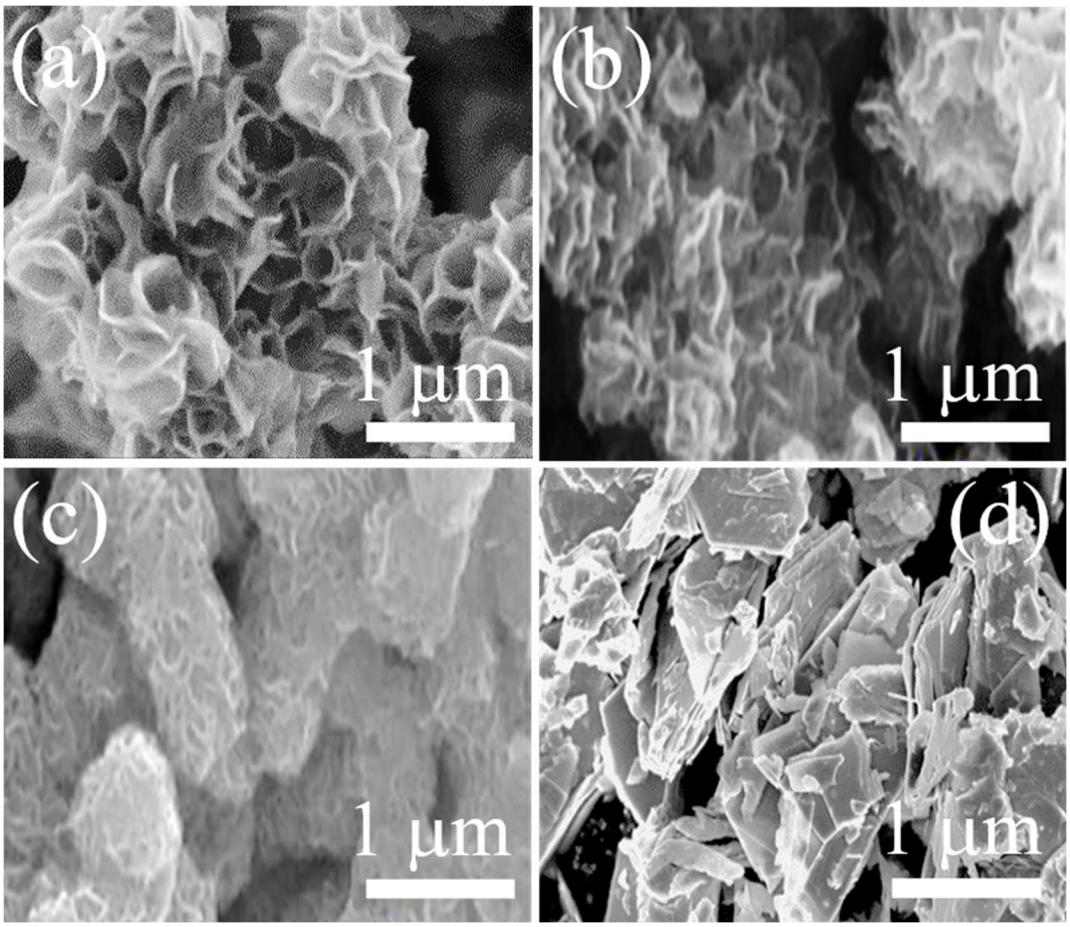

Figure 3A.1: FESEM images of synthesized MoS_2 nanosheets at 180 ^{0}C with variation in reaction time from (a) 24 hours, (b) 30 hours, (c) 36 hours, (d) BMS (for comparison from bulk to nanostructure).

Figure 3A.2 shows the morphology of nano MoS_2 , synthesized with different concentrations of reducing agent. As shown in Figure 3A.2, we observed a small difference in morphology from FESEM images of MoS_2 samples which were synthesized at different hydrothermal reaction times, shown in figure 3A.1. With reducing agent variation, formation of micro balls with nanosheets decorated over it are observed. The micro balls help in increasing the surface area with increment in density of nanosheets. In addition, the smaller size of micro balls provides more surface area as compared to micro balls of larger size [1]. Figure 3A.2 shows the distinct formation of micro balls which is not observed in sample MS-R0; sample without reducing agent. Moreover, these micro balls show reduction in their size with the reducing agent concentration variation. The distinct formation of micro balls with reduction in their size helps to increase the density of nanosheets, grown over micro ball's surface (Inset images of Figure 3A.2). The diameter of micro balls is calculated to be from 5 - 3 μm at lower concentration of reducing agent; (Figure 3A.2 b, c) and 2 μm - 500 nm for higher concentration

of reducing agent; (Figure 3A.2 d & e). Dimensions of nanosheets are estimated with thickness of ~5 nm and length from 20 nm to 50 nm. Further higher concentration of reducing agent (Figure 3A.2 f) lead to agglomeration of micro balls and decrease in the density of nanosheets, grown over at the surface of balls, resulting in lower catalytic activity of MoS_2.

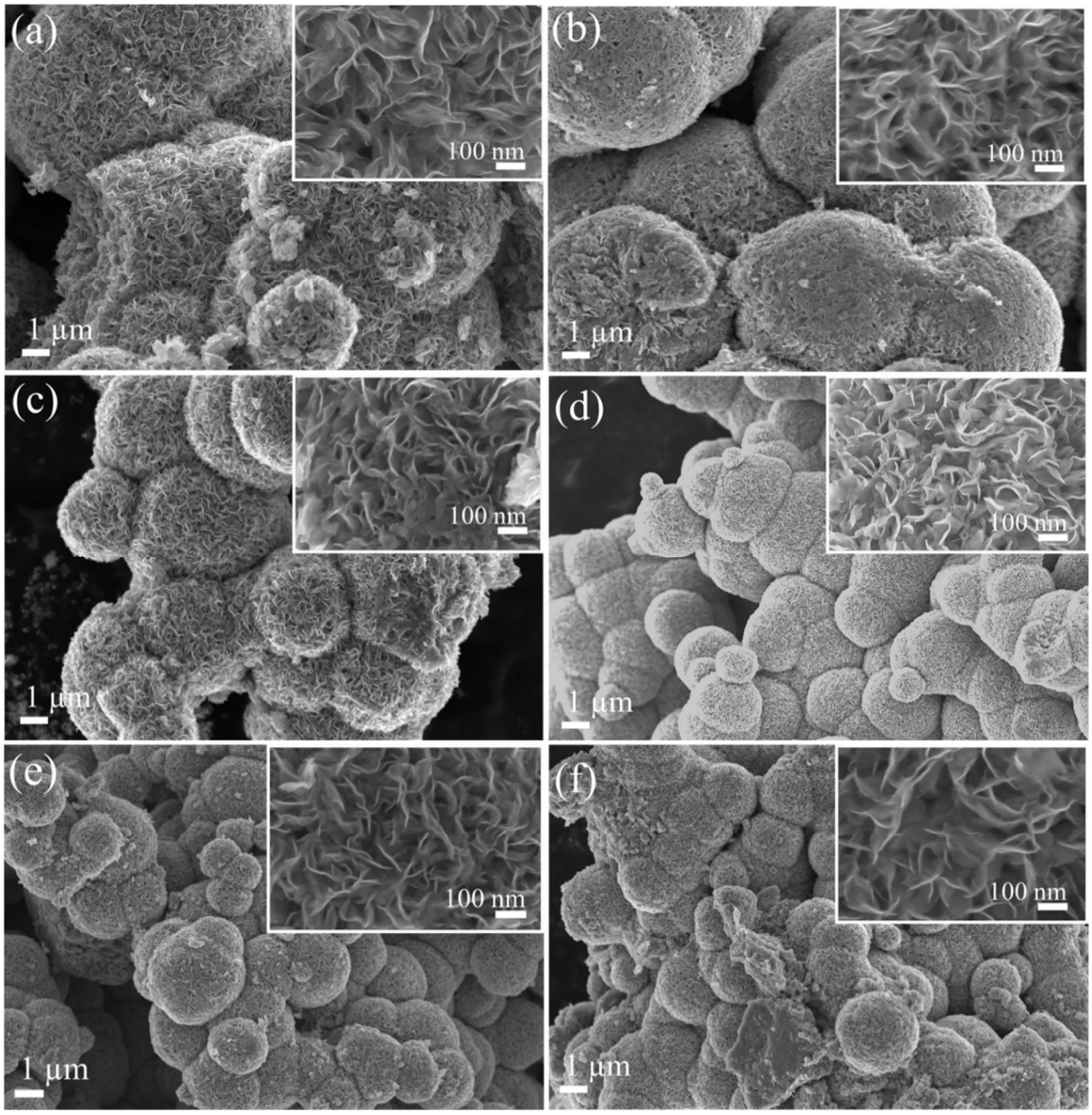

Figure 3A.2: FESEM images of nanostructured MoS_2 with variation in reducing agent concentration (a) MS-R0, (b) MS-R1, (c) MS-R2, (d) MS-R3, (e) MS-R4, and (f) MS-R5.

For the *in-depth* investigation of the morphology of synthesized nanostructured MoS_2 electrocatalyst, TEM characterization tool was utilized (details have been briefly discussed in section 2.3.1.2, Chapter 2). The low magnification TEM image, HRTEM image, and SAED pattern of sample MS-R4 are shown in Figure 3A.3. TEM analysis has been done for the only

sample MS-R4 since it has given most efficient HER performance among synthesized nanostructured MoS_2 samples.

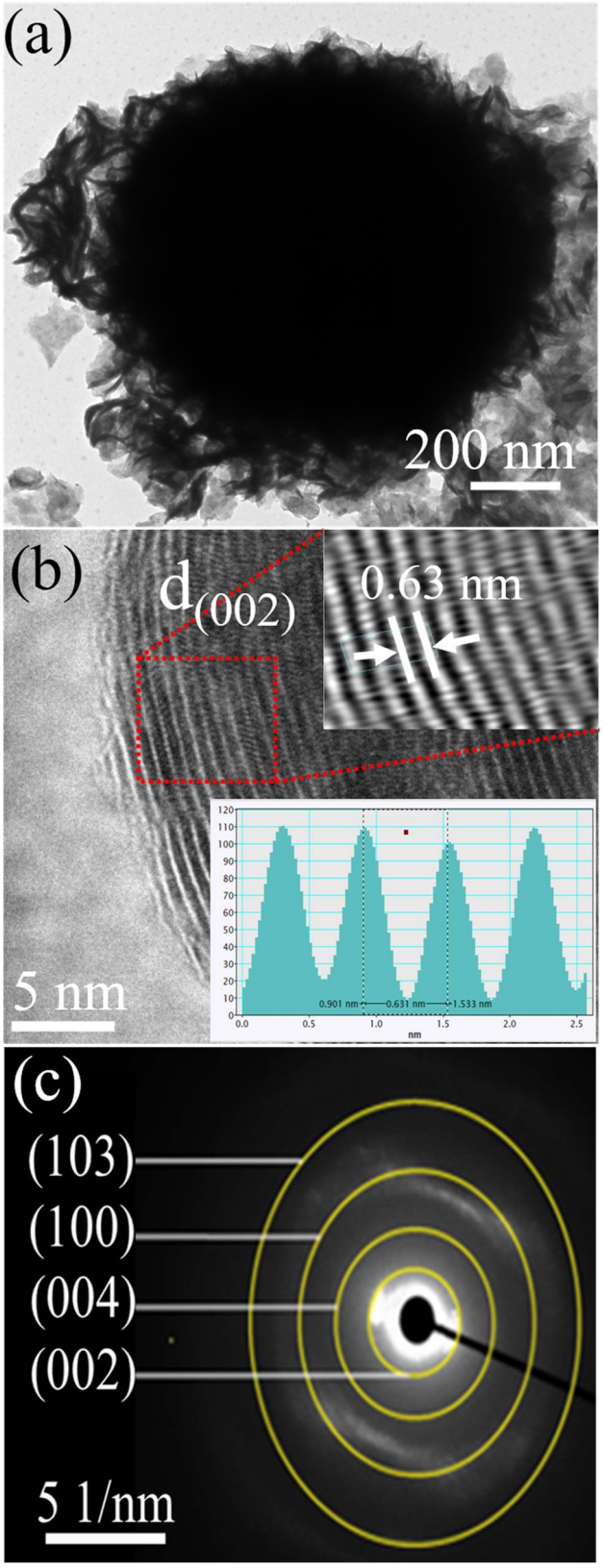

Figure 3A.3: (a) TEM, (b) HRTEM (inset shows calculate IFFT image and its live profile) and (c) SAED pattern for sample MS-R4 (optimized sample).

Low magnification TEM image (Figure 3A.3a) shows the nanosheets formation over the surface of the micro ball of ~500 nm. These images are in coherence with the FESEM images for sample MS-R4 (Figure 3A.2e). Existence of nanosheets is more visible from lattice fringes, shown in the HRTEM images (figure 3A.3b). These lattice fringes correspond to (002) plane of 2H phase of MoS_2, confirming the exposure of edges as compared to basal pane in sample [2]. Inset image of the Figure 3A.3 (b) shows the calculated IFFT image of area with dotted region of HRTEM image (Figure 3A.3b). This IFFT image is used to calculate the interlayer spacing of (002) plane. The second image represents the live profile of shown IFFT image shown. The distance between two consecutive peaks represents the interlayer spacing. The calculated interlayer spacing of (002) plane in sample MS-R4 is calculated to be 0.63 nm [3,4]. SAED pattern (Figure 3A.3, c) and the corresponding interlayer spacing of sample MS-R4 supports the presence of 2H-MoS_2 which is further confirmed by XRD patterns and Raman spectra.

3A.1.2: Elemental analysis by EDAX

For qualitative as well as quantitative analysis of presence of elements in the samples, EDAX has been used. The characterization tools used and the details of the respective technique has been well explained in chapter 2. Figure 3A.4 shows the EDAX spectrum for sample MS-R4, and Table 3A.1 shows the atomic percentage (at%) of Mo and S elements in the samples, as well as probable stoichiometry for the corresponding samples.

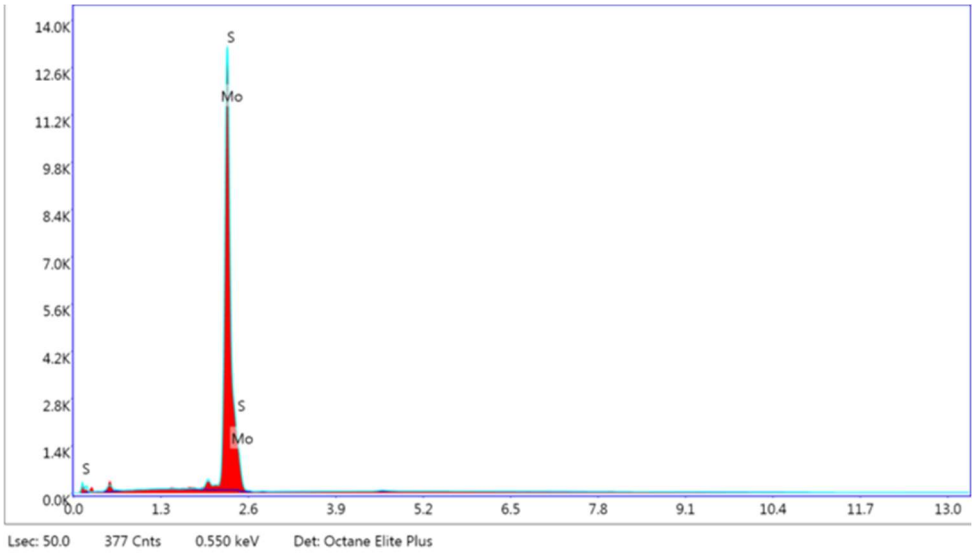

Figure 3A.4: EDAX spectrum for nanostructured MoS_2 sample (MS-R4).

We have observed the presence Mo and S with no presence of any other elements (Figure 3A.4 and Table 3A.1).

Table 3A.1: EDS report for hydrothermally synthesized MoS_2 electrocatalysts.

Sample	Mo (at%)	S (at %)	Stoichiometry (approx.)
MS-R0	31.43	68.57	1: 2
MS-R1	29.77	70.23	1: 2
MS-R2	30.19	69.81	1: 2
MS-R3	32.47	67.53	1: 2
MS-R4	31.09	68.91	1: 2
MS-R5	29.45	70.55	1: 2

All the hydrothermally synthesized samples followed a stoichiometry (Mo: S) of 1:2 approximately (Table 3A.4) which corresponds to MoS_2.

3A.1.3: Structural investigation of the synthesized nanostructured MoS_2 samples

The structural properties investigation and phase formation of hydrothermally synthesized MoS_2 samples have been done with help of micro XRD pattern and Raman spectra (the characterization tools and respective techniques have been well explained in section 2.3.1.4.1 and 2.3.1.4.3, Chapter 2).

Figure 3A.5 (a) shows the XRD patterns of the hydrothermally synthesized nanostructured MoS_2 using *microfocus* XRD diffractometer with Cr ($\lambda = 2.29$ Å) as target. The observed diffraction patterns by using XRD, validates the formation of 2H-MoS_2 as the major phase in all the samples. The XRD pattern of BMS has been included for comparison. An increment in FWHM (*Full width half maxima*) has been observed for the peaks corresponding to all planes and is co-relatable with nanostructuring nature of the synthesized MoS_2. It can be clearly observed from XRD pattern of BMS and MS-R1 to MS-R5 that the intensity of the peak corresponding to (002) plane in BMS is high *compared to* intensity of the peak corresponding to (100) plane which is vice versa in case of nanostructured MoS_2. This change validates the 2D nature and layer formation of the synthesized nanostructured MoS_2 (petal like nanosheets) [5], which supports the nanosheet morphology formation.

Further, for structural investigation, Raman spectroscopy has been used. Being surface sensitive technique, it is a very effective tool to measure the minute changes in vibrational

frequencies which are attributed to the molecules, their crystal structure chemical bond and their length etc [6]. Figure 3A.5 (b) displays the Raman spectra for the nanostructured MoS_2 samples (MS-R0 to MS-R5) and bulk MoS_2sample (BMS). For each sample, occurrence of the two main peaks at 383 cm^{-1} and 402 cm^{-1} confirms the presence of 2H phase of MoS_2.These peaks correspond to the characteristics peak of E^1_{2g} and A_{1g} of 2H phase of MoS_2 [7].

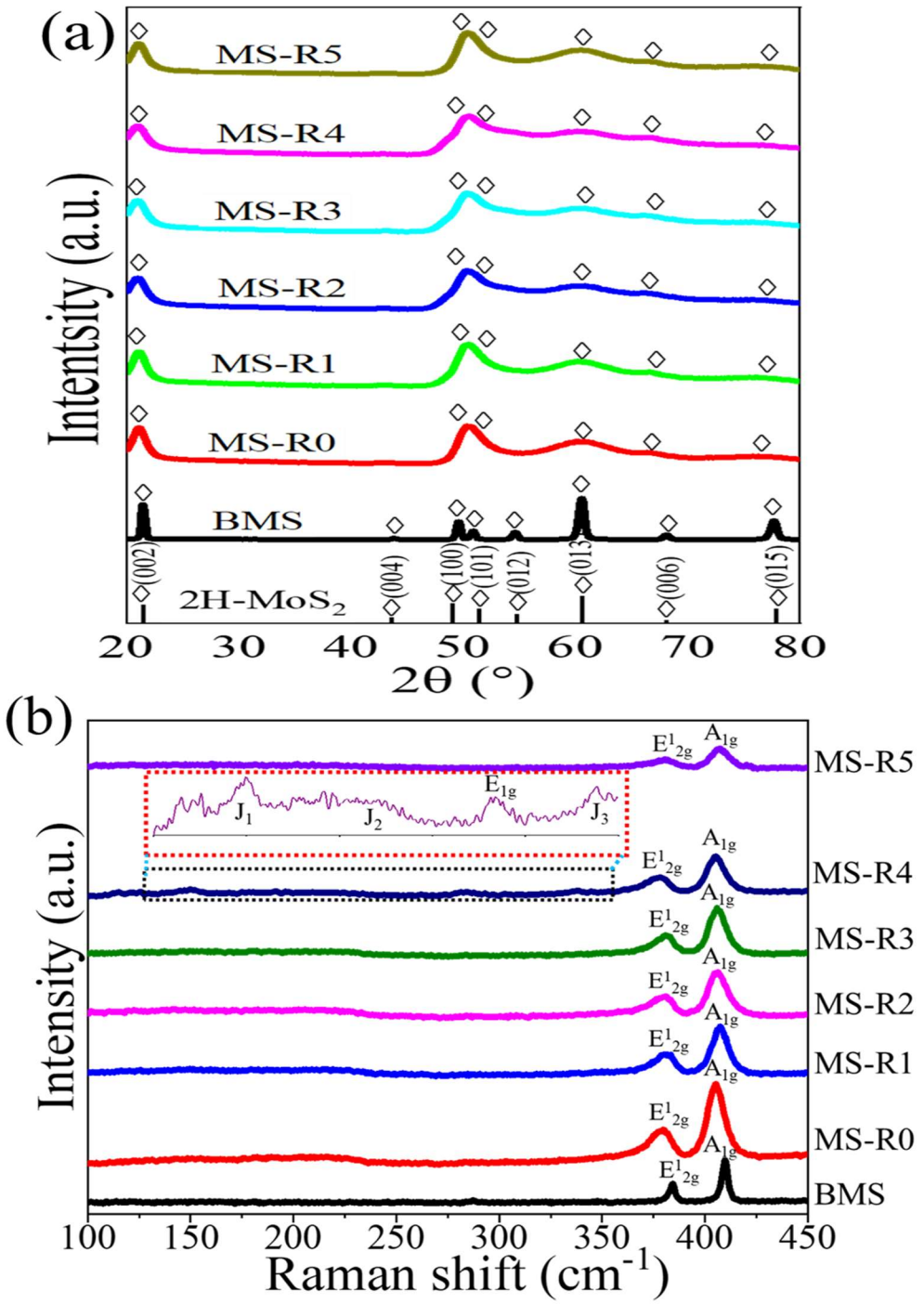

***Figure 3A.5**: (a) XRD pattern and (b) Raman spectra of hydrothermally synthesized MoS_2 with variation in reducing agent concentration and BMS.*

The increment in FWHM (*Full Width High Maxima*) and shift to lower wave number as compared to BMS is because of nanostructuring of MoS_2 and induced tensile stress [6]. However, an interesting feature has been observed in sample MS-R4, which showed a distinct difference in the spectrum in the range of 100 to 350 cm^{-1}, as compared to other samples. This sample showed additional three peaks with low intensity at 148 cm^{-1}, 238 cm^{-1} and 343 cm^{-1}. These peaks correspond to J_1, J_2 and J_3 phonon vibrations of 1T phase of MoS_2 [8], which confirms the presence of 1T phase as minor fraction along with major fraction of 2H phase of MoS_2. *Nonetheless*, these three additional peaks do not exist in other samples, indicated that other samples do not contain 1T phase of MoS_2.

3A.3.4: Chemical composition analysis using XPS

XPS tool is surface sensitive technique and very useful for qualitative and quantitative analysis. It helps to provide information about the elements present and their chemical composition based on binding energy.

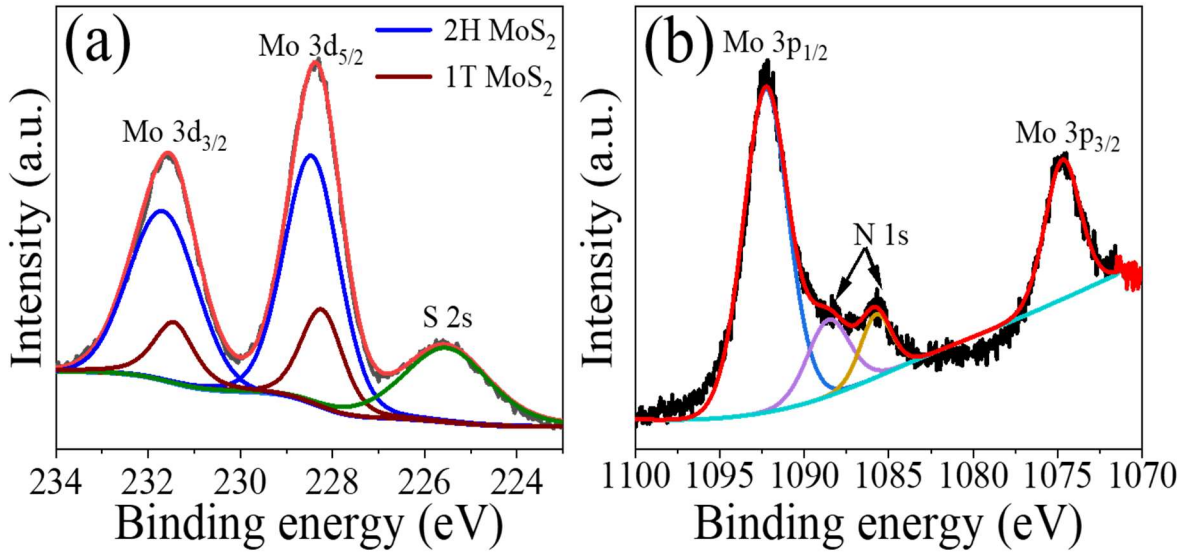

Figure 3A.6: High resolution XPS spectra of (a) Mo 3d, (b) Mo 3p and N 1s orbitals for sample MS-R4.

Figure 3A.6 displays high resolution XPS spectra for the sample MS-R4. All peaks have been normalised to the C1s peak, which has a binding energy (B.E.) of 284.8 eV (C-C bond) [9]. After the deconvolution, two characteristics peaks corresponding to Mo $3d_{5/2}$ and Mo $3d_{3/2}$ orbitals at 229.2 eV and 232.1 eV are observed which reflects the presence of 2H-MoS_2 [10]. Peaks at binding energy of 228.6 eV and 231. 8 eV are correspond to 1T-MoS_2 respectively which confirms the contribution of 1T-MoS_2 along with the 2H-MoS_2 [11]. In

figure 3A.6 (b), we have also observed the presence of N 1s orbitals at 398 eV and 400 eV which arises due to presence of amine (NH_2) and ammonium (NH_4^+) groups in the sample [12].

3A.3.5: Electrochemical characterization

After investigation of physico-chemical properties of hydrothermally synthesized nanostructured MoS_2 samples, Electrochemical characterization has been performed to calculate electrocatalytic parameters and evaluate HER efficiency of synthesized nanostructured MoS_2-based electrode as an electrocatalyst. For electrochemical measurements, the nanostructured MoS_2 powders were drop casted onto a conducting substrate (Carbon paper; C.P.). The schematic of the procedure followed for drop casting process has been shown in figure 2.3 and detailed in section 2.2.1.1, (Chapter 2). For all electrochemical measurements, an aqueous solution of 0.5 M H_2SO_4 was used as an electrolyte with a three-electrode configuration system that included a drop-casted electrode, a Saturated Calomel Electrode (SCE, +0.243 V *vs. SHE*), and a platinum rod as a working electrode, reference electrode and counter electrode respectively. During electrochemical characterization, potential was applied *w.r.t.* reference electrode which was converted *w.r.t.* RHE (E_{RHE}) using following formula…

$$\boldsymbol{E_{RHE} = E_{SCE} + 0.059 \times pH + E^0_{SCE}} \qquad \ldots \boldsymbol{3A.1}$$

E_{SCE} is the recorded potential *w.r.t.* reference electrode during electrochemical measurements, pH of 0.5 M H_2SO_4 acidic solution is measured 0.5 and E^0_{SCE} is the standard potential value of reference electrode.

Figure 3A.7 depicts the polarization curves recorded for nanostructured MoS_2 based electrodes, synthesized at different hydrothermal reaction time (24, 30 and 36 hours) and the variation in reducing agent concentration (from 0.14 M to 0.35 M), recorded at potential window of 0 V to -0.7 V *vs. SCE* at a scan rate of 2 $mV.sec^{-1}$ and their respective Tafel slopes. (All the nanostructured MoS_2 powders have been drop casted on carbon paper and used as working electrode during electrochemical characterization). Onset potential, overpotential (η), and their corresponding Tafel slopes (b) using polarization curves have been tabulated in Table 3.2. Figure 3A.7 (a) shows the polarization curve of nanostructured MoS_2, synthesized at different hydrothermal reaction time (24 to 36 hours) and Figure 3A.7 (b) shows corresponding Tafel slopes. To generate 10 $mA.cm^{-2}$ current density, sample MS 24, synthesized at hydrothermal reaction time of 24 hours, required a lower overpotential of 340 mV *vs. RHE*,

shown in Table 3A.2. Sample MS 24 demonstrate a highest HER activity and exhibited Tafel slope of 99 mV.dec^{-1} which is lowest among the samples, synthesized with variation in hydrothermal reaction time. Therefore, hydrothermal reaction time of 24 hours was optimized for further synthesis of nanostructured MoS_2 electrocatalyst which was used further in all experiments for the optimization of the reducing agent concentration. Polarization curves were recorded for hydrothermally synthesized nanostructured MoS_2 with reducing agent concentration variation (0.14 M to 0.35 M), Figure 3A.7 (c). Figure 3A.7 (d) shows their corresponding Tafel slope.

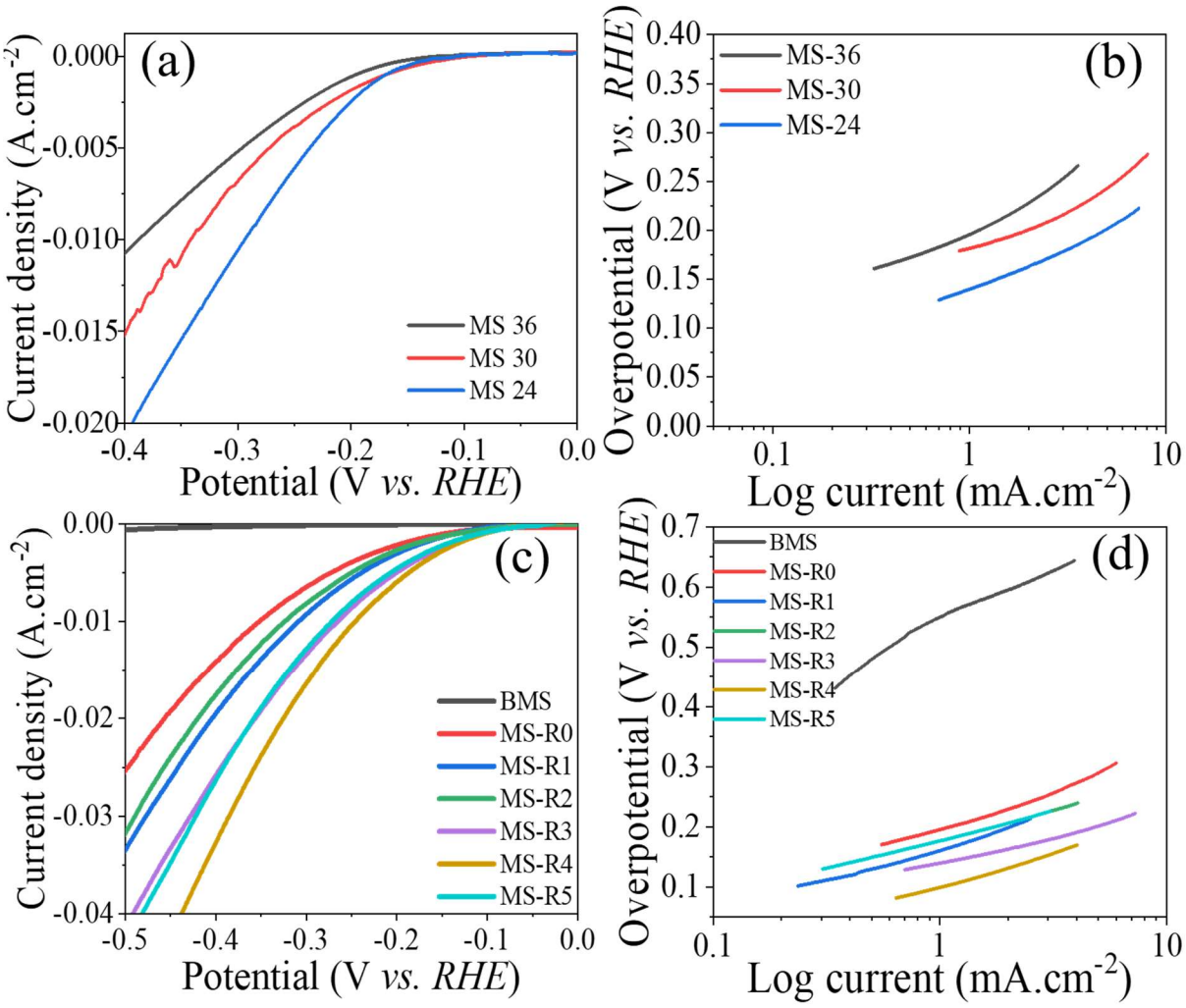

Figure 3A.7: HER parameter evaluation for nanostructured MoS_2 electrocatalyst; (a) Polarization curve for hydrothermally synthesized MoS_2 at different hydrothermal reaction time, (b) corresponding Tafel slope, (c) Polarization curve for hydrothermally synthesized MoS_2 at various concentrations of reducing agent and (d) corresponding Tafel slope.

Figure 3A.7 (c) clearly shows higher HER performance of nanostructured MoS_2 than bulk MoS_2, which validates that nanostructuring is one of the efficient approaches to improve

the HER activity of MoS_2, due to higher exposure of catalytically active edges. Among all nanostructured MoS_2 based electrodes, synthesized with variation in reducing agent concentration, sample MS-R4 with a hydrothermal reaction time of 24 hours and 0.28 M of reducing agent, exhibited 10 $mA.cm^{-2}$ current density at lowest value of overpotential (248 mV *vs. RHE*). This sample demonstrated the most efficient performance toward HER and displayed Tafel slope of 91 $mV.dec^{-1}$. It also exhibited lowest onset potential (potential at 1 $mA.cm^{-2}$) of 140 mV *vs. RHE*. The efficient HER performance of sample MS-R4 is attributed to presence of minute 1T phase along with major 2H-MoS_2.

Table 3A.2: The results of electrochemical characterization for synthesized MoS_2 at different reaction temperature and reducing agent concentration and bulk MoS_2 (commercial) electrocatalysts.

Sample name	Onset potential (mV *vs. RHE*)	Overpotential (η) @ 10 $mA.cm^{-2}$ (mV *vs. RHE*)	Tafel slope (b) ($mV.dec^{-1}$)
MS 30	195	350	105
MS 36	196	390	110
MS-R0	198	361	131
MS-R1 (MS 24)	195	340	99
MS-R2	190	326	97
MS-R3	171	296	94
MS-R4	140	248	91
MS-R5	143	272	93
BMS	549	739	191

With the optimized concentration of reducing agent, present amine groups intercalate the MoS_2 layers, resulting in 1T phase formation along with 2H phase of MoS_2 in sample [4,13]. Whereas, higher concentration of reducing agent distort the lattice structure of host system which lead to lower HER performance. Since, the values of Tafel slopes lies between 40 – 120 $mV.dec^{-1}$, the synthesized MoS_2 nanostructures follow the Volmer-Heyrovsky mechanism during HER application [14].

As it has been discussed, ECSA also plays a significant role to explore the electrocatalytic efficiency of sample for HER application. Figure 3A.8 (a) shows the linear

relationship between scan rates and difference in anodic & cathodic current density. The slope of this curve gives the value of C_{dl}. Figure 3A.8 (a) displays the values of C_{dl} for all the nanostructured MoS_2 samples. Sample MS-R4 exhibits a higher C_{dl} value of 3.36 $mF.cm^{-2}$ and the calculated ECSA is 56 cm^2 as compared with other synthesized samples (ECSA value of the samples has been calculated based on eq. 2.1 & eq. 2.2 in section 2.3.2.1.5 of Chapter 2). To further understand the kinetics of electrode/electrolyte interface, EIS has been performed for the nanostructured MoS_2 samples synthesized with variation in reducing agent concentration. Nyquist plot of respective samples have been displayed in Figure 3A.8 (b). Inset image of Figure 3A.8 (b) shows the best fitted equivalent circuit of the plot. The Nyquist plot for sample MS-R4 shows that it possesses the lowest resistance for charge transfer among all, which accelerates the number of transferred electrons electrode's surface to electrolyte, resulting in higher activity towards HER application [15,16].

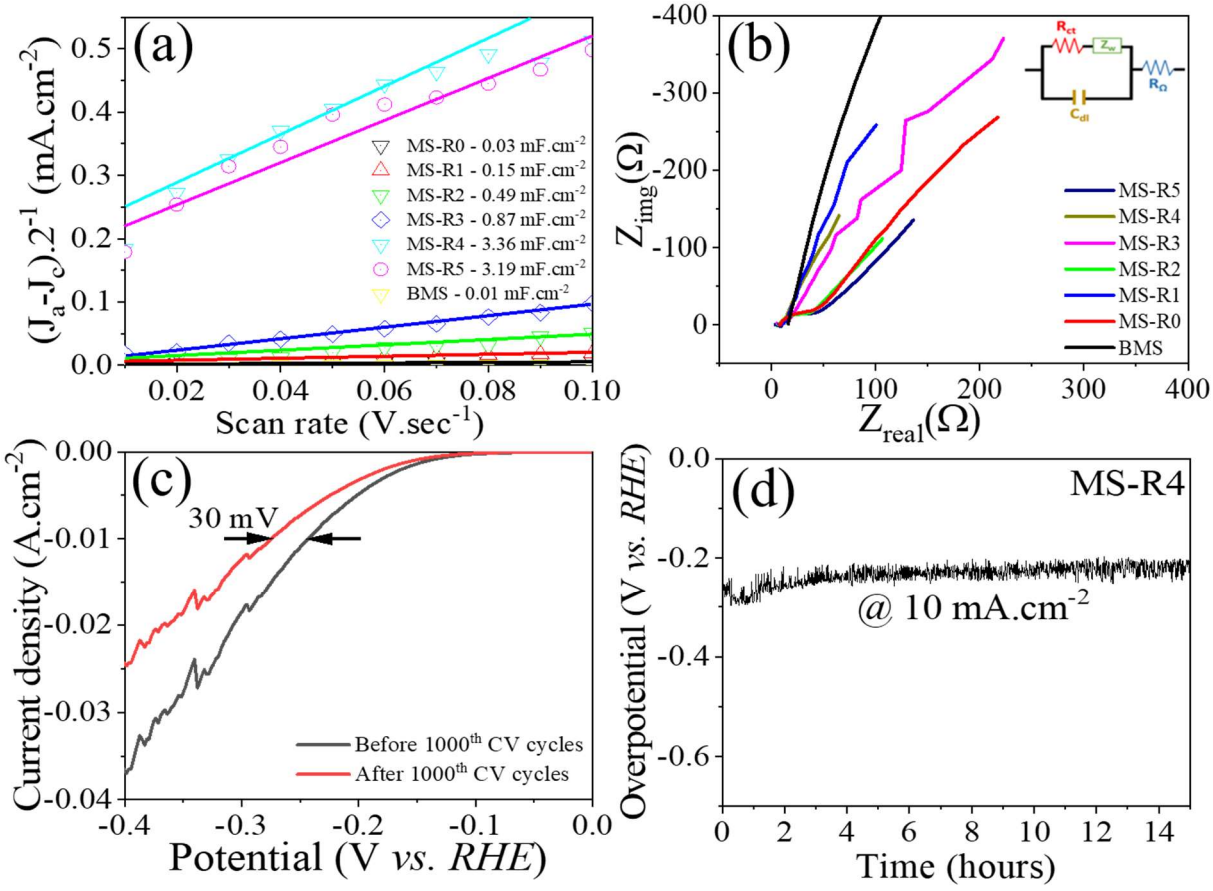

Figure 3A.8: (a) linear relationship between scan rate and difference in anodic and cathodic current density to estimate double layered capacitance of nanostructured MoS_2 electrocatalysts (reducing agent variation), (b) EIS curve and equivalent circuit (inset image), (c) polarization curve before and after 1000 CV cycles and (d) chronopotentiometry at 10 $mA.cm^{-2}$ current density for sample MS-R4.

In case of stability measurements, sample MS-R4 shows only 30 mV decay in overpotential @ 10 $mA.cm^{-2}$ current density after 1000 CV cycles (figure 3A.8 c), in addition to nearly constant value of overpotential at 10 $mA.cm^{-2}$ for a continuous 15 hours run, which reflects its significant stability of in acidic media (0.5 M H_2SO_4). Table 3A.3 compares the results obtained for HER reported in literature and present work. This table shows the electrocatalytic performance of various MoS_2 systems & its phases, synthesis method and respective morphologies. To enhance the efficiency of MoS_2 towards HER, some researchers have adopted top-down method like ball milling [17,18] but they were not able to achieve higher HER activity of MoS_2. To further enhance the efficiency of MoS_2, modification in morphology like synthesis of nanocolumns, quantum dots has been approached [19–21]. Additionally, for the synthesis of metallic MoS_2 *i.e.*, 1T MoS_2, chemical exfoliation method has been processed, but formation of hazardous materials as by products and difficulty in achieving electrochemical stability [22], limit its application. Expensive precursors like ammonium thiomolybdate, molybdenum chloride; several steps synthesis strategies; have been adopted to develop MoS_2 as an efficient electrocatalyst for HER application, which needed extra efforts, time consuming and not economical [23–26].

Table 3A.3: Value of overpotential and Tafel slope of reported MoS_2 systems in literatures.

S. No.	System	Method of synthesis	Phase	Electrocatalytic performance		Ref.
				Overpotential (η) (V) @ 10 $mA.cm^{-2}$	Tafel slope (b) ($mV.dec^{-1}$)	
1.	**Expanded MoS_2 - nanosheets**	Microwave assisted reduction	2H	0.149	49	[26]
2.	**MoS_2 nanodots**	Ionic liquid assisted exfoliation	2H	0.24	61	[21]
3.	**Micro/ nano MoS_2 microspheres**	Hydrothermal and annealing	2H	0.21	74	[19]

4.	**MoS_2 nanosheets/ Vulcan carbon**	Two step hydrothermal method	1T/2H	0.64	49	[24]
5.	**MoS_2 nanoplates**	Solvothermal method	2H	-	53	[27]
6.	**Hydrazine treated MoOx/MoS_2 nanowires**	CVD deposition, sulfurization using hydrothermal method, hydrazine treatment	1T/2H	0.40 V @ 22 $mA.cm^{-2}$	50	[23]
7.	**MoS_2 nanoflower**	Hydrotherma l method	2H	0.3 V @ 13.8 $mA.cm^{-2}$	52	[28]
8.	**MoS_2 nanosheets**	Ball milling	2H	0.48 @ 3 $mA.cm^{-2}$	138	[17]
9.	**MoS_2 nanosheets**	Annealing and hydrothermal	2H	0.28 @ 25 $mA.cm^{-2}$	90	[29]
10.	**MoS_2 nanocolumns**	Solvothermal	2H	0.25	57	[20]
11.	**2D MoS_2**	Plasma treatment	2H	0.35 @16.3 $mA.cm^{-2}$	108	[30]
12.	**Distorted MoS_2**	Ball milling	2H	0.2 V @ 0.9 $mA.cm^{-2}$	104	[18]
13.	**MoS_2 spheres**	Solvothermal	2H	-	100	[31]
14.	**MoS_2 nanosheets**	CTAB* assisted hydrothermal method	2H	0.2 @ 25 $mA.cm^{-2}$	55	[32]

15.	**MoS_2 loaded on Au electrode**	Liquid exfoliation	2H	-	94.1	[25]
16.	**MoS_2 MBNS[#]**	**Single step hydrothermal method**	**1T/2H**	**0.24**	**91**	**This work**
* Cetyl Trimethyl Ammonium Bromide, [#]Micro Balls decorated with Nano Sheets						

We have employed a single step synthesis approach in the present study to generate a mixed phase, *i.e.*, 1T/2H-MoS_2 using a hydrothermal process and obtained comparable efficiency of MoS_2 towards HER. This single step hydrothermal technique requires minimum possible efforts for production of efficient electrocatalyst with no hazardous materials as by products. The synergistic effect of 1T and 2H provides higher electrocatalytic activity as well as stability to the MoS_2 system. Single step synthesis of 1T/2H MoS_2 using hydrothermal method, makes MoS_2 economic, eco-friendly, and efficient electrocatalyst towards HER application.

3A.3.6: Application of nanostructured MoS_2 for hydrogen evolution

To estimate the rate of hydrogen evolution of optimized MoS_2 sample *i.e.*, MS-R4, electrolysis was initiated using three electrode configurations consisting of micro cell (10 ml volume) in acidic solution (0.5 M H_2SO_4). Particularly, drop casted MS-R4 on C.P. (working electrode) with Graphite rod (counter electrode) and Ag/AgCl in 3M KCl solution (reference electrode) was utilized to estimate real time hydrogen evolution. Real time hydrogen evolution over MS-R4 and MS-R0 was compared. Interestingly, MS-R4 electrode yielded 2 times higher hydrogen evolution (46 μmol h^{-1}) as compared to that over MS-R0 (23 μmol h^{-1}). Thus, a superior HER electrode has been achieved for nanostructured MoS_2 in this study.

3A.2: Conclusion

In conclusion, one-step hydrothermal approach was used to successfully synthesise nanostructured MoS_2 electrocatalyst with mixed phase (1T/2H). The formation of mixed phase was optimized at hydrothermal reaction time of 24 hours and concentration of reducing agent of 0.28 M. The optimized nanostructured MoS_2 proves itself as an efficient electrocatalyst for HER application. Morphological studies confirm the nanostructuring of MoS_2 and showed morphology of nanosheets, decorated over micro balls, which are completely difference from

bulk MoS_2. FESEM analysis demonstrate that nanostructured MoS_2 has a greater edge-to-basal plane ratio than bulk MoS_2. TEM images showed the lattice fringes of MoS_2 nanosheets and expanded interlayer spacing of 0.63 nm which is corresponding to 2H-MoS_2. In case of structural studies, XRD revealed the formation of 2H phase of MoS_2 without any impurities. In addition to this, we also observed that intensity of (002) plane peak of Bulk MoS_2 is higher while in case of nanostructured MoS_2 which confirms the lesser exposure of basal plane after nanostructuring of MoS_2. The ratio of (100)/ (002) plane intensity is higher in nanostructured MoS_2 as compared to bulk MoS_2, confirming the 2-dimensional layered MoS_2 formation after hydrothermal reaction. Raman analysis demonstrate that the sample MS-R4 exhibits a little fraction of 1T-MoS_2 along with 2H phase, which is quite fascinating. XPS also validates the formation of 1T-MoS_2 with minor fraction of only 23% along with remaining 2H phase of MoS_2 in sample MS-R4 which may be attributed to intercalation of present amine groups in reducing agent. Electrochemical studies also support the physico-chemical investigation. Nanostructured MoS_2 showed drastic change in electrochemical performance as compared to that of bulk MoS_2 due to increment in exposure of nanosheets edges and edges to basal plane ratio. In case of hydrothermally synthesized nanostructured MoS_2, sample MS-R4 exhibited lowest overpotential, small Tafel slope, higher ECSA and lowest charge transfer resistance with good electrochemical stability among other synthesized samples due to presence of metallic phase *i.e.*, 1T phase along with 2H phase of MoS_2.

3A.3: References

1. X. Li and H. Zhu, J. Mater. **1**, 33 (2015).

2. W. Zhao, X. Liu, X. Yang, C. Liu, X. Qian, T. Sun, W. Chang, J. Zhang, and Z. Chen, Nanomaterials **10**, (2020).

3. K. D. Rasamani, F. Alimohammadi, and Y. Sun, Mater. Today **20**, 83 (2017).

4. M. Li, Z. Zhou, L. Hu, S. Wang, Y. Zhou, R. Zhu, X. Chu, A. Vinu, T. Wan, C. Cazorla, J. Yi, and D. Chu, ACS Appl. Mater. Interfaces **14**, 16338 (2022).

5. G. Huang, T. Chen, W. Chen, Z. Wang, K. Chang, L. Ma, F. Huang, D. Chen, and J. Y. Lee, Small **9**, 3693 (2013).

6. B. C. Ghos, S. F. U. Farhad, M. A. M. Patwary, S. Majumder, M. A. Hossain, N. I. Tanvir, M. A. Rahman, T. Tanaka, and Q. Guo, ACS Omega **6**, 2665 (2021).

7. Y. Yao, K. Ao, P. Lv, and Q. Wei, Nanomaterials **9**, (2019).

8. U. Gupta, B. S. Naidu, U. Maitra, A. Singh, S. N. Shirodkar, U. V Waghmare, and C. N. R. Rao, APL Mater. **2**, 92802 (2014).

9. M. R. Linford, V. S. Smentkowski, J. T. Grant, C. R. Brundle, P. M. A. Sherwood, M. C. Biesinger, J. Terry, K. Artyushkova, A. Herrera-Gómez, S. Tougaard, W. Skinner, J.-J. Pireaux, C. F. McConville, C. D. Easton, T. R. Gengenbach, G. H. Major, P. Dietrich, A. Thissen, M. Engelhard, C. J. Powell, K. J. Gaskell, and D. R. Baer, Microsc. Microanal. **26**, 1 (2020).

10. C. Zhang, Z. Wang, S. Bhoyate, T. Morey, B. L. Neria, V. Vasiraju, G. Gupta, S. Palchoudhury, P. K. Kahol, S. R. Mishra, F. Perez, and R. K. Gupta, C **3**, (2017).

11. Y. Huang, Y. Sun, X. Zheng, T. Aoki, B. Pattengale, J. Huang, X. He, W. Bian, S. Younan, N. Williams, J. Hu, J. Ge, N. Pu, X. Yan, X. Pan, L. Zhang, Y. Wei, and J. Gu, Nat. Commun. **10**, 982 (2019).

12. Y. Wang, M. Zhen, H. Liu, and C. Wang, J. Solid State Electrochem. **22**, 3069 (2018).

13. R. Khatri and N. K. Puri, Vacuum **175**, 109250 (2020).

14. Q. Tang and D. Jiang, ACS Catal. **6**, 4953 (2016).

15. S. R. Kadam, U. V Kawade, R. Bar-Ziv, S. W. Gosavi, M. Bar-Sadan, and B. B. Kale, ACS Appl. Energy Mater. **2**, 5900 (2019).

16. Y. Xie and P. Sun, J. Nanoparticle Res. **20**, 183 (2018).

17. A. Ambrosi, X. Chia, Z. Sofer, and M. Pumera, Electrochem. Commun. **54**, 36 (2015).

18. D. Wang, Z. Wang, C. Wang, P. Zhou, Z. Wu, and Z. Liu, Electrochem. Commun. **34**, 219 (2013).

19. B. Guo, K. Yu, H. Li, H. Song, Y. Zhang, X. Lei, H. Fu, Y. Tan, and Z. Zhu, ACS Appl. Mater. Interfaces **8**, 5517 (2016).

20. X. Shang, W.-H. Hu, X. Li, B. Dong, Y.-R. Liu, G.-Q. Han, Y.-M. Chai, and C.-G. Liu, Electrochim. Acta **224**, 25 (2017).

21. J. Benson, M. Li, S. Wang, P. Wang, and P. Papakonstantinou, ACS Appl. Mater. Interfaces **7**, 14113 (2015).

22. J. Xia, J. Wang, D. Chao, Z. Chen, Z. Liu, J.-L. Kuo, J. Yan, and Z. X. Shen, Nanoscale **9**, 7533 (2017).

23. D. R. Cummins, U. Martinez, A. Sherehiy, R. Kappera, A. Martinez-Garcia, R. K. Schulze, J. Jasinski, J. Zhang, R. K. Gupta, J. Lou, M. Chhowalla, G. Sumanasekera, A. D. Mohite, M. K. Sunkara, and G. Gupta, Nat. Commun. **7**, 11857 (2016).

24. S. Shi, D. Gao, B. Xia, P. Liu, and D. Xue, J. Mater. Chem. A **3**, 24414 (2015).

25. T. P. Nguyen, S. Choi, J.-M. Jeon, K. C. Kwon, H. W. Jang, and S. Y. Kim, J. Phys. Chem. C **120**, 3929 (2016).

26. T. F. Jaramillo, K. P. Jørgensen, J. Bonde, J. H. Nielsen, S. Horch, and I. Chorkendorff, Science (80-.). **317**, 100 (2007).

27. Y. Yan, B. Xia, X. Ge, Z. Liu, J. Y. Wang, and X. Wang, ACS Appl. Mater. Interfaces **5**, 12794 (2013).

28. D. Wang, Z. Pan, Z. Wu, Z. Wang, and Z. Liu, J. Power Sources **264**, 229 (2014).

29. S. Muralikrishna, K. Manjunath, D. Samrat, V. Reddy, T. Ramakrishnappa, and D. H. Nagaraju, RSC Adv. **5**, 89389 (2015).

30. L. Tao, X. Duan, C. Wang, X. Duan, and S. Wang, Chem. Commun. **51**, 7470 (2015).

31. D. Y. Chung, S.-K. Park, Y.-H. Chung, S.-H. Yu, D.-H. Lim, N. Jung, H. C. Ham, H.-Y. Park, Y. Piao, S. J. Yoo, and Y.-E. Sung, Nanoscale **6**, 2131 (2014).

32. Z. Guo, Q. Ma, Z. Xuan, F. Du, and Y. Zhong, RSC Adv. **6**, 16730 (2016).

CHAPTER 3B

IN-SITU DEPOSITION OF MoS_2 ON LARGE AREA CONDUCTING SUBSTRATE *VIA.* HYDROTHERMAL METHOD AND ITS EFFICIENCY EVALUATION FOR HER APPLICATION

The utilization of binder like Nafion or Polytetratafluoroethene (PTFE) in preparation of homogenous ink, used for drop casting over the surface of the substrate, enhances the series resistance, blocks active sites and inhibits diffusion during electrochemical measurements of materials which leads the reduction in electrocatalytic activity of materials [1,2]. Therefore, the direct deposition of nanostructured MoS_2 over the conducting substrate can facilitate better electrocatalytic HER activity without blocking the active sites or help of various binders.

In the present Chapter, we have approached direct growth of MoS_2 nanosheets over the conducting substrate using hydrothermal method. We have used stainless steel sheet (S.S.: area 2.5 ×2.5 cm^2) as the substrate due to its excellent corrosion resistance and higher electrical conductivity (1.45×10^6 S/m at 20 ^{0}C) than carbon and its composites (1.25×10^3 to 2.00×10^3 S/m) in addition to its and low cost compared to other metals like Nickel (Ni), Molybdenum (Mo) [3].

In this chapter, we discuss the physico-chemical and electrochemical properties of *in-situ* deposited MoS_2 nanosheets over large area S.S. substrates. The schematic and the procedures followed for *in-situ* deposition of MoS_2 have been well explained in section 2.2.2 of Chapter 2. Sample name convention during physico-chemical and electrochemical properties evaluation has been compiled in table 2.2, Chapter 2.

3B.1: Result and discussion

3B.1.1: Morphological studies

For the investigation of surface morphology of *in-situ* deposited MoS_2 film, FESEM images have been recorded. These MoS_2 films were hydrothermally deposited at a temperature of 180 ^{0}C and a reaction time of 24 hours with various concentrations of reducing agent. Since, nanostructured MoS_2 electrocatalyst (chapter 3A) showed efficient HER performance synthesized with similar reaction parameters, therefore same hydrothermal reaction parameters

have been considered in present chapter for the *in-situ* deposition of MoS_2. Figure 3B.1 shows the surface morphology of *in-situ* deposited MoS_2 films with variation in reducing agent concentrations. Comparison of the surface morphologies of these MoS_2 films with nanostructured MoS_2 samples studied in Chapter 3A (Figure 3A.1), shows a clear difference in the morphology of nanosheets formation.

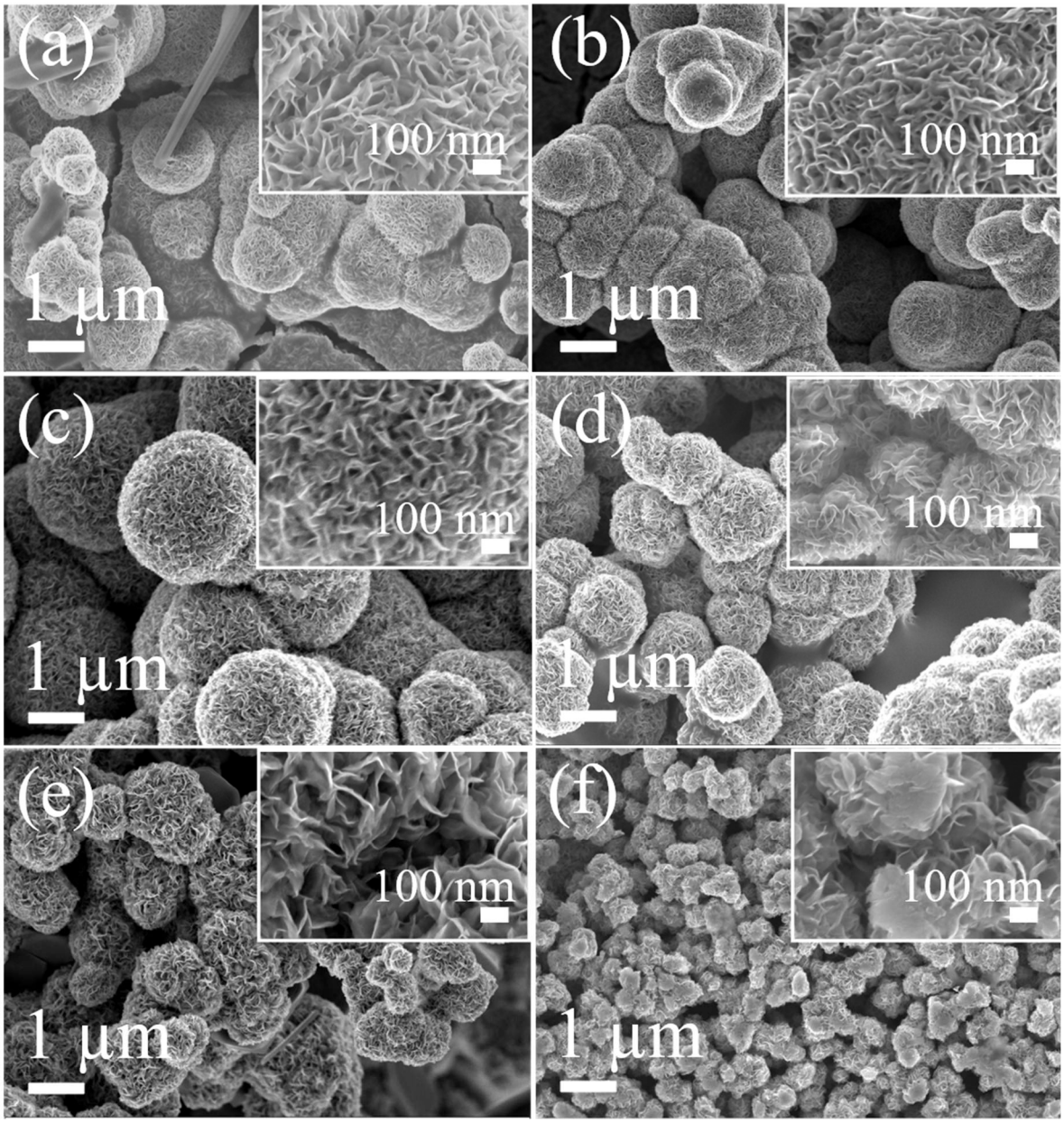

Figure 3B.1: FESEM images of in-situ deposited MoS_2 film on S.S. with variation in reducing agent concentration (a) MS00, (b) MS07, (c) MS14, (d) MS21, (e) MS28, (f) MS35. All samples have been synthesized at reaction temperature 180 ^{0}C and reaction time 24 hours.

In the deposited films, distinct nanosheets appeared which are vertically oriented (Inset of FESEM images, Figure 3B.1). Diameter of micro balls is decreased with increase in concentration of reducing agent and lowest in case of sample MS28 which can be clearly

observed form Figure 3B.1. The smaller size of micro ball provides larger surface area to grow nanosheets over its surface, resulting in the increment active sites density therefore, enhances the electrocatalytic efficiency of sample MS28 [4]. The dimensions of nanosheets are calculated to be with a thickness of ~5 nm and length 20 nm - 50 nm. The thickness of the *in-situ* deposited MoS_2 films on S.S., are calculated to be 1.5 - 2 μm.

3B.1.2: Elemental analysis by EDAX

For qualitative as well as quantitative analysis for the presence of elements in samples, EDAX has been used. The characterisation tool and respective technique has been briefly discussed in section 2.3.1.3.1 of Chapter 2.

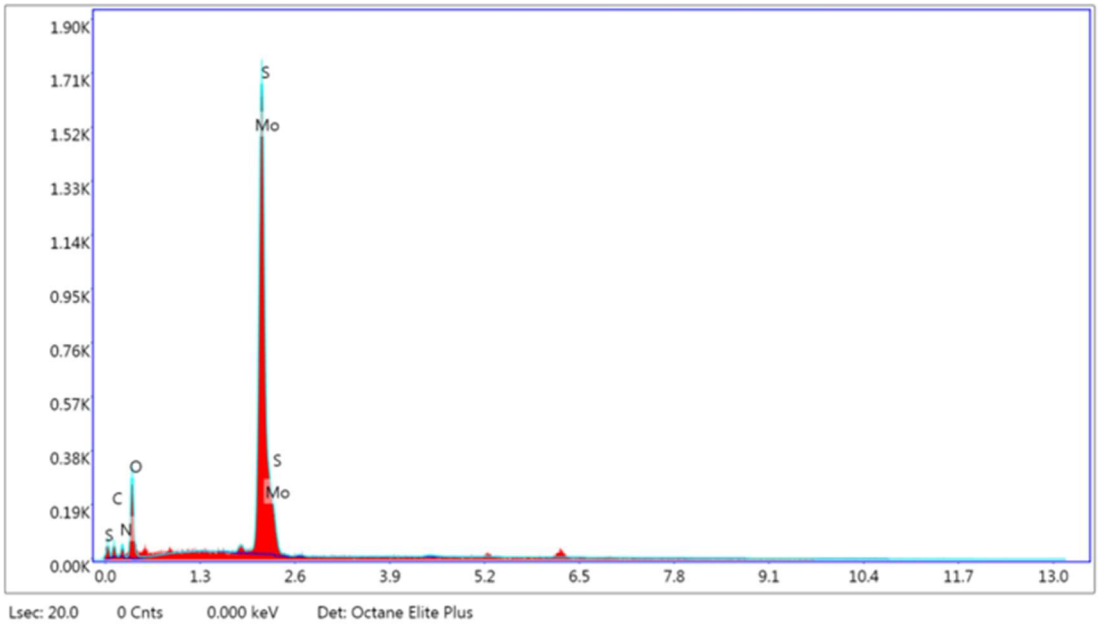

Figure 3B.2: EDAX spectrum for optimized sample MS28.

Table 3B.1: EDS report for hydrothermally deposited MoS_2 films on S.S.

Sample	Mo (at%)	S (at %)	Stoichiometry (approx.)
MS00	1.32	3.09	-
MS07	18.31	38.56	1: 2
MS14	15.98	32.66	1: 2
MS21	12.96	25.51	1: 2
MS28	10.85	20.9	1: 2
MS35	13.40	27.45	1: 1

EDAX spectrum of sample MS28 (optimized sample for HER application) has been shown in Figure 3B.2 and Table 3B.1, which shows the atomic percentage (at%) of the elements, present in respective samples. We have observed presence of Mo and S along with little at% of other elements like Fe, C, N, O which might have reflected from S.S. substrate. However, we have selected and compiled only Mo and S at% in the table. All *in-situ* deposited samples exhibited the stoichiometry (Mo: S) of 1:2 approximately which corresponds to MoS_2.

3B.1.3: Structural investigation of *in-situ* deposited MoS_2 films

To investigate the phase formation/structural properties of hydrothermally synthesized MoS_2 films, (samples to be measured, were scratched out and collected from the thin film surface and recorded XRD pattern) micro XRD has been utilized, related characterization tools and respective technique has been well explained in section 2.3.1.4.1 of Chapter 2.

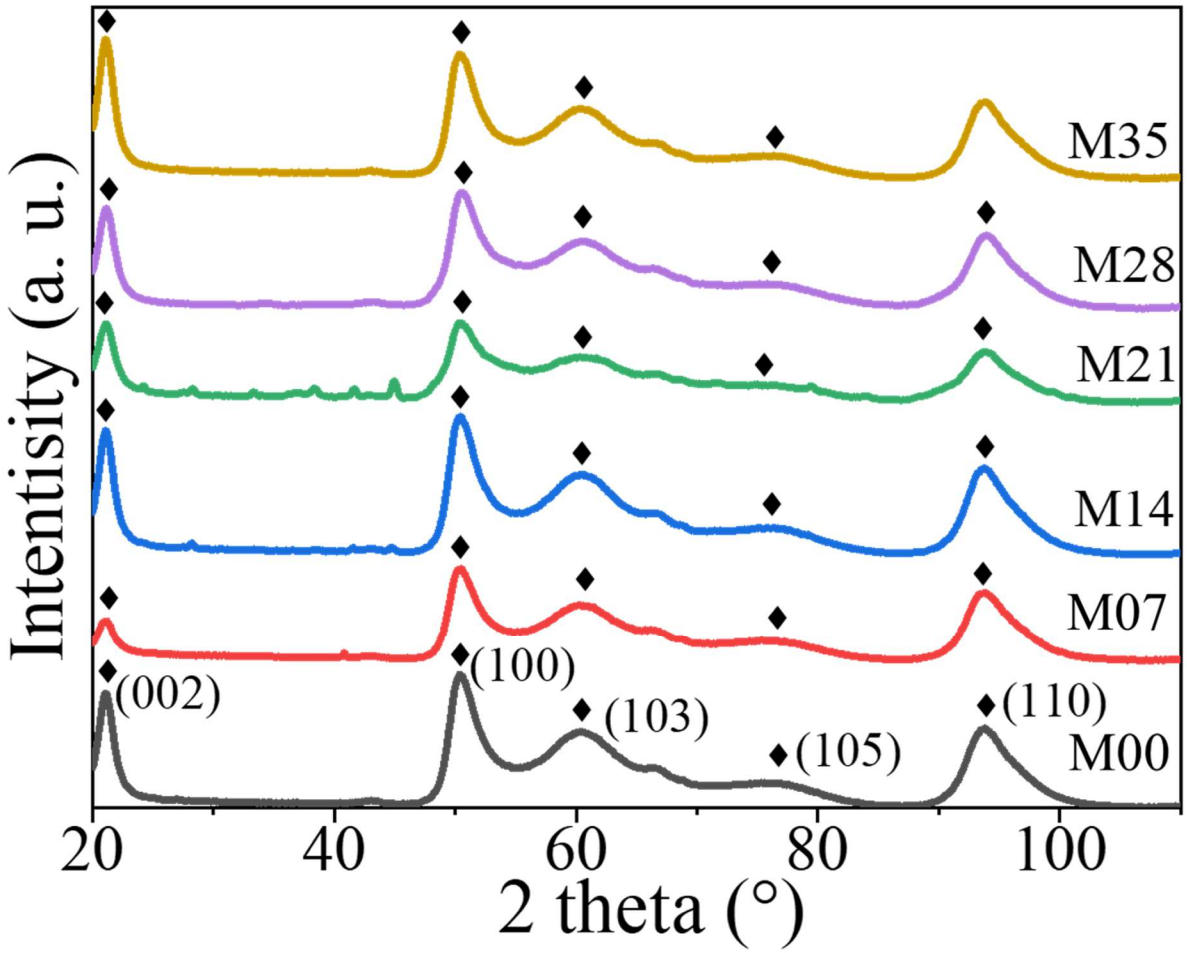

Figure 3B.3: XRD pattern for in-situ deposited MoS_2 films using hydrothermal method with variation in reducing agent concentration.

The XRD patterns for the *in-situ* deposited MoS_2 films are shown in Figure 3B.3. The XRD pattern validates the production of the 2H-MoS_2 in all samples, with no impurity phase.

XRD patterns, corresponding to PDF no. 00-037-1492 was observed. The ratio of peak intensity for plane (100) to (002) is more than 1, confirming the 2D nature of deposited nanostructured MoS_2 films.

Further, for structural investigation, Raman spectroscopy has been used. Being surface sensitive technique, it is a very effective tool to measure the minute changes in vibrational frequencies which are attributed to the molecules, their crystal structure chemical bond and their length etc [5].

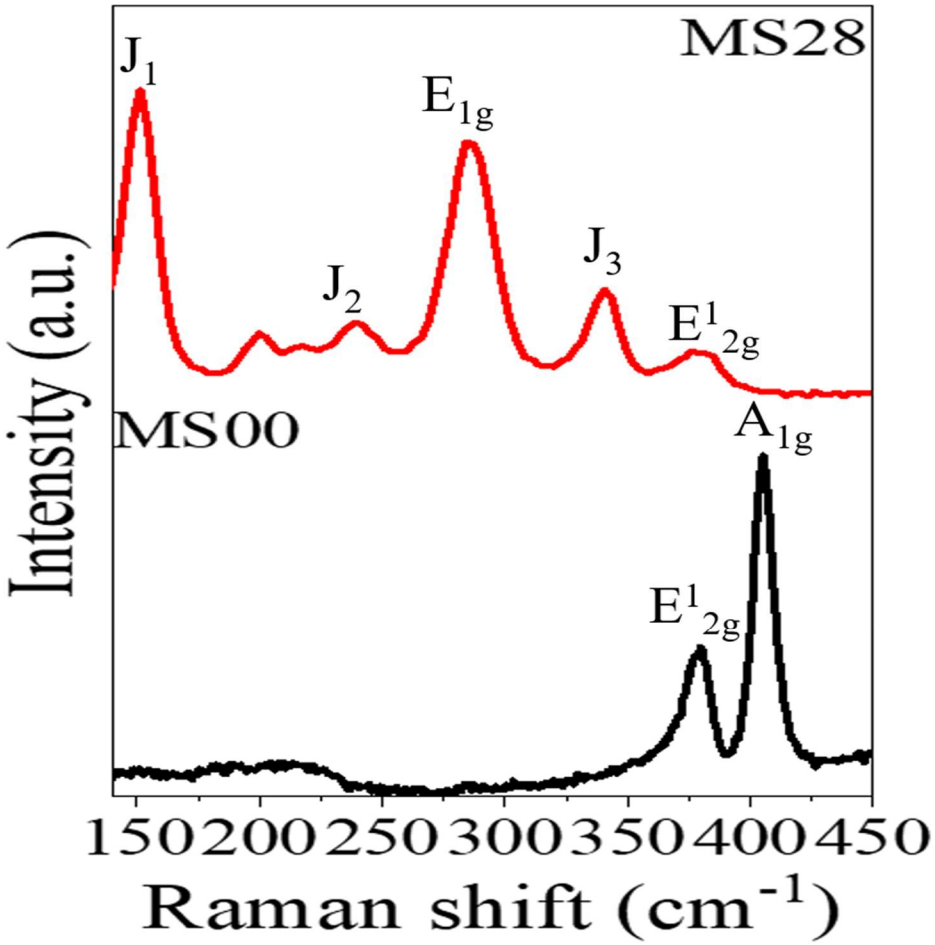

Figure 3B.4: Raman spectra of in-situ deposited nanostructured MoS_2 (MS00 and MS28).

Figure 3B.4 displays the Raman spectra for the hydrothermally deposited MoS_2 film (MS00 and MS28). For MS00 sample, occurrence of the two main peaks at 383 cm^{-1} and 402 cm^{-1} , correspond to the characteristics peak of E^1_{2g} and A_{1g}, confirms the presence of 2H phase of MoS_2 [6]. In sample MS28, presence of E^1_{2g} and E_{1g} confirms the formation of 2H phase of MoS_2. The higher intensity of peak E_{1g} confirms the higher exposure of edges which is due to vertically oriented nanosheets on the substrate [7]. However, an interesting feature has been observed in sample MS28, which showed a distinct difference in the spectrum in the range of

100 to 350 cm^{-1}, as compared to other samples. This sample showed additional three peaks with low intensity at 148 cm^{-1}, 238 cm^{-1} and 343 cm^{-1}. These peaks correspond to J_1, J_2 and J_3 phonon vibrations of 1T phase of MoS_2 [8], which confirms the presence of 1T phase as minor fraction along with major fraction of 2H phase of MoS_2.

3B.1.4: Electrochemical characterization

After investigation of the physico-chemical properties of the *in-situ* deposited nanostructured MoS_2 films, electrochemical characterization has been performed to evaluate electrocatalytic parameters and MoS_2's efficiency as an electrocatalyst towards HER application. For the electrochemical measurements, *in-situ* deposited MoS_2 films were directly taken as working electrode (2.5 × 2.5 cm^2) without any further modification. Figure 3B.5 shows the digital image of MoS_2 film, used as working electrode during electrochemical characterization.

Figure 3B.5: Digital image of one of the working electrodes, used during electrochemical measurements.

Figure 3B.6 shows the electrochemical studies of *in-situ* deposited MoS_2 films on S.S. substrate with variation in reducing agent concentration during the hydrothermal reaction at a temperature of 180 ^{0}C for 24 hours (MS00 to MS35) along with the respective Tafel slopes (Please refer to Table 2.2 for sample details). Electrochemical characterization for all the films has been performed in acidic solution (0.5 M H_2SO_4). The electrocatalytic parameters for HER application have been tabulated in Table 3B.2. Figure 3B.6 (a) well explains HER performance of *in-situ* deposited MoS_2 films. Similar kind of pattern for HER performance has been

observed as that for nanostructured MoS_2 (chapter 3A). Sample MS28, synthesized at a reducing agent concentration of 0.28 M, hydrothermal reaction time of 24 hours and hydrothermal reaction temperature of 180 ^{0}C, exhibited efficient performance toward HER application and displayed 82 mV *vs. RHE* of onset overpotential (overpotential at 1 mA.cm^{-2}) (Figure 3B.6 and Table 3B.2).

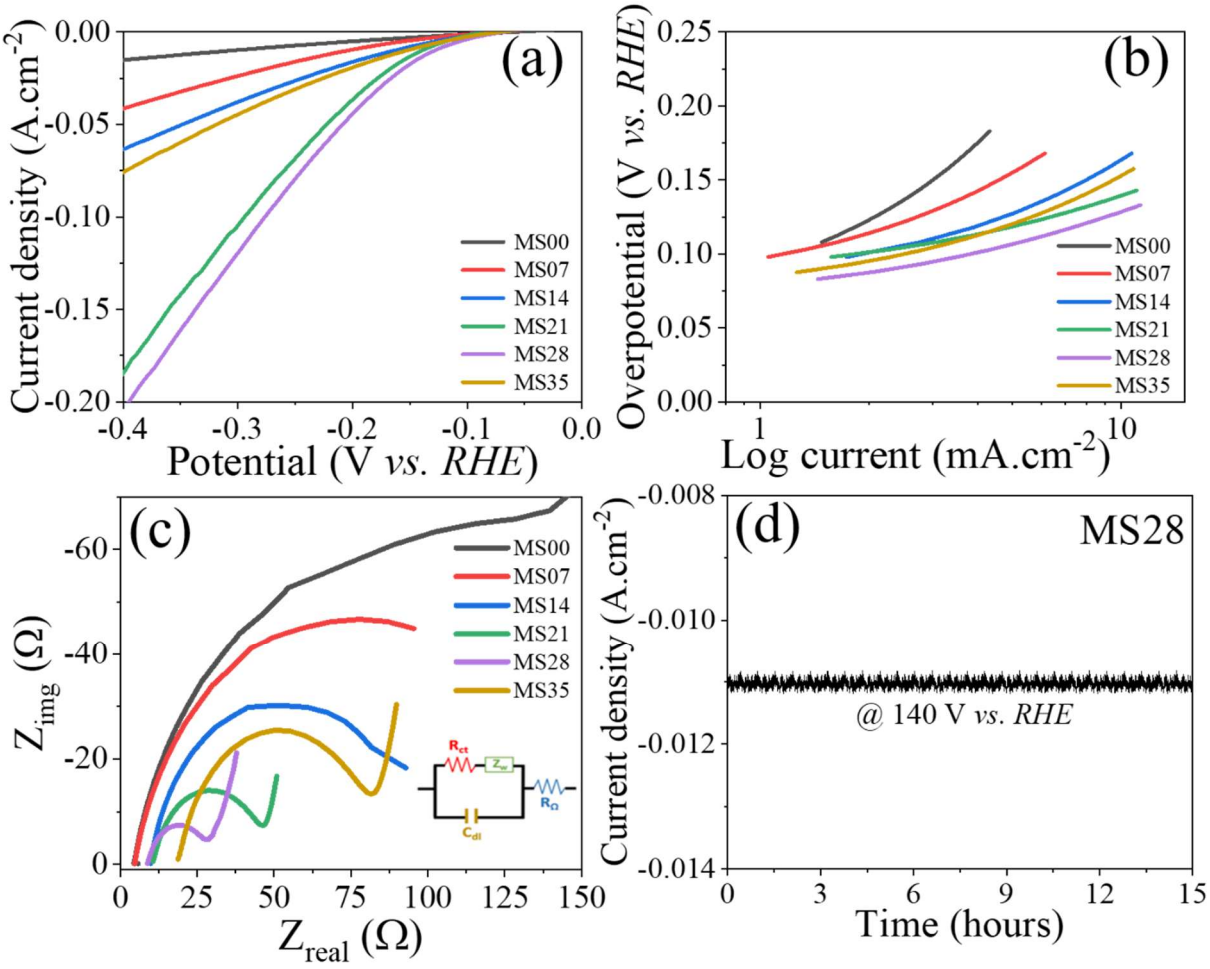

Figure 3B.6: HER parameter evaluation for in-situ deposited nanostructured MoS_2 films at different concentrations of reducing agent; (a) polarization curve, (b) their corresponding Tafel slopes, (c) EIS curve (inset image shows equivalent circuit of curve) and (d) long run stability curve only for sample MS28 (efficient sample).

This nanostructured MoS_2 film (MS28) required an overpotential of only 132 mV *vs. RHE* at 10 mA.cm^{-2} cathodic current density. This film demonstrated higher HER activity among other synthesized samples by exhibited lowest value of Tafel slope i.e., 55 mV.dec^{-1}. CVD, PVD etc. methods are also significant ways for the direct growth of MoS_2 over substrate's surface. This vertically grown 2H-MoS_2 nanosheets over Si/SiO_2 substrate using CVD method exhibited 90 mV.dec^{-1} Tafel slope [9]. Similarly, amorphous MoS_2 nanosheet grown on carbon cloth using physical vapor deposition (PVD) exhibited 224 mV *vs. RHE*

overpotential at 10 $mA.cm^{-2}$ and 58 $mV.dec^{-1}$ with remarkable stability up to 1000 CV cycles [10]. The better electrocatalytic efficiency of *in-situ* deposited MoS_2 film than reported MoS_2 systems is attributed to utilization of S.S. substrate and presence of 1T phase along with major 2H-MoS_2.

Table 3B.2: Value of onset potential, overpotential (η), Tafel slope (b) and charge transfer resistance (R_{ct}) for in-situ deposited MoS_2 films at different concentration of reducing agent.

Sample name	Overpotential (*η*) @ 10 $mA.cm^{-2}$ (mV *vs. RHE*)	Onset potential (mV *vs. RHE*)	Tafel slope (b) ($mV.dec^{-1}$)	Charge transfer resistance (R_{ct}) (Ω)
MS00	307	97	91	248
MS07	209	97	88	153
MS14	165	97	86	81
MS21	142	97	55	35
MS28	132	82	55	20
MS35	157	87	76	62

To further understand the kinetics of electrode/electrolyte interface, EIS has been performed for all films (with reducing agent variation) in acidic solution (0.5 M H_2SO_4). Nyquist plots of the samples has been displayed in Figure 3B.6 (c). Inset image of Figure 3B.6 (c) shows the best fitted equivalent circuit. Sample MS28 exhibits smallest curve among all the samples and lowest value of R_{ct} (20 Ω). The smallest value of R_{ct} illustrates that MS28 possesses lowest resistance value for charge transfer which accelerates number of transferred charges from the electrode's surface to electrolyte, resulting in higher activity towards HER application [11,12]. Figure 3B.6 (d) presents the current *vs.* time graph at constant potential of -140 V *vs. RHE* for 15 hours continuous run. This curve illustrates the excellent stability of *in-situ* deposited MoS_2 film on S.S. substrate with negligible change in current density.

Table 3B.3 summarizes approached various efforts in the direction to increase the efficiency of MoS_2 for HER application and compare with present study as well. This table has

been compiled among MoS_2 systems grown on various substrates, possessing different surface morphologies, its phases, method of deposition and improvement achieved towards HER application. The comparative studies mentioned in the table use direct growth of vertical MoS_2 nanosheets over various substrates like silicon/silica (Si/SiO_2), carbon paper, carbon cloth, rGO, Mo foil, Ni foam etc. using different methods where CVD/PVD, solvothermal methods are general approaches.

Table 3B.3: HER performance of nanostructured MoS_2 thin films reported in literatures.

S. No.	**System**	**Method of synthesis**	**Phase**	**Electrocatalytic performance**			**Ref.**
				η (mV *vs. RHE*) @ 10 $mA.cm^{-2}$	**Tafel slope (b) ($mV.dec^{-1}$)**	**Stability run**	
1.	**MoS_2 NS*/ Si/SiO_2**	CVD	2H	-	90	1000 cycles	[9]
2.	**MoS_2/ DG# silica template**	Electrodeposition and sulfurization	2H	230	50	-	[14]
3.	**MoS_2 NS/ Graphite**	CVD and Li intercalation	1T	195	43	15% decay after 1000 cycles	[13]
4.	**MoS_2 nanofilm/ Mo foil**	Two step CVD	2H	64	55	40000 sec and 5000 cycles	[15]
5.	**MoS_2 NS/3D carbon cloth**	Solvothermal	2H	205 @ 200 $mA.cm^{-2}$	39	1500 cycles	[16]

6.	**MoS_2 - nanoporous film/ Mo foil**	Anodization and sulfurization	2H	300 @ 18.6 $mA.cm^{-2}$	50	83% retention after 2000 cycles	[17]
7.	**MoS_2 thin film/ GC^+ electrode**	Electrodeposition	2H	600 @ 22 $mA.cm^{-2}$	106	-	[18]
8.	**MoS_2/ Carbon cloth**	PVD	2H	224	58	1000 cycles	[10]
9.	**MoS_2/ Carbon foam**	Pyrolysis and solvothermal	2H	230 @ 16 $mA.cm^{-2}$	44	-	[19]
10.	**MoS_2 nanopyramids/Si/SiO_2**	CVD	2H	393	93	1000 cycles	[20]
11.	**MoS_2/S.S. (large area)**	*In-situ* hydrothermal deposition	2H	132	55	15 hours of continuous run	This work
*NS – Nanosheets, $^{\#}$DG – Double Gyroid, $^{+}$GC – Glassy Carbon.							

Utilization of CVD/ PVD needs higher temperature and special arrangements to prepare the nanostructures whereas many step deposition methods consume time, efforts, needs number of precursors. Therefore, sophisticated experimental arrangement, utilization of expensive precursors/solvents can be provided at lab scale but it is not acceptable at industrial level.

In present study, we have approached the *in-situ* deposition of MoS_2 on large area S.S. substrate (2.5×2.5 cm^2) *via.* one step hydrothermal method and utilized it as cathode during HER performance. One step hydrothermal synthesis needs minimum possible efforts and time. Moreover, this method of synthesis does not require any special type of arrangement and can be performed at lower temperatures. The comparative HER performance of *in-situ* deposited

nanostructured MoS_2 films with other reported systems makes it economic and efficient electrocatalyst for HER application.

3B.2: Conclusion

An efficient nanostructured MoS_2 film to be used as cathode for HER application has been deposited at fixed reaction temperature of 180 ^{0}C and reaction time of 24 hours with variation in reducing agent concentration using one step hydrothermal method. Morphological studies confirm the nanostructuring of MoS_2 and showed morphology of nanosheets, decorated over micro balls, with film thickness of 1.5 μm-2 μm. XRD studies revealed the formation of 2H phase of MoS_2 with no other phase formation. Intensity ratio of (100)/ (002) plane more than one represents 2-dimensional layered MoS_2 formation after hydrothermal reaction. Electrochemical studies reveal efficient electrocatalytic performance of in-situ deposited MoS_2 films towards HER application. Sample MS28 exhibited the lowest overpotential of 132 mV, Tafel slope of 55 mV.dec^{-1} among other synthesized MoS_2 samples. Sample MS28 also shows excellent electrochemical stability in acidic solution up to 15 hours of continuous run. The enhanced electrochemical efficiency of MoS_2 films is attributed to metallic substrate which smoothen the number of electrons transfer to the electrode's surface. In addition, the binder free deposition reduces the series resistance.

3B.3: References

1. Y. Li, H. Wang, L. Xie, Y. Liang, G. Hong, and H. Dai, J. Am. Chem. Soc. **133**, 7296 (2011).

2. D. Voiry, M. Salehi, R. Silva, T. Fujita, M. Chen, T. Asefa, V. B. Shenoy, G. Eda, and M. Chhowalla, Nano Lett. **13**, 6222 (2013).

3. H. Grünewald, Angew. Chemie Int. Ed. English **11**, 449 (1972).

4. G. Yilmaz, T. Yang, Y. Du, X. Yu, Y. P. Feng, L. Shen, and G. W. Ho, Adv. Sci. **6**, 1900140 (2019).

5. B. C. Ghos, S. F. U. Farhad, M. A. M. Patwary, S. Majumder, M. A. Hossain, N. I. Tanvir, M. A. Rahman, T. Tanaka, and Q. Guo, ACS Omega **6**, 2665 (2021).

6. Y. Yao, K. Ao, P. Lv, and Q. Wei, Nanomaterials **9**, (2019).

7. X. Shang, W.-H. Hu, X. Li, B. Dong, Y.-R. Liu, G.-Q. Han, Y.-M. Chai, and C.-G. Liu,

Electrochim. Acta **224**, 25 (2017).

8. U. Gupta, B. S. Naidu, U. Maitra, A. Singh, S. N. Shirodkar, U. V Waghmare, and C. N. R. Rao, APL Mater. **2**, 92802 (2014).

9. H. Li, H. Wu, S. Yuan, and H. Qian, Sci. Rep. **6**, 21171 (2016).

10. X. Zhang, Y. Zhang, B.-B. Yu, X.-L. Yin, W.-J. Jiang, Y. Jiang, J.-S. Hu, and L.-J. Wan, J. Mater. Chem. A **3**, 19277 (2015).

11. S. R. Kadam, U. V Kawade, R. Bar-Ziv, S. W. Gosavi, M. Bar-Sadan, and B. B. Kale, ACS Appl. Energy Mater. **2**, 5900 (2019).

12. Y. Xie and P. Sun, J. Nanoparticle Res. **20**, 183 (2018).

13. M. A. Lukowski, A. S. Daniel, F. Meng, A. Forticaux, L. Li, and S. Jin, J. Am. Chem. Soc. **135**, 10274 (2013).

14. J. Kibsgaard, Z. Chen, B. N. Reinecke, and T. F. Jaramillo, Nat. Mater. **11**, 963 (2012).

15. T. Hu, K. Bian, G. Tai, T. Zeng, X. Wang, X. Huang, K. Xiong, and K. Zhu, J. Phys. Chem. C **120**, 25843 (2016).

16. N. Zhang, S. Gan, T. Wu, W. Ma, D. Han, and L. Niu, ACS Appl. Mater. Interfaces **7**, 12193 (2015).

17. Y. Yang, H. Fei, G. Ruan, C. Xiang, and J. M. Tour, Adv. Mater. **26**, 8163 (2014).

18. S. Murugesan, A. Akkineni, B. P. Chou, M. S. Glaz, D. A. Vanden Bout, and K. J. Stevenson, ACS Nano **7**, 8199 (2013).

19. X. Guo, G. Cao, F. Ding, X. Li, S. Zhen, Y. Xue, Y. Yan, T. Liu, and K. Sun, J. Mater. Chem. A **3**, 5041 (2015).

20. Q. Zhou, S. Su, P. Cheng, X. Hu, X. Gao, Z. Zhang, and J.-M. Liu, J. Mater. Chem. C **8**, 3017 (2020).

3: Conclusion

In the summary of chapter 3, nanostructuring of MoS_2 and *in-situ* deposition of nanostructured MoS_2 over conducting substrate as well, have been achieved *via.* economic and facile technique *i.e.*, hydrothermal route. Nanostructuring increased the catalytically active edges in nanostructured MoS_2 samples and the presence of metallic (1T)-MoS_2 combined with semiconducting (2H)-MoS_2 provides higher intrinsic conductivity to the MoS_2 system, which results improved HER performance and made nanostructured MoS_2 more efficient and stable towards HER application. Moreover, higher HER activity of single step hydrothermally deposited nanostructured MoS_2 film is synergistic effect of vertically oriented nanosheets, presence of 1T phase along with 2H phase of MoS_2 and binder free deposition over conducting substrate. Therefore, the single step hydrothermally synthesized 1T/2H mixed phase MoS_2 electrocatalyst and *in-situ* deposited nanostructured MoS_2, makes MoS_2 an efficient, stable, sustainable, scalable, and cost-effective HER electrocatalyst which is desired at industrial level.

CHAPTER 4

NOBLE METAL (PALLADIUM; Pd) DOPED MoS_2 AS AN EFFICENT ELECTROCATALYST FOR HER APPLICATION

Noble metals such as Pt, Pd, Au, Ag etc. are well known for their excellent electrocatalytic properties. However, due to the lack of cost effectiveness of these electrocatalysts, scaling up of Hydrogen generation is hindered to a large extent. In order to use the benefits of noble metals effectively and reduce the cost of the electrocatalyst, noble metal loading or doping into MoS_2 is an effective route to increase the efficiency of MoS_2 towards HER. Even though, noble metal loading eases the charge transfer and reduces the hydrogen adsorption energy, it does not affect the lattice of MoS_2 system. However, noble metal doping tunes the electronic structure, morphology, induces defects, vacancies, forms new active sites as well, induces 1T phase fraction in MoS_2 which is much more effective than the loaded noble metal itself and in addition to be cost-effective as compared to noble metal loading [1].

Among noble metal doped MoS_2 systems, electrocatalytic efficiency of Pd doped MoS_2 (Pd-MoS_2) was found to be superior for HER application. Theoretical studies revealed that Pd doped MoS_2 exhibits -0.02 eV Gibb's free energy for hydrogen adsorption. It helps in phase transition from semiconducting 2H phase to metallic 1T phase and also introduces defects in MoS_2's crystal structure by creating sulfur vacancies [2,3].

In this chapter, in order to investigate the effect of Pd doping in increasing the electrocatalytic efficiency of MoS_2 towards HER application, we have systematically varied the Pd dopant concentration. One step hydrothermal synthesis method is a facile and economic route and is not a time-consuming process. Nanostructured Pd-MoS_2 electrocatalyst has been synthesized by one step hydrothermal method. The details of the synthesis procedure for Pd-MoS_2 have been explained in section 2.2.3 of Chapter 2. Herein, we have discussed the physico-chemical and electrochemical characteristics of the nanostructured Pd-MoS_2 electrocatalyst Ultimately, we have also studied the overall water splitting reaction in acidic, alkaline, and saline water using Pd-MoS_2 as HER cathode.

4.1 Result and discussion

4.1.1 Morphological studies

To synthesize of the Pd doped MoS_2 (Pd-MoS_2) nanostructured electrocatalysts with better HER efficiency, precursor concentration of $PdCl_2$ was optimized systematically.

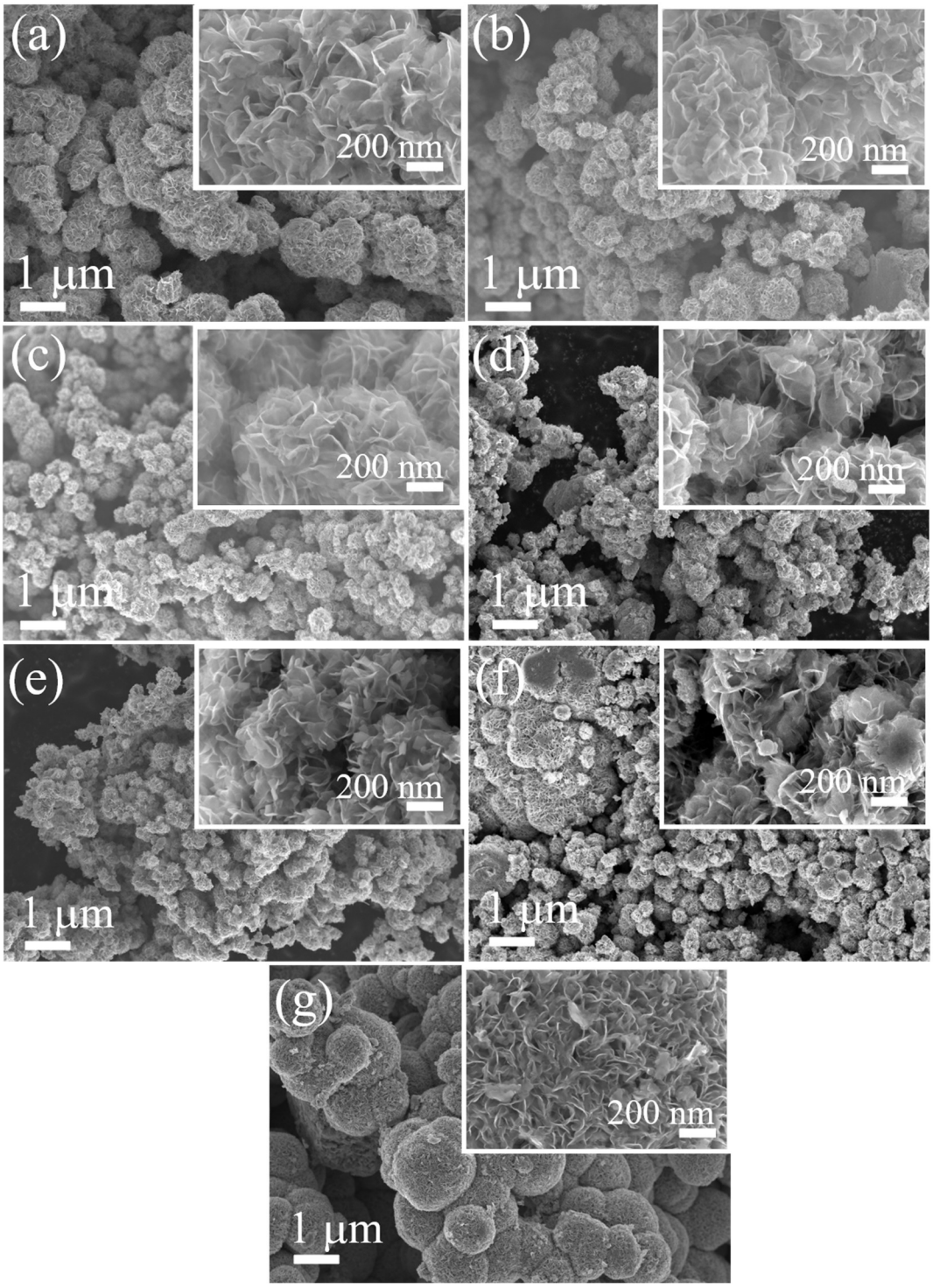

Figure 4.1: Morphological investigations for samples Pd-MoS_2; (a) Pd-MS1, (b) Pd-MS2, (c) Pd-MS3, (d) Pd-MS4, (e) Pd-MS5, (f) Pd-MS6 and (g) pristine MoS_2.

The hydrothermal reaction time and temperature were 24 hours and 180 ^{0}C respectively to synthesized Pd doped MoS_2 system. The amount of Pd based precursor added to each sample have been varied from 5 mg to 50 mg. Related details have been mentioned in section 2.2.3, Chapter 2. Figure 4.1 shows the FESEM images of Pd-MoS_2 samples, synthesized using different Pd precursor concentrations. We have also included FESEM image of pristine MoS_2 for comparison. In Figure 4.1, difference in the morphology of Pd-MoS_2 samples with different Pd loading and pristine MoS_2 can be clearly seen. Pd-MoS_2 as well as pristine MoS_2exhibit morphology of micro balls decorated with petal like (nanosheets) structures. A dramatic reduction in the dimension of the micro balls as well as nanosheets was observed in case of Pd-MoS_2 as compared to pristine MoS_2. Lowest diameter of the micro balls was estimated to be approximately 0.5 μm for sample Pd-MS5 whereas it was 5-2 μm for pristine MoS_2.

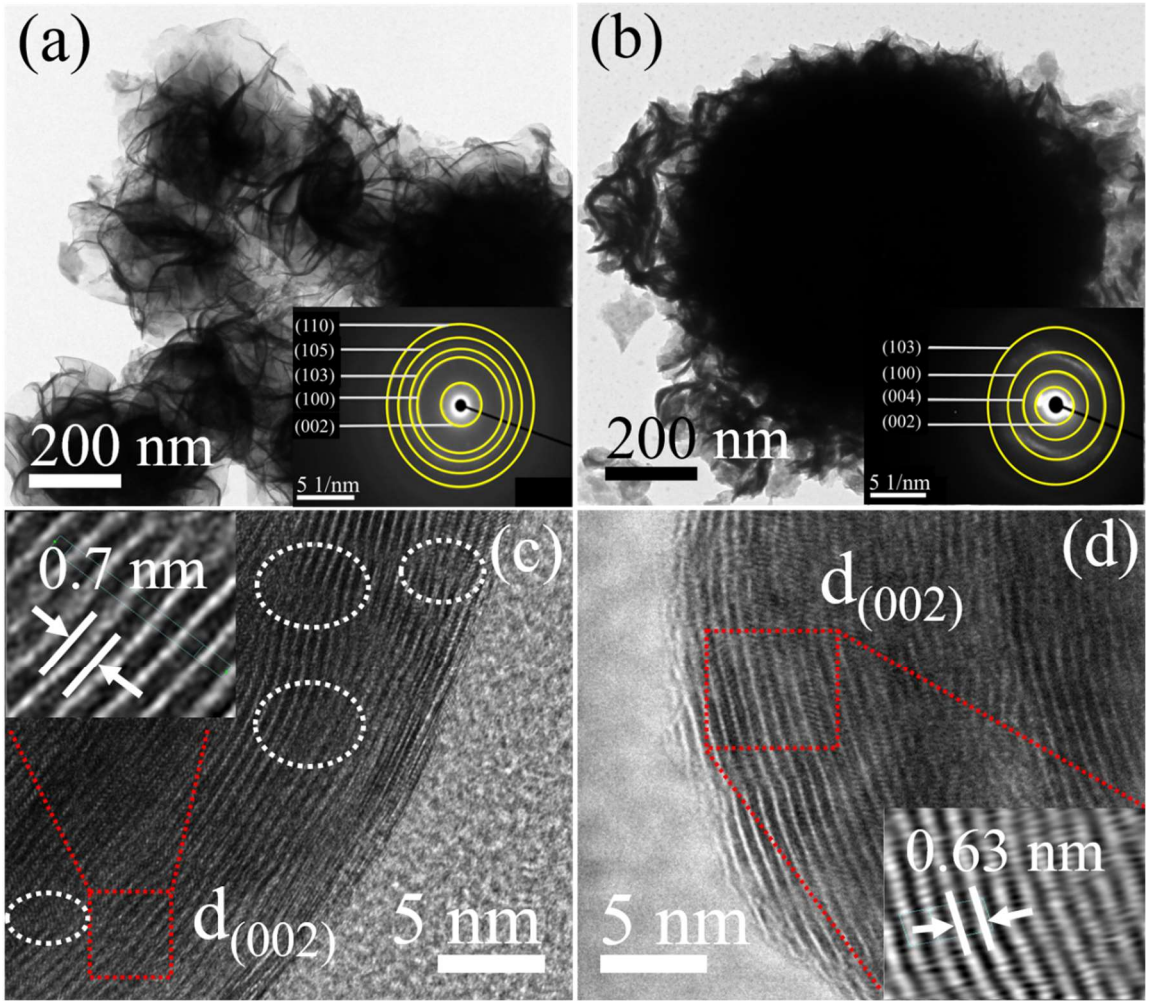

Figure 4.2: (a, b) Low magnification TEM images (inset image shows corresponding SAED pattern) (c, d) HRTEM images (inset images shows corresponding IFFT images, used for interplanar distance calculation) of sample Pd-MS5 (optimized sample) and pristine MoS_2.

An *in-depth* analysis of the sample Pd-MS5 and pristine MoS_2 was done by the imaging the samples using TEM. TEM analysis has been done only for sample Pd-MS5 since it has given most efficient HER performance among synthesized Pd doped MoS_2 samples. TEM image of pristine MoS_2 have been added for the comparison. As shown in Figure 4.2 (a), low magnification TEM images confirm the reduction in micro ball dimensions with larger number of active sites on the nanosheets in sample Pd-MS5 as compared to pristine MoS_2 (Figure 4.2.b) and corroborate with the FESEM images (Figure 4.1e). It has been extensively studied that doping of foreign element into electrocatalyst is one of the best strategies to tune the morphology. Doping of foreign element leads to distortion in the local structure of host lattice and affects the crystal growth resulting in a differed morphology [4,5]. Moreover, reduction in micro ball dimension provides room for nanosheets of larger surface area to be grown. Thereby, yields a higher density of catalytic sites ultimately results in accelerated hydrogen evolution [6]. Figure 4.2 (c & d) shows HRTEM images of Pd-MS5 and pristine MoS_2 respectively. In both cases, a distinct interlayer spacing corresponding to (002) plane of MoS_2 was confirmed and the IFFT image (inset of respective HRTEM image) from dotted square region was used to estimate interplanar distance. For Pd-MS5, interplanar distance was found to be 0.7 nm whereas it was 0.63 nm for pristine MoS_2. Such increased interplanar distance in case of doped MoS_2 system can be attributed to the NH_2/NH^{+4} group intercalation, present in reducing agent and Mo precursor or Pd metal atom which can be due to the interaction between the Pd and S atoms of the S–S interlayer and ultimately affects the expansion of c-axis and interlayer spacing [7][8]. It has been well reported that the extended interlayer spacing modifies the electronic structure of individual MoS_2 monolayer, in particular, the atoms at the edge sites and also enables each S-Mo-S layer to establish an efficient electrochemical performance equivalent to freestanding MoS_2 monolayers, results in improved intrinsic conductivity and catalytic performance towards HER application [9,10]. The interlayer spacing for sample Pd-MS5 and pristine MoS_2 was found *in-line* with the selected area electron diffraction (SAED) pattern, carried out separately (inset of figure 4.2, a & b). Despite the expanded interplane spacing, we have also observed rich defect formation in nanosheets of sample Pd-MS5, shown in circular region with white dotted boarder in figure 4.2 (c), which is attributed to the disorder induced in the lattice after Pd doping in MoS_2. These defects tend to form unsaturated sulphur which makes Pd-MS5 more catalytically active for HER application [11].

4.1.2 Elemental analysis by EDAX

Qualitative as well as quantitative analysis of the elements present in samples, have been done using EDAX spectra. Figure 4.3 (a) presents the EDAX spectrum and Figure 4.3 (b-d) shows the elemental mapping for Mo, S and Pd elements present in the sample Pd-MS5. Table 4.1 displays increment in atomic percentage (at%) of Pd with increase in Pd precursor concentration in the respective samples whereas, decrement in at% of Mo is observed for all Pd doped MoS_2 samples.

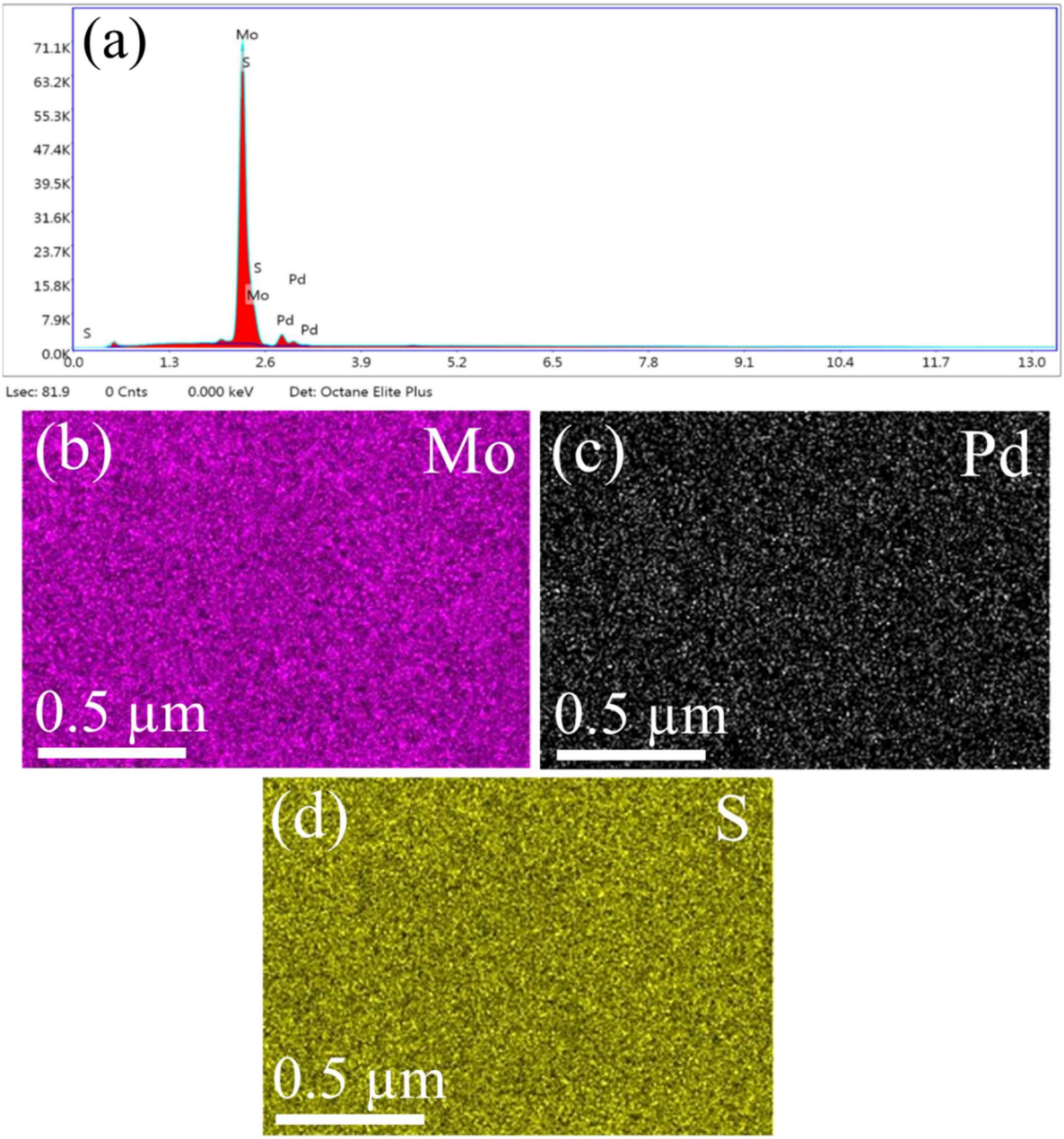

Figure 4.3: (a) EDAX pattern and (b, c, & d) area mapping for element Mo, Pd and S respectively present in sample Pd-MS5.

Table 4.1: EDS report for hydrothermally synthesized Pd-MoS_2 and pristine MoS_2 electrocatalysts.

Sample	Mo (at%)	S (at %)	Pd (at %)
Pd-MS1	30.95	68.66	0.4
Pd-MS2	31.77	66.61	1.61
Pd-MS3	29.13	68.22	2.65
Pd-MS4	29.22	66.79	3.99
Pd-MS5	26.16	67.59	5.25
Pd-MS6	28.78	64.89	6.33
pristine MoS_2	31.09	68.91	-

It has been reported that Pd doping in MoS_2 induces formation of sulfur vacancies (SVs) [13], which is experimentally validated by the loss of S element as compared to pristine MoS_2, shown in element stoichiometry analysis (Table 4.1).

4.1.3 Structural investigation

4.1.3.1 XRD analysis

To investigate phase formation/structural properties of all hydrothermally synthesized Pd-MoS_2 and pristine MoS_2 samples, smart lab XRD has been utilized (related characterization tools and respective technique has been well explained in section 2.3.1.4.1, Chapter 2).

Figure 4.4 shows the XRD pattern of all Pd-MoS_2 samples with variation in Pd concentration as well as pristine MoS_2. All synthesized samples exhibited analogous feature and major reflections due to (002), (100), (103) and (110) planes related to 2H phase of MoS_2 (space group – P6 3/mmc, entry number 96-101-1287 in PDF+4 database) were observed. XRD patterns of synthesised nanostructured electrocatalysts show a higher intensity of (002) plane in comparison to (100) plane which confirms the 2-dimensional (2d) layered MoS_2 formation [29]. We have also observed the slight peak shift at lower angle in case of Pd-MoS_2 samples corresponding to (002) plane which can be due to induced strain into MoS_2 lattice after doping, resulting in defects formation in MoS_2 lattice.

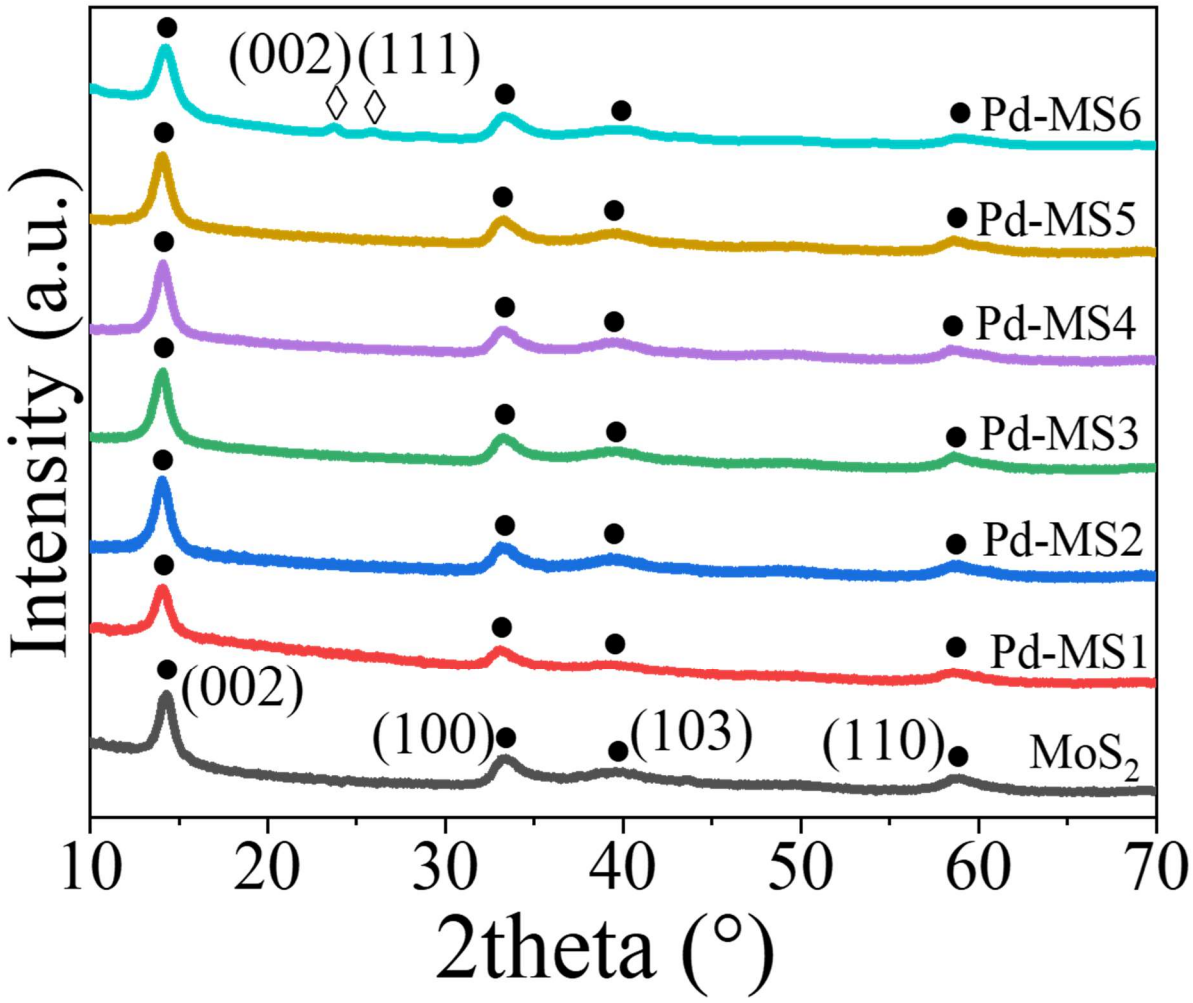

Figure 4.4: XRD pattern for hydrothermally synthesized Pd-MoS_2 and pristine MoS_2 nanostrcutres.

Moreover, XRD patterns of sample Pd-MS6 have shown the presence of two more peaks other than those of MoS_2 at 23.720 and 25.930 which are corresponds to PdS_2 (space group – P b c a, entry number 96-231-0590 from PDF+4 database), confirming the PdS_2 phase formation at higher concentration of Pd based precursor along with major MoS_2 2H phase formation.

4.1.3.2 Raman analysis

For further investigation for phase formation, Raman technique has been applied on the Pd-MS5 sample and compared its Raman spectrum with pristine MoS_2 and bulk MoS_2. Figure 4.5 represents the Raman spectra of hydrothermally synthesized Pd-MS5, pristine MoS_2 and bulk MoS_2 (commercial) samples. The increase in FWHM in case of Pd-MoS_2 and pristine MoS_2 as compared to bulk MoS_2 is due to nanostructuring of synthesized samples. All the samples validated the existence of peaks due to 2H phase of MoS_2 *viz.* due to A_{1g}, E^1_{2g} and E_{1g} (405 cm^{-1}, 378 $cm^{-1}$and 290 cm^{-1} *respectively*) and Pd-MS5 and pristine MoS_2 validates

presence of 1T phase of MoS_2 *i.e.*, phonon induced mode J_1, J_2 and J_3 (197 cm^{-1}, 238 cm^{-1} and 343 cm^{-1} *respectively*) [12]. However, unlike pristine MoS_2, Pd-MoS_2 showed prominent features at lower wave number in the range of 200 to 350 cm^{-1}. Pd doped MoS_2 exhibited strong peaks due to E_{1g} and phonon modes (J_1, J_2 and J_3) and weak peaks corresponding to E^1_{2g} and A_{1g} which illustrate the higher edge exposure as well as higher fraction of 1T phase *w.r.t.* 2H phase as compared to pristine MoS_2. The *red shift* in A_{1g} and E^1_{2g} (~4cm^{-1}) can be correlated to the doping induced tensile stress in the MoS_2 lattice [13] and a prominent enhancement in the E_{1g} vibrational intensity is correlated to the higher exposure of the edge-structure of MoS_2 [14].

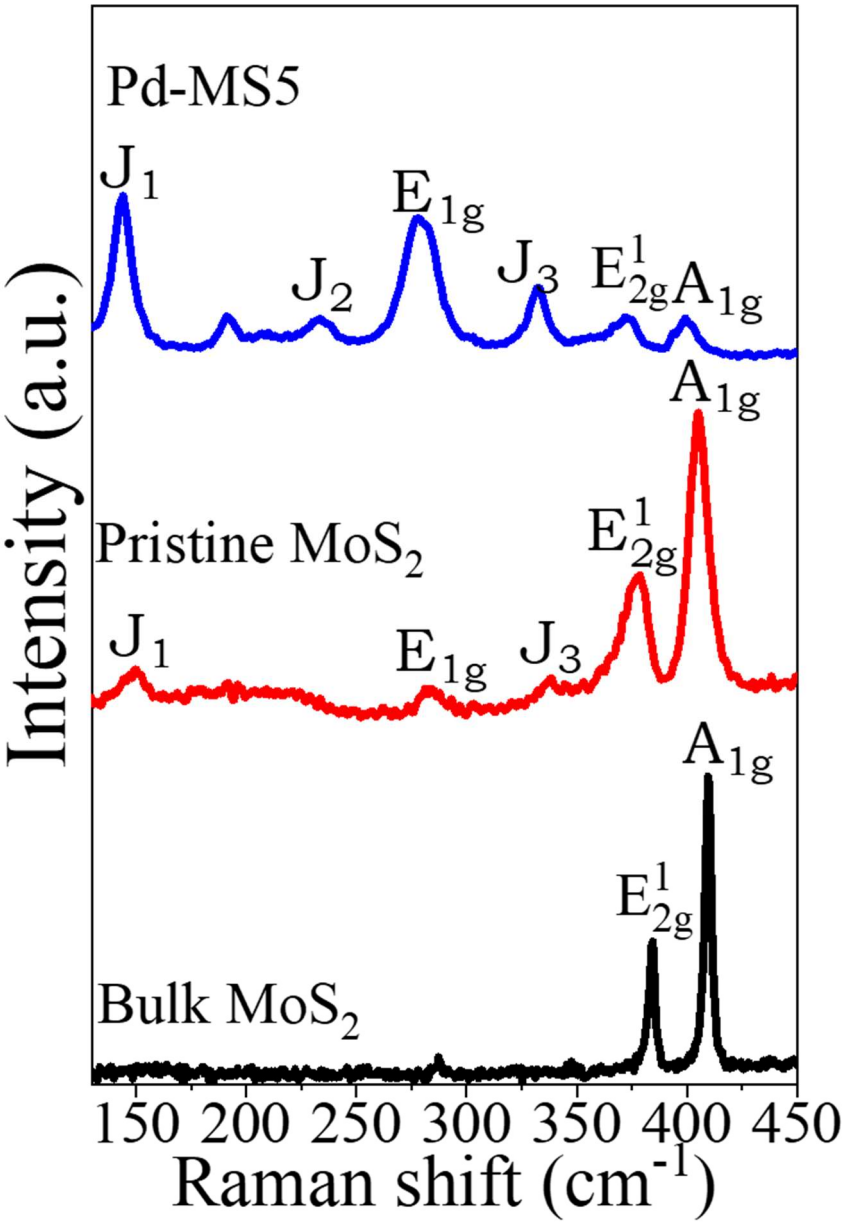

Figure 4.5: Raman spectra of the samples Pd-MS5, pristine MoS_2 and bulk MoS_2 (commercial).

4.1.4 Chemical composition analysis using XPS

The high resolution XPS spectra of Mo 3d, S 2p, Mo 3p, N 1s and Pd 3d orbitals for sample Pd-MS5 has been shown in figure 4.6 (a-d), respectively.

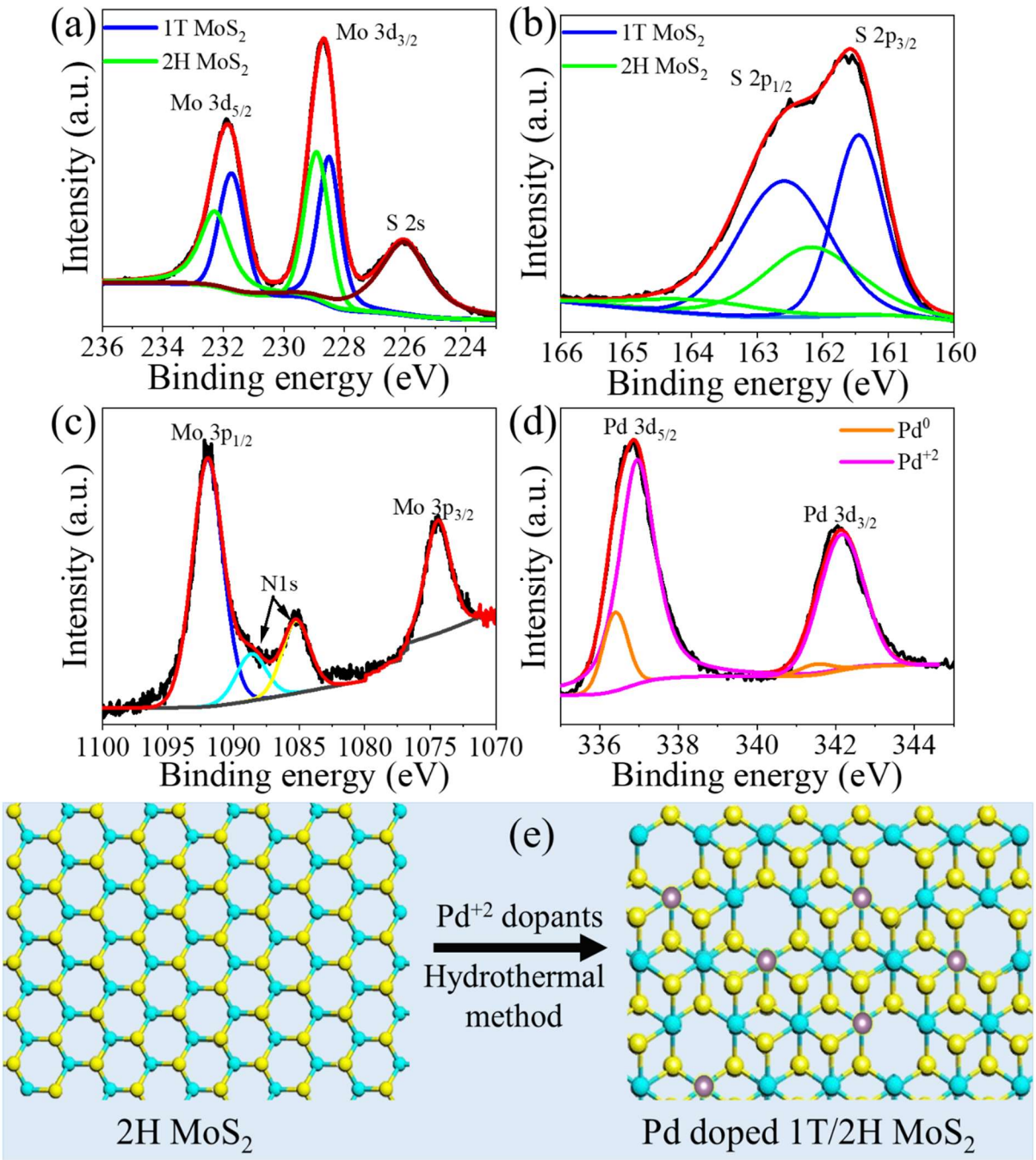

Figure 4.6: High resolution XPS spectra of Mo 3d (a), S 2p (b), Mo 3p, N 1s (c) and Pd 3d (d) orbitals for sample Pd-MS5 and (e) schematic representation for sulfur vacancies creation in MoS_2 lattices and MoS_2 phase transformation from 2H to 1T via. Pd doping into MoS_2 lattice during hydrothermal reaction.

After the deconvolution of Mo $3d_{5/2}$ and $3d_{3/2}$ peaks, present in Mo 3d region (figure 4.6a), 4 peaks were found at 228.2 eV, 229 eV, 231.2 eV and 232 eV, characteristics peaks of Mo^{+4} oxidation state. Peaks, observed at 229 eV and 232 eV correspond to 2H phase of MoS_2 whereas peaks present at lower binding energy i.e., 228.2 eV and 231.8 eV correspond to 1T phase of MoS_2 [15], confirming the presence of 1T phase along with 2H phase in Pd-MS5. In S 2p orbital (figure 4.6b), doublets at 163 eV and 164 eV, correspond to S $2p_{3/2}$ and S $2p_{1/2}$ respectively can be attributed to 2H phase of MoS_2. The other doublets present at 161.2 eV and 162.2 eV correspond to $S2p_{3/2}$ and S $2p_{1/2}$ and are attributed to 1T phase,, further proving the metallic (1T) phase formation in sample Pd-MS5 [16].

Figure 4.6 (c) shows incorporation of N1s orbital along with Mo $3p_{1/2}$ orbital at 397.6 eV and 401.02 eV which can be attributed to amine (NH_2) and ammonium group (NH^{4+}), responsible for intercalation in MoS_2 layers [17]. In Pd 3d orbital (Figure 4.6 d), doublets at 337.0 eV and 342.3 eV are corresponding to Pd $3d_{5/2}$ and Pd $3d_{3/2}$ attributed to Pd^{+2} oxidation state which confirms the substitutional doping of Pd in MoS_2 lattice [18]. Peaks at 336.2 eV and 341.9 eV binding energies are attributed to Pd metal atoms ($3d_{5/2}$ and $3d_{3/2}$ respectively) which is observed due to presence of unbonded Pd metal atoms into MoS_2 system [19,20]. Figure 4.6 (b) shows the schematic representation of Pd doped 1T/2H MoS_2. On the basis of EDAX, Raman and XPS analysis, it can be concluded that substitutional Pd doping modifies the electronic structure of pristine MoS_2 by creating sulfur vacancies' in MoS_2 lattices (Table 4.1) and activates the inert basal plane of pristine MoS_2 sites into basal plane resulting in phase transition from 2H to 1T of MoS_2 (confirmed by Raman and XPS studies, Figure 3b and 4a respectively) and optimizes the free energy for H species adsorption, resulting enhancement in intrinsic HER activity [21,22].

4.1.5 BET surface area

The BET surface area of samples Pd-MS5 and pristine MoS_2 was determined by N_2 adsorption/desorption. Figure 4.7 (a & b) shows the N_2 adsorption–desorption isotherms of samples Pd-MS5 and pristine MoS_2 respectively. The BET surface area for both samples have been shown in respective graphs. The shown N_2 adsorption/desorption curve in figure 4.7 exhibits H3 hysteresis loop with type IV isotherm, suggest that both samples possess mesoporous structure. Brunauer-Emmett-Teller (BET) calculation presents that Pd-MS5 exhibits four times larger specific area of 40.67 $m^2.g^{-1}$ than that of pristine MoS_2 (15.45 $m^2.g^{-1}$), inset of figure 4.7, respectively. Pd-MS5 displayed an average pore size of 158 Å with total

pore volume of 0.161 $cm^3.g^{-1}$, whereas pristine MoS_2 consisted of pores with an average size of 13.44 Å and total pore volume of 0.052 $cm^3.g^{-1}$.

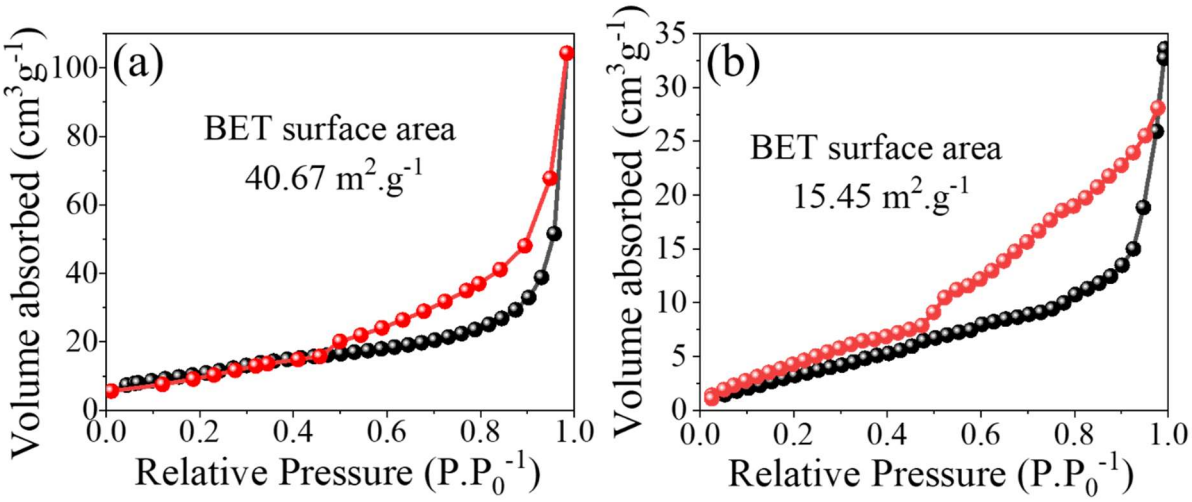

Figure 4.7: N_2 adsorption/desorption isotherms of sample (a) Pd-MS5 and (b) pristine MoS_2.

Pd-MS5 exhibited larger surface area which resulted due to the presence of more active sites for hydrogen adsorption, beneficial for faster HER kinetics inside the porous structure of the sample [40]. The higher BET surface area of Pd-MS5 suggests the presence of more active sites to absorb the electrochemical species (H*) therefore, facilitate the rapid hydrogen evolution reaction [23].

4.1.6 Electrochemical characterization

After investigating physico-chemical properties of synthesized Pd-MoS_2 nanostructured powder, electrochemical characterization has been performed to optimize the doping concentration of Pd in MoS_2 lattice and evaluate electrocatalytic efficiency of Pd-MoS_2 as an electrocatalyst towards HER application. The details for electrochemical measurements have been mentioned in Chapter 2. Herein, we have performed the HER activity of the Pd-MoS_2 samples in acidic water (0.5 M H_2SO_4), alkaline water (1M KOH) electrolyte and saline water (1M KOH+0.5M NaCl) [41]. For the sake of comparison, standard electrocatalyst for HER i.e., Pt/C was also characterized under the same experimental condition. Before performing electrochemical measurements, hydrothermally synthesized Pd-MoS_2 nanostructured powders were drop casted on C.P., which were used as working electrodes. Fabrication of the working electrode is as similar as explained in section 2.2.1.1. Figure 4.8 shows HER performance of all Pd-MoS_2 and pristine MoS_2 samples in acidic water. Polarization curves for Pd-MoS_2 with variation in Pd concentration, pristine MoS_2 and Pt/C are shown in figure 4.8 (a). As per expectations, Pd-MoS_2 samples exhibited higher HER activity

as compared to pristine MoS_2, as a result of the incorporation of Pd atoms into MoS_2 lattice, higher 1T phase fraction, defect formations etc. [36,42].

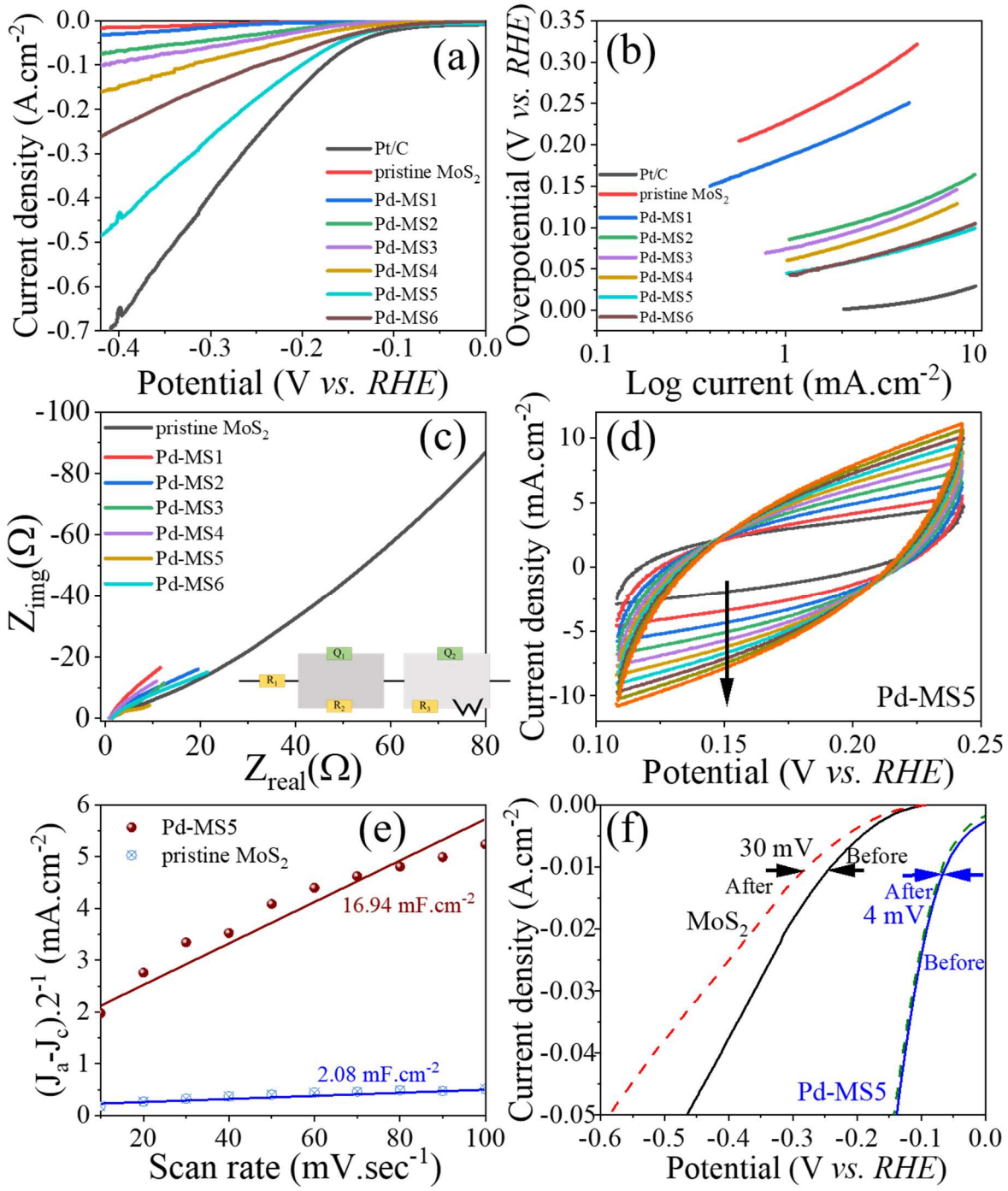

Figure 4.8: (a) Polarization curves of Pt/C, Pd-MS1, Pd-MS2, Pd-MS3, Pd-MS4, Pd-MS5, Pd-MS6 and pristine MoS_2, (b) corresponding Tafel slopes, (c) EIS curve for Pd-MoS_2 samples and pristine MoS_2, (d) CV curve for sample Pd-MS5 recorded with scan rates, (e)) linear plot of difference in anodic and cathodic current density vs. scan rate to calculate ECSA (f) stability curve recorded before and after 1000 cycles of CV for samples Pd-MS5 and pristine MoS_2.

Moreover, Pd-MS5 has shown the highest HER activity among other Pd-MoS_2 samples and comparable to Pt/C which indicates that Pd doping concentration plays an important role to tune MoS_2 electronic structure for efficient hydrogen evolution [43]. In the search of simple and sustainable electrocatalyst for HER application, MoS_2 has been chemically activated by Pd interfacial doping by Z. Luo *et.al.*, [3]. It was theoretically calculated that the sulfur atoms next to the palladium sites exhibited low hydrogen adsorption energy of only –0.02 eV and Pd doped MoS_2 exhibited exchange current density of 805 $\mu A.cm^{-2}$ and 78 mV overpotential at 10 mA cm^{-2}, accompanied by a good stability. Similarly, F. Sultana *et.al.*, [24] insighted the catalytic activity of Pd doped MoS_2 for HER application using a solvothermally synthesized Pd (2 wt%) doped MoS_2 nanorods which exhibited a small overpotential of 119 mV at 100 $mA.cm^{-2}$ current density and 46 $mV.dec^{-1}$ Tafel slope, accompanied by high stability. In the present work, Pd-MS5 required only 0.02 mV *vs. RHE* onset potential (overpotential @ 1 $mA.cm^{-2}$), 89 mV *vs. RHE* overpotential to generate 10 $mA.cm^{-2}$ of cathodic current density (current density has been calculated as per geometrical surface area) which is very close to Pt/C (40 mV *vs. RHE*) and comparable to reported systems. Whereas, pristine MoS_2 displayed 140 mV *vs. RHE* onset potential and 248 mV *vs. RHE* overpotential at 10 $mA.cm^{-2}$.

Table 4.2: The results of electrochemical characterization for synthesized Pd-MoS_2 with different doping concentration, pristine MoS_2 and standard electrocatalyst (Pt/C).

Sample name	Onset potential (mV *vs. RHE*)	Overpotential @ 10 $mA.cm^{-2}$ (mV *vs. RHE*)	Tafel slope ($mV.dec^{-1}$)
Pt/C	0	40	31
pristine MoS_2	140	248	91
Pd-MS1	70	236	90
Pd-MS2	40	198	80
Pd-MS3	40	156	76
Pd-MS4	25	134	65
Pd-MS5	20	89	56
Pd-MS6	20	91	59

Figure 4.8 (b) displays the Tafel plots for all Pd-MoS_2 samples and pristine MoS_2. Tafel slopes of the systems are closer to the Tafel value known for Heyrovsky mechanism (40 $mV.dec^{-1}$), indicating that these systems follow the Volmer-Heyrovsky mechanism for

hydrogen molecule evolution from their surface. From figure 4.8 (b) and table 4.2, sample Pd-MS5 showed the lowest Tafel slope of 56 $mV.dec^{-1}$, among all Pd doped samples and pristine MoS_2 (91 $mV.dec^{-1}$).

To further investigate the electrode/electrolyte kinetics during HER process, EIS curve has been recorded. Figure 4.8 (c) represents the Nyquist plots for all Pd-MoS_2 samples and pristine MoS_2 and fitted equivalent circuit is show in the inset of figure 4.8 (c). The Nyquist plot represents the electrode-electrolyte/electrolyte interface resistance as well as the charge transfer resistance (R_{ct}) during HER [46]. The smallest Nyquist plot for sample Pd-MS5 shows the lowest charge transfer resistance, resulting in accelerated HER. Figure 4.8 (d) shows recoded cyclic voltammogram (CV) at different scan rates *i.e.*, 10 to 100 $mV.sec^{-1}$ in non-Faradaic region. This curve has been used to evaluate the double layer capacitance (C_{dl}) using eq. 2.1. Figure 4.8 (e) has been plotted between difference in anodic and cathodic current density at 0.15 V *vs. RHE* vs. scan rate, which enables one to estimate electrochemical active surface area (ECSA). Figure 4.8 (e) clearly indicates that sample Pd-MS5 possesses 8 times higher C_{dl} value (16.94 $mF.cm^{-2}$) than that of pristine MoS_2 (2.08 $mF.cm^{-2}$) which gives 282 cm^2 ECSA for sample Pd-MS5 whereas for MoS_2, ECSA value found to be 34 cm^2. The higher value of ECSA for sample Pd-MS5 indicates that it would render higher population of exposed active site density. Comparison of catalytic activities of electrocatalyst can be analysed by estimation of available active site density for synthesized systems. Operational stability of an electrocatalyst during HER process, is also a key parameter which makes electrocatalyst commercially acceptable. To understand the stability of synthesized electrocatalyst in acidic condition, stability measurement of Pd-MS5 and pristine MoS_2 electrocatalysts were carried out by recording polarization curve before and after 1000 cycles of CV in 0.5M H_2SO_4. Figure 4.8 (f) shows polarization curves of Pd-MS5 and pristine MoS_2, recorded before and after 1000 CV cycles for both the samples. A very negligible drift in value of overpotential was observed in case of Pd-MoS_2, indicating its excellent stability in acidic condition. It shows a lowest drift in overpotential of ~4 mV at current density of 10 $mA.cm^{-2}$. This result demonstrates. a superior operational efficiency of the Pd doped MoS_2 as an electrocatalyst for HER application in acidic water.

Herein, we have summarized and compared the present results with those reported for noble metal loaded/ doped MoS_2 systems in table 4.3. Many efforts have been put forward for noble metal loading/doping on to MoS_2 to improve its HER performance.

Table 4.3: Summarization of researches on noble metal loaded/doped MoS_2 electrocatalysts for HER application.

S. No.	System	Method of synthesis	Phase	Electrocatalytic performance			Ref.
				Overpotential (mV) @ 10 $mA.cm^{-2}$	Tafel slope ($mV.dec^{-1}$)	Stability run	
1.	**Pt NPs @MoS_2 NS[a]/ 3D Carbon cloth**	Hydrothermal and time dependent PEC[b] control	2H	70	36	8 hours	[25]
2.	**Au NCs[c]/ MoS_2 NSs**	Hydrothermal and ultrasonication	2H	280	79.3	1000 cycles	[26]
3.	**MoS_2 @ Pt scrolls**	Multi step fabrication process	1T/2H	125	39	-	[27]
4.	**Au-Pd NCs/MoS_2 nanosheets**	Multi step dispersion process	2H	91	67	1000 cycles	[28]
5.	**Pt doped MoS_2**	Hydrothermal followed by electrodeposition	1T/2H	88.3	55.69	20 hours @130 mV	[29]
6.	**Pd-O doped MoSx**	Two step electrodepositions	2H	23	18	24 hours @ 200 mV and	[30]

	NCs/ CNTs[d]					1000 cycles	
7.	**Pd doped 1T MoS_2**	Sonochemical doping on 1T MoS_2	1T	140	50	10 mV decay after 1000 cycles	[2]
8.	**Pd modulated Co-MoS_2 NS**	Hydrothermal and chemical reduction	1T	60	42	40 hours @ 10 and 20 $mA.cm^{-2}$	[31]
9.	**Pd-1T MoS_2/ BP[e]**	Chemical and electrochemical exfoliation and sonication	1T	152	86	-	[32]
10.	**Pd doped MoS_2/C. P.[f]**	Hydrothermal	2H	204	-	-	[33]
11.	**Pt-Pd doped MoS_2**	Hydrothermal and electrodeposition	2H	64	-	1000 cycles and 20 hours @ 200 mV	
12.	**Pd doped MoS_2 nanorods**	Solvothermal	2H	119	48	1000 cycles and 3000 sec	[24]

13.	**Pd-MoS_2 nanosheets**	Single step hydrothermal method	2H/1T	89	56	1000 cycles	This work

[a]NS – Nanosheets, [b]PEC– Photo-electrochemical, [c] NCs – Nanoclusters, [d]CNTs – Carbon Nano Tubes, [e]B.P. – Black Phosphorous, [f]C.P. – Carbon Paper.

Noble metal doped MoS_2 systems, reported till date, were synthesized by either several step processes or synthesis of composites using carbon materials to enhance the HER activity of pristine MoS_2. These strategies make noble metal doped MoS_2 synthesis further complicated as well as non-economical. Therefore, in the present work, we have approached a simple, economic and one step hydrothermal technique to synthesize an efficient Pd doped MoS_2 electrocatalyst without mixing with any conducting material (like rGO, Carbon black etc.) and directly drop casted over carbon paper (C. P.) which takes no extra efforts and exhibits excellent HER activity which is comparative to other reported systems for HER application.

Inclusion of above discussion, we have also performed HER and overall water splitting in alkaline and saline water using Pd-MoS_2 sample (Pd-MS5; *optimized for highest HER activity among synthesized samples*). Figure 4.9 represents the electrocatalytic activity of sample Pd-MS5 and pristine MoS_2 towards HER application in alkaline and saline water. Electrocatalytic performance of Pt/C has been included for comparison. Figure 4.9 (a) and 4.9 (c) illustrate the polarization curves recorded in alkaline and saline water respectively and Figure 4.9 (b) and 4.9 (d) display the corresponding Tafel slopes. Pd-MS5 exhibited higher electrocatalytic activity and required only 149 mV *vs. RHE* and 165 mV *vs. RHE* overpotential to achieve 10 $mA.cm^{-2}$ cathodic current density during HER process in alkaline and saline water respectively. Pristine MoS_2 exhibited 356 mV *vs. RHE* & 425 mV *vs. RHE* to achieve 10 $mA.cm^{-2}$ cathodic current in alkaline and saline water respectively. The electrocatalytic efficiency obtained for pristine MoS_2 is much larger than those observed for Pd-MS5 and close to Pt/C (45 mV *vs. RHE* & 60 mV *vs. RHE* respectively), indicating the superior electrocatalytic activity of Pd-MoS_2 in comparison to pristine MoS_2. Tafel plots extracted from corresponding polarization curves have been shown in Figure 4.9 (b & d). Tafel plots, calculated for sample Pd-MS5 are found to be 72 $mV.dec^{-1}$ in alkaline water and 86 $mV.dec^{-1}$ in saline water which is much smaller than those observed for pristine MoS_2 (136 $mV.dec^{-1}$ and 178 $mV.dec^{-1}$). These

values are very close to those for Pt/C (41 mV.dec^{-1} and 43 mV.dec^{-1}). The value of Tafel slopes indicates that Volmer-Heyrovsky is the rate-determining steps during HER process [53].

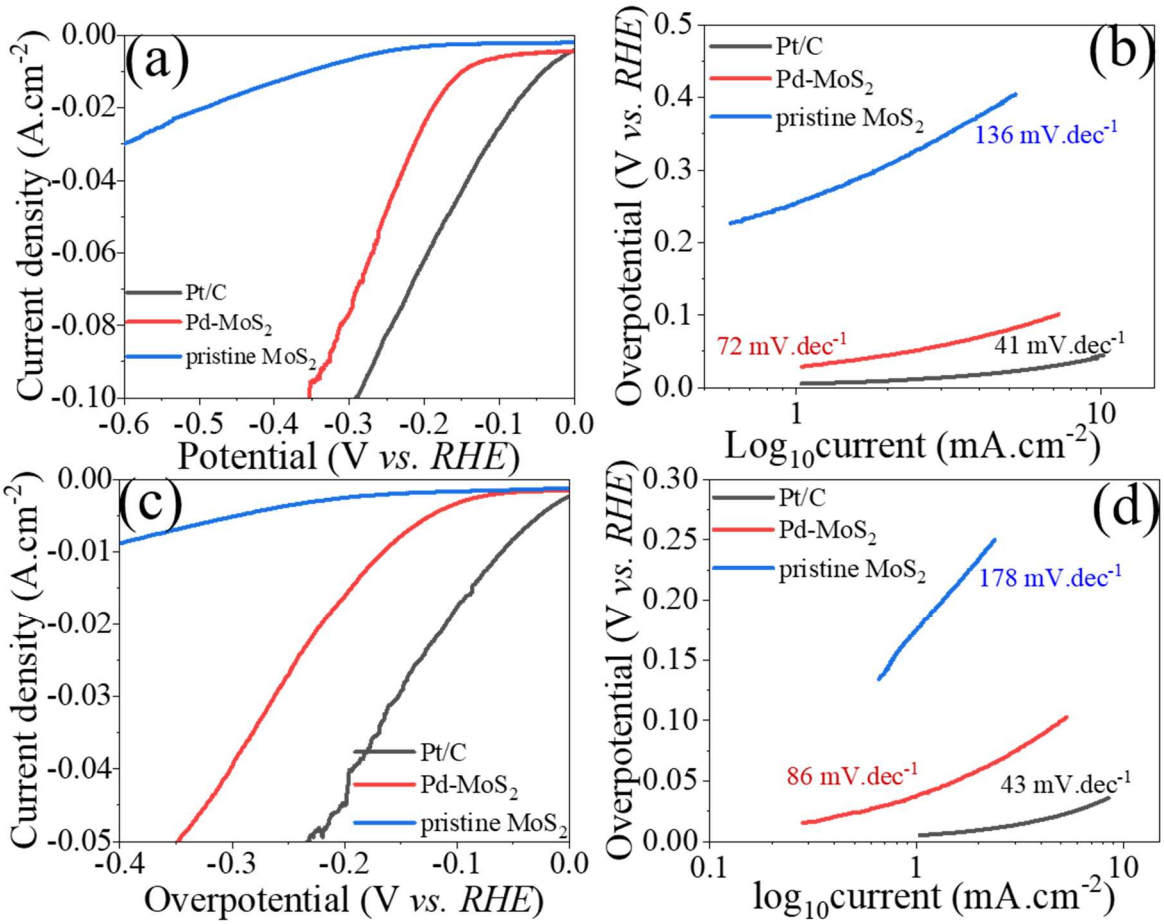

Figure 4.9: HER performance of sample Pd-MS5 and pristine MoS_2 in alkaline and saline water (a) polarization curve, (b) corresponding Tafel curve in alkaline water, (c) polarization curve and (d) corresponding Tafel curve in saline water.

It is observed that electrocatalyst followed trend for HER performance in acidic water, alkaline water and saline water in such a way acidic $_{HER}$> alkaline $_{HER}$>saline water $_{HER}$ [34,35]. Electrocatalyst possesses lowest HER performance in saline water medium and then alkaline medium as compared to acidic water which can be attributed to lower hydrogen binding energy for the hydrogen adsorption/desorption in case of acidic water whereas due to extra water dissociation step, large value of energy barrier is required for hydrogen adsorption involve in alkaline as well as saline medium [36]. However, the lower performance of electrocatalyst in saline water is attributed to the presence of chlorine ions (Cl^-) in alkaline water. Presence of c

hlorine ions poison the electrocatalyst's surface and block the actives sites of materials [37] which is *in-line* with the obtained results in present studies and most of state of art

transition metal based HER electrocatalyst [38–41]. These results indicate that Pd-MoS_2 can be a promising HER electrocatalyst for overall water splitting in acidic, alkaline and sea water media.

4.1.7 Electrocatalytic water splitting

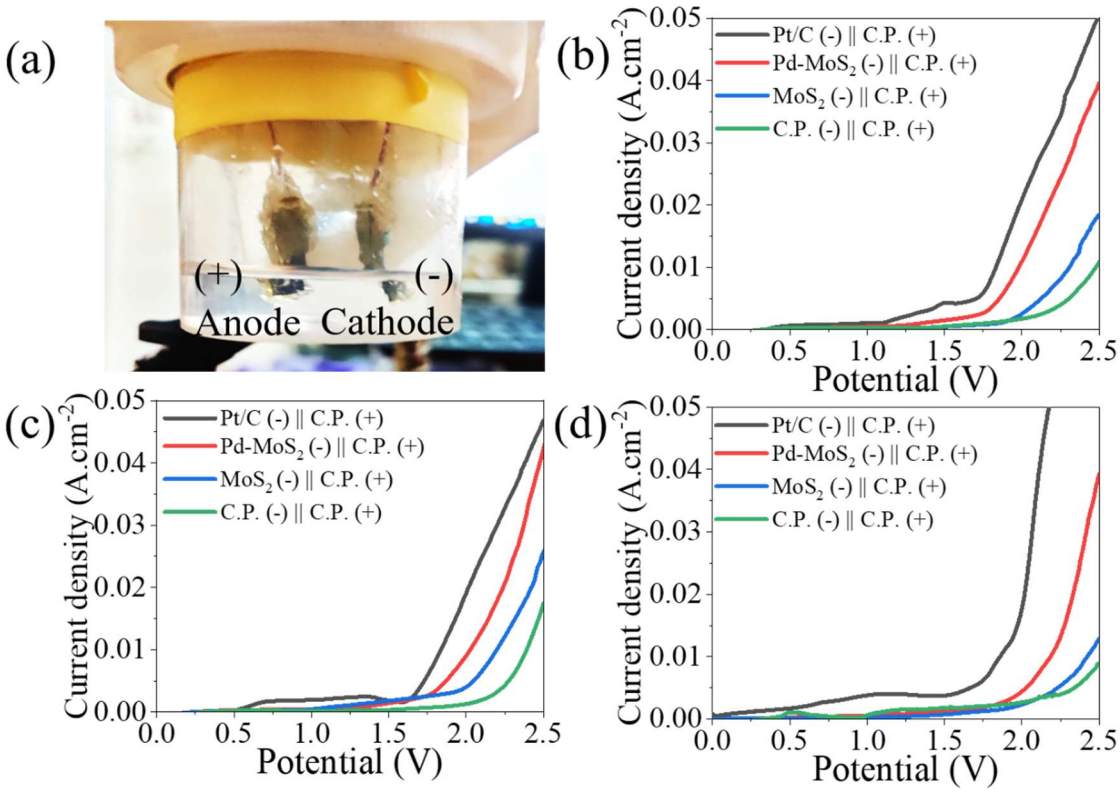

Figure 4.10: (a) A digital photograph of two electrode electrochemical cell for overall water splitting at lab scale, LSV curves for Pd-MoS_2\|\|C.P., MoS_2\|\|C.P., C.P.\|\|C.P. and Pt/C\|\|C.P. during electrocatalytic water splitting in (b) acidic water, (c) alkaline water and (d) saline water. Catalyst loading 0.5 mg on C.P. for HER, bare C.P. for OER.

After the electrochemical property evaluation, Pd-MoS_2 (Pd-MS5) was studied for its efficiency or HER. It showed an excellent HER performance in acidic, alkaline, and saline water, a two-electrode system using Pd-MoS_2 on C.P. as cathode and carbon paper (C.P.) as anode to perform overall water splitting in all three electrolytes. Equal amount of electrocatalysts (Pd-MS5, MoS_2 and Pt/C) were loaded one by one onto the C.P. using drop casting method. Figure 4.10 represents the overall water splitting performance in acidic (Figure 4.10b), alkaline (Figure 4.10c) and saline water (Figure 4.10 d). The comparison of water splitting performance of C.P. loaded with Pd-MoS_2, pristine MoS_2, Pt/C and bare C.P. has also been shown in Figure 4.10. Among them, Pd-MoS_2 loaded on C.P. required +1.98 V (acidic water), +2.03 V (alkaline water) and +2.18 (saline water) to drive 10 $mA.cm^{-2}$ current density

whereas bare C.P. system requires +2.40 V, +2.48 V and +2.53 V respectively. The lower cell potentials of Pd-MoS_2||C.P. *w.r.t.* other systems clearly reflect the higher electrocatalytic efficiency towards HER application.

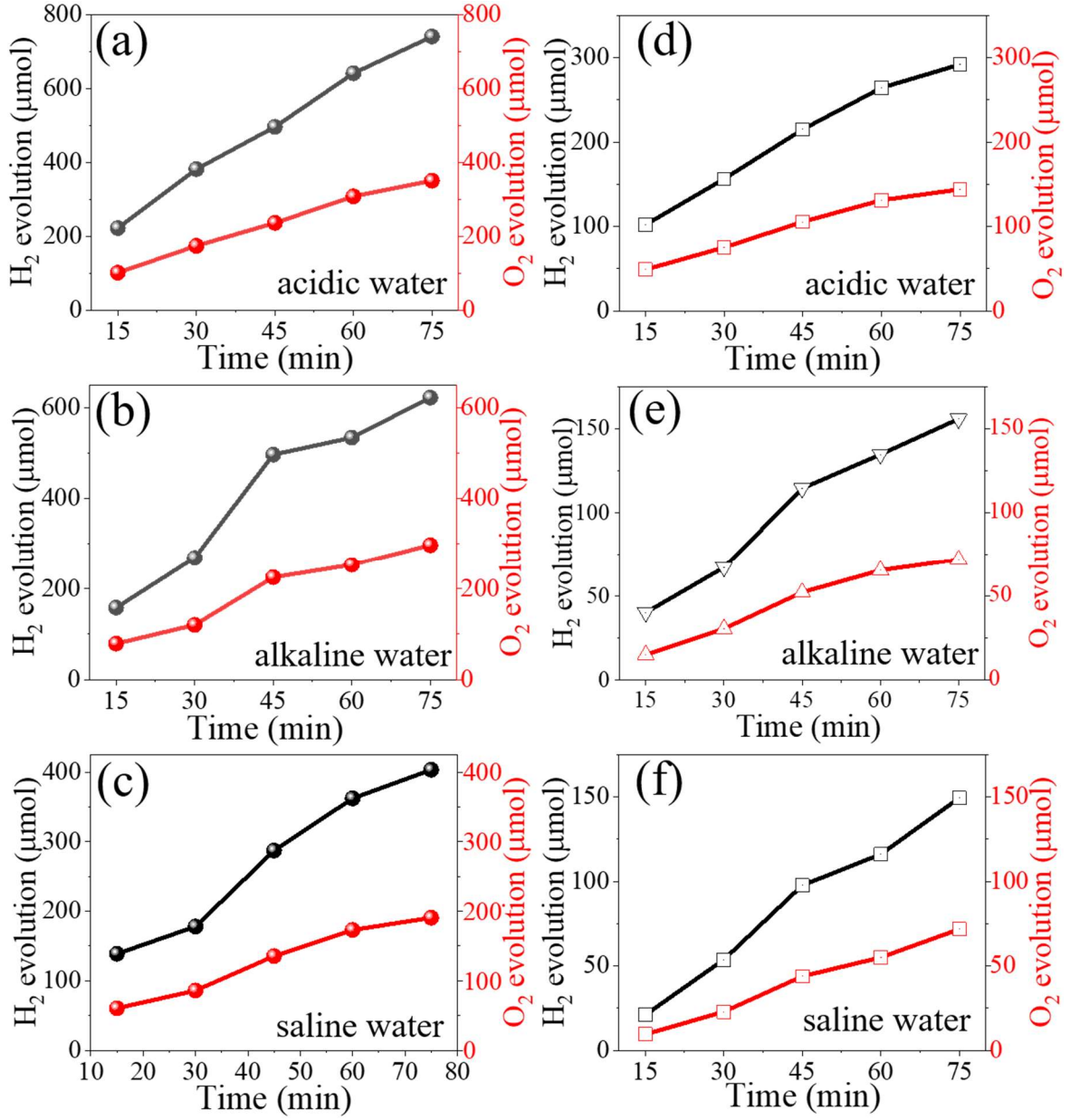

Figure 4.11: Volume of generated H_2 and O_2 in µmols at constant potential of +2.2 V for system Pd-MoS_2||C.P. (a, b, c) and MoS_2||C.P (d, e, f).

Additionally, evolved H_2 and O_2 gases during water splitting reaction have also been quantified using Gas chromatography (GC). A constant cell voltage of +2.2 V was applied to Pd-MoS_2||C.P. in acidic, alkaline, and saline water. Figure 4.11 represents volume of electrocatalytically generated H_2 and O_2 gas at cell potential of +2.2 V in all the three electrolytes for systems Pd-MoS_2||C.P. and MoS_2||C.P. The quantification of the evolved H_2

and O_2 gases for Pd-MoS_2||C.P. and MoS_2||C.P. has been tabulated in table 4.4. The ratio of collected H_2 gas to O_2 gas has been found to be approximately 2:1 during electrolysis in agreement with the theoretical values [55].

Table 4.4: Quantification of evolved H_2 and O_2 gases from system Pd-MoS_2||C.P. and MoS_2||C.P. during electrocatalytic water splitting in acidic, alkaline, and saline water.

Electrolyte	**Time (min)**	**H_2 (µmol)**		**O_2 (µmol)**	
		Pd-MoS_2||C.P.	**MoS_2||C.P.**	**Pd-MoS_2||C.P.**	**MoS_2||C.P.**
Acidic water (0.5 M H_2SO_4)	15	221.86	104.93	101.98	48.95
	30	381.52	173.76	156.24	75.12
	45	495.90	235.96	214.98	105.49
	60	641.09	307.54	264.26	131.13
	75	740.80	350.19	291.97	143.99
Alkaline water (1M KOH)	15	158.22	40.12	79.10	15.06
	30	268.70	67.09	120.35	30.54
	45	496.61	114.42	225.40	52.21
	60	534.08	134.65	253.04	65.32
	75	622.10	155.77	297.05	71.88
Saline water (1M KOH+0.5M NaCl)	15	138.84	20.97	64.45	9.48
	30	177.97	53.61	85.99	22.83
	45	287.02	97.66	140.51	43.83
	60	362.07	116.06	179.04	55.03
	75	403.23	149.47	201.02	71.73

The maximum amount of evolved H_2 gas has been estimated to be 704 µmol, 622 µmol and 403 µmol in acidic, alkaline, and saline water solutions respectively, for Pd-MoS_2||C.P. system which is around two time higher than that for MoS_2||C.P. system. These results indicate that Pd-MoS_2 can be promising HER electrocatalyst for overall water splitting in acidic, alkaline, and saline water media.

4.2 Conclusion

To conclude present chapter, Pd doped MoS_2 has been synthesized by employing a one-step hydrothermal method while optimizing the Pd doping concentration to achieve superior electrocatalytic activity and excellent stability towards HER application. This excellent performance of Pd-MoS_2 (Pd-MS5) over pristine MoS_2 is due to synergistic effect of amine/ammonium ions intercalation as well as noble metal (Pd) doping in MoS_2 system which creates defects, induces disorder, expands inter layer and transform the 2H phase of MoS_2 into 1T phase. These features result in enhanced HER performance for Pd-MoS_2 with the smallest overpotential of 89 mV *vs. RHE* at 10 $mA.cm^{-2}$ current density and a Tafel slope of 56 $mV.dec^{-1}$ in 0.5M H_2SO_4 (acidic) solution. It showed an overpotential of 149 mV *vs. RHE* and 165 mV *vs. RHE* in 1M KOH (alkaline) and 1M KOH+0.5M NaCl (saline) solutions respectively. In addition, by utilizing Pd-MoS_2 as cathode and C.P. as anode for water splitting, a cell potential of +1.98 V, +2.03 V and +2.18 V was required to generate 10 $mA.cm^{-2}$ current density. The system generated 740 μmol, 622 μmol and 403 μmol of H_2 gas at a constant potential of +2.2 V in acidic, alkaline and saline water respectively. Present work indicates a simple and economic way for structural regulation for high performance electrocatalyst for HER application which gives a new direction for MoS_2 and based systems in the area of acidic, alkaline and sea water splitting.

4.3 References

1. Z. Zhang, K. Chen, Q. Zhao, M. Huang, and X. Ouyang, Nano Mater. Sci. **3**, 89 (2021).

2. T. H. M. Lau, S. Wu, R. Kato, T.-S. Wu, J. Kulhavý, J. Mo, J. Zheng, J. S. Foord, Y.-L. Soo, K. Suenaga, M. T. Darby, and S. C. E. Tsang, ACS Catal. **9**, 7527 (2019).

3. Z. Luo, Y. Ouyang, H. Zhang, M. Xiao, J. Ge, Z. Jiang, J. Wang, D. Tang, X. Cao, C. Liu, and W. Xing, Nat. Commun. **9**, 1 (2018).

4. A. Kudo, R. Niishiro, A. Iwase, and H. Kato, Chem. Phys. **339**, 104 (2007).

5. R. D. Shannon, Acta Crystallogr. Sect. A **32**, 751 (1976).

6. J. Singh, Rishikesh, S. Kumar, and R. K. Soni, J. Alloys Compd. **849**, 156502 (2020).

7. Q. Liu, X. Li, Q. He, A. Khalil, D. Liu, T. Xiang, X. Wu, and L. Song, Small **11**, 5556 (2015).

8. S. Chen and Y. Pan, Int. J. Hydrogen Energy **46**, 21040 (2021).

9. J. Xie, J. Zhang, S. Li, F. Grote, X. Zhang, H. Zhang, R. Wang, Y. Lei, B. Pan, and Y. Xie, J. Am. Chem. Soc. **135**, 17881 (2013).

10. K. D. Rasamani, F. Alimohammadi, and Y. Sun, Mater. Today **20**, 83 (2017).

11. S. M. Gali, A. Pershin, A. Lherbier, J.-C. Charlier, and D. Beljonne, J. Phys. Chem. C **124**, 15076 (2020).

12. T. Liu, C. Fang, B. Yu, Y. You, H. Niu, R. Zhou, J. Zhang, and J. Xu, Inorg. Chem. Front. **7**, 2497 (2020).

13. S. Shi, D. Gao, B. Xia, P. Liu, and D. Xue, J. Mater. Chem. A **3**, 24414 (2015).

14. G. Yao, Z. Weixuan, W. Hanchun, H. Junfeng, Z. Yongliang, L. Shenghuang, L. Chunru, X. Kang, Q. Jingsi, J. Wei, C. Qing, G. Song, Z. Wenjing, Z. Xiangdong, and C. Yang, Sci. Adv. **4**, eaau6252 (2021).

15. D. Wang, X. Zhang, S. Bao, Z. Zhang, H. Fei, and Z. Wu, J. Mater. Chem. A **5**, 2681 (2017).

16. J. H. Lee, W. S. Jang, S. W. Han, and H. K. Baik, Langmuir **30**, 9866 (2014).

17. A. Anto Jeffery, C. Nethravathi, and M. Rajamathi, J. Phys. Chem. C **118**, 1386 (2014).

18. K. Qi, S. Yu, Q. Wang, W. Zhang, J. Fan, W. Zheng, and X. Cui, J. Mater. Chem. A **4**, 4025 (2016).

19. P. Wu, Y. Huang, L. Kang, M. Wu, and Y. Wang, Sci. Rep. **5**, 14173 (2015).

20. X. Wang, J. Chen, J. Zeng, Q. Wang, Z. Li, R. Qin, C. Wu, Z. Xie, and L. Zheng, Nanoscale **9**, 6643 (2017).

21. J. Zhang, X. Xu, L. Yang, D. Cheng, and D. Cao, Small Methods **3**, 1900653 (2019).

22. Z. Luo, Y. Ouyang, H. Zhang, M. Xiao, J. Ge, Z. Jiang, J. Wang, D. Tang, X. Cao, C. Liu, and W. Xing, Nat. Commun. **9**, 2120 (2018).

23. Y. Li, F. Xiang, W. Lou, and X. Zhang, IOP Conf. Ser. Earth Environ. Sci. **300**, 52021 (2019).

24. F. Sultana, M. Mushtaq, J. Wang, K. Althubeiti, A. Zaman, A. Kalsoom Rais, A. Ali, and

Q. Yang, Arab. J. Chem. **15**, 103735 (2022).

25. X. Y. Xu, X. F. Dong, Z. J. Bao, R. Wang, J. G. Hu, and H. B. Zeng, J. Mater. Chem. A **5**, 22654 (2017).

26. S. Zhao, R. Jin, Y. Song, H. Zhang, S. D. House, J. C. Yang, and R. Jin, Small **13**, 1701519 (2017).

27. D. Y. Hwang, K. H. Choi, J. E. Park, and D. H. Suh, Phys. Chem. Chem. Phys. **19**, 18356 (2017).

28. Y. Du, J. Xiang, K. Ni, Y. Yun, G. Sun, X. Yuan, H. Sheng, Y. Zhu, and M. Zhu, Inorg. Chem. Front. **5**, 2948 (2018).

29. Y. Li, Q. Gu, B. Johannessen, Z. Zheng, C. Li, Y. Luo, Z. Zhang, Q. Zhang, H. Fan, W. Luo, B. Liu, S. Dou, and H. Liu, Nano Energy **84**, 105898 (2021).

30. Y. Zhan, X. Zhou, H. Nie, X. Xu, X. Zheng, J. Hou, H. Duan, S. Huang, and Z. Yang, J. Mater. Chem. A **7**, 15599 (2019).

31. S. Liu, L. Zhou, W. Zhang, J. Jin, X. Mu, S. Zhang, C. Chen, and S. Mu, Nanoscale **12**, 9943 (2020).

32. X. Song, B. Li, W. Peng, C. Wang, K. Li, Y. Zhu, and Y. Mei, Nanoscale **13**, 5892 (2021).

33. H. young Jung, M. ju Chae, J. hwan Park, Y. il Song, J. chul Ro, and S. jeong Suh, ACS Appl. Energy Mater. **4**, 10748 (2021).

34. M. Sarno, E. Ponticorvo, and D. Scarpa, Electrochem. Commun. **111**, 106647 (2020).

35. J. Mohammed-Ibrahim and H. Moussab, Mater. Sci. Energy Technol. **3**, 780 (2020).

36. J. Zhang, T. Wang, P. Liu, S. Liu, R. Dong, X. Zhuang, M. Chen, and X. Feng, Energy Environ. Sci. **9**, 2789 (2016).

37. Y. Kuang, M. J. Kenney, Y. Meng, W.-H. Hung, Y. Liu, J. E. Huang, R. Prasanna, P. Li, Y. Li, L. Wang, M.-C. Lin, M. D. McGehee, X. Sun, and H. Dai, Proc. Natl. Acad. Sci. **116**, 6624 (2019).

38. X. Lu, J. Pan, E. Lovell, T. H. Tan, Y. H. Ng, and R. Amal, Energy Environ. Sci. **11**, 1898 (2018).

39. C. Bai, S. Wei, D. Deng, X. Lin, M. Zheng, and Q. Dong, J. Mater. Chem. A **5**, 9533 (2017).

40. X.-Y. Yu, Y. Feng, Y. Jeon, B. Guan, X. W. (David) Lou, and U. Paik, Adv. Mater. **28**, 9006 (2016).

41. S. Feng, Y. Yu, J. Li, J. Luo, P. Deng, C. Jia, Y. Shen, and X. Tian, Catal. Commun. **162**, 106382 (2022).

CHAPTER 5

EARTH ADUNDANT TRANSITION METAL (VANADIUM; V) DOPED MoS_2 NANOSHEETS FOR IMRPOVED ELECTROCTALYTIC EFFICIENCY TOWARDS HER APPLICATION

It has been well studied that heteroatom doping modifies the electronic structures and optimized the Gibb's free energy to adsorb hydrogen molecules, provides the catalytically active sites density which enhances the electrocatalytic efficiency of MoS_2 towards HER application [1,2]. Among various transition metal doping, Vanadium (V) doping has been reported to enhance HER activity by increasing the inter layer spacing and activating inert basal plane of MoS_2, transforming the 2H phase into 1T phase of MoS_2 and by optimizing the hydrogen adsorption energy [3–5]. However, single step synthesis for V doped MoS_2 and phase engineering of MoS_2 *via.* V doping and utilizing it as efficient HER electrocatalyst in acidic, alkaline, and saline water is not studied much.

Herein, we have investigated the effect of V doping in MoS_2 towards HER application by systematic variation of V dopant concentration in MoS_2 lattice. To synthesize the nanostructured V-MoS_2 electrocatalyst, we have approached a single step hydrothermal route, since it is facile and economic and does not require any special experimental environment like high temperature, pressure etc. Experimental details of V-MoS_2 single step synthesis have been mentioned in section 2.2.4, Chapter 2 and Figure 2.7 displays the schematic representation of the synthesis process of nanostructured V-MoS_2 electrocatalyst. Synthesized nanostructured V-MoS_2 samples have been characterized for physico-chemical and electrochemical properties and ultimately employed for the overall water splitting (OWS) studies in acidic (0.5M H_2SO_4), alkaline (1M KOH) and saline water (1M KOH+0.5M NaCl) media. These results will be discussed in the following sections.

5.1: Results & Discussion

5.1.1: Morphological studies

Figure 5.1 shows FESEM images of the V-MoS_2 nanostrcutres, synthesized by a single step process while varying the vanadium (V) precursor concentration. Pristine MoS_2 is also synthesized for comparison, by the same process without addition of vanadium precursor.

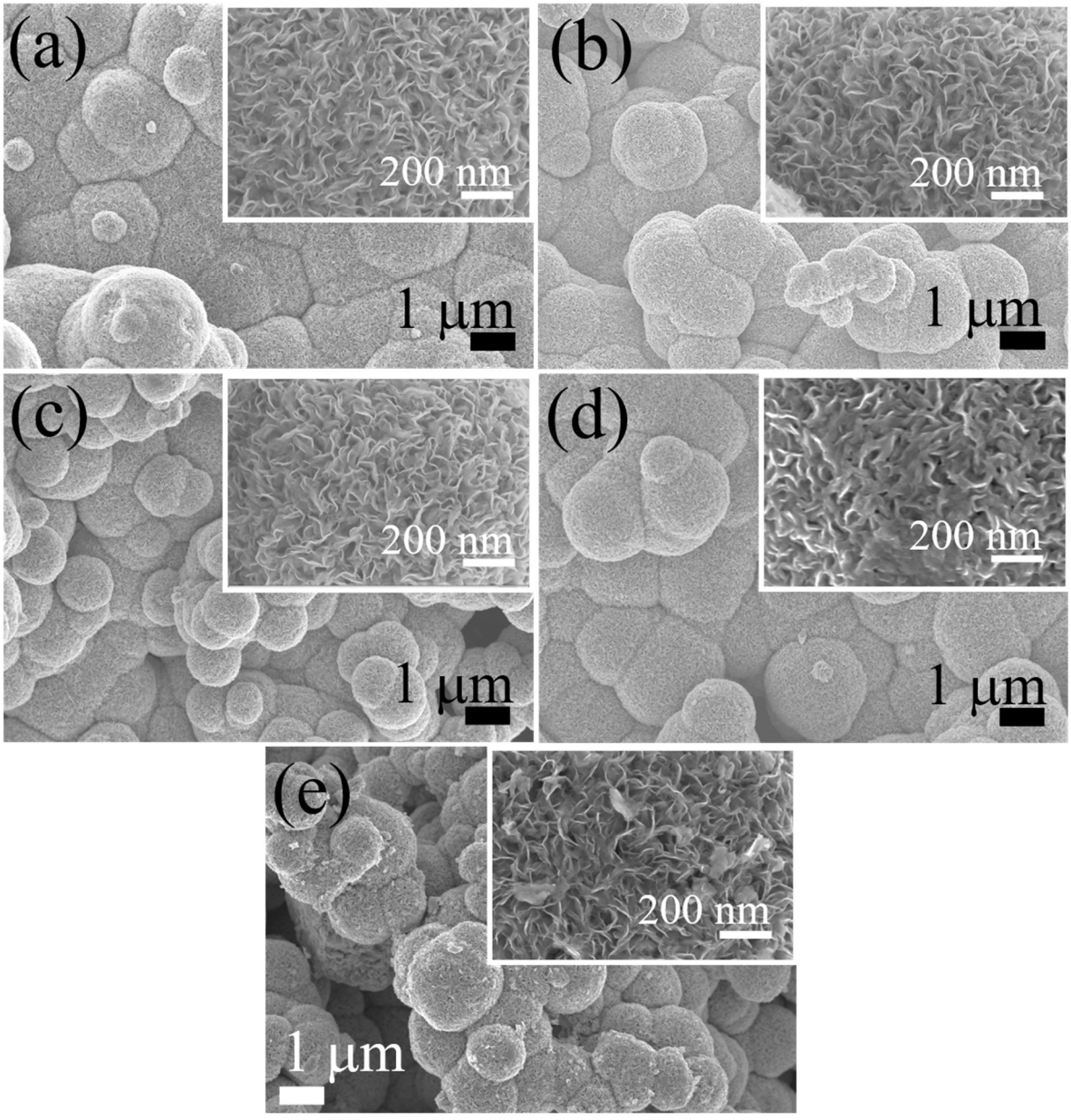

Figure 5.1: FESEM images of V-MoS_2 samples (a) V-MS6, (b) V-MS12, (c) V-MS24, (d) V-MS36 and (e) pristine MoS_2(respective inset images shows FESEM images at higher magnification).

It is clear from the FESEM images that all the synthesized nanostructured samples exhibit the morphology of micro balls, with vertically grown nanosheets on the surface of the micro balls. A distinct reduction in the size of micro balls from 5 μm for pristine MoS_2 to ~ 1 -

2 μm for V-MoS_2) can be clearly observed. We have observed that with increase in the V dopant concentration in MoS_2, the micro balls formed, become distinct and connected with each other at higher V dopant concentrations (V-MS36). The smaller size and the distinct formation of micro balls provide higher surface area for the growth of nanosheets in comparison to large sized micro balls, results in formation of maximum possible nanosheets density within same area in case of V-MoS_2 which helps to increases the HER activity. Moreover, we have not found any obvious difference in nanosheets morphology except for sample V-MS36 (prepared with 36 mg of vanadium precursor). At higher V doping (V-MS36), the nanosheets formed, get agglomerated, as shown in inset of figure 5.2 (d). The agglomeration in the morphology of V doped MoS_2 may be attributed to the higher concentration of V.

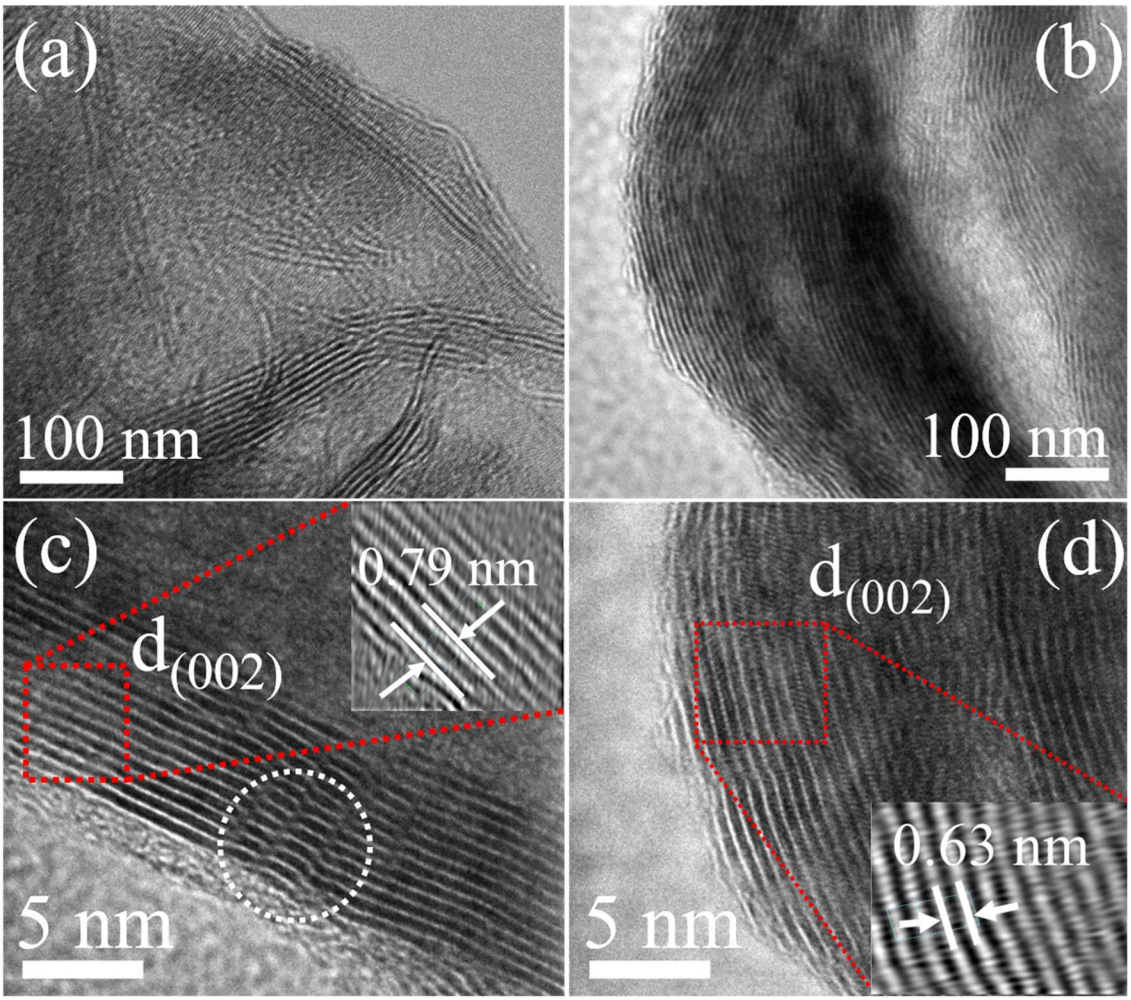

Figure 5.2: (a, b) TEM images and (c, d) HRTEM images (inset images shows corresponding calculated IFFT images, used for interplanar distance calculation) of samples V-MS24 and pristine MoS_2.

It has been extensively studied that doping of foreign element into electrocatalyst leads to distortion of the local structure of the host lattice and affects the crystal growth and results

in differed morphology [6,7]. However, V doping into MoS_2 system changes its morphology which can be optimized for efficient electrocatalytic activity [13].

An in-depth analysis of the sample V-MS24 and pristine MoS_2 was done using TEM imaging. As shown in figure 5.2 (a), TEM images confirm the formation of few layers (~9 layers) in sample V-MS24 whereas, aggregation of the layers has been observed in pristine MoS_2 (figure 5.2 b). The layers aggregation in pristine MoS_2 deteriorates its electrocatalytic activity with exposure of fewer active sites [8]. Moreover, few layers formation in sample V-MS24 provides higher exposure of electrocatalytically active sites which tends towards further improvement in HER activity [9].

Figure 5.2 (c & d) shows HRTEM images of V-MS24 and pristine MoS_2 respectively. In both cases, a distinct interlayer spacing corresponding to (002) plane of MoS_2 was confirmed and the IFFT image (inset of respective HRTEM image) from dotted circular region was used to estimate interplanar distance. The interplanar distance was determined to be 0.79 nm for V-MS24 and 0.63 nm for pure MoS_2. Such increased interplanar distance in case of doped MoS_2 system can be attributed to the incorporation/existence of amine (NH_2) and ammonium (NH_4^+) group, present in precursors or presence of V atoms [10,11][12] . In addition to the expanded interplanar spacing, we have also observed rich defect formation in sample V-MS24, shown as white dotted region in figure 5.2 (c), which is attributed to induce disorder in the lattice after V doping in MoS_2. These defects tend to form unsaturated sulphur which makes V-MS24 more catalytically active for HER application.

5.1.2: Elemental analysis by EDAX

For qualitative as well as quantitative analysis of the elements present in samples, EDAX technique has been used. The details of the specifications have been mentioned in section 2.3.1.3.1, Chapter 2. Figure 5.3 (a) presents the EDAX spectrum and area mapping for sample V-MS24. Table 5.1 summarizes the at% of the elements present as well as stoichiometry for all V-MoS_2 samples and pristine MoS_2. Figure 5.3 (b-d) shows area mapping of V-MS24, which validates the existence of the elements Mo (Figure 5.3 b), V (Figure 5.3 c), and S (Figure 5.3 d) and their homogeneous distribution throughout the sample, which is overlaid in Figure 5.3 (e). Figure 5.3 (a) shows that the spectrum exists the presence of V, Mo, and S in the V-MS24 sample, whereas the existence of other peaks belongs to Cu and might be from the Cu grid used for sample analysis.

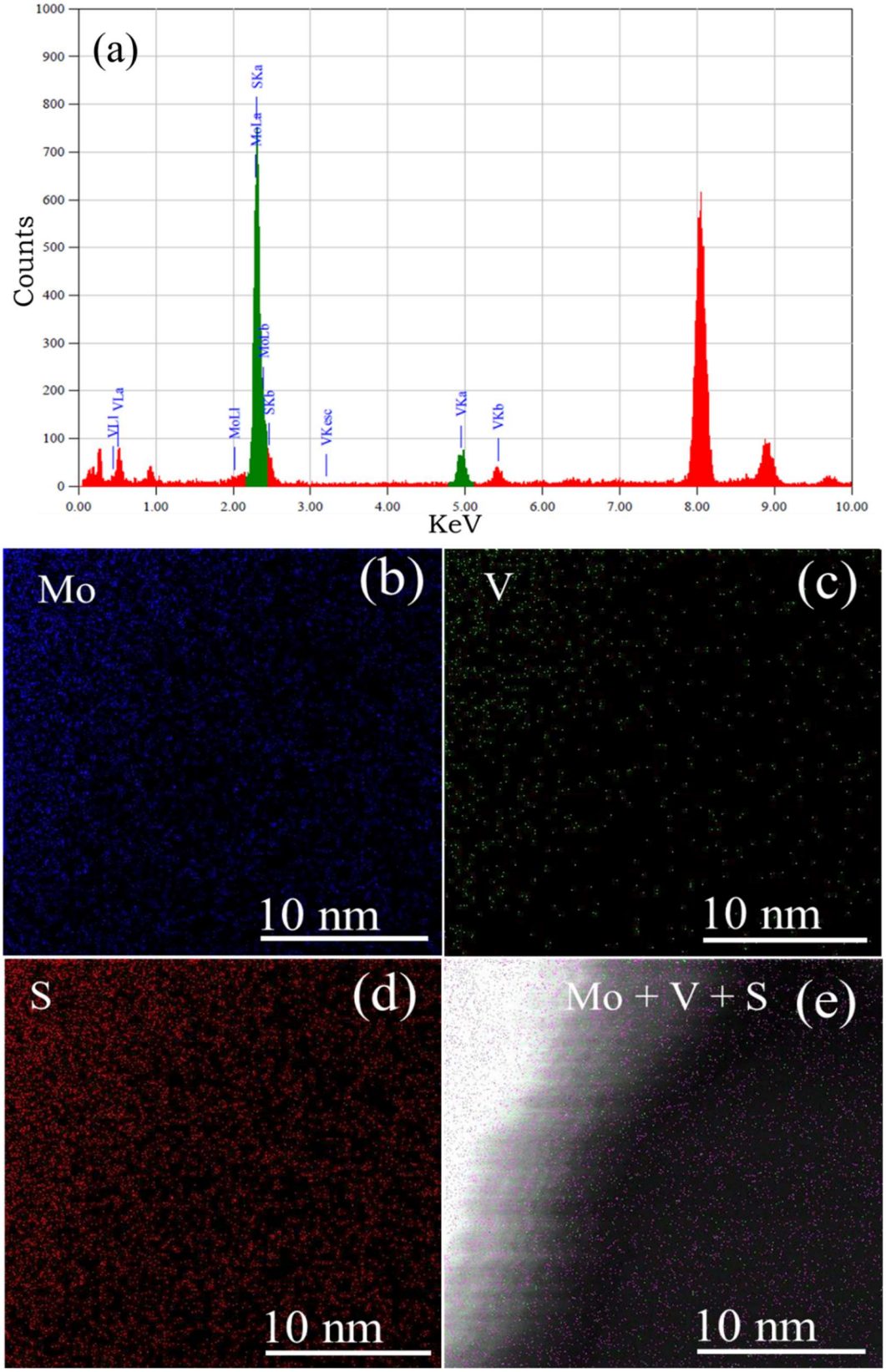

Figure 5.3: (a) EDAX pattern and (b, c, d & e) area mapping for element Mo, V and S and overlay of all element in scanned image respectively for sample V-MS24.

S at% is twice as high as (Mo + V) at% for V-MS6 and declines with increasing V dopant concentration (Table 5.1).

Table 5.1: EDS report of element presence in hydrothermally synthesized V-MoS_2 and pristine MoS_2 and their possible stoichiometry.

Sample	Element Present	at%	Stoichiometry (Approx.)
Pristine MoS_2	Mo: S	32.26: 67.74	MoS_2
V-MS6	Mo: V: S	31.10: 1.95: 66.95	$Mo_{0.94}V_{0.06}S_2$
V-MS12	Mo: V: S	30.98: 2.38: 66.64	$Mo_{0.93}V_{0.07}S_{1.99}$
V-MS24	Mo: V: S	30.43: 4.15: 65.42	$Mo_{0.88}V_{0.12}S_{1.89}$
V-MS36	Mo: V: S	30.32: 4.11: 65.57	$Mo_{0.89}V_{0.11}S_{1.90}$

Higher at% of V dopant in sample V-MS24 leads to optimized experimental condition for synthesis of V- MS24 which is attributed to V based precursor, its melting point and bond energy [14]. Sulphur vacancies formation and optimum concentration of V doping in MoS_2 lattices are expected to reduce the free energy for hydrogen adsorption and making the basal plane of MoS_2 nanosheets catalytically active, resulting in improved HER activity for sample V-MS24 [11,15].

5.1.3: Structural investigation

5.1.3.1: XRD analysis

XRD is a useful technique for overall structural investigation of materials based on Bragg's law. To investigate phase formation/structural properties of all hydrothermally synthesized V-MoS_2 and pristine MoS_2, XRD tool has been utilized. Figure 5.4 displays the XRD pattern of V-MoS_2 with variation in V dopant concentration and pristine MoS_2. XRD pattern of all hydrothermally synthesized samples exhibited analogous feature and similar XRD patterns of hexagonal (2H) MoS_2. The XRD peaks correspond to (002), (100), (103) and (110) planes related to 2H phase of MoS_2 (space group – P6 3/mmc, entry number 96-101-1287 in PDF+4 database). The lesser intensity and broadening of peaks confirm the few layers formation of V-MoS_2 with lower crystallinity [13]. Higher intensity of (002) plane in comparison to (100) plane which confirms the 2-dimensional (2D) MoS_2 phase formation [16].

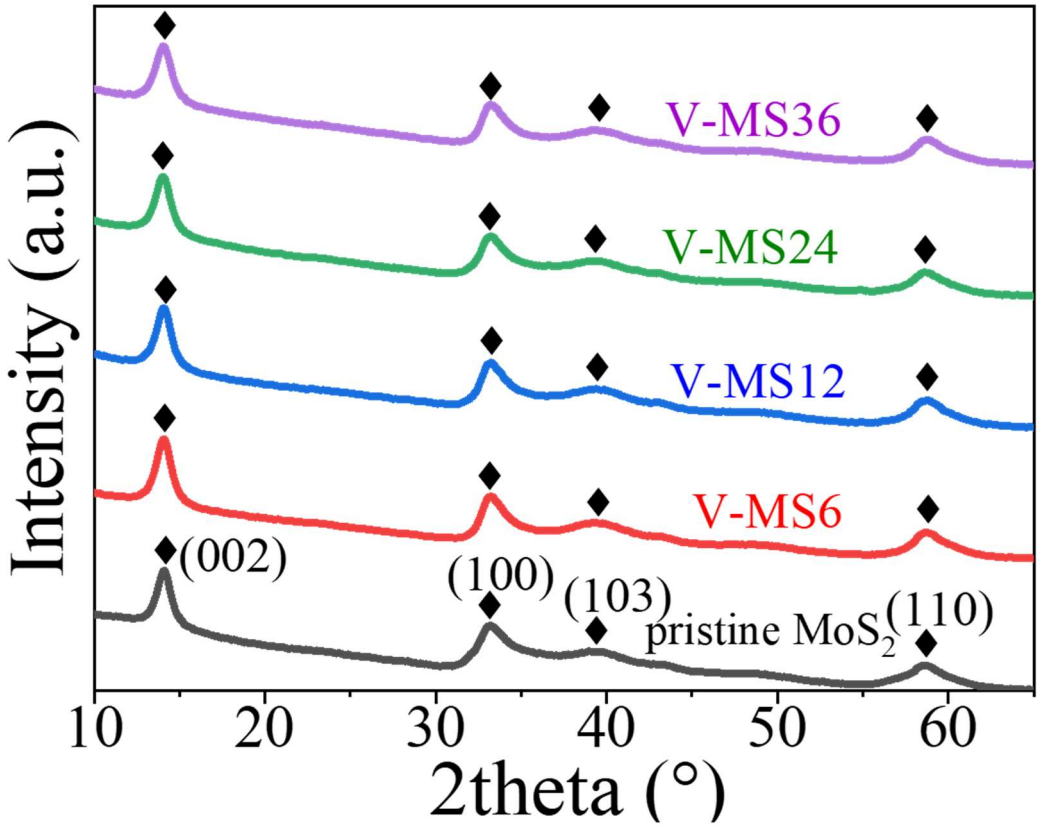

Figure 5.4: XRD pattern of V-MoS_2 samples with variation in V dopants and pristine MoS_2, synthesized by single step hydrothermal method.

Moreover, absence of high order diffraction peaks [(104), (105), (106), (008) *etc.* in the XRD patterns are due to the low crystallinity and short-range disorder in the samples which provide more catalytic active sites for HER application [14].

5.1.3.2: Raman analysis

Being a surface sensitive tool, Raman technique is very effective to identify the phase transition and crystallographic orientation of materials. For *in-depth* analysis of phase formation, Raman technique has been used to study all the hydrothermally synthesized V-MoS_2 and pristine MoS_2 samples. Figure 5.5 displays the Raman spectra of the V-MoS_2 samples with different V dopant concentration and pristine MoS_2 sample. A discernible difference can be seen in V-MoS_2 samples *w.r.t.* pristine MoS_2 spectra. The presence of three Raman peaks in pure MoS_2 samples at 405 cm^{-1}, 378 cm^{-1}, and 290 cm^{-1} is ascribed to A_{1g} (Out of plane mode), E^1_{2g} (In-plane mode), and E_{1g} (forbidden), which are distinctive peaks of MoS_2's 2H phase. whereas, other peaks observed at197 cm^{-1}, 238 cm^{-1} and 343 cm^{-1} Raman shift, correspond to phonon induced J_1, J_2 and J_3 mode of 1T MoS_2. In figure 5.5, pristine MoS_2 confirms the existence of 2H phase of MoS_2 along with minor phase fraction of 1T MoS_2. Unlike pristine

MoS_2, V-MoS_2 samples displayed a different feature by exhibiting strong Raman peaks corresponding to 1T phase of MoS_2 i.e., J_1, J_2 and J_3. The red shift in E^1_{2g} peaks and absence of A_{1g} peak can be consequences of the doping induced tensile stress in the MoS_2 lattice as well as strong interaction between S and V which reduce the Mo-S vibrations [15,16].

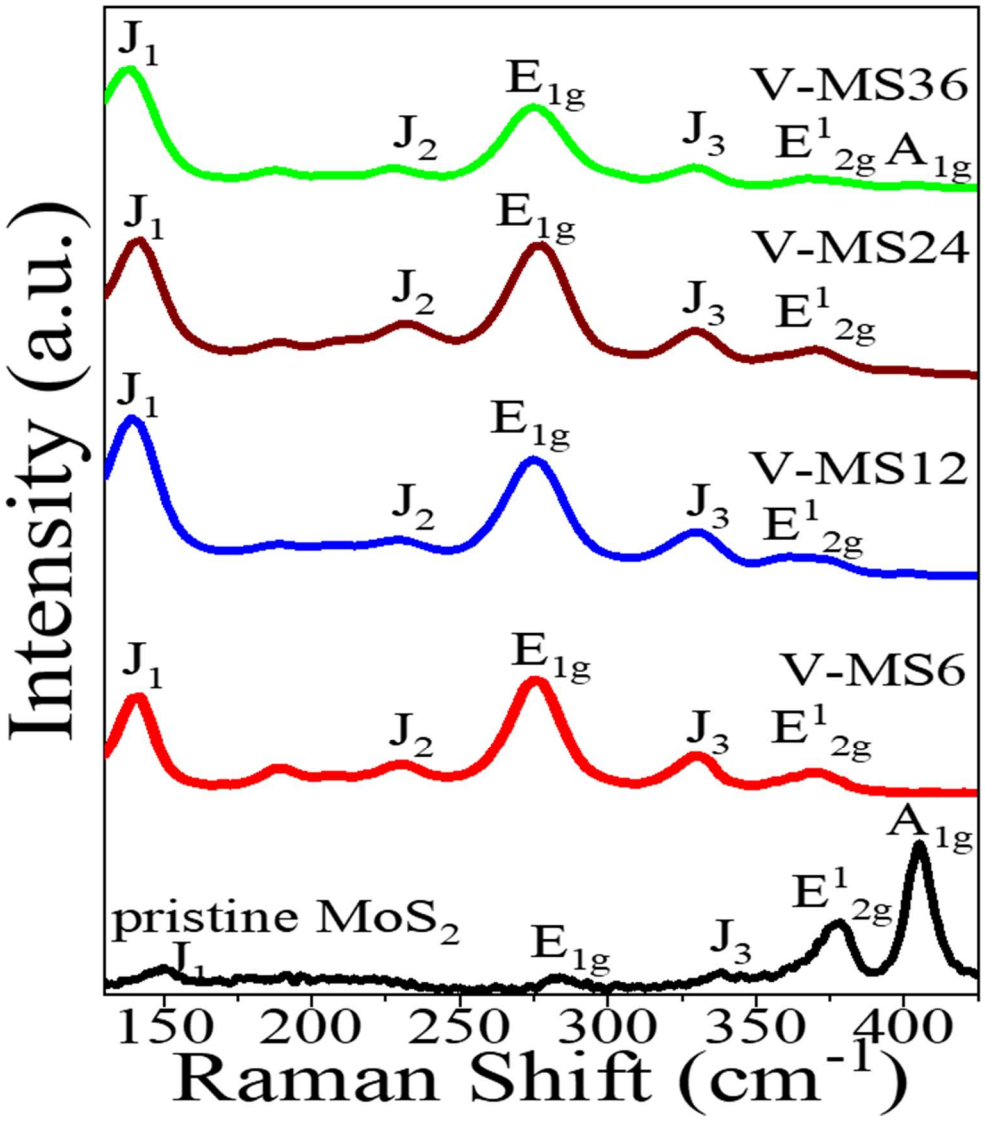

Figure 5.5: Raman spectra of all V-MoS_2 samples, synthesized with variation in V dopant concentration and pristine MoS_2.

Moreover, occurrence of strong E_{1g} vibrational intensity for V-doped MoS_2 samples is correlated to the edge-structure of MoS_2 [17]. A significant increase in the intensity of E_{1g} peaks in V doped MoS_2 samples verifies the high exposure of vertically developed nanosheets compared to their pristine counterpart, suggesting a potential benefit for enhanced catalytic sites. Occurrence of A_{1g} peaks along with E^1_{2g} peak in sample V-MS36 led to conversion of 1T phase to 2H phase of MoS_2, tend to decreased HER catalytic activity for sample V-MS36.

5.1.4: Chemical composition analysis using XPS

XPS characterization technique was utilised to investigate the surface element's composition and its chemical state, as well as to confirm multiphase development in sample V-MS24. The high resolution XPS spectra of Mo 3d, S2p, Mo 3p, N 1s and V 2p orbitals for sample V-MS24 have been shown in figure 5.6 (a-d). Mo 3d core level spectrum, exhibiting two peaks (Figure 5.6a), shows that each of the peaks is well fitted with two sets of doublet peaks. Peaks doublet at 228.2 eV and 231.2 eV can be attributed to 1T-MoS_2's Mo^{+4} $3d_{5/2}$ and Mo^{+4} $3d_{3/2}$. The other set of doublets have higher binding energies of 229 eV and 232 eV, respectively, and correspond to Mo^{+4} $3d_{5/2}$ and Mo^{+4} $3d_{3/2}$ of 2H-MoS_2. This analysis confirms the existence of mixed 1T/2H phase of MoS_2 in sample V-MS24 corroborating with Raman analysis. The increased intensity of doublets corresponding to the 1T-MoS_2 at the surface of V-MS24 verifies the dominating behaviour over the 2H-MoS_2, which is consistent with Raman studies, and hence tends to display higher HER activity. An extra peak observed at binding energy of 226 eV corresponds to the S 2s orbital. Doublets at 162.2 eV and 163.1 eV, corresponding to S $2p_{3/2}$ and S $2p_{1/2}$ (Figure 5.6b), can be attributed to the 2H-MoS_2, whereas other doublets at 161.2 eV and 162.9 eV, corresponding to $S2p_{3/2}$ and S $2p_{1/2}$, can be attributed to the metallic (1T) phase formation in sample V-MS24. [18]. Figure 5.6 (c) shows incorporation of N1s orbital along with Mo $3p_{1/2}$ orbital at 397.6 eV and 401.02 eV which is attributed to amine (NH_2) and ammonium group (NH^{4+}) [19]. These groups are accommodated in the layer of V-MoS_2 nanosheets and responsible for intercalation of layers, also observed in HRTEM image (figure 5.2c). Figure 5.6 (d) depicts V 2p core level XPS spectra. We found two prominent peaks at binding energies of 516.5 eV and 523.2 eV, corresponding to V^{+4} $2p_{3/2}$ and V^{+4} $2p_{1/2}$ orbitals, respectively [20,21]. Along with V^{+4} 3p orbital peaks, the presence of two weak peaks at lower binding energies of 513.9 eV and 521.5 eV is attributed to V^{+2} $3p_{3/2}$ and V^{+2} $3p_{1/2}$, respectively [5,20,21]. Both of the oxidation state of V *i.e.*, V^{+2} and V^{+4} are incorporated into MoS_2 system which illustrate the co doping of V^{+4} and V^{+2} in MoS_2 [3]. Both these oxidation states of V substitute the Mo^{+4} sites in S-Mo-S layers, as shown in Figure 5.6 (e). Figure 5.6 (e) depicts a schematic to produce the 1T/2H-MoS_2 with sulphur vacancy by co doping of V^{+2}/V^{+4}. Incorporation of V^{+2}/V^{+4} at Mo sites resulted in V reduction and Mo oxidation, leading in the development of Mo vacancies in the MoS_2 lattice. Metallic V (V^0) is thermodynamically favoured to occupy the Mo vacancies and creates V-S bond [22] and leach out extra S and therefore, formation of S vacancies, results in phase conversion to form 1T V-

MoS_2 [23]. In case of V^{+4} doping, it just takes the place of Mo sites, and form bonds with surrounding sulfur without changing the phase structure [24].

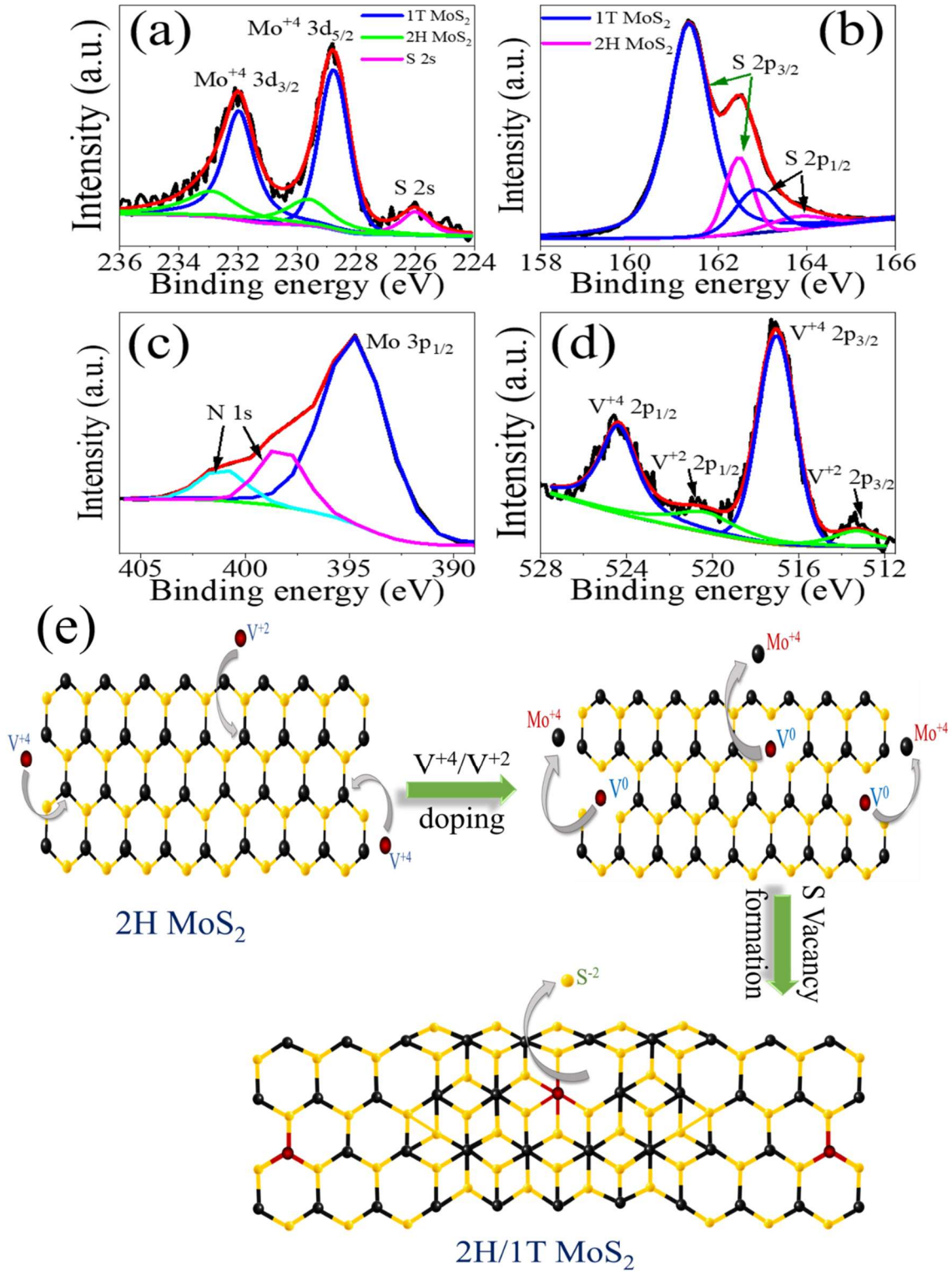

Figure 5.6: (a) High resolution XPS spectra of Mo 3d (b) S 2p orbitals, (c) Mo 3p & N 1s, (d) V 2p of sample V-MS24 and (e) schematic illustration for the formation of 1T/2H mixed phase of MoS_2 with sulfur vacancy via. V^{+2}/V^{+4} substitutional doping at Mo location.

Substitutional V doping (Figure 5.6e) modifies the electronic structure of pristine MoS_2 by creation of the sulfur vacancies and mixed phase of 1T and 2H which activates the inert basal planes of MoS_2 and optimizes the H adsorption behaviour, optimizing the adsorption energy for H species and resulting enhancement of intrinsic HER activity [4,25,26].

5.1.5: BET surface area

N_2 adsorption/desorption was used to calculate the BET surface area of the samples V-MS24 and pure MoS_2. The N_2 adsorption-desorption isotherms of the materials V-MS24 and pristine MoS_2 are shown in Figures 5.7 (a & b). Measured BET surface area for both samples have been shown in respective graph. Figure 5.7 shows a N_2 adsorption/desorption curve with an H3 hysteresis loop and a type IV isotherm, indicating that both materials have a mesoporous structure. Brunauer-Emmett-Teller (BET) calculation shows that V-MS24 exhibits approx. 2 times larger specific area (27.15 $m^2.g^{-1}$) than that of pristine MoS_2 (15.45 $m^2.g^{-1}$)I (inset of Figure 5.7). However, V-MS24 displayed an average pore size of 91.0 Å with total pore volume of 0.075 $cm^3.g^{-1}$ whereas pristine MoS_2 contains pores with average size of 13.44 Å and total pore volume of 0.052 $cm^3.g^{-1}$.

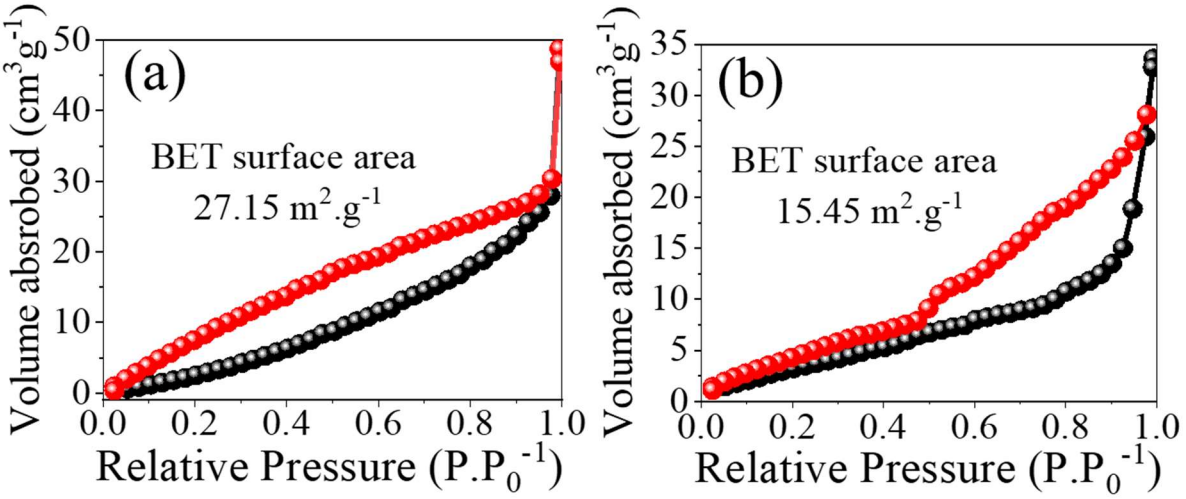

Figure 5.7: N_2 adsorption/desorption isotherms of sample (a) Pd-MS5 and (b) pristine MoS_2.

V-MS24 yields larger surface area, results in presence of more catalytically active sites for hydrogen adsorption which is beneficial for faster HER kinetics inside the porous structure of the sample [27].

5.1.6: Electrochemical characterization

To study the influence of V doping on the HER activity of pure MoS_2, single step hydrothermally synthesised V-MoS_2 nanostructured samples with varying V dopant

concentrations were employed as electrocatalysts. The electrochemical studies for the MoS_2 and V-MoS_2 samples have been performed by using the respective electrocatalyst modified carbon paper in 0.5 M H_2SO_4 (acidic water) solution (working electrode preparation has been mentioned in section 2.2.1.1, Chapter 2). After optimizing the V dopant concentration in MoS_2 for the efficient electrocatalytic HER activity, electrochemical measurements have been employed only for optimized sample *i.e.*, V-MS24 in 1M KOH (alkaline water) and 1M KOH+0.5M NaCl (saline water) solutions and compared the HER efficiency with pristine MoS_2 and standard electrocatalyst (Pt/C). Figure 5.8 (a) shows polarization curves of V-MS6, V-MS12, V-MS24, V-MS36, pristine MoS_2 and Pt/C samples in acidic water. To generate 10 $mA.cm^{-2}$, pristine MoS_2 requires an overpotential of 248 mV *vs. RHE*. As V doping modifies the electronic structure and enhances the active sites for HER, significant decrement in overpotential has been observed for the V-MoS_2 samples with increasing V doping concentration. The value of overpotential is reduced to 240 mV *vs. RHE* for V-MS6, 189 mV *vs. RHE* for V-MS12, 111 mV *vs. RHE* for V-MS24 and 202 mV *vs. RHE* for V-MS36. Among all V-MoS_2 samples, V-MS24 exhibited most efficient electrocatalytic activity with higher current density at low overpotential (Figure 5.8a and Table 5.2). To achieve 10 $mA.cm^{-2}$ current density, the lowest overpotential of just 111 mV *vs. RHE* (near to Pt/C: 40 mV *vs. RHE*) leads to greater electrocatalytic activity for HER for V-MS24. Tafel analysis was also performed to further understand the electrocatalytic activity of the samples and the HER mechanism on the surface of the electrocatalyst. Figure 5.8 (b) presents the Tafel curve of the corresponding samples. The linear regions of Tafel curve for all samples were well fitted with Tafel equation ($\eta = blog|j| + a$) where a & b are known as Tafel constants (b as Tafel slope and a as exchange current density) and j stands for current density. The Tafel slope (b) for V-MoS_2 is calculated to be 89 $mV.dec^{-1}$ for V-MS6, 67 $mV.dec^{-1}$ for V-MS12, 53 $mV.dec^{-1}$ for V-MS24 and 71 $mV.dec^{-1}$ for V-MS36. The Tafel value of V-MS24 is much smaller compared to that for pristine MoS_2 (91 $mV.dec^{-1}$) while exhibiting a value close to Pt/C (31 $mV.dec^{-1}$), indicating its better electrocatalytic activity. Among all the synthesized samples, V-MS24 exhibits lowest overpotential and Tafel slope, revealing the improved electrocatalytic activity of sample V-MS24. EIS analysis was performed and the corresponding curves were acquired to further examine the electrode/electrolyte dynamics during the HER process. Nyquist plot represents the electrode-electrolyte/electrolyte interface resistance as well as the charge transfer resistance (R_{ct}) during HER. Figure 5.8 (c) presents the Nyquist plots for all V-MoS_2 samples and pristine MoS_2 along with the fitted equivalent circuit in the inset. The smallest Nyquist plot for sample

V-MS24 illustrates the lowest charge transfer resistance, indicating faster charge transfer at electrode/electrolyte interface and results superior HER kinetics.

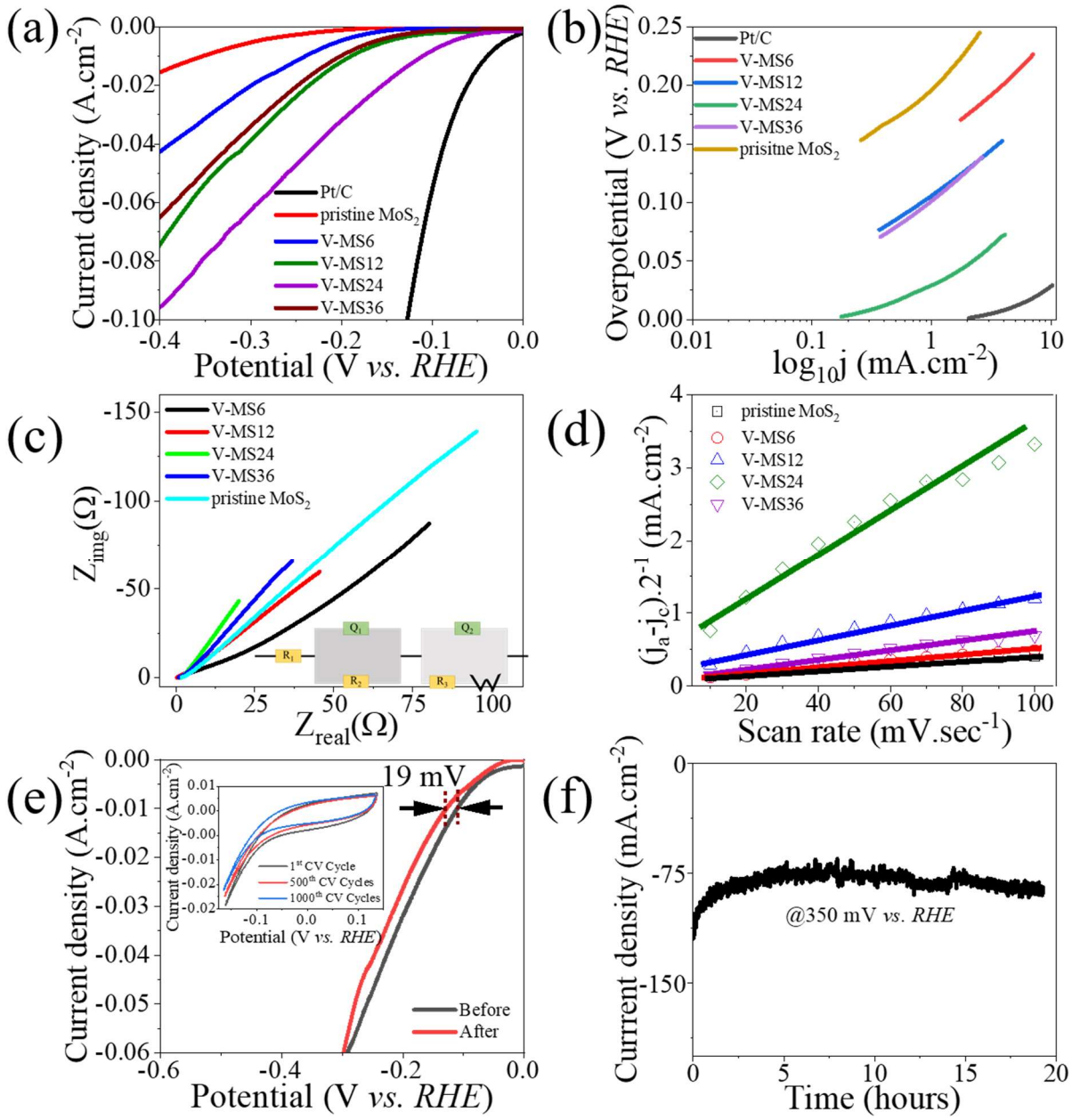

Figure 5.8: HER performance of synthesized electrocatalysts (doped/ undoped MoS_2) and Pt/C in acidic water (0.5 M H_2SO_4), (a) polarization curve, (b) corresponding Tafel curve, (c) Nyquist plot with equivalent circuit (inset), (d) C_{dl} calculation, (e-f) Stability profile for V-MS24, (e) polarization curve before and after 1000 CV cycles (inset represents change in area covered in 1st, 500th and 1000th CV cycles) and chronoamperometric curve at higher current density (100 mA.cm^{-2}).

Electrochemically active surface area (ECSA) is one of the important descriptors to identify the electrocatalytic efficiency of material towards HER application since it depends on the active site density of the electrocatalyst. ECSA calculation has been done using eq. 2.1 &

2.2 (Chapter 2). C_{dl} values were calculated by linear fitting of curve which was plotted using difference in anodic and cathodic current density at different scan rates, and shown in figure 5.8 (d). Among all V-MoS_2 samples, V-MS24 delivers highest value of C_{dl} (27.32 $mF.cm^{-2}$) which is approx. 10 times higher than pristine MoS_2 (2.08 $mF.cm^{-2}$).

Table 5.2: Calculated HER parameters for all synthesized V-MoS_2 samples, pristine MoS_2 and standard electrocatalyst for HER (Pt/C).

Sample name	**Overpotential (η) @ 10 $mA.cm^{-2}$ (mV *vs. RHE*)**	**Tafel slope (b) ($mV.dec^{-1}$)**	**C_{dl} ($mF.cm^{-2}$)**	**ECSA (cm^2)**
Pt/C	40	31		-
pristine MoS_2	248	91	2.08	34
V-MS6	240	89	4.11	68.5
V-MS12	189	67	9.72	162.0
V-MS24	111	53	27.32	455.3
V-MS36	200	71	5.98	99.7

The highest C_{dl} value indicates that V-MS24 with moderate V doping exhibits maximum possible exposed active sites for HER application. Calculated value of ECSA for all synthesized samples has been mentioned in table 5.2. The drastic increment in ECSA for sample V-MS24 can be attributed to few layer formations.

Operational stability is also a key parameter for evaluating HER electrocatalyst which leads to make electrocatalyst commercially acceptable. We have examined the electrochemical stability for the sample V-MS24 (superior electrocatalyst found over other synthesized samples, as referred) Figure 5.8 (e) depicts the recorded polarisation curve before and after the 1000th CV cycle and the difference in area covered at the 1st, 500th, and 1000th cycles (inset of Figure 5.8e). Change in overpotential values of 19 mV at 10 $mA.cm^{-2}$ current density overpotential has been observed from 1st cycle to 100th cycle and slight difference in area covered from 0.0011 cm^2 at 1st cycle to 0.0008 cm^2 at 1000th cycle has been recorded which

represents a remarkable electrochemical stability of V-MS24 towards HER application in acidic water. Figure 5.8 (f) presents the time-resolved current plot. Samples V-MS24 can continuously generate hydrogen at a higher current density of 100 $mA.cm^{-2}$ by maintaining stable electrochemical reaction up to 20 hours. The results illustrate an excellent continuous operational stability of sample V-MS24.

To understand and compare the improved HER performance of V doped MoS_2, we have compared with results of some published reports on transition metal doped MoS_2 and their electrocatalytic activity towards of HER application. Table 5.3 summarizes the HER performance of reported transition metal doped MoS_2 systems and compares the HER efficiency of single step synthesized V-MoS_2.

Table 5.3: Summarization of few researches on earth abundant transition metal doped MoS_2 electrocatalysts for HER application.

S. No.	**System**	**Method of synthesis**	**Phase**	**Electrocatalytic performance**			**Ref.**
				η^{10} (mV *vs. RHE*)	**Tafel slope ($mV.dec^{-1}$)**	**Stability run**	
1.	Co doped MoS_2 @ CFP	Hydrothermal	2H	181	50	-	[28]
2.	Mn doped MoS_2 @ rGO*	Hydrothermal	2H	200 @ 4.52 $mA.cm^{-2}$	76	1000 cycles	[29]
3.	MoS_2: Ni	Sol-gel and hydrothermal	2H	207	60.5	15 hours at 20 $mA.cm^{-2}$ and 1200 cycles	[30]

4.	Zn doped MoS_2	Solvothermal	2H	130	51	1000 cycles	[31]
5.	V doped MoS_2	Hydrothermal	1T/2H	146	48	80 hours at 160 mV and 1000 cycles	[3]
6.	W doped 1T MoS_2	Hydrothermal	1T/2H	292	55.7	15 hours and 3000 cycles	[32]
7.	V doped MoS_2	Hydrothermal	2H	194	59	9 hours @ 235 mV and 1000 cycles	[33]
8.	V doped MoS_2 NSs[#]	Solvothermal	2H	262	71	1000 cycles	[34]
9.	V-MoS_2 NSs	Single step hydrothermal method	1T/2H	111	53	1000 cycles and ~20 hours of continuous run @ 350 mV	This work

*rGO – Reduced Graphene Oxide [#]NS – Nanosheets, [$]$\eta^{10}$ – Overpotential @ 10 $mA.cm^{-2}$.

The single step hydrothermal synthesis and using a simple experimental arrangement and simple precursors, makes the present process simple and cost-effective. Moreover, synergistic effect of V (V^{+4}/V^{+2}) co-doping, mix of 1T/2H phases and expanded interlayers, plentiful defects/ disorders, sulfur vacancies making V-MoS_2 an efficient, sustainable, and commercially acceptable HER electrocatalyst compared to other reported transition metal doped MoS_2 systems.

Inclusion of above discussion, to investigate the electrocatalytic efficiency of V-MoS_2 *(optimized sample form above studies, this sample will be referred as V-MoS_2 in further studies)* towards HER application in alkaline and saline water, electrochemical characterization was performed. Additionally, overall water splitting and rate estimation electrocatalytic hydrogen/oxygen evolution in acidic, alkaline, and saline water using V-MS24 as HER cathode was also performed. Figure 5.9 displays the electrocatalytic HER activity of sample V-MS24 and pristine MoS_2 and Pt/C towards HER application in alkaline and saline water. In comparison to the synthesized V-MoS_2 and pristine MoS_2 samples, Figure 5.9 (a & c) shows that Pt/C requires the lowest overpotential (45 mV *vs. RHE* and 60 mV *vs. RHE* in alkaline and saline water, respectively) to obtain 10 $mA.cm^{-2}$ current density. V-MS24 outperforms pristine MoS_2 in electrocatalytic activity by having a lower overpotential of 218 mV *vs. RHE* and 266 mV *vs. RHE* at 10 $mA.cm^{-2}$ current in alkaline and saline water, which is substantially lower than that of pristine MoS_2 (356 mV *vs. RHE* and 425 mV *vs. RHE*).

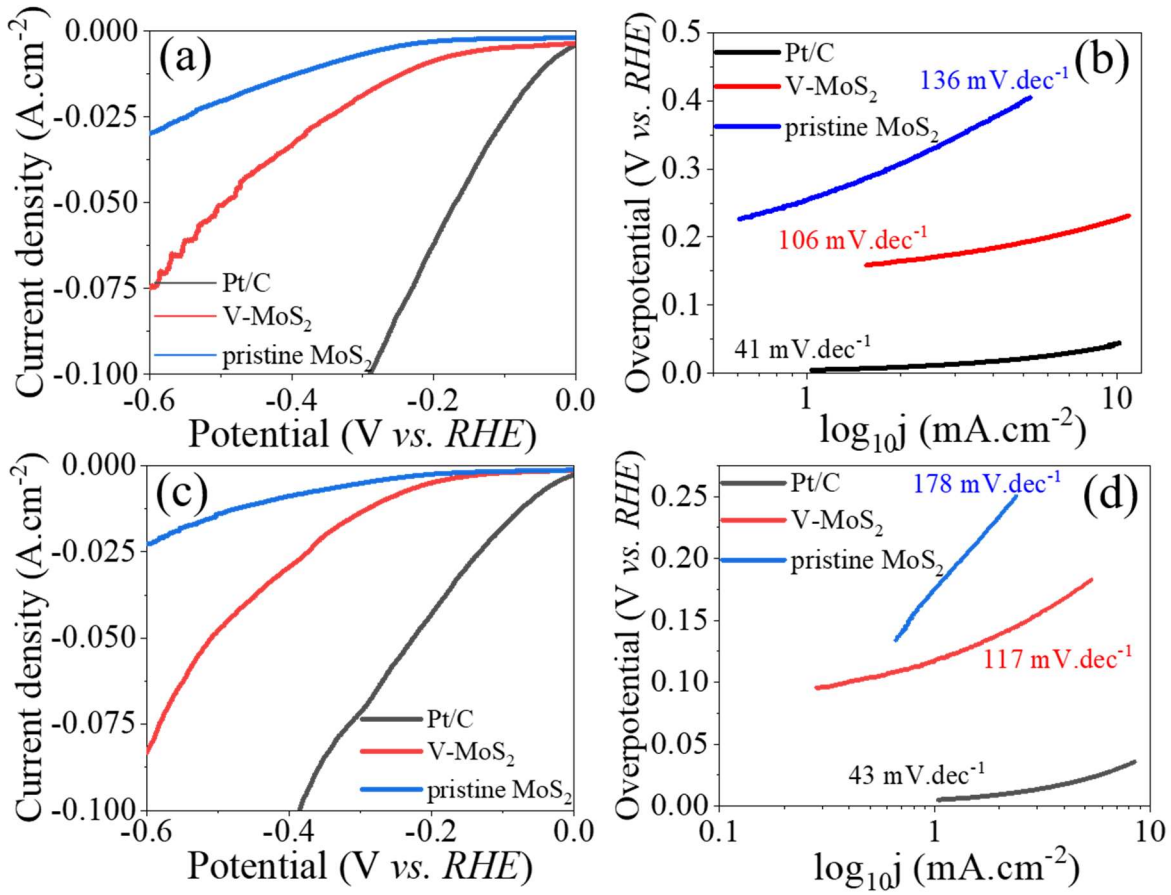

Figure 5.9: (a) HER polarization curves, (b) corresponding Tafel curve in alkaline water, (c) HER polarization curves and (d) corresponding Tafel curve in saline water for samples VMS24, pristine MoS_2 and Pt/C.

To understand the involved HER mechanism for electrocatalysis in alkaline and saline water, Tafel analysis was carried out. The corresponding Tafel curve and its value for V-MoS_2, pristine MoS_2 and Pt/C in alkaline and saline water have been shown in Figure 5.9 (b & d) respectively. Pt/C, V-MoS_2 and pristine MoS_2 possess Tafel slope of 41, 106, 136 $mV.dec^{-1}$ and 41, 117, 178 $mV.dec^{-1}$ in alkaline and saline water respectively. V-MoS_2 displays lower value of Tafel slope over the pristine MoS_2, hence is a superior electrocatalytic active material for HER application. Furthermore, a detailed examination of the Tafel slope value of the sample V-MS24 predicted that the rate determining step was the Heyrovsky step. It has been observed that the sample V-MS24 is a promising electro-catalyst for HER in acidic, alkaline, and saline water, and that its HER performance is equivalent to that of previously published materials.

It is observed that HER performance of electrocatalyst in acidic water is fastest, moderate in alkaline water and lowest in alkaline water [35,36]. Samples requires an extra value of overpotential in alkaline and saline medium to achieve fixed amount of current density as compared to acidic water. The faster HER kinetic in acidic medium may be attributed to lower hydrogen binding energy for the hydrogen adsorption/desorption in case of acidic water whereas due to extra water dissociation step, large value of energy barrier is required for hydrogen adsorption involve in alkaline as well as saline medium [37]. HER mechanism is more feasible and faster in acidic medium as compared to the alkaline medium owing to different mechanistic pathways associated with the two different media. The sluggish kinetics of HER in alkaline medium is the cause of lesser concentration of H^+ ions and difficulty in the formation of M−H*. However, the lower performance of electrocatalyst in saline water than alkaline water can be attributed to the presence of chlorine ions (Cl^-) in alkaline water. Presence of chlorine ions poison the electrocatalyst's surface and block the actives sites of materials [38].

In order to support above claim, F. Yang *et.al.*, reported electrocatalytic water splitting in alkaline and saline water by utilizing Pt/Ni-Mo alloy as an efficient and durable HER electrocatalyst. Developed Pt/Ni-Mo system generated higher current density of 2000 $mA.cm^{-2}$ at an overpotential of only 42 mV and 113 mV in alkaline and saline water respectively [39]. Similarly, system Ni_2P-FeP/Fe foam needed overpotential of 42 mV and 89 mV to generate 10 $mA.cm^{-2}$ current during HER performance in alkaline and saline water respectively. Moreover, overall water splitting was performed using NiFe LDH/Fe foam as anode and Ni_2P-FeP/Fe foam as cathode in alkaline and saline water. This two electrode configured cell required +1.53

V cell potential at 10 mA.cm^{-2} current which is 90 mV large than alkaline water splitting (+1.44 V) [40].

5.1.7: Electrocatalytic water splitting

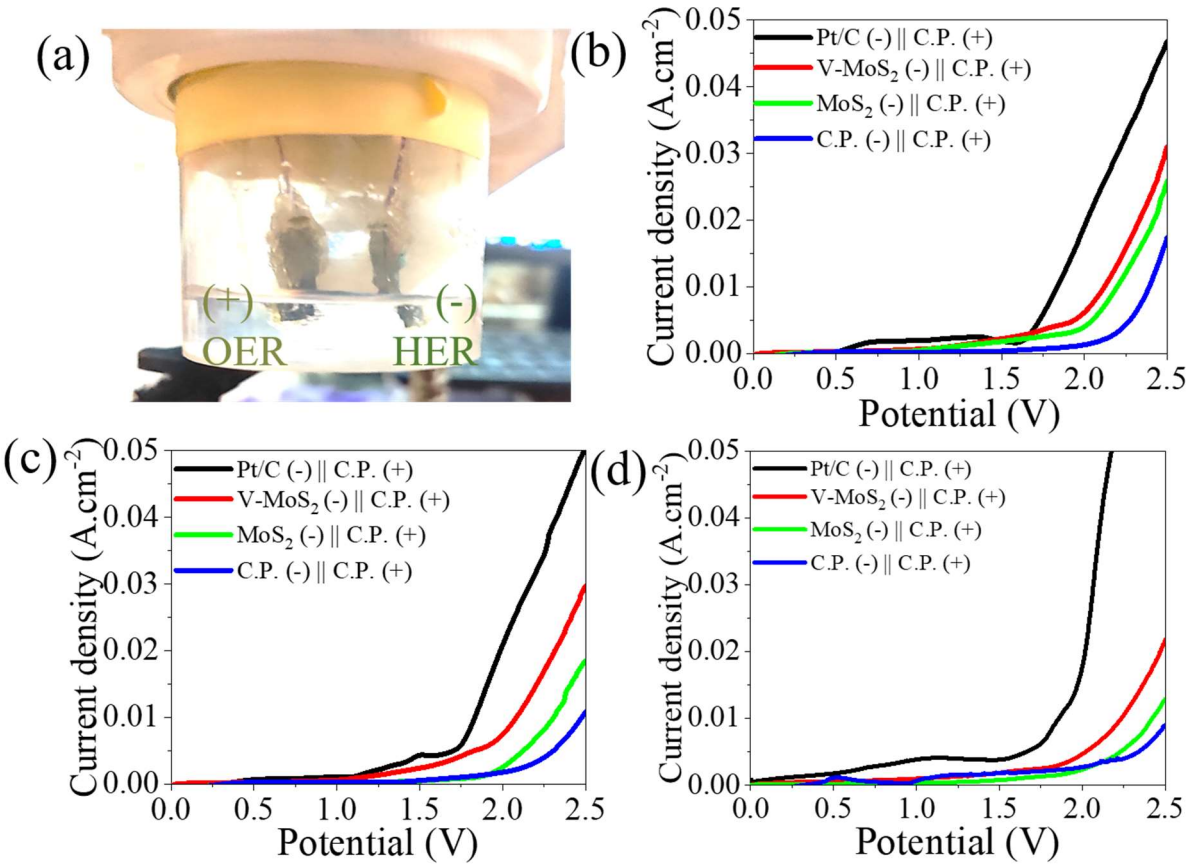

Figure 5.10: (a) A digital photograph of two electrode electrocatalytic cell for overall water splitting, LSV curves for V-MoS$_2$||C.P., MoS$_2$||C.P., C.P.||C.P. and Pt/C||C.P. during electrocatalytic water splitting in (a) acidic, (b) alkaline and (c) saline water.

V-MoS$_2$ (V-MS24) has shown excellent HER performance in acidic, alkaline, and saline water in earlier sections, we have evaluated the performance of V-MoS$_2$ as HER cathode during OWS process in acidic, alkaline, and saline water. During electrocatalytic water splitting process, we have used a two-electrode system with V-MoS$_2$ (V-MS24) modified carbon paper as HER cathode and bare carbon paper (C.P.) as OER anode. Equal amount of HER electrocatalysts (V-MoS$_2$, MoS$_2$ and Pt/C) were loaded one by one onto the C.P. (C.P. were ultrasonicated in water and ethanol one by one for 30 min prior to loading) using drop casting method. Figure 5.10 represents the overall water splitting performance at lab scale in acidic, alkaline, and saline water (Figure 5.10 a, b & c). Comparison of electrocatalytic water splitting performance of V-MoS$_2$, pristine MoS$_2$, Pt/C and bare C.P. has also been shown in Figure 5.10.

V-MoS_2 requires +2.08 V (acidic water), +2.12 V (alkaline water) and +2.23 V (saline water) to drive 10 $mA.cm^{-2}$ current density in electrocatalytic cell which is lower than pristine MoS_2 (acidic water: +2.20 V, alkaline water: +2.31 V, saline water: +2.42 V) and bare C.P. (acidic water: 2.40 V, alkaline water: 2.48 V, saline water: 2.53 V) and close to Pt/C (acidic water: +1.84 V, alkaline water: +1.84 V, saline water: +1.86 V).

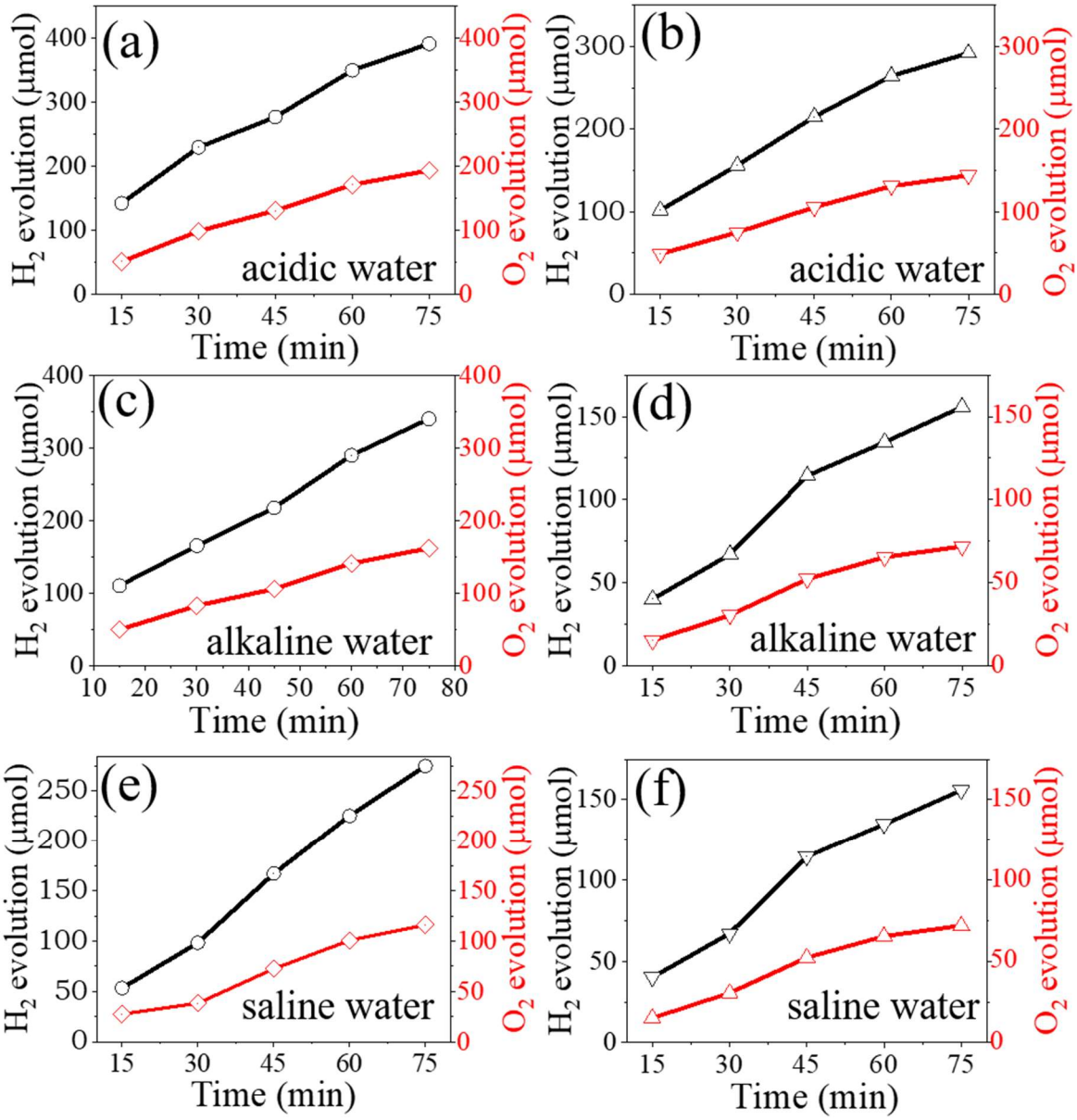

Figure 5.11: Volume of generated H_2 and O_2 in µmols at constant potential of +2.2 V for systems V-MoS_2||C.P. (a, b, c) and MoS_2||C.P (d, e, f) in acidic water (a, b), alkaline water (c, d) and saline water (e, f).

The reduced cell potential of V-MoS_2||C.P. over pristine MoS_2 clearly reflect the higher electrocatalytic efficiency for hydrogen generation. Therefore, to identify the electrocatalytic efficiency, ultimately, we have performed real-time H_2 and O_2 generation and quantified the

rate of evolution during OWS process using Gas chromatography (GC). Throughout the electrocatalytic water splitting process, a constant cell voltage of +2.2 V was applied for both the systems *i.e.*, V-MoS_2||C.P. and MoS_2||C.P. in acidic, alkaline, and saline water.

Table 5.4: Quantification of electrocatalytically evolved H_2 and O_2 gases from system V-MoS_2||C.P. and MoS_2||C.P. during electrocatalytic water splitting in acidic, alkaline, and saline water.

Electrolyte	**Time (min)**	**H_2 (µmol)**		**O_2 (µmol)**	
		V-MoS_2||C.P.	**MoS_2||C.P.**	**V-MoS_2||C.P.**	**MoS_2||C.P.**
Acidic water (0.5 M H_2SO_4)	15	141.83	104.93	50.91	48.95
	30	228.94	173.76	98.47	75.12
	45	276.21	235.96	130.45	105.49
	60	349.11	307.54	170.56	131.13
	75	390.39	350.19	193.19	143.99
Alkaline water (1M KOH)	15	110.31	40.12	49.85	15.06
	30	165.34	67.09	82.67	30.54
	45	217.50	114.42	105.75	52.21
	60	289.82	134.65	140.91	65.32
	75	339.86	155.77	161.93	71.88
Saline water (1M KOH+0.5M NaCl)	15	53.43	20.97	27.58	9.48
	30	98.35	53.61	38.40	22.83
	45	167.06	97.66	72.61	43.83
	60	225.26	116.06	100.80	55.03
	75	275.34	149.47	116.10	71.73

Figure 5.11 represents volume of electrocatalytically generated H_2 and O_2 gas at cell potential of +2.2 V in all the three electrolytes for systems V-MoS_2||C.P. and MoS_2||C.P. The quantified evolute H_2 and O_2 gas for systems V-MoS_2||C.P. and MoS_2||C.P. have been tabulated in table 5.4. The ratio of collected H_2 gas to collected O_2 gas has been found approximately 2:1 during electrolysis as per theoretical values [41]. The maximum amount of evolute H_2 gas has been estimated to be 390 µmol, 339 µmol and 275 µmol in acidic, alkaline, and saline water

respectively for V-MoS_2||C.P. system, which is higher than MoS_2||C.P. systems (acidic: 291 μmol, alkaline:155 μmol and saline: 149 μmol). These findings suggest that V-MoS_2 can be a promising HER electrocatalyst for overall water splitting (OWS) in acidic, alkaline, and saline media, and they point the way forward for MoS_2-based electrocatalyst systems.

5.2: Conclusion

In conclusion, V-MoS_2 electrocatalyst was effectively synthesized by utilizing a simple and cost-effective one step hydrothermal approach and showed outstanding HER activity. The improved performance of V-MoS_2 is attributed V^{+2}/V^{+4} which helps for phase transition from 2H to 1T of MoS_2, few layered formations with expanded interlayers, induces defects and sulfur vacancies in MoS_2 lattice. The V-MoS_2 system with these special features, improved the HER performance for V-MoS_2 with a minimum overpotential of 111 mV *vs. RHE* at 10 $mA.cm^{-2}$ current density with a Tafel slope of 53 $mV.dec^{-1}$ in acidic (0.5M H_2SO_4) solution, whereas it displayed overpotentials of 218 mV *vs. RHE* and 266 mV *vs. RHE* in alkaline (1M KOH and saline (1M KOH+0.5M NaCl) solutions. In addition, we have achieved +2.08 V, +2.12 V and +2.23 V by utilizing V-MoS_2 as HER cathode to generate 10 $mA.cm^{-2}$ current density during OWS as well as it gives 390 μmol, 339 μmol and 275 μmol volume of generated H_2 gas at constant potential of +2.2 V in acidic, alkaline, and saline water respectively. Present work results in a simple and economic way for structural regulation for high performance electrocatalyst for HER applications and gives a new direction for MoS_2 based systems in area of acidic, alkaline, and sea water splitting as promising alternative to noble metal electrocatalyst for HER application.

5.3: References

1. P. Sundara Venkatesh, N. Kannan, M. Ganesh Babu, G. Paulraj, and K. Jeganathan, Int. J. Hydrogen Energy **47**, 37256 (2022).

2. T. H. M. Lau, X. Lu, J. Kulhavý, S. Wu, L. Lu, T.-S. Wu, R. Kato, J. S. Foord, Y.-L. Soo, K. Suenaga, and S. C. E. Tsang, Chem. Sci. **9**, 4769 (2018).

3. T. Liu, C. Fang, B. Yu, Y. You, H. Niu, R. Zhou, J. Zhang, and J. Xu, Inorg. Chem. Front. **7**, 2497 (2020).

4. M. Li, B. Cai, R. Tian, X. Yu, M. B. H. Breese, X. Chu, Z. Han, S. Li, R. Joshi, A. Vinu, T. Wan, Z. Ao, J. Yi, and D. Chu, Chem. Eng. J. **409**, 128158 (2021).

5. J. Xu, Y. Zhu, B. Yu, C. Fang, and J. Zhang, Inorg. Chem. Front. **6**, 3510 (2019).

6. A. Kudo, R. Niishiro, A. Iwase, and H. Kato, Chem. Phys. **339**, 104 (2007).

7. R. D. Shannon, Acta Crystallogr. Sect. A **32**, 751 (1976).

8. N. Xue and P. Diao, J. Phys. Chem. C **121**, 14413 (2017).

9. J. N. Coleman, M. Lotya, A. O'Neill, S. D. Bergin, P. J. King, U. Khan, K. Young, A. Gaucher, S. De, R. J. Smith, I. V Shvets, S. K. Arora, G. Stanton, H.-Y. Kim, K. Lee, G. T. Kim, G. S. Duesberg, T. Hallam, J. J. Boland, J. J. Wang, J. F. Donegan, J. C. Grunlan, G. Moriarty, A. Shmeliov, R. J. Nicholls, J. M. Perkins, E. M. Grieveson, K. Theuwissen, D. W. McComb, P. D. Nellist, and V. Nicolosi, Science (80-.). **331**, 568 (2011).

10. K. D. Rasamani, F. Alimohammadi, and Y. Sun, Mater. Today **20**, 83 (2017).

11. M. Li, Z. Zhou, L. Hu, S. Wang, Y. Zhou, R. Zhu, X. Chu, A. Vinu, T. Wan, C. Cazorla, J. Yi, and D. Chu, ACS Appl. Mater. Interfaces **14**, 16338 (2022).

12. J. Xu, J. Zhang, W. Zhang, and C.-S. Lee, Adv. Energy Mater. **7**, 1700571 (2017).

13. W. J. Rohrbaugh and E. L. Wu, in *Charact. Catal. Dev.* (American Chemical Society, 1989), pp. 27–279.

14. J. Xie, J. Zhang, S. Li, F. Grote, X. Zhang, H. Zhang, R. Wang, Y. Lei, B. Pan, and Y. Xie, J. Am. Chem. Soc. **135**, 17881 (2013).

15. J. Mann, Q. Ma, P. M. Odenthal, M. Isarraraz, D. Le, E. Preciado, D. Barroso, K. Yamaguchi, G. von Son Palacio, A. Nguyen, T. Tran, M. Wurch, A. Nguyen, V. Klee, S. Bobek, D. Sun, T. F. Heinz, T. S. Rahman, R. Kawakami, and L. Bartels, Adv. Mater. **26**, 1399 (2014).

16. S. Shi, D. Gao, B. Xia, P. Liu, and D. Xue, J. Mater. Chem. A **3**, 24414 (2015).

17. Y. Guo, W. Zhang, H. Wu, J. Han, Y. Zhang, S. Lin, C. Liu, K. Xu, J. Qiao, W. Ji, Q. Chen, S. Gao, W. Zhang, X. Zhang, and Y. Chai, Sci. Adv. **4**, eaau6252 (2023).

18. J. H. Lee, W. S. Jang, S. W. Han, and H. K. Baik, Langmuir **30**, 9866 (2014).

19. S. Jayabal, G. Saranya, Y. Liu, D. Geng, and X. Meng, Sustain. Energy Fuels **3**, 2100 (2019).

20. M. Naguib, J. Halim, J. Lu, K. M. Cook, L. Hultman, Y. Gogotsi, and M. W. Barsoum, J.

Am. Chem. Soc. **135**, 15966 (2013).

21. J. Zhang, C. Zhang, Z. Wang, J. Zhu, Z. Wen, X. Zhao, X. Zhang, J. Xu, and Z. Lu, Small **14**, 1703098 (2018).

22. S. Zhang, J. Hao, H. Zhu, X. Jiang, X. Sang, G. Gao, H. Zhu, S. Lu, and M. Du, Appl. Surf. Sci. **527**, 146755 (2020).

23. Z. Luo, Y. Ouyang, H. Zhang, M. Xiao, J. Ge, Z. Jiang, J. Wang, D. Tang, X. Cao, C. Liu, and W. Xing, Nat. Commun. **9**, 1 (2018).

24. Z. Luo, Y. Ouyang, H. Zhang, M. Xiao, J. Ge, Z. Jiang, J. Wang, D. Tang, X. Cao, C. Liu, and W. Xing, Nat. Commun. **9**, 2120 (2018).

25. Z. Cui, R. Sa, W. Du, C. Xiao, Q. Li, and Z. Ma, Appl. Surf. Sci. **542**, 148535 (2021).

26. L. Li, Z. Qin, L. Ries, S. Hong, T. Michel, J. Yang, C. Salameh, M. Bechelany, P. Miele, D. Kaplan, M. Chhowalla, and D. Voiry, ACS Nano **13**, 6824 (2019).

27. H. Li, F. Xie, W. Li, B. D. Fahlman, M. Chen, and W. Li, RSC Adv. **6**, 105222 (2016).

28. R. Bose, M. Seo, C.-Y. Jung, and S. C. Yi, Electrochim. Acta **271**, 211 (2018).

29. L. Wu, X. Xu, Y. Zhao, K. Zhang, Y. Sun, T. Wang, Y. Wang, W. Zhong, and Y. Du, Appl. Surf. Sci. **425**, 470 (2017).

30. X. Kong, N. Wang, Q. Zhang, J. Liang, M. Wang, C. Wei, X. Chen, Y. Zhao, and X. Zhang, ChemistrySelect **3**, 9493 (2018).

31. Y. Shi, Y. Zhou, D.-R. Yang, W.-X. Xu, C. Wang, F.-B. Wang, J.-J. Xu, X.-H. Xia, and H.-Y. Chen, J. Am. Chem. Soc. **139**, 15479 (2017).

32. J. Rong, Y. Ye, J. Cao, X. Liu, H. Fan, S. Yang, M. Wei, L. Yang, J. Yang, and Y. Chen, Appl. Surf. Sci. **579**, 152216 (2022).

33. S. Bolar, S. Shit, J. S. Kumar, N. C. Murmu, R. S. Ganesh, H. Inokawa, and T. Kuila, Appl. Catal. B Environ. **254**, 432 (2019).

34. A. K. Singh, J. Prasad, U. P. Azad, A. K. Singh, R. Prakash, K. Singh, A. Srivastava, A. A. Alaferdov, and S. A. Moshkalev, RSC Adv. **9**, 22232 (2019).

35. M. Sarno, E. Ponticorvo, and D. Scarpa, Electrochem. Commun. **111**, 106647 (2020).

36. J. Mohammed-Ibrahim and H. Moussab, Mater. Sci. Energy Technol. **3**, 780 (2020).

37. J. Zhang, T. Wang, P. Liu, S. Liu, R. Dong, X. Zhuang, M. Chen, and X. Feng, Energy Environ. Sci. **9**, 2789 (2016).

38. Y. Kuang, M. J. Kenney, Y. Meng, W.-H. Hung, Y. Liu, J. E. Huang, R. Prasanna, P. Li, Y. Li, L. Wang, M.-C. Lin, M. D. McGehee, X. Sun, and H. Dai, Proc. Natl. Acad. Sci. **116**, 6624 (2019).

39. F. Yang, Y. Luo, Q. Yu, Z. Zhang, S. Zhang, Z. Liu, W. Ren, H.-M. Cheng, J. Li, and B. Liu, Adv. Funct. Mater. **31**, 2010367 (2021).

40. J. Li, M. Song, Y. Hu, C. Zhang, W. Liu, X. Huang, J. Zhang, Y. Zhu, J. Zhang, and D. Wang, Nano Res. **16**, 3658 (2023).

41. C. Bai, S. Wei, D. Deng, X. Lin, M. Zheng, and Q. Dong, J. Mater. Chem. A **5**, 9533 (2017).

CHAPTER 6
CONCLUSION & FUTURE SCOPE OF WORK

6.1 Conclusion

Hydrogen has been considered as an alternative of fossil fuels and it provides a great motivation for developing eco-friendly and sustainable energy resources. Electrochemical water splitting offers a promising and non-polluting route for H_2 generation from water using the renewable energy sources, but this technology is currently not viable for widespread due to utilization of expensive materials as electrodes during water splitting. Therefore, the development of efficient, cost-effective, stable and scalable electrode materials is required to boost the kinetics of water splitting. Hence, numerous materials for HER have been developed including precious-metal based catalysts, metal-free catalysts, metal oxides, and metal–nonmetals catalysts. Among the earth abundant materials, molybdenum sulfide (MoS_2) is interesting due to its near zero value of Gibb's free energy for hydrogen adsorption, excellent stability and scalability.

In this dissertation, various efforts like nanostructuring, heteroatom doping are done to make MoS_2 as an efficient, stable, and cost-effective electrocatalyst using simple and economic hydrothermal method and employed it for electrocatalytic hydrogen evolution and water splitting as well. The outcome of the appended chapters can be summarized as follows:

It has been found that basal planes of MoS_2 are catalytically inert whereas, its edges are active for HER application. Therefore, nanostructuring helps to increase the active sites density, resulting in higher HER activity. First part of chapter 3 presented the nanostructuring of MoS_2 using facile and economic single step hydrothermal synthesis and its utilization as electrocatalyst for HER application. Nanostructuring of MoS_2 helps to increase the formation of active edges, which helps to improve its HER activity. Presence of metallic phase (1T) of MoS_2 has been found by optimization of reducing agent concentration during single step hydrothermal synthesis of nanostructured MoS_2. The presence of metallic (1T) phase of MoS_2 along with 2H phase of MoS_2 was found more interesting for HER application. Nanostructured MoS_2 (MS-R4) exhibited 248 mV *vs. RHE* overpotential to achieve 10 $mA.cm^{-2}$ current density and 91 $mV.dec^{-1}$ Tafel slope (Table 6.1). This sample also displayed remarkable electrochemical stability up to 15 hours of continuous run and 1000 CV cycles with 46 μmol

of hydrogen evolution. The superior performance of nanostructured MoS_2 electrocatalyst towards HER than bulk MoS_2 is attributed to higher exposure of active sites in form of nanosheets and presence of metallic (1T) phase of MoS_2 along with 2H phase.

Table 6.1: Summarization of results obtained for nanostructured and heteroatom doped MoS_2 electrocatalysts for HER application.

S. No.	System	Method of synthesis	Phase	Electrocatalytic parameters		
				Overpotential (mV) @ 10 $mA.cm^{-2}$	**Tafel slope ($mV.dec^{-1}$)**	**Stability**
1	**MoS_2 (MS-R4)**	Single step hydrothermal method	1T/2H	248	91	1000 CV cycles, 15 hours at 10 mA/cm^2
2	***In-situ* deposited MoS_2 film (MS28)**	Single step hydrothermal method	1T/2H	132	55	15 hours at 10 $mA.cm^{-2}$
3	**Pd doped MoS_2(Pd-MS5)**	Single step hydrothermal method	1T/2H	89	56	1000 CV cycles
4	**V doped MoS_2 (V-MS24)**	Single step hydrothermal method	1T/2H	111	53	1000 CV cycles, 20 hours at 10 $mA.cm^{-2}$

Second part of chapter 3 included employment of *in-situ* deposited large area MoS_2 film over conducting substrate using single step hydrothermal method as HER cathode. The optimized *in-situ* deposited nanostructured MoS_2 film possessed 132 mV *vs. RHE* overpotential for 10 $mA.cm^{-2}$ cathodic current density with Tafel slope of 55 $mV.dec^{-1}$ (Table 6.1). This film also displays the electrochemical stability up to 15 hours. The enhanced electrocatalytic activity of MoS_2 films over nanostructured MoS_2 electrocatalystarises due to direct growth of

nanostructured MoS_2, tends to maximum exposure of vertically aligned active edges, presence of metallic (1T) phase along with semiconducting (2H) phase of MoS_2, support of metallic substrate, facilitates the charge transfer from electrolyte to the electrode surface and binder free deposition which reduces the series resistance.

To further enhance the electrocatalytic efficiency of MoS_2 towards HER application, synthesis of noble metal doping in MoS_2 using one step hydrothermal method has been attempted. Noble metal doping reduces the cost of electrocatalyst as well as make it efficient for HER. In this section we have successfully doped Pd into MoS_2 lattice within single step hydrothermal method. The nanostructured Pd-MoS_2 electrocatalyst required 89 mV *vs. RHE* overpotential to drive 10 $mA.cm^{-2}$ cathodic current density with Tafel slope of 56 $mV.dec^{-1}$ in acidic solution (Table 6.1). In case of alkaline and saline water, Pd-MoS_2 electrocatalyst exhibited 149 mV *vs. RHE* and 165 mV *vs. RHE* with Tafel slope of 72 $mV.dec^{-1}$ and 86 $mV.dec^{-1}$ respectively. The excellent performance of Pd-MoS_2 (Pd-MS5) over pristine MoS_2 is due to synergistic effect of amine intercalation as well as noble metal (Pd) doping in MoS_2 system which creates defects, induces disorder, expands inter layer and transform 2H phase of MoS_2 into 1T phase.

Substitutional doping of Vanadium (V) in MoS_2 lattice using single step hydrothermal method was also approached to make MoS_2 as an efficient and cost effective electrocatalyst. Substitutional doping of transition metal modifies the electronic structure of the host system and tunes the free energy for hydrogen adsorption. Nanostructured V-MoS_2 based electrode exhibited only 111 mV *vs. RHE* overpotential to drive 10 $mA.cm^{-2}$ cathodic current density with Tafel slope of 53 $mV.dec^{-1}$ in acidic solution (Table 6.1). In case of alkaline and saline water, V-MoS_2 electrode displayed 218 mV *vs. RHE* and 266 mV *vs. RHE* with Tafel slope of 117 $mV.dec^{-1}$ and 106 $mV.dec^{-1}$ *respectively*. The nanostructured V-MoS_2based electrode also displayed the excellent electrochemical stability with negligible loss in current density after 20 hours of continuous run and 1000 CV cycles. The improved HER performance of V-MoS_2 is attributed V^{+2}/V^{+4} which helps for phase transition from 2H to 1T of MoS_2, few layered formations with expanded interlayers, induces defects, sulfur vacancies in MoS_2 lattice.

During electrochemical water splitting, nanostructured MoS_2 based cathode requires +2.20 V in acidic solution, +2.31 V in alkaline water and +2.42 V in saline water to achieve 10 $mA.cm^{-2}$ current density in electrolytic cell. This nanostructured MoS_2 cathodeshowed the hydrogen evolution of 350 μmols in acidic water, 155 μmols in alkaline water and 149 μmols

in saline water at +2.2 V of cell potential. Further, cathodic nanostructured Pd-MoS_2 electrode requires +1.98 V in acidic solution, +2.03 V in alkaline water and +2.18 V in saline water to drive 10 $mA.cm^{-2}$ current during water splitting. Nanostructured Pd-MoS_2 cathodic electrode showed the hydrogen evolution of 740 μmols in acidic water, 622 μmols in alkaline water and 403 μmols in saline water at +2.2 V of cell potential. Whereas, nanostructured V-MoS_2 based cathode requires +2.08 V in acidic solution, +2.12 V in alkaline water and +2.23 V in saline water. V-MoS_2 cathode showed the hydrogen evolution of 390 μmols in acidic water, 339 μmols in alkaline water and 275 μmols in saline water at +2.2 V of cell potential. The utilization of these nanostructured and heteroatom doped MoS_2 as HER electrocatalysts for electrocatalytic water splitting in acidic, alkaline, and saline water gives a new direction to MoS_2 and based electrocatalysts as a potential alternative to noble metal and based electrocatalysts for HER application.

In the conclusion, the research findings and the as-synthesized advanced electrocatalysts that are presented in this thesis can significantly boost and advance the practical exploitation of the water-splitting process.

6.2 Future Scope of Work

1. There is a good scope to extend the work with non-metal as well as metal/non-metal doping in MoS_2 using hydrothermal method and its utilization as electrocatalyst for HER application.
2. Synthesis of MoS_2 based nanocomposites and its electrocatalytic properties investigation for HER application can be done.
3. Synthesized nanostructured MoS_2 and doped MoS_2 can be optimized for Oxygen Evolution Reaction (OER) application in future studies.
4. The present study has utilized synthesized MoS_2 and based electrocatalyst has been utilized as HER cathode for water splitting. The future study can undertake synthesized MoS_2 and based electrocatalyst as bifunctional electrocatalyst during water splitting procedure.

A. List of Publications from the Current Research Work

1. ***Jyoti Gupta***, Dibakar Das, Pramod H. Borse, "Nanosheets Decorated MoS_2 Micro Balls: Effect of 1T/2H Composition", Chemistry Select 2020, 5, 11764– 11768, Impact Factor: 2.30.

2. ***Jyoti Gupta***, Dibakar Das, Anirudha Karati, Joydip Joardar, Pramod H. Borse, "Nanostructure MoS_2 electrocatalyst modified large area carbon electrode for efficient hydrogen evolution", Physica Scripta 97 (2022) 095003 Impact Factor: 3.08.

3. ***Jyoti Gupta***, Dibakar Das, Pramod H. Borse, B. V. Sarada, "In-situ Pd doped MoS_2 nanosheets as HER electrocatalyst for enhanced electrocatalytic water splitting", (*Manuscript is ready for submission*).

4. ***Jyoti Gupta***, Dibakar Das, Pramod H. Borse, B. V. Sarada, "Single step synthesized V-doped few layered MoS_2 nanosheets as an efficient HER cathode for electrocatalytic saline water splitting" (*Manuscript is ready for submission*).

5. Alka Pareek, Rekha Dom, ***Jyoti Gupta***, Jyothi Chandran, Vivek Adepu, Pramod H. Borse, "Insights into renewable hydrogen energy: Recent advances and prospects," Materials Science for Energy Technologies 3 (2020) 319–327, Impact Factor: 7.63.

B. Conference Presentation

1. Poster presentation on "**Nanosheets decorated spherical MoS_2 electrocatalyst for water splitting application"**, ***Jyoti Gupta***, Dibakar Das, Pramod H. Borse, ACS publications symposium: The Power of Chemical Transformations (Virtual event) held on 20th-21st May, 2021.

2. Oral presentation on "**Noble metal doped MoS_2 electrocatalyst: A comparative study for hydrogen evolution reaction**", ***Jyoti Gupta***, Dibakar Das, Pramod H. Borse, International Conference of Condensed Matter and Device Physics (ICCMDP)-2021 held on 9^{th} Sept – 11^{th} Sept, 2021.

3. Poster presentation on "**Heteroatom doping of V into MoS_2 for efficient Hydrogen Evolution Reaction**", ***Jyoti Gupta***, Dibakar Das, B. V. Sarada, International conference on H_2 & CO_2 (virtual event) held on 17^{th} – 19^{th} November, 2022.

Awards

1. Received **10,000 Rs.** cash prize under scheme of ***IOE publication Incentives Award, University of Hyderabad*** for the publication "***Jyoti Gupta*****, Dibakar Das, Pramod H. Borse, "Nanosheets Decorated MoS_2 Micro Balls: Effect of 1T/2H Composition", Chemistry Select 2020, 5, 11764– 11768**."

C. Reprints

Paper I

Nanosheets Decorated MoS_2 Micro Balls: Effect of 1T/2H Composition

Jyoti Gupta, Dibakar Das, and Pramod H. Borse

ChemistrySelect, 2020, *5*, 11764– 11768,

DOI: 10.1002/slct.202003351

Catalysis

Nanosheets Decorated MoS_2 Micro Balls: Effect of 1T/2H Composition

Jyoti Gupta,[a, b] Dibakar Das,[b] and Pramod H. Borse*[a]

Nanosheets Decorated Micro Balls (NDMB) of MoS_2 have been synthesized using hydrothermal technique for their utilization in electrocatalytic hydrogen generation. A synergetic effect of 2H and 1T phase in NDMB was found to yield efficient hydrogen evolution reaction (*HER*) for splitting water molecules. NDMB electrode, fabricated by immobilization over transparent conductive substrate yielded lowest tafel slope of 40 mV/dec with smallest onset potential of 90 mV *vs.* RHE. Superior performance of NDMB for hydrogen evolution reaction can be attributed to synergy of 1T/2H composition and high electrochemical surface area of 170 cm^2 as compared to the bulk MoS_2.

Reverse reaction of water splitting yields usable energy and water as by-product, which is harmless to earth's environment.[1–3] Among various water-splitting techniques, electro-catalytic hydrogen generation *i.e.* hydrogen evolution reaction (HER) is considered to be one of the most efficient alternative ways to produce clean hydrogen energy.[4] Platinum and platinum-based materials having zero Gibb's free energy for hydrogen adsorption; mechanical and chemical stability while possessing lowest tafel slope and over potential; are known to be conventionally best electrocatalysts for HER application. However, as platinum is one of an expensive rare earth metal, it limits the lower economy for HER based technology.[5,6] Thus, it is highly desirable to discover a potential alternative for the platinum-based electro catalyst suited for HER application. Transition metal dichalcogenides (TMDs) are evolving as efficient electro catalysts/photo electro catalysts, *especially*, MoS_2 system is foreseen as a potential alternative to replace Pt, due to its low cost, nontoxicity & its abundance in nature. Theoretically, MoS_2 is predicted to be a highly active electro catalyst in view of its low Gibb's free energy for hydrogen adsorption (0.08 eV) which is closer to that of platinum.[7,8] Thus, we have chosen MoS_2 system in present study.

In spite of potential significance of the TMDs, MoS_2 has not replaced Pt metal-electrocatalyst, this is because of its poor electrical conductivity ($10^{-4}\ \Omega^{-1}\,cm^{-1}$),[9,10] and due to the inertness (*catalytically active site density*) of the basal plane (*say* 2H MoS_2 phase). In order to overcome this challenge, several strategies have been reported in literature.[11,12] *Accordingly*, for designing an efficient electrocatalyst following category can be stated. (1) Nanostructuring of MoS_2; (2) Anionic or cationic doping of MoS_2; (3) Phase transformation of semiconducting (*2H MoS_2*) to metallic (*1T MoS_2*) phase; and (4) Syntheses of composites. These approaches have been recently reported in search of identifying efficient MoS_2 electrocatalyst.[13–17] *Apart* from these strategies there have been interesting reports on the syntheses of efficient nanostructured MoS_2 (*nanosheets, nanoflower, nanosphere*) electrocatalyst by using various methods as -gas-vapor reaction, laser ablation, thermal decomposition, magnetron sputtering, sonochemical synthesis.[18,19] *However*, there is tremendous interest in synthesizing two-dimensional (2D) 1T phase MoS_2 for HER application as it is expected to exhibit *high active site density* as well as exhibit a metallic nature. On the other hand, 2H phase MoS_2 has been known to show moderate electrocatalytic activity for HER. This indicates that the phase evolution of hexagonal (2H) crystal structure to tetragonal (1T) crystal structure modulates the electronic band structure making transforming its *semiconducting nature* to *metallic type*. This fact can be exploited to design new, stable and efficient electrocatalyst of 2D – MoS_2.[20]

In past, Krishan *et. al.* reported 1T phase (*thermodynamically unstable*) is preferred over 2H phase of MoS_2, as *edge* as well as *basal* plane sites are catalytically active. It is possible to transform 2H to 1T phase by Lithium intercalation, however it is found to be an expensive option as it involves less abundant Lithium (Li) metal. *Furthermore*, it is known to transform to Li_2S, as an impurity[21] with usage. Similarly, Liu *et. al.*[22] reported the formation of 1T-2H MoS_2 vertical nanosheets array configuration. It showed high efficiency of hydrogen evolution as indicated by the lower tafel slope of 35 mV/dec. In another report, Xie *et. al.* reported the formation of highly efficient oxygen incorporated 2H-MoS_2 nanosheet for HER application. It exhibited a lower tafel slope of 55 mV/dec.[23] Wang *et. al.*[24] reported synthesis of nanoflower of 2H-MoS_2 those displayed a tafel slope of 52 mV/dec.

It is important to note that synthesis of efficient undoped MoS_2 remains a challenge which can be attempted via. control on the chemical synthesis parameter optimization.[25,26,27,28] In

[a] *J. Gupta, Dr. P. H. Borse*
Centre for Nanomaterials
International Advanced research centre for Powder Metallurgy and New Materials
Balapur, Hyderabad-500005, Telangana, India
E-mail: phborse@arci.res.in
[b] *J. Gupta, Prof. Dr. D. Das*
School for Engineering Science and Technology
University of Hyderabad
Gachibowli, Hyderabad-500046, Telangana India

Supporting information for this article is available on the WWW under https://doi.org/10.1002/slct.202003351

one analogous report, Tang *et. al.*[29] reported hydrothermal synthesis of MoS_2 by exploitation of reducing agent. We have utilized fact to discover an efficient undoped MoS_2 electrocatalyst.

In present study, we have nanostructured MoS_2 to achieve it in the form of Nanosheets Decorated Micro Balls (NDMB) *via.* hydrothermal methodology, and utilize them for HER application (*see Figure SI 1*). The modified NDMBs were found to yield lowest tafel slope of 40 mV/dec, which is among one of the lowest values.

We have achieved highly efficient MoS_2 that displays synergetic composition of 1T/2H phase. An in-depth detailed study would be published elsewhere. This work can give a new direction for the development of efficient electrocatalysts, in a very eco-friendly and economic way.

Figure 1 shows the results of electrochemical and morphological characterization of Nano and bulk MoS_2. Figure 1a presents the polarization curves for NDMB-R and NDMB *along with* BMS (bulk MoS_2). NDMB-R shows an onset potential shifted to lowest value (90 mV *vs* RHE), as compared to the other two samples of NDMB (270 mV *vs* RHE) and BMS (510 mV *vs* RHE). In line with the polarization studies, the Tafel curve also demonstrates that NDMB-R exhibits a lowest Tafel slope of 40 mV/dec, as compared to NDMB (85 mV/dec) and BMS (178 mV/dec), Figure 1b. Further, electrochemical impedance spectroscopic (EIS) studies indicate that, all the samples show similar behavior of *semicircle with a straight line of specific slope*, as seen in Figure 1c for NDMB samples. The noted distinguishing feature is the smaller diameter (5 Ω) of NDMB samples, in contrast to very large diameter (6301 Ω) for the case of BMS sample (*See Figure SI 6)*. The results are tabulated in the Table 1. An in-depth analysis of *Nyquist plots* can be fitted to Randell's circuit (Figure 1c inset) where the NDMB-R exhibits lowest R_{CT} value thus validating that it yields high efficiency electrocatalyst for HER reaction. This clearly demonstrates that in present study, NDMB-R acts as a superior and efficient HER electrocatalyst.

Figure 1(d and e) shows the typical morphology of nanostructured MoS_2 samples displaying their nanosheets decorated micro balls (NDMB) configuration. Figure 1(f) shows the morphology of bulk MoS_2 for the sake of comparison. In Figure 1 (d and e) magnified view of samples is provided in *respective* figure, both samples NDMB & NDMB-R exhibit beautifully nanosheets decorated micro balls of MoS_2. Typical micro balls diameter of 4 μm (NDMB-R) & 6 μm (NDMB) can be observed in case of Figure 1(d & e). Further in given field of view (as shown in *respective* inset), the number of nanosheets per unit surface area of micro balls is very high in NDMB-R as compared to NDMB, indicating the size of sheet dimension is very small in NDMB-R. It can be noted in Figure 1(f) that bulk MoS_2 shows several constituents of nearly hexagonal shaped stacked layers.

A further insight of the morphology is shown in HRTEM images (TEM images *inset*) of Figure 2 (a & c) for NDMB-R and NDMB *respectively*. Corresponding SAED image is shown in Figure 2(b & d). Nanosheets structure of both samples is evident from HRTEM image of Figure 2 (a & c). In both the cases, the lattice fringes displaying the d-spacing value of 0.63 nm which is comparable to 2H/1T phase of MoS_2 along $d_{(002)}$.[30] It can be noted that SAED analysis does show the existence of 2H phase MoS_2 in NDMB-R and NDMB as seen in Figure 2(b & d). Figure 2 (e) compares the XRD spectra of NDMB-R, NDMB & BMS. Preliminary analysis indicates the existence of 2H MoS_2 in NDMB-R & NDMB which is correlatable to XRD spectrum of BMS. An *in-depth* analysis of the ratio of $I_{(002)}$ to $I_{(100)}$ indicates an existence of 2D structure of MoS_2. This result is correlatable with high-resolution TEM studies. XRD spectrum of NDMB-R indicates a possible existence of minor fraction of 1T phase MoS_2. This can be distinctly noticed by peculiar feature of (100) & (013) peaks in NDMB-R & NDMB. In order to ascertain existence of 1T phase in 2H dominated NDMB-R sample, a detailed study was carried out using Raman and X-Ray photoelectron spectroscopy (*See supplementary information- Figure SI 4*-Raman *spectra & Figure SI 5- XPS region scan of nano MoS_2 samples)*. The Raman analysis confirms an existence of fraction of 1T phase in NDMB-R in line with above discussions. It may be further added that XPS, being surface sensitive technique displays possibly a higher ratio $Conc_{1T}$/$Conc_{2H}$ phase. Nonetheless, it does validate an existence of 1T in NDMB-R, as found from our investigations. As shown in Table 1, NDMB-R shows very interesting values of tafel slope & *onset* potential indicating that NDMB-R is potential efficient electrocatalyst for HER. It shows a surprisingly lowest Tafel slope of 40 mV/dec. It is thus necessary to understand the

Table 1. Results of electrochemical characterization of different nanosheets prepared in present study as well as reported studies.

Sample name	Overpotential (V *vs.* RHE) @ 10 mA/cm^2	Tafel Slope (mV/dec)	Onset Potential (V *vs.* RHE)	R_{CT}	Ref.
Pt/C	0.05 @ 8.2 mA/cm^2	31	NR[a]	–	[32]
1T -MoS_2 (Cracked)	0.156	42.7	−0.11	NR[a]	[33]
MoS_2 (1T-2H)	0.13	35	−0.09	–	[31]
MoS_2 (2H: Nanoflower assembled with lamellar nanosheets)	0.30@ 13.80 mA/cm^2	52	−0.13	–	[34]
MoS_2 (2H: nanosheets)	0.30@ 126.50 mA/cm^2	55	NR[a]	–	[23]
Hydrazine treated MoS_2/MoO_3 nanowires (2H)	0.40@ 22.00 mA/cm^2	50	~0.10	–	[35]
NDMB-R	0.42	40	−0.09	5	This work
NDMB	0.61	85	−0.27	50	
BMS	0.67@ 5 mA/cm^2	178	−0.57	6301	

[a] Not reported.

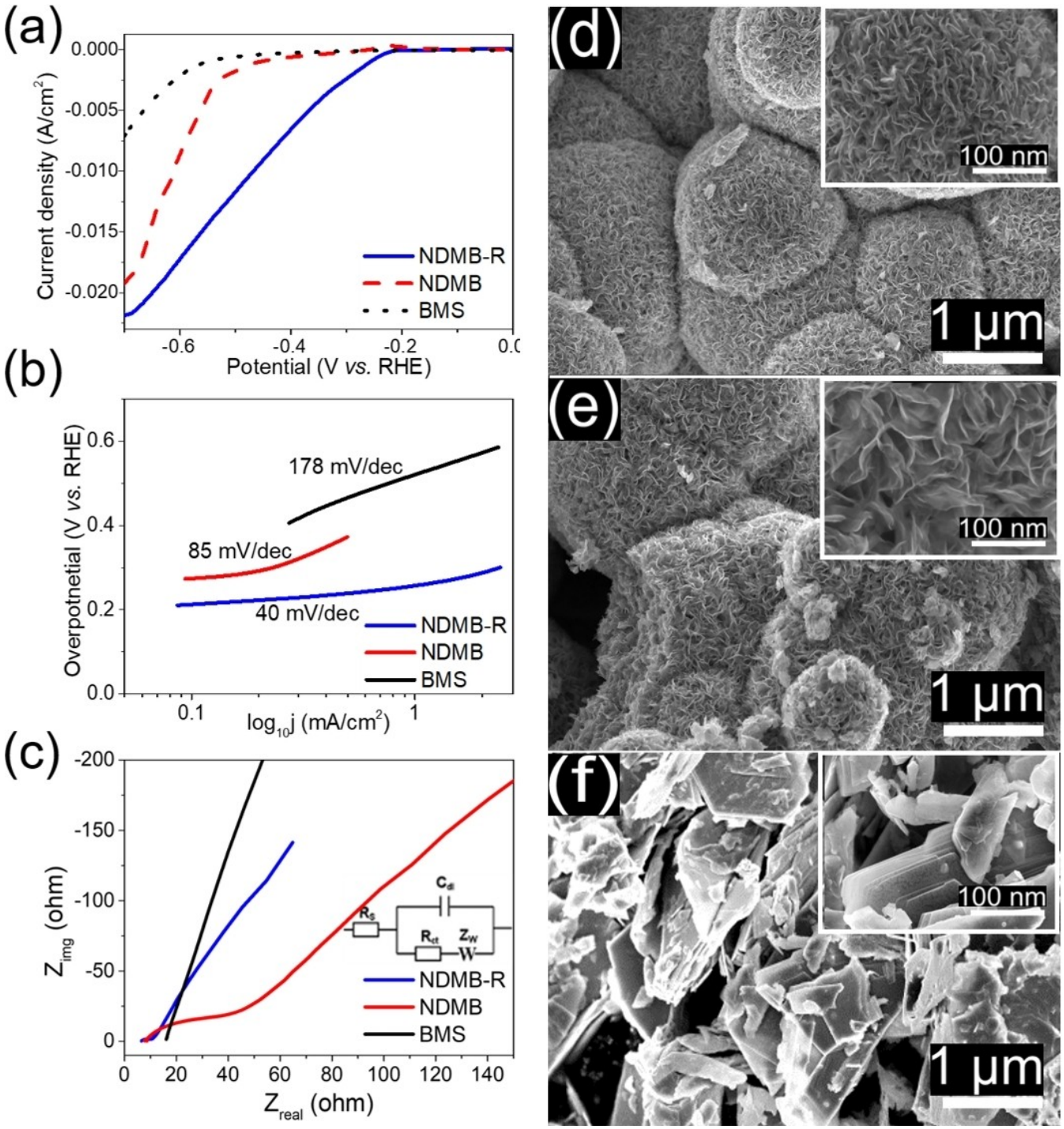

Figure 1. Electro-catalytic and morphological characterization of NDMB - (a) Polarization, (b) Tafel and (c) EIS curves of *respective* samples; FESEM images of (d) NDMB-R; (e) NDMB, (f) BMS samples.

superiority of NDMB-R based on present studies. It may be recalled that, Jayabal *et al*[31] has shown that a tuning of ratio of 1T/2H phase of MoS_2 in electrocatalyst yeilded them an efficient HER electrocatalyst. *Analogously*, in present studies we do have contribution of 1T phase as one reason for improved HER performance. It indicates that the synergetic effect of 1T/2H phase plays a crucial role in present study.

In addition, it can be added that resulting nanostructure of electrocatalyst under study probably renders an improved HER activity. However, it may not be limited to structural phase composition, but it can be correlated to other possibilities *viz.* electrical properties, physical surface area and electrochemical surface area of electrocatalyst. Accordingly, electrocatalyst size *i.e.* its physical surface area is another factor that affects HER

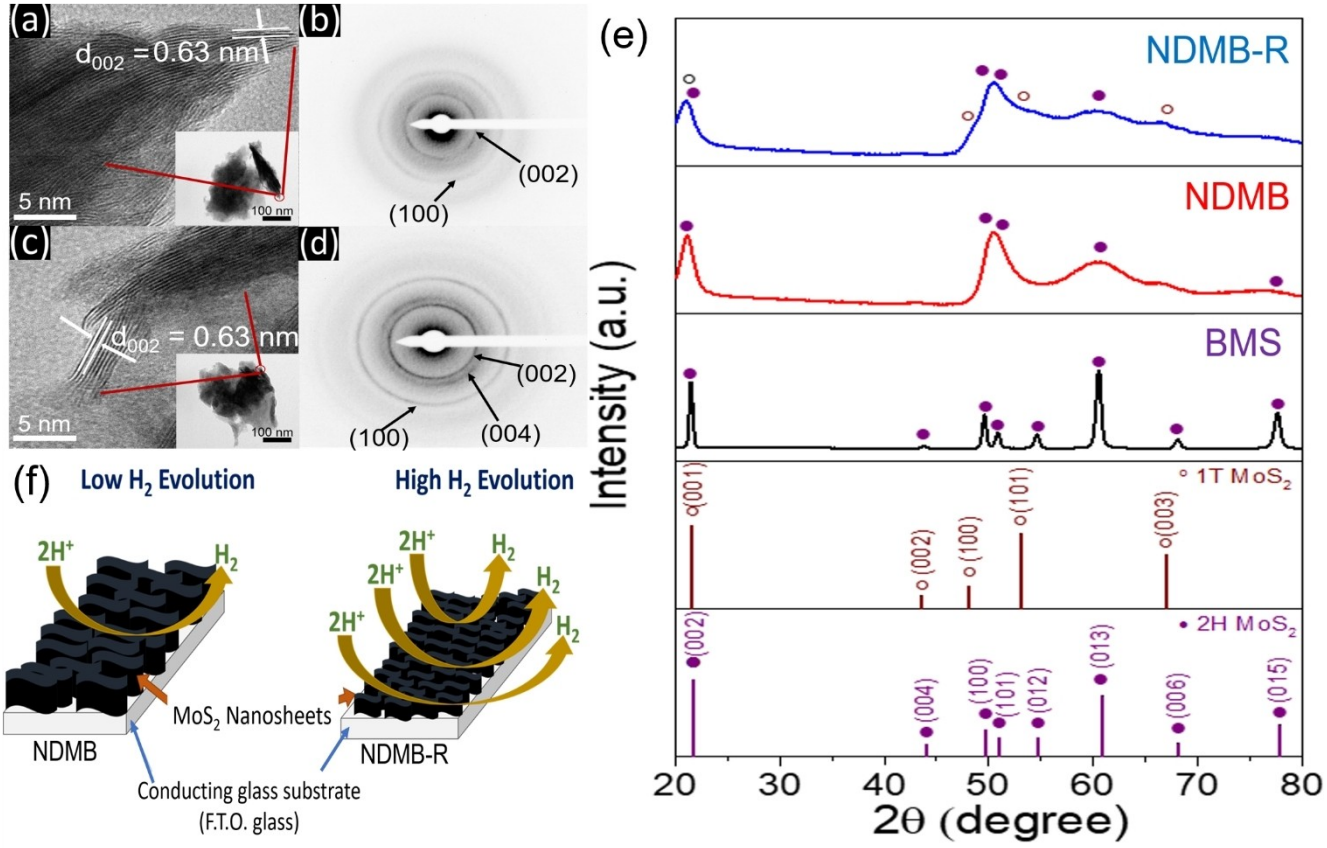

Figure 2. HRTEM images along with the respective TEM images (inset) (a & c) showing their respective SAED patterns (b & d) for synthesized MoS_2 nanoflower NDMB-R (a & b) with & NDMB (c & d) without reducing agent respectively and (e) shows XRD pattern for sample NDMB-R, NDMB and BMS and (f) shows the schematic for hydrogen evolution.

efficiency. It can be noted from Figure 1 (*d & e*), that smaller sized NDMB-R (4 μm) behaves more efficiently than NDMB (6 μm). This can be clearly understood from the schematic representation of the occurrence of efficient HER reaction in NDMB-R than in NDMB in Figure 2 (f).

As, electrolysis relies on the charge transport in an electrolyte, and at the electrocatalyst/electrolyte interface, electrochemically active surface area (ECSA) is a crucial parameter that can affect the HER performance. Accordingly, a thorough ECSA measurement was carried out (*See Figure SI 7 and SI section of estimation of ESCA of electrode*) and estimated values are presented in Table 2. Interestingly, NDMB-R showed highest active site density with one order higher value than NDMB and bulk counterpart.

Table 2. Flat band potential, Capacitance of double layer, electrochemically active surface area (ECSA) and Density of active sites of synthesized nano MoS_2 and commercial bulk MoS_2 ((Figure SI7, Procedure in SI section – estimation of ESCA for electrode.)).

Sample Name	ECSA (cm^2)	Density of Active Site (mol)
NDMB-R	170.0	20.7×10^{-10}
NDMB	56.2	3.1×10^{-10}
BMS	2.7	4.1×10^{-10}

This is *in line* with the estimated trend in variation of ECSA and active site density in electrocatalysts under present study. As seen in Table 2, NDMB-R shows highest ESCA value of 170 cm^2_{ECSA}, which is 3 times of NDMB and 7 times of BMS.

The overall analyses demonstrate that NDMB-R is best and efficient electrocatalyst than other sample under study. Above discussion also validates that physico-chemical properties of NDMB-R are in accordance with the electrical property as indicated by lowest R_{CT} value of 5 Ω. Therefore, the film deposited using NDMB-R shows more efficient HER performance as compared to NDMB.

This work demonstrates the synthesis of an efficient 1T/2H phase 2D MoS_2. It shows competitively lowest Tafel slope (40 mV/dec) and correspondingly lower over-potential value that is desirable for efficient HER electrocatalyst. We synthesized an excellent performance electrocatalyst for HER application. This communication provides a simple methodology for synthesis of 2D MoS_2 electrocatalyst. The role of reducing agent in synthesis has a prime importance to achieve present HER electrocatalyst.

Supporting Information summary

Detailed experimental procedure, elemental proof, spectra and estimation of ECSA of electrode for samples can be found in supporting information.

Acknowledgements

The authors wish to thank Dr. J. Joardar, Dr. N. Hebalkar, Dr. B.V. Sarada and Mr. A. Harish Kumar, for their support towards film characterization. Permission granted by Director, ARCI to publish the work is gratefully acknowledge.

Conflict of Interest

The authors declare no conflict of interest.

Keywords: Molybdenum disulphide · Electrocatalyst · Hydrogen Evolution Reaction · Nanomaterials

[1] J. Theerthagiri, M. Ashokkumar, *J. Solid State Chem.* **2017**, *252*, 43–71.
[2] A. A. Gewirth, M. S. Thorum, *Inorg. Chem.* **2010**, *49(8)*, 3557–3566.
[3] D. M. Andoshe, H. W. Jang, *J. Mater. Chem. A* **2016**, *4(24)*, 9477–9485.
[4] K. Ayers, M. Bornstein, *Annu. Rev. Chem. Biomol. Eng.* **2019**, *10*, 219–239.
[5] S. Akbar, A. M. Squires, *Mater. Sci. Technol. (United Kingdom)* **2019**, *35(1)*, 1–11.
[6] C. C. L. McCrory, T. F. Jaramillo, *J. Am. Chem. Soc.* **2015**, *137(13)*, 4347–57.
[7] B. Hinnemann, J. K. Nørskov, *J. Am. Chem. Soc.* **2005**, *127(15)*, 5308–5309.
[8] F. Wang, J. He, *Nanotechnology* **2015**, *26(29)*, 292001.
[9] R. R. Chianelli, R. Kershaw, *J. Catal.* **1985**, *92(1)*, 56–63.
[10] O. E. Beqqali, G. G. Gamoudi, *Synth. Met.* **1997**, *90*, 165–172.
[11] C. Wang, X. Deng, *Front. Chem.* **2019**, *7*, 1–9.
[12] Y. Yan, X. Wang, *ACS Catal.* **2014**, *4(6)*, 1693–1705.
[13] P. D. Tran, V. Artero, *Nat. Mater.* **2016**, *15(6)*, 640–646.
[14] M. Wang, J. Yang, *ACS Appl. Mater. Interfaces* **2013**, *5(3)*, 1003–1008.
[15] W. Jaegermann, H. Tributsch, *Prog. Surf. Sci.* **1988**, *29(1)*, 1–167.
[16] E. G. S. Firmiano, E. R. Leite, *Chem. Commun.* **2012**, *48(62)*, 7687–7689.
[17] A. B. Laursen, I. Chorkendorff, *Energy Environ. Sci.* **2012**, *5(2)*, 5577–5591.
[18] J. Kibsgaard, T. F. Jaramillo, *Nat. Mater.* **2012**, *11(11)*, 963–969.
[19] A. E. Russell, *Preface. Faraday Discuss.* **2009**, *140(0)*, 9–10.
[20] D. Voiry, M. Chhowalla, *Nano Lett.* **2013**, *13(12)*, 6222–6227.
[21] U. Krishnan, A. Kumar, *Superlattices Microstruct.* **2019**, *128*, 274–297.
[22] Z. Liu, S. Miao, *Appl. Catal. B* **2019**, *24*, 296–302.
[23] J. Xie, Y. Xie, *J. Am. Chem. Soc.* **2013**, *135(47)*, 17881–17888.
[24] X. Wang, J. Li, *J. Alloys Compd.* **2014**, *600*, 84–90.
[25] M. Debbarma, M. Saha, *Adv. Manuf.* **2013**, *1*, 183–186.
[26] Z. P. Cheng, J. Z. Yin, *Rare Met.* **2017**, *36 (10)*, 799–805.
[27] K. Winkler, M. Fialkowski, *Plasmonics* **2011**, *6(4)*, 697–704.
[28] Z. Miao, Q. Sui, *J. Hazard. Mater.* **2015**, *300*, 530–537.
[29] G. Tang, H. Tang, *Mater. Lett.* **2012**, *86*, 9–12.
[30] W. Ren, C. Cheng, *Electrochim. Acta* **2017**, *241*, 316–322.
[31] S. Jayabal, X. Meng, *J. Mater. Chem. A* **2017**, *5*, 24540–24563.
[32] N. Cheng, X. Sun, *Nat. Commun.* **2016**, *7*, 1–9.
[33] Y. Li, Y. Liu, *Catal. Sci. Technol.* **2017**, *7(3)*, 718–724.
[34] D. Wang, Z. Liu, *J. Power Sources* **2014**, *264*, 229–234.
[35] D. R. Cummins, G. Gupta, *Nat. Commun.* **2016**, *7*, 1–10.

Submitted: August 24, 2020
Accepted: September 25, 2020

Paper II

Nanostructure MoS_2 electrocatalyst modified large area carbon electrode for efficient hydrogen evolution

Jyoti Gupta, Dibakar Das, Anirudha Karati, Joydip Joardar and Pramod H. Borse

Physica Scripta 2022, 97, 095003

DOI: 10.1088/1402-4896/ac8648

PAPER

Nanostructure MoS_2 electrocatalyst modified large area carbon electrode for efficient hydrogen evolution

Physica Scripta

PAPER

Nanostructure MoS_2 electrocatalyst modified large area carbon electrode for efficient hydrogen evolution

Jyoti Gupta[1,2], **Dibakar Das**[2], **Anirudha Karati**[1], **Joydip Joardar**[1] **and Pramod H Borse**[1,*]

[1] International Advanced Research Centre for Powder Metallurgy and New Materials, Balapur PO, Hyderabad-500005, TS, India
[2] School of Engineering Science and Technology, Hyderabad Central University, Gachibowli, Hyderabad-500046, TS, India
[*] Author to whom any correspondence should be addressed.

E-mail: phborse@arci.res.in **and** gupta.jyoti952@gmail.com

Keywords: electrocatalyst, hydrogen evolution reaction, large area electrode, graphite, molybdenum disulfides

Supplementary material for this article is available online

RECEIVED
15 May 2022

REVISED
15 July 2022

ACCEPTED FOR PUBLICATION
1 August 2022

PUBLISHED
12 August 2022

Abstract

Hydrothermally synthesized nanostructured MoS_2 was immobilized over large area graphite paper ($5 \times 5\ mm^2$) to fabricate electrode for hydrogen evolution application. The chemical optimization via. variation in hydroxylamine hydrochloride(HAH) concentration, led to nanosheets containing surface over the micro-balls, with a 1T and 2H phase of MoS_2. A physicochemical and electrochemical characterization yielded a lowest Tafel slope of ~67 mV dec^{-1}, a lowest over potential of 0.19 V with a significant electrocatalytic stability in acidic. An electrocatalytic hydrogen evolution over optimized MoS_2 evolved 2 times (~46 μmol h^{-1}) of hydrogen gas as compared to that from MoS_2 synthesized without HAH. The improved performance of electrocatalyst can be attributed to the combination of phase, and electrochemical properties 2D structure of MoS_2.

1. Introduction

Depletion of non—renewable fossil fuel resources on earth due to increasing human population has necessitated exploration of renewable energy alternatives [1]. *Accordingly*, it is important to discover a *pollution-free* and an economic option to generate energy. It is known that hydrogen can be generated by water via. well-known water splitting reaction ($2H_2O \rightarrow 2H_2 + O_2$). Among various water splitting techniques, electro-catalytic hydrogen generation *i.e.* hydrogen evolution reaction (HER) is considered to be one of the most efficient alternative ways to produce clean hydrogen energy [2]. For conventional HER electro-catalysis, a rare metal *i.e.* platinum is used due to its low-over potential. It exhibits zero Gibbs' free energy for hydrogen adsorption and, thus is an ideal electrocatalyst with lowest Tafel slope (30 mV dec^{-1}). However, usage of high cost platinum for HER application [3, 4] hinders its commercial feasibility. Therefore, it is necessary to discover an alternate material to replace platinum, hence there have been tremendous research on several carbides, sulfide, nitrides and MAXenes [5–10].

2-dimensional (2D) MoS_2 shows a huge potential as electrocatalyst, with a low cost, non-toxicity and abundance in nature [11–14]. It can be noted that b***ulk*** form of the naturally occurring 2H-MoS_2 is not an effective electrocatalyst due to its poor electrical conductivity ($10^{-4}\ \Omega^{-1}cm^{-1}$), This is total contrast to **2-*dimensional*** MoS_2, which is expected to exhibit an improved HER performance [15–27]. Defect engineering is one of the important strategies known for efficiency improvement of these electro-catalysts [15, 26, 28]. Especially, the synergy of defects plays a crucial role to achieve an efficient electrocatalyst. *Accordingly*, defect engineering via. synthesis of metallic 1T phase 2D MoS_2 is highly desirable for the HER application, as it exhibits high population of active catalytic sites [21] over the 1T lattice. Material engineering of the single 1T phase is a big challenge, *though recently* defect induction of MoS_2 lattice in the form of vacancy, dopant etc has been attempted. Lithium intercalation in the 2H phase of MoS_2 has been exploited to achieve 1T phase of MoS_2 [19]. However, such lithium intercalation technique leads to an unwanted impurity of Li_2S [20]. *Interestingly*, a suited phase composition of 1T and 2H of MoS_2 is known to affect the electronic properties and thus yield an efficient

electrocatalyst. Likewise, Liu *et al* reported the hydrothermal synthesis of 1T/2H-MoS_2 nanosheet photocatalyst that showed improved performance as compared to 2H phase MoS_2 [22]. Zhang *et al.* reported the formation of hybrid phase 1T/2H MoS_2 with controllable 1T concentration by optimizing the concentration of dimethylformamide (DMF) [23]. Yao *et al.* reported synthesis of 1T@2H MoS_2 for efficient hydrogen evolution application to obtain electrocatalyst with onset potential 180 mV versus RHE onset potential and a Tafel slope of 88 mV dec^{-1} [21]. *Similarly*, Wang *et al.* reported an *in situ* hydrothermal formation of 1T/2H-MoS_2 phased *hierarchical* nano-rods, those exhibited an excellent HER catalytic performance with *over-potential* of 156 mV @10 mA cm^{-2} and Tafel slope of 47.9 mV dec^{-1} [24]. There are several reports of formation of 1T/2H nano MoS_2, by controlling the chemical parameters, as—precursor, *p*H, reaction time and temperature [29], reducing agent (*sodium borohydride, hydrazine hydrate, urea*) [30] *etc Accordingly*, Geng *et al* [31] reported the use of urea and hydrazine as reducing agents for syntheses of MoS_2. Some reports exist on the use of hydroxylamine hydrochloride as reducing agent for the synthesis of single layer reduced graphene oxide and nano-flower 2D MoS_2. In order to have a commercial applicability of efficient MoS_2, its immobilization over a 'economic and stable base electrode as graphite' is very important. Such work would enhance the scope of economic and sustainable hydrogen generation in future.

In the present work, an efficient 2D MoS_2 electrocatalyst was prepared by using simple hydrothermal methodology. The chemical parameter optimization, immobilization of the synergistic electrocatalyst *over* economic graphite paper (large area 5 × 5 mm^2), and the real time hydrogen evolution has been demonstrated.

Further, the salient feature in this work is an *in-depth* analysis of these synergetic electro catalysts using high resolution '*micro-XRD*' and Raman techniques to characterize the existence of the crucial metallic 1T phase in major 2H phase in MoS_2.

2. Experiment

2.1. Materials

Ammonium molybdate tetrahydrate (Fisher scientific; 99%), Thiourea (Fisher scientific; 99.5%), Hydroxylamine hydrochloride (Fisher scientific; 99%), Sodium hydroxide (Fisher scientific; 98%), Molybdenum disulfide (commercial grade), PVDF (*Polyvinylidene fluoride*) in an organic solvent (NMP- *N-Methyl-2-pyrrolidone*). All the chemicals were used directly without any purification.

2.2. Synthesis of Nano MoS_2

To synthesize nanostructured MoS_2, following procedure of hydrothermal synthesis has been adopted; inclusion of reducing agent was decided at appropriate stage. *T*he aqueous solutions of Mo and S precursors was prepared by using deionized water solvent (*resistivity:* 18 MΩ—cm). A 4*m*M aqueous solution of ammonium molybdate tetrahydrate, and 36 mM thiourea were mixed thoroughly. The mixture *p*H was adjusted to the *p*H value of 6, by using 1 M of sodium hydroxide. Next, the mixture was transferred to the hydrothermal reactor. The variation in the parameters *viz.* reaction time (10–36 h) and reaction temperature (140 °C–200 °C) was carried out; at preliminary stage (*See* figures SI1, SI2 (available online at stacks.iop.org/PS/97/095003/mmedia); *FESEM images, and XRD pattern of synthesized* MoS_2 w.r.t. *time variation, figure SI3; Digital images of the immobilized (a) bulk* MoS_2 *and (b) nano* MoS_2.). According to the optimization, we have used specific reaction time of 24 h and reaction temperature of 180 °C throughout; to achieve an efficient electrocatalyst. After the completion of the reaction, the reactor was allowed to cool naturally to room temperature. The black precipitate formed was vacuum filtered, and washed further using deionized water and ethanol, followed by vacuum drying at 100 °C for 2 h. This procedure was adopted for synthesis of MS-R0 (see table 1).

For the syntheses of MS-R1 to MS-R5, hydroxylamine hydrochloride (HAH) was used in the concentration range of 70 to 350 *m*M (*Figure SI4 FESEM images of Nano* MoS_2 *with variation in the HAH*). The above method was used, where the aqueous HAH solution was added to the ammonium molybdate tetrahydrate solution, before it's mixing with thiourea.

The chemical reaction involved in the hydrothermal methodology used here can be expressed as:

$$(NH_4)_6Mo_7O_{24}.4H_2O + HONH_2.HCl + 15CH_4N_2S + 27H_2O + 5O_2 \rightarrow 7MoS_2 + NH_4Cl + H_2S(g) + 36NH_4 + 15CO_2 \quad (1)$$

The name convention of the samples is as shown in table 1. These samples were used further for the required study.

Table 1. Sample name convention of synthesized nano MoS_2 and commercial bulk MoS_2.

Sample Name	Molarity of HAH (mM)
MS-R0	0
MS-R1	70
MS-R2	140
MS-R3	210
MS-R4	280
MS-R5	350
BMS - Bulk MoS_2 (*Commercial*)	*Not applicable*

3. Characterization of nano MoS_2

3.1. Morphology and phase investigation

Morphological studies of synthesized nano MoS_2, was carried out using Filed Emission Scanning Electron Microscope (Model: Gemini 500 SEM). The elemental analysis was done using Energy dispersive spectroscope (EDS) attachment to the FESEM. High-resolution Micro X-Ray Diffraction (XRD) patterns were recorded using special Microfocus X—Ray Diffraction System (Model: Rigaku RINT Rapid-II using Cr—Kα, $\lambda = 2.29$ Å) to analyse the minor crystal structure details of the samples. It is a *unique* x-ray diffractometer, equipped with Micromax TM—007 *high flux microfocus anode* (Cu/Cr dual wavelength). It exhibits a very *high brilliance* nearing synchrotron sources, as compared to the conventional laboratory x-ray diffractometer. Unlike conventional XRD system (which employs a line focus), this special diffractometer employs a *spot focus range of* 10 μm – 800 μm. It possesses a large size cylindrical *two-dimensional image plate* as detector with active area of 460 $\times$ 256 mm^2. XRD patterns were recorded using a Debye–Scherrer geometry with a fixed angle of incidence of 20°. Raman spectra were recorded using Hobira Jobin-Yvon Lab Raman HR-800 spectrometer, where Ar-ion laser with an excitation wavelength of 514 nm as light source used. This spectrometer is equipped with CCD detector.

3.2. Electrochemical characterization

PARSTAT® MC (PMC) 2000A electrochemical workstation was used for all electrochemical measurements by using three-electrode cell configuration. All electrochemical studies were carried out under acidic condition using 0.5 M of H_2SO_4 electrolyte.

3.3. Immobilization of Nano MoS_2 on graphite paper

The working electrodes were fabricated by immobilization of MoS_2 on *graphite paper* prepared as per the procedure described here. Typically, 5 mg of catalyst powder, isopropyl alcohol (IPA) and Nafion 117 solution (10 vol% of IPA) were thoroughly mixed and ultrasonicated for one hour to obtain a homogeneous ink. A 60 μl of ink was drop-casted on the graphite paper (*dimension* 5 $\times$ 5 mm) and allowed to dry at room temperature. All the working electrodes were fabricated by same procedure used for electrochemical studies. Platinum wire (*counter electrode*), Ag/AgCl (*reference electrode*) and working electrode were typically used for all the electrochemical measurements in 3-*electrode* cell reactor. Linear sweep voltammetry and polarization studies were conducted with scan rate of 10 mV sec^{-1} in the potential window of 0.0 V to -1.0 V versus SCE. Cyclic Voltammetry was performed with potential bias in the range of 0.04 to 0.35 V(or *as per case*), scan rate of 10 mV sec^{-1} to 100 mV sec^{-1} with interval of 10 mV sec^{-1}. For the electrochemical impedance measurements, an AC voltage of 10 mV was used in the frequency is range of 100 *k*Hz to 100 *m*Hz.

3.4. Estimation of electro-catalytically evolved hydrogen

The rate evolved hydrogen was estimated by Gas Chromatography (GC-2010 Plus), equipped with splitless/split and direct injector, capillary column (made up of fused silica, length - 30 meter; internal diameter - 0.25 mm) and TCD (Tungsten Rhenium filament) as well as FID (Fused quartz) detector. This unit can be operated in the temperature range of 4 °C to 450 °C. The gas accumulated was extracted from cell by using a gas tight micro syringe (SGE, 10 μl). Negative biasing of 500 mV versus *SCE* was applied during electrolysis procedure.

4. Results

Electrochemical investigations of the nanostructured MoS_2 powders were carried out for investigating their electro-catalytic performance. Figure 1(a) shows the polarization curves, and figure 1(b) shows the corresponding Tafel curves of MS-R0 to MS-R5 samples, those have been immobilized on large area graphite

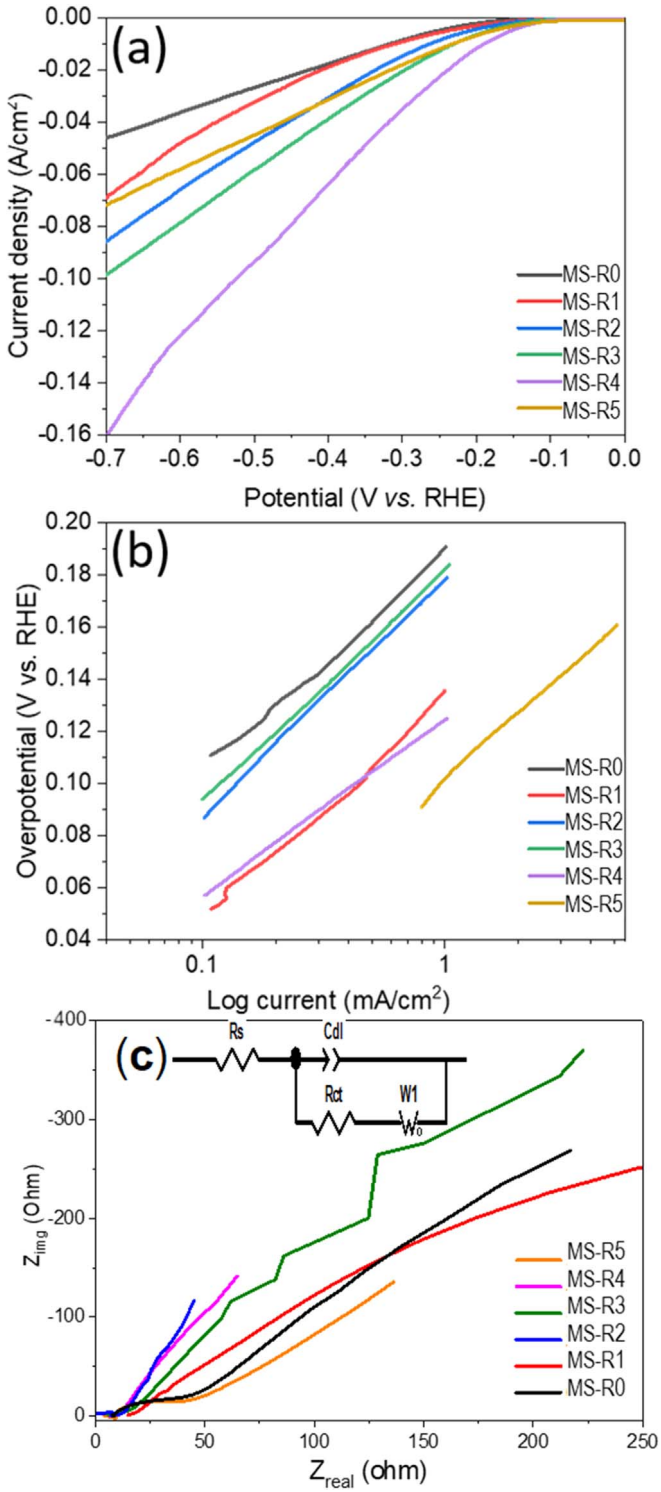

Figure 1. Electrocatalytic performance of MS-R0 to MS-R5, for HER application - (a) Polarization curves; (b) Tafel slopes; and (c) Electrochemical impedance spectra of MS-R0 to MS-R5, indicating the overlay of Nyquist plots, inset shows equivalent model for the electrochemical cell.

paper. The results are tabulated in table 2. It is observed that among all the samples, MS-R4 exhibited the lowest onset potential of 190 mV versus RHE. *Similarly,* MS-R4 also displayed lowest onset potential, and a lowest Tafel slope of 67 mV/dec. This clearly demonstrates that as compared to the MS-R0 (*sample made without reducing agent*), the optimized sample of MS-R4 is the efficient electro catalyst. *Further*, figure 6(c) shows the results of electrochemical impedance spectroscopic (EIS) studies of nano MoS_2. Nyquist plots of all the samples show similar variation, which can be fitted to a combination of semicircle and a straight line. The parametric fitting of Randel's cell indicated that the *charge-transfer resistance* (R_{ct}) values of the samples show the differences (*see* table 2). It is imperative from plots that the MS-R4 shows smallest diameter of semicircle in the high frequency

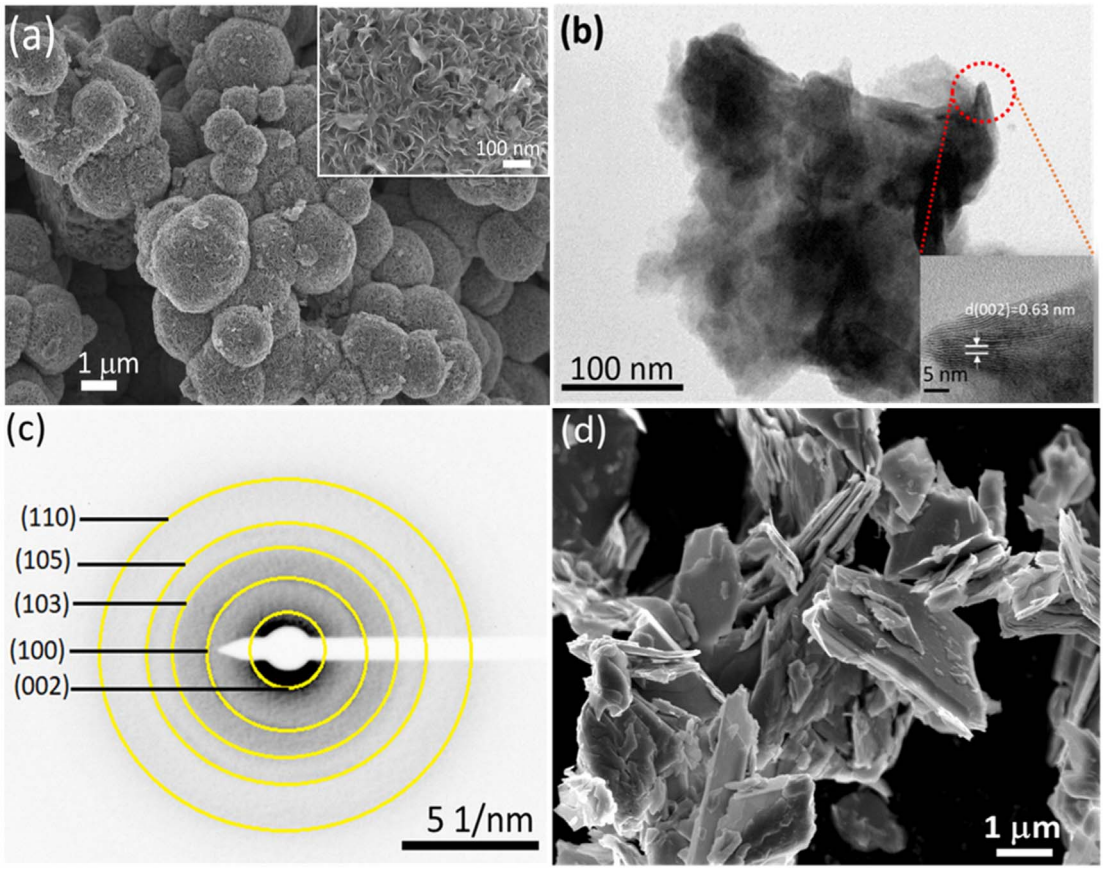

Figure 2. (a) FESEM, (b) TEM (*Inset shows corresponding HRTEM image*), and (c) SAED- for MS-R4; (d) FESEM of Bulk MoS_2 (BMS) for comparison with figure 2(a).

Table 2. The results of electrochemical characterization of nano MoS_2 based for all synthesized electrocatalyst with known literature electrocatalysts.

S.No	Sample Name (V versus RHE)	Onset potential	Overpotential (V versus RHE) @ 10 mA cm^{-2}	Tafel slope (mV dec^{-1})	Charge transfer resistance (R_{CT}) (ohm)	References
1	MS-R0	−0.6	0.36	84	500.0	This work
2	MS-R1	−0.004	0.31	84	663.0	
3	MS-R2	−0.003	0.26	90	605.0	
4	MS-R3	−0.001	0.23	86	553.0	
5	MS-R4	−0.001	0.19	67	5.0	
6	MS-R5	−0.004	0.20	86	8.0	
7	BMS	−0.57	—	178	1160.0	
8	Hybrid phase 1T/2H MoS_2	−0.146	—	71	20.9	[23]
9	1T/2H MoS_2-HN[a]	−0.12	0.15	47	40	[24]
10	M-$MoS_2^{\$}$	—	0.17	41	1	[31]
11	Li-MoS_2	−0.17	0.29	77	292.1	[32]
12	FS laser exfoliated 1T-MoS_2	−0.17	0.26	35	131.1	
13	1T/2H MoS_2	0.12	0.22	61	30	[33]

[a] Hierarchical nanorods, $Metallic.

zone, *thereby* yielding lowest resistance (R_{ct}) of 5 ohm. This demonstrates that in comparison to the bulk-MoS_2 (1160 Ω), MS-R4 shows highest conductivity due to the favorable nanostructuring. Such electro catalyst is expected to yield high HER rate in comparison to its bulk counterpart.

Figure 2 shows the FESEM and TEM images of the optimized MS-R4 electrocatalyst. FE-SEM images (figures 2(a) and (c)) show the presence of beautiful and *well-decorated* MoS_2 micro balls with petal containing surface. The high resolution micrograph shows the formation of distinct microballs (*inset*) which is clear from

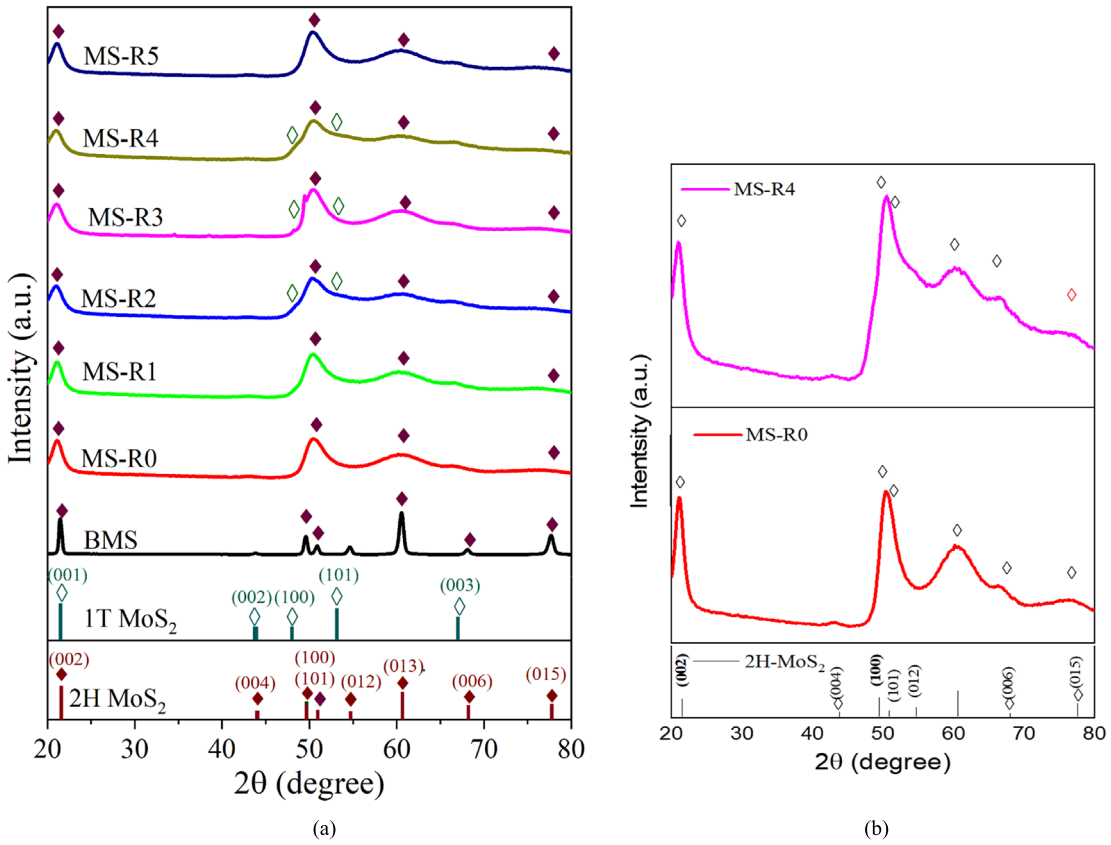

Figure 3. (a): XRD spectra of nano MoS_2 for *MS-R0 to MS-R5(bottom to top)*, Bulk MoS_2 spectrum included for comparison. (b): XRD spectra of nano MoS_2 for *MS-R0 and MS-R4*,showing the peculiar difference of 002 and 100 peaks of 2H phase of MoS_2.

the TEM image (figure 2(b)). The minimum diameter of these synthesized micro balls was found to be 1 μm those are covered with 5 nm thick surface decorated nanosheets.

Existence of nanosheets over the surface is clear from high resolution SEM image (figure 2(a)), and the lattice fringes in HRTEM image (*inset* of figure 2(b)). The calculated interlayer spacing of 0.63 nm corresponds to (002) plane of 2H phase MoS_2. The FESEM of MS-R4 and BMS shows clear different of nanoscopic surface of MS-R4 sample that is probably useful for enhancing active site, render enhanced the hydrogen evolution.

Figure 3(a) displays the XRD patterns of the nano MoS_2 recorded by using *microfocus* XRD diffractometer, to understand their structural properties. The analyses confirms the existence of main 2H phase MoS_2 in all the samples. The XRD pattern for bulk MoS_2 (BMS) was recorded for the sake of comparison with samples under the study. An increment in FWHM (*Full width half maxima*) of peaks corresponding to all plane has been observed for nano MoS_2 that is correlatable with its nanostructure nature.

The 2D nature of surface (*petal like nanosheets*) of MoS_2 is revealed by an *in-depth investigation* of the ratio of the **2H phase** related peak intensities corresponding to (*002*) plane and (*100*) plane of 2H phase, i.e. the ratio of $I_{(002)}/I_{(100)}$. As shown in figure 3(b), the XRD patterns of MS-R0 and MS-R4, the (002) and (100) peak show *distinct differences* in shape symmetry and the diffracted intensity ratios, which are not very clear from figure 3(a). *Accordingly*, the said ratios were calculated for all the samples shown in figure 3(a), which led to an interesting conclusion. Figure 4(a) shows the graph of $I_{(002)}/I_{(100)}$ ratio-variation w.r.t. each sample in context to 2H phase. For BMS (which contains 2H phase), $I_{(002)}/I_{(100)}$ value was found **to be 1.9**; *whereas* in case of other *nano MoS_2 samples*, the $I_{(002)}/I_{(100)}$ value was found **to be less than 1**. This implies that the intensity of the (*100*) plane is higher than that of (*002*) plane in case of nanostructured MoS_2 samples as indicated by Region -II. It also can be concluded that HAH inhibits the growth of (002) plane in these samples, and thus results in formation of few layered MoS_2, that is the signature for the 2D nanostructure [34]. This is confirmed by observing the combined decrease in the net intensity and increase in the peak broadening of the (002) plane in comparison to the BMS sample.

Further, Existence of additional ***weak*** peaks were also identified near the peaks corresponding to (100) and (101) planed (figure 3), those are attributed to (**100**) and (**101**) plane of **1T phase** of MoS_2 [35]. In order to understand a relative concentration variation in 1T phase w.r.t. 2H phase, we used the peak intensity ratio of $I^{1T}_{(003)}/I^{2H}_{(013)}$. Figure 4(b) shows the graph of ratio of $I^{1T}_{(003)}/I^{2H}_{(013)}$ w.r.t. sample 0 to sample 5. The graph clearly shows the relative increment in (003) plane intensity of 1T plane with the decrement of (013) plane intensity of

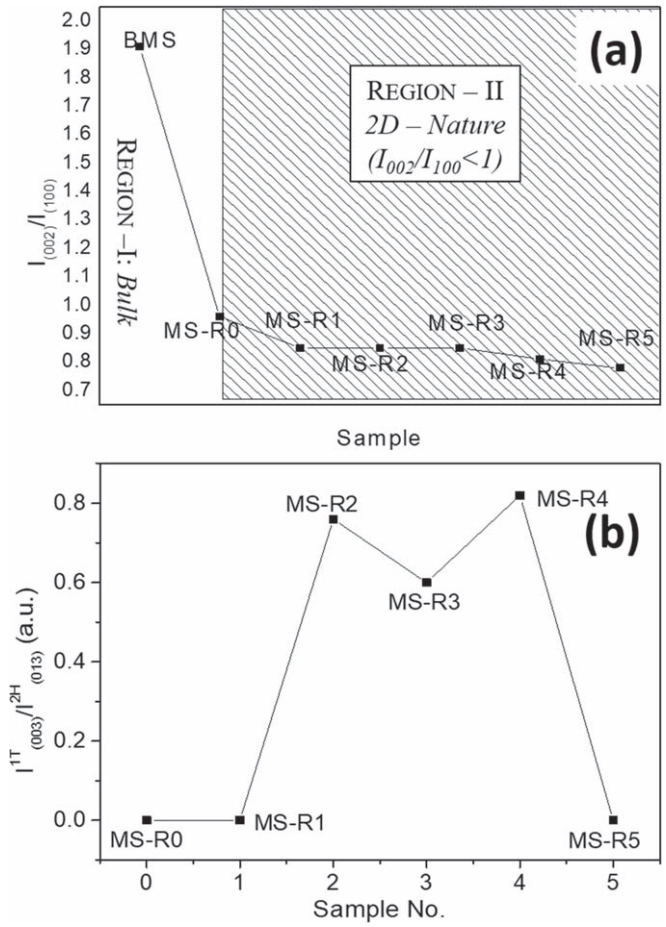

Figure 4. Intensity ratio of (a) (002) plane to (100) plane of 2H phase for 2D nature of synthesized nano MoS_2; and (b) of the (003) plane of 1T to (013) plane of 2H phase, to estimate the concentration of 1T phase in MoS2 electrocatalyst.

2H phase of MoS_2 This graph indicates that there is existence of low fraction of 1T phase. The graph shows that MS-R4 exhibits comparatively high fraction of 1T as compared to other samples. The challenge of identification and detection of such low concentration (of 1T phase) has been thus demonstrated by making use of micro-focus XRD in present case.

In line with above discussion on existence of 1T fraction, Raman studies does confirm the fact. Figure 5 displays the Raman spectra of all nano samples. All the spectra show, occurrence of two main peaks at 383 cm^{-1} and 402 cm^{-1}, those correspond to the characteristics peak of E^1_{2g} and A_{1g} of 2H phase MoS_2. However, sample MS-R4, shows a distinct difference in the spectrum in the range of 100 to 350 cm^{-1}, as compared to MS-R0. It shows additional three peaks at 148 cm^{-1}, 238 cm^{-1} and 343 cm^{-1}. These peaks correspond to J_1, J_2 and J_3 related phonon vibrations of 1T phase of MoS_2. *Nonetheless*, these three additional peaks do not exist in MS-R2 and MS-R3 samples, indicating that the small fraction of the 1T phase of MoS_2 is not present. The high-resolution XPS spectrum (figure SI5) of Mo 3d and S 2p is correlatable to1T phase in MS-R4 *along with* the 2H phase of MoS_2, which is not similar to sample MS-R0. It may be noted that XPS is surface sensitive technique, and hence discussed only in indicative purpose in this paragraph. It can also be mentioned that number of active sites (Supplementary information figures SI6 , SI7 and table SI1) in the nanostructure electrocatalyst can be expected to be higher than bulk. In view of main focus on phase synergy, the less relevant results are not included here, but can be found in supplementary information.

5. Application of optimized electrocatalyst for evolved hydrogen

To estimate the rate of hydrogen evolution of this efficient electrocatalyst, electrolysis was done using three electrode configurations under acidic condition (0.5 M H_2SO_4). Particularly, large area working electrode of MoS_2 (MS-R4) deposited stainless steel was fabricated, as working electrode. Thus, fabricated working electrolytic reactor comprising of working electrode, counter electrode (Graphite rod) and reference electrode (Saturated Calomel Electrode, SCE) was utilized to estimate real time hydrogen evolution.

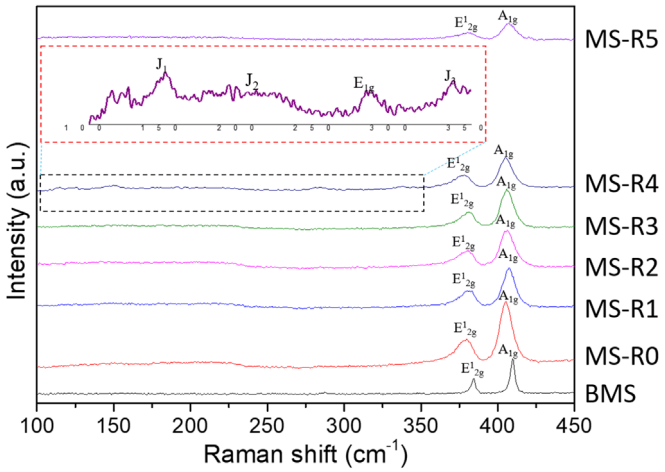

Figure 5. Raman spectra of hydrothermally synthesized Nano MoS_2 powder and bulk MoS_2.

Real time hydrogen evolution over MS-R4 and MS-R0 was compared (*See supplementary information Movie 1 - Typical electrocatalytic hydrogen evolution over nano MoS_2 electrode*) *Interestingly*, MS-R4 electrode yielded 2 times the (46 μmol h^{-1}) higher hydrogen evolution as compared to that over MS-R0 (23 μmol h^{-1}). Thus, a superior HER electrode has been achieved in the form of nano MoS_2 from this study.

6. Conclusion

In the summary of reported work, an efficient nano MoS_2 has been achieved, as an efficient electrocatalyst for HER application, by making use of hydrothermal methodology. The large are of immobilization of these electro catalysts on large area graphite paper has been shown feasible via. real time hydrogen evolution. *An* improved performance is attributed to low values of over-potential, Tafel slope, charge transfer resistance and high electrochemical surface area of the best electrocatalyst. This work clearly validates that present approach allow us to utilized these efficient 2D MoS_2 electrocatalyst for real time hydrogen generation.

Acknowledgments

The authors wish to thank Mr K. Ramesh Reddy, Mr M. Ramkrishna and Dr L. Venkatesh, Dr B.V. Sarada, Dr N. Hebalkar for their help support. Permission granted by Director, ARCI to publish the work is gratefully acknowledged. J. G. acknowledges the fellowship given by Director, ARCI, DST lab, during this work.

Data availability statement

All data that support the findings of this study are included within the article (and any supplementary files).

ORCID iDs

Jyoti Gupta https://orcid.org/0000-0001-7748-2990
Dibakar Das https://orcid.org/0000-0002-4040-9607
Anirudha Karati https://orcid.org/0000-0001-8444-7851
Joydip Joardar https://orcid.org/0000-0003-4498-8308
Pramod H Borse https://orcid.org/0000-0002-2577-8754

References

[1] Pareek A, Dom R, Gupta J, Chandran J, Adepu V and Borse P H 2020 Insights into renewable hydrogen energy: recent advances and prospects *Materials Science for Energy Technologies* **3** 319–27
[2] Ayers K, Danilovic N, Ouimet R, Carmo M, Pivovar B and Bornstein M 2019 Perspectives on low-temperature electrolysis and potential for renewable hydrogen at scale *Annual Review of Chemical and Biomolecular Engineering* **10** 219–39

[3] Akbar S, Anwar A, Noon M Z, Elliott J M and Squires A M 2019 Platinum as an electrocatalyst: effect of morphological aspects of Pt/Pt-based materials *Mater. Sci. Technol.* **35** 1–11
[4] McCrory C C L, Jung S, Ferrer I M, Chatman S M, Peters J C and Jaramillo T F 2015 Benchmarking hydrogen evolving reaction and oxygen evolving reaction electrocatalysts for solar water splitting devices *JACS* **137** 4347–57
[5] Bai S, Yang M, Jiang J, He X, Zou J, Xiong Z, Liao G and Liu S 2021 Recent advances of MXenes as electrocatalysts for hydrogen evolution reaction *Npj 2D Materials and Applications* **5** 78
[6] Sun Y, Zhang T, Li C, Xu K and Li Y 2020 Compositional engineering of sulfides{,} phosphides{,} carbides{,} nitrides{,} oxides{,} and hydroxides for water splitting *J. Mater. Chem. A* **8** 13415–36
[7] Zahra S A and Rizwan S 2022 MWCNT-modified MXene as cost-effective efficient bifunctional catalyst for overall water splitting *RSC Adv.* **12** 8405–13
[8] Wang Z, Wu H H, Li Q, Besenbacher F, Li Y, Zeng X C and Dong M 2020 Reversing interfacial catalysis of ambipolar WSe_2 single crystal *Adv. Sci.* **7** 1901382
[9] Qin T, Wang Z, Wang Y, Besenbacher F, Otyepka M and Dong M 2021 *Recent Progress in Emerging Two-Dimensional Transition Metal Carbides* vol 13 (Singapore: Springer)
[10] Cao Y 2021 Roadmap and direction toward high-performance MoS_2 hydrogen evolution catalysts *ACS Nano* **15** 11014–39
[11] Shang X, Hu W-H, Li X, Dong B, Liu Y-R, Han G-Q, Chai Y-M and Liu C-G 2017 Oriented stacking along vertical (002) Planes of MoS_2: a novel assembling style to enhance activity for hydrogen evolution *Electrochim. Acta* **224** 25–31
[12] Tsai C, Abild-Pedersen F and Nørskov J K 2014 Tuning the MoS_2 edge-site activity for hydrogen evolution via support interactions *Nano Lett.* **14** 1381–7
[13] Su M, Zhou W, Liu L, Chen M, Jiang Z, Luo X, Yang Y, Yu T, Lei W and Yuan C 2022 Micro eddy current facilitated by screwed MoS_2 structure for enhanced hydrogen evolution reaction *Adv. Funct. Mater.* **32** 1–7
[14] Liu S, Zhou L, Zhang W, Jin J, Mu X, Zhang S, Chen C and Mu S 2020 Stabilizing sulfur vacancy defects by performing 'click' chemistry of ultrafine palladium to trigger a high-efficiency hydrogen evolution of MoS_2 *Nanoscale* **12** 9943–9
[15] Xiao Y, Tan M, Li Z, He L, Gao B, Chen Y, Zheng Y and Lin B 2021 Ethylenediamine-assisted phase engineering of 1T/2H–MoS_2/graphene for efficient and stable electrocatalytic hydrogen evolution *Int. J. Hydrogen Energy* **46** 11688–700
[16] Darshan B N, Kareem A, Maiyalagan T and Edwin Geo V 2021 CoS_2/MoS_2 decorated with nitrogen doped reduced graphene oxide and multiwalled carbon nanotube 3D hybrid as efficient electrocatalyst for hydrogen evolution reaction *Int. J. Hydrogen Energy* **46** 13952–9
[17] Wei Y, Tran V, Zhao C, Liu H, Kong J and Du H 2019 Robust photodetectable paper from chemically exfoliated MoS2 − MoO3 Multilayers *ACS Appl. Mater. Interfaces* **11** 21445–53
[18] Hussain S, Vikraman D, Truong L, Akbar K, Rabani I, Kim H-S, Chun S-H and Jung J 2019 Facile and cost-effective growth of MoS_2 on 3D porous graphene-coated Ni foam for robust and stable hydrogen evolution reaction *J. Alloys Compd.* **788** 267–76
[19] He H-Y, He Z and Shen Q 2018 Efficient hydrogen evolution catalytic activity of graphene/metallic MoS_2 nanosheet heterostructures synthesized by a one-step hydrothermal process *Int. J. Hydrogen Energy* **43** 21835–43
[20] Guo Z, Ma Q, Xuan Z, Du F and Zhong Y 2016 Facile surfactant-assisted synthesis of CTAB-incorporated MoS_2 ultrathin nanosheets for efficient hydrogen evolution *RSC Adv.* **6** 16730–5
[21] Yao Y, Ao K, Lv P and Wei Q 2019 MoS_2 coexisting in 1T and 2H phases synthesized by common hydrothermal method for hydrogen evolution reaction *Nanomaterials* **9** 844
[22] Liu H, Wu R, Zhang H and Ma M 2020 Microwave hydrothermal synthesis of 1T@2H−MoS_2 as an excellent photocatalyst *ChemCatChem* **12** 893–902
[23] Zhang Y, Kuwahara Y, Mori K, Louis C and Yamashita H 2020 Hybrid phase 1T/2H-MoS_2 with controllable 1T concentration and its promoted hydrogen evolution reaction *Nanoscale* **12** 11908–15
[24] Wang C, Wang H, Lin Z, Li W, Lin B, Qiu W, Quan Y, Liu Z and Chen S 2019 *In situ* synthesis of edge-enriched MoS_2 hierarchical nanorods with 1T/2H hybrid phases for highly efficient electrocatalytic hydrogen evolution *Cryst. Eng. Comm.* **21** 1984–91
[25] Ma D, Ju W, Li T, Zhang X, He C, Ma B, Tang Y, Lu Z and Yang Z 2016 Modulating electronic, magnetic and chemical properties of MoS_2 monolayer sheets by substitutional doping with transition metals *Appl. Surf. Sci.* **364** 181–9
[26] Yin Y *et al* 2016 Contributions of phase, sulfur vacancies, and edges to the hydrogen evolution reaction catalytic activity of porous molybdenum disulfide nanosheets *JACS* **138** 7965–72
[27] Yang W *et al* 2020 Conversion of intercalated MoO_3 to multi-heteroatoms- doped MoS_2 with high hydrogen evolution activity *Advanced Materials* **32** 2001167
[28] Gupta J, Das D and Borse P H 2020 Nanosheets decorated MoS_2 micro balls: effect of 1T/2H composition *ChemistrySelect* **5** 11764–8
[29] Xuan T T, Long L N and Van Khai T 2020 Effect of reaction temperature and reaction time on the structure and properties of MoS_2 synthesized by hydrothermal method *Vietnam Journal of Chemistry* **58** 92–100
[30] Debbarma M, Das S and Saha M 2013 Effect of reducing agents on the structure of zinc oxide under microwave irradiation *Advances in Manufacturing* **1** 183–6
[31] Geng X, Sun W, Wu W, Chen B, Al-Hilo A, Benamara M, Zhu H, Watanabe F, Cui J and Chen T 2016 Pure and stable metallic phase molybdenum disulfide nanosheets for hydrogen evolution reaction *Nat. Commun.* **7**
[32] Zuo P, Jiang L, Li X, Tian M, Ma L, Xu C, Yuan Y, Li X, Chen X and Liang M 2021 Phase-reversed MoS_2 nanosheets prepared through femtosecond laser exfoliation and chemical doping *The Journal of Physical Chemistry C* **125** 8304–13
[33] Liu Z, Gao Z, Liu Y, Xia M, Wang R and Li N 2017 Heterogeneous nanostructure based on 1T-Phase MoS_2 for enhanced electrocatalytic hydrogen evolution *ACS Appl. Mater. Interfaces* **9** 25291–7
[34] Ma L, Huang G, Chen W, Wang Z, Ye J, Li H, Chen D and Lee J Y 2014 Cationic surfactant-assisted hydrothermal synthesis of few-layer molybdenum disulfide/graphene composites: Microstructure and electrochemical lithium storage *J. Power Sources* **264** 262–71
[35] Yang Q, He Y, Fan Y, Li F and Chen X 2017 Exfoliation of the defect-rich MoS_2 nanosheets to obtain nanodots modified MoS_2 thin nanosheets for electrocatalytic hydrogen evolution *J. Mater. Sci., Mater. Electron.* **28** 7413–8

Paper III

Insights into renewable hydrogen energy: Recent advances and prospects

Alka Pareek, Rekha Dom, Jyoti Gupta, Jyothi Chandran, Vivek Adepu and Pramod H. Borse

Materials Science for Energy Technologies, 2020, 3, 319–327

Materials Science for Energy Technologies 3 (2020) 319–327

Contents lists available at ScienceDirect

Materials Science for Energy Technologies

journal homepage: www.keaipublishing.com/en/journals/materials-science-for-energy-technologies

Insights into renewable hydrogen energy: Recent advances and prospects

Alka Pareek [1], Rekha Dom [2], Jyoti Gupta, Jyothi Chandran, Vivek Adepu, Pramod H. Borse *

International Advanced Research Centre for Powder Metallurgy and New Materials (ARC International), Balapur PO, Hyderabad, Telangana 500 005, India

ARTICLE INFO

Article history:
Received 11 October 2019
Revised 19 December 2019
Accepted 20 December 2019
Available online 8 January 2020

Keywords:
Renewable energy
Hydrogen production
Electrolysis
Steam methane reforming
Bio hydrogen
Thermochemical

ABSTRACT

Presently the fulfilment of world's energy demand highly relies on the fossil fuel *i.e.* coal, oil and natural gas. Fossil fuels pose threat to environment and biological systems on the earth. Usage of these fuels leads to an increase in the CO_2 content in the atmosphere that causes global warming and undesirable climatic changes. Additionally, these are limited sources of energy those will eventually dwindle. There is huge urge of identifying and utilizing the renewable energy resources to replace these fossil fuels in the near future as it is expected to have no impact on environment and thus would enable one to provide energy security. Hydrogen is one of the most desirable fuel capable of replacing vanishing hydrocarbons. In this review we present the status of energy demands, recent advances in renewable energy and the prospects of hydrogen as a future fuel are highlighted. It gives a broad overview of different energy systems and mainly focuses on different technologies and their reliability for the production of hydrogen in present and future.

1. An overview of energy system – past, present and future

Energy is very crucial for the growth and survival of all living beings and it plays a vital role in the socio-economic development as well as human welfare of a country. Energy is regarded as a '*strategic commodity*' [1]. Insecurity of its supply poses great threat for the functioning of the economy, particularly in developing economies. Achievement of energy security in a strategic way holds importance for Indian economy as well as for the growth of the human development especially with respect to get rid of poverty, unemployment and meeting the Millennium Development Goals (MDGs) [2]. A great deal of planning is required for achieving the alternate source of energy which ensures long-lasting energy supply to address the issues related to energy demand, energy poverty and the environmental effects of energy growth.

In present era, the energy requirements are satisfied by petroleum-based fuels and electricity powered by the fossil fuels. These resources have dwindling stocks of energy and therefore, they are not considered as sustainable. These energy sources pose huge negative impact on the environment in several ways that are unacceptable for mankind. The main *by-product* in the use of fossil fuel is carbon dioxide, which contributes up to 82% of the estimated green house gases [3]. An urge to find alternative energy source to supersede non-carbon genic resources is highly unavoidable. Such efforts are expected in order to stabilize the negative environmental issues in the future. Presently, fossil fuels *viz.* oil, coal and natural gas are contributing about 95% of the total energy demands in world. By 2020, the consumption of fossil fuels is estimated to be 3.3 terawatts (TW) *i.e.* with respect to year 2000, there will be an increase by 32% with same proportions of oil, natural gas and coal [4]. For the next 10 years, global energy consumption is projected to further rise as shown in Fig. 1 as projected in earlier report [5,6].

Fossil fuels are not evenly distributed resources on the globe; they are generally controlled by only certain nations in the world. The major resources are existing in Organization of the Petroleum Exporting Countries (OPEC) those include *Iran, Saudi Arabia, United Arab Emirates and Iraq*. This questions the security of supply and distribution of these resources evenly to the developing countries. In addition, due to limited availability of these resources, a global competition for these resources and increase of prices in the future is not ruled out and may *roll-up* to unaffordable numbers. A 2013 report published by the International Monetary Fund concluded

* Corresponding author.
E-mail address: phborse@arci.res.in (P.H. Borse).
[1] Present address: Bioengineering and Environmental Science Lab, CEEFF, CSIR-Indian Institute of Chemical Technology (CSIR-IICT), Hyderabad 500007, India.
[2] Present address: M.V.S.R. Engineering College, Nadergul, Hyderabad 501510, India.

https://doi.org/10.1016/j.mset.2019.12.002
2589-2991/

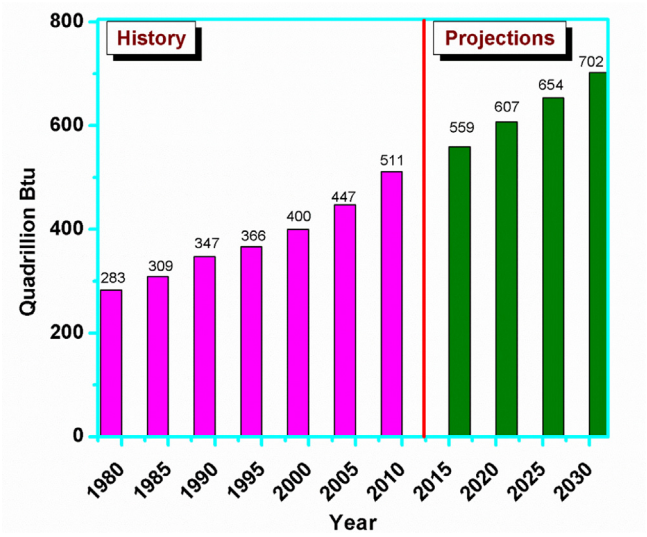

Fig. 1. Projection of Global energy consumption for the period 1980–2030 [Based on Ref. [6]].

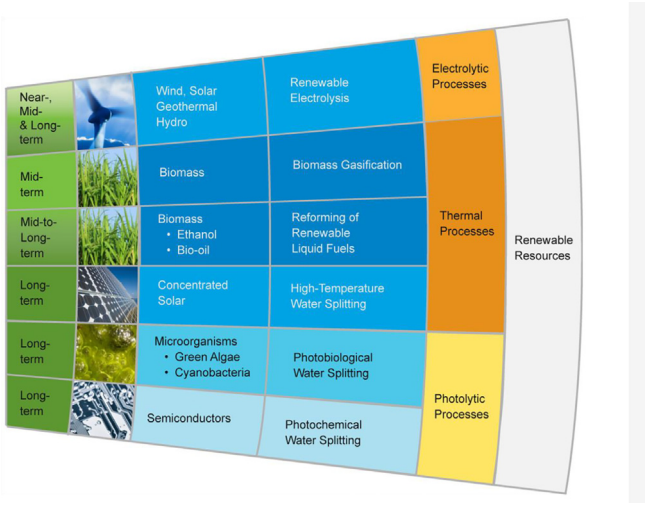

Fig. 2. Different methods of hydrogen production from renewable resources [Based on Ref. [13]].

that global fossil fuel subsidies amount to $1.9 trillion annually. $1.4 trillion of this is due to externalities, $800 billion due to climate change. This estimate is based on a conservative social cost of carbon of $25 per tonne of CO_2 emitted. An arguably more realistic estimate of $100 per tonne of COwould bring global fossil fuel subsidies to over $4 trillion per year, with $3.2 trillion due to climate change. This increases the levalized costs to approximately 18–28 cents per kWh, which is more than hydroelectric, onshore wind, geothermal, biomass, nuclear, natural gas, and on par with solar photovoltaic and solar thermal (whose costs are falling rapidly), and offshore wind.

Therefore, now it is highly desirable to explore the renewable resources of energy that could look after future needs. This necessitates one to *re-look* at the advances and prospects available in renewable hydrogen energy sources. This article concisely describes various possibilities *wrt.* present and future scenario for production of hydrogen energy. Presently, the rapid development in solar, wind, biomass and geothermal energy utilisation has set plenty of options in exploiting renewable energy sources. Numerous options among the current renewable sources are available for large scale energy generation, some of which are – Hydropower, Solar energy, Geothermal, Biogas, *etc* [5,6]. This can be clearly understood from the presentation in Fig. 2.

2. Renewable sources of energy

(1) *Hydropower* methodology is one where electrical energy is generated *via.*, abundant renewable source of water [7]. A common method employed for generation of hydropower is by building dams near flowing water bodies. The idea is based on utilizing the kinetic energy of flowing water that drives the mechanical dynamos thus generating electricity. The dams however are relatively expensive and are usually considered for a long-term investment. They also are known to bring geological change in the surroundings and a probable imbalance in the ecology. Since ages, this has been one of the major methodology world relied for electricity generation.

(2) *Wind energy* represents the nearest term cost competitive renewable energy source [8]. The winds are mainly produced by the convective effect that is induced by solar heating of earth's surface. Such wind energy thus produced is known to be proportional to the cube of its velocity. This type of energy presents a *dual-use* technology: *i.e.* while utilization of wind; the land can still be used for farming, ranching and forestry, and the collection of solar energy. European countries as United Kingdom and Denmark are known to have significant offshore wind power generation capacity.

(3) *Solar energy*, is obtained from the natural resource as sun, Sun can be used to generate electricity *via.* photovoltaics and concentrators [9] and thus categorized as a best and never dying renewable energy generating option. It has its advantages over hydropower and wind energy due to its cheaper maintenance cost. However, the downside is that solar energy largely depends on the geological location and season for the maximum exposure to the sun.

(4) *Geothermal energy* is heat extracted from rocks beneath water beds or underground [10]. It is considered as very reliable source, since it is not intermittent and is long lasting. However, the heat is not restored as rapidly by the environment as it is extracted which puts a limitation on the life of geothermal plants. United States of America and Philippines are known to have significant geothermal energy generating capacity.

These are various known ways to utilize the existing renewable energy sources as described above. However they lack with expected realization in human life either for geographical reasons or technological reasons. In an urge to identify new ways or to modify existing ways to extract maximum energy out of energy resources hydrogen has been looked upon as a potential energy carrier.

3. Hydrogen as future fuel

Hydrogen is the lightest and most abundant element on earth. It is a *zero emission* or *emission free* fuel that can be easily produced by the domestic sources. The interest in hydrogen as an alternate fuel (under the Energy policy Act 1992) has drastically increased recently. The preference to hydrogen as a potentially green fuel is due to its clean burning qualities, potential for domestic production and fuel cell vehicle and it is *2–3 times* higher efficiency prospects than gasoline [11,12]. Hydrogen has high energy–density hence it was demonstrated to be highly useful in 1970s for

propelling the spacecrafts and rockets by NASA. It has low volumetric energy density, as energy derived from 1 kg of hydrogen is equivalent to energy produced from 1 gallon of gasoline [13].

However, the main challenge in utilizing hydrogen as a fuel is its production in pure form. Hydrogen is present in enormous quantities in water (H_2O), hydrocarbons (methane) and other organic matter. There are different technologies used for production of pure hydrogen as shown in Fig. 2. It is clearly seen from the figure that hydrogen can be utilized with respect to near term and long term goals not only from hydro/wind/ solar/geothermal sources but also from biomass/concentrated solar power/microor ganism/semiconductors.

Today industrially, 96% of hydrogen is produced by *steam reforming* method [14]. It is a well-established technology to extract hydrogen from fossil fuel stocks. Almost 10–11 million tonnes of hydrogen requirements of U.S. is fulfilled using steam reforming every year.

Another 4% of hydrogen is produced from *electrolysis* method [15]. In this technology, water is splitted into oxygen and hydrogen using electric current. Some other techniques also contribute to hydrogen production like thermochemical cycles, wind, biomass gasification and solar. But these technologies are still at *primary stage* of research.

As for overall hydrogen production potential, a 2009 analysis by the National Renewable Energy Laboratory (NREL) titled "*Hydrogen Potential from Coal, Natural Gas, Nuclear, and Hydro Resources*" examined the combined hydrogen production potential from the non-renewable energy sources, from renewable sources as wind, solar, and biomass [16]. The study found that out of total energy produced in US from coal, natural gas, hydro-electric, and nuclear power one can generate about 72 million metric tonnes of energy *via.* hydrogen that will have energy share of 30% with respect to the current annual energy used [16,17].

A key point related to hydrogen for energy production is that it is a substance that is "*found*" like crude oil or natural gas, but rather "*made*" *in a similar to* electricity from one of the many different means [18,19]. As with electricity, the environmental impacts of hydrogen use vary significantly by production method and its accompanying value or fuel chain. Recently, *Borse* et al. reported a similar information which indicated that, though hydrogen is a potential fuel, but it needs tremendous efforts with respect to its commercial viability. Ultimately it means hydrogen based technology still waits for identification of best ways to generate hydrogen for it commercial usage. In following section we have described various methodologies for production of hydrogen and it scope towards commercialization in future.

4. Paths of hydrogen production

4.1. Steam methane reforming

Natural gas is a not a recent advancement but a mature pathway for hydrogen production. It uses existing natural gas as an energy source, which is extracted from the earth's crust. Around 96% of U.S. hydrogen production depends on this technology. Natural gas contains methane which can be combined with steam using thermal processes such as *steam methane reformation* and *partial oxidation* to produce hydrogen. In this technology steam maintained at high temperature (700–1000 °C) and pressure (3–25 bar) reacts with methane (CH_4) in presence of a catalyst to produce hydrogen, carbon monoxide and carbon dioxide. Further carbon monoxide and steam reacts over a catalyst to form carbon dioxide and more hydrogen. Further carbon dioxide and other impurities are removed to obtain pure hydrogen, above process is known as *pressure swing adsorption*. In place of CH_4 there are also other fuels those can be used *such as* propane, gasoline, diesel and ethanol. Mainly some nickel based catalysts are needed to carry out such reaction. This is also known as *steam methane reforming* (SMR). The process in schematically summarized in Fig. 3.

The following reactions are involved in steam reforming process [14,20]:

$$CH_4 + H_2O \rightarrow CO + 3H_2$$

$$CO + H_2O \rightarrow CO_2 + H_2$$

Most of the hydrogen produced in U.S. is mainly contributed by SMR methodology. This technique is highly preferred since it promises the commercial hydrogen production to fulfil all the demands in a very cost effective manner. In addition, emission of greenhouse gases is much less than the gasoline dependent methodologies. The main disadvantage of this method is it depends on dwindling fossil fuel stocks.

4.2. Coal gasification

Coal gasification is another important ways to generate hydrogen. Coal is an important material that is useful to obtain variety of products. There are different methods to utilize coal as a source for fuel. One of them is *coal gasification*, which could yield power, liquid fuels, chemical and hydrogen. During such process, coal reacts with hydrogen (H_2), oxygen (O_2) and steam under high pressure to form a mixture of carbon monoxide and hydrogen (*synthesis gas*). Carbon monoxide further reacts with steam *via. Water-gas shift reaction* to form additional hydrogen and carbon. After this process pure hydrogen is separated from the system and carbon is captured and sequestered. The schematic of method [21] is shown in Fig. 4. The reactions occurring during this process can be given in following manner [22]:

$$3C + O_2 + H_2 \rightarrow H_2 + 3CO$$

$$CO + H_2O \rightarrow CO_2 + H_2$$

Though USA has abundant coal source that can last for more than 250 years, but the greenhouse gas emission is a major threat for our environment.

Consequently, this technology needs attention with respect to making it eco-friendlier so that it will hamper the environment. Accordingly, this technology could be made efficient and environment friendly if the coal gasification is further improved with respect to carbon capture and sequestration thus ensuring zero carbon dioxide release, that also involves employment of techniques other than cryogenic processes to separate oxygen from air, and possibly development of membranes to separate out pure hydrogen from the system. However, it needs time as well as financial investment to make the methodology an *eco-friendly* technique.

4.3. Electrolysis

In the electrolysis process, water splits into hydrogen and oxygen by the application of electrical current. Generally, two electrodes (cathode and anode) are used in an aqueous solution containing KOH electrolyte as shown in Fig. 5. This unit is known as electrolyser. Electrolysers can be small and large based on small scale and large scale hydrogen production *respectively*. This technology is relevant for "*distributed hydrogen production*". Hydrogen production *via* electrolysis can be made completely zero greenhouse gas emissions depending upon the source used to provide energy to split water molecule. Accordingly, researchers are concentrating on wind energy or nuclear option to replace energy for electrolyser. It is predicted that usage of such energy source

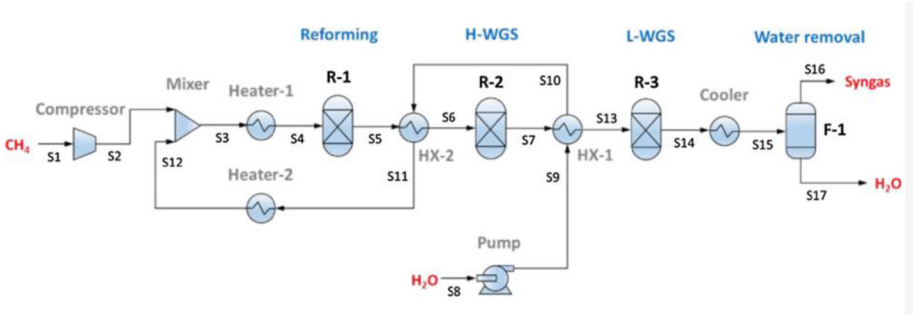

Fig. 3. Schematic of production of hydrogen by steam reforming process [Adapted from Ref. [20] with permission [20]].

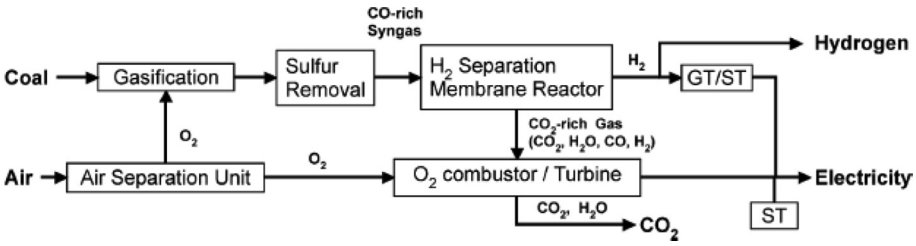

Fig. 4. Schematic showing hydrogen production *via* coal gasification [Adapted from Ref. [21] with permission [21]].

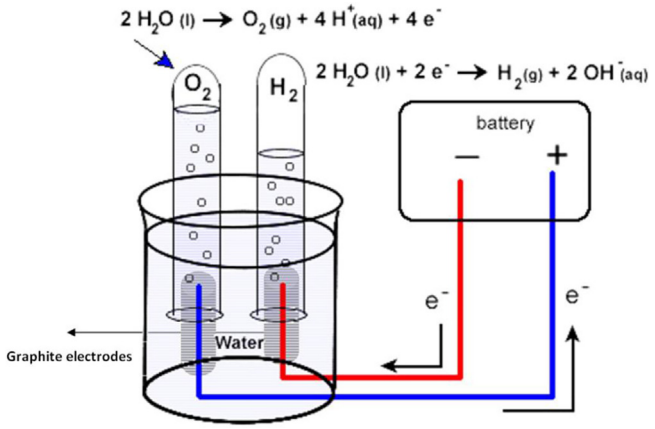

Fig. 5. Schematic showing hydrogen production *via.* electrolysis [Adapted from Ref. [23] with License under www.creativecommons.org].

would result in reduction of cost incurred in delivering the electrical energy. The reaction occurring during the electrolysis can be written in following manner [23]:

Electrolyte $4H_2O \rightarrow 4H^+ + 4OH^-$

Cathode $4H^+ + 4e^- \rightarrow 2H_2$

Anode $4OH^- \rightarrow O_2 + 2H_2O + 4e^-$

Over all $2H_2O \rightarrow O_2 + 2H_2$

This technology is used quite easily at industrial stage. There are various techniques[24] adopted for the improvement of this method like (1) Use of acidic polymer membrane rather than liquid electrolyte; (2) High temperature electrolysis, since energy needed at higher temperature is less than at lower temperature; (3) Use of photovoltaic system to provide electric power using solar energy to electrolyser.

The main advantage of this technique is that, (1) it is a potential method for renewable energy generation; and (2) no greenhouse gas emission occurs. The main challenge associated with this technology involves a reduction in the cost of electrolyser manufacturing as well as improving efficiency of process. Another challenge is to interface the compressor in electrolyser so as to avoid cost of separate compressor that is desirable for high pressure hydrogen storage.

4.4. Biomass gasification

Biomass is one of the potential energy resources for hydrogen generation [25]. It is generally referred to the biological organic energy resources such as *corn stover, wheat straw, forest residues, witch grass, willow trees, human waste and animal waste*. There are various methods (*viz.* physical, thermal, chemical and biological conversion) to generate energy from biomass. The biomass could be converted to heat, electricity, solid fuels such as coal, liquid fuels such as bio-oil, methanol, etc. and gas fuels such as hydrogen and syngas.

Gasification is a thermochemical process for destruction of feedstocks (*i.e.* biomass, lignocellulosic residues, agriculture waste, refuse derived fuel and organic wastes) to produce energy carrier. However, the technology with steam alone requires additional energy cost for increasing temperature of the steam. Further, the steam gasification reaction being an endothermic reaction, to reduce the energy cost by partial oxidation (exothermic reaction) reaction of biomass, air is also used. Thus, Biomass can be productively converted into mixture of hydrogen, carbon monoxide and carbon dioxide on reaction with steam and oxygen under high temperature and pressure.

The unit used for carrying out such reactions is known as gasifier. The synthesis gas produced in this technology is produced by breaking down biomass chemically by heat, steam and oxygen present in the gasifier. Further to this, a reaction similar to coal gasification *i.e. water gas shift reaction*, occurs to convert carbon monoxide (CO) into carbon dioxide (CO_2) and hydrogen (H_2), and ultimately the separation of hydrogen. Biomass gasification generally involves thermal treatment of organic or fossil fuels based matter and its conversion into carbon monoxide, hydrogen and

carbon dioxide. The schematic of biomass gasification is shown in Fig. 6. The reaction is carried out at high temperature more than 700 °C without letting combustion to occur. It involves chain of reaction in which firstly steam reacts with char to produce carbon monoxide and hydrogen via reaction [25]:

$$C + H_2O \rightarrow CO + H_2$$

Further steam is reacted with carbon monoxide and gives more hydrogen

$$CO + H_2O \rightarrow CO_2 + H_2$$

The main challenge involved in this technology is *biomass gasification*, as it is not as simple as coal gasification, and it also leads to other undesirable hydrocarbon compounds as by-products. Thus some extra steps are required to reform these hydrocarbons into pure *synthesis gas* by using catalyst. This technology is most appropriate for large scale, centralized hydrogen production. This holds advantages as (1) Abundance of Biomass as energy source; (2) Near-zero release of greenhouse gases as growth of biomass gasification reaction carbon dioxide is consumed, which in turn consumes it from atmosphere and makes it clean. Thus, the gasification of the biomass and/or the agriculture waste can efficiently generate the hydrogen and the syngas. If this process can be fully utilized, the gasification of these materials not only partially solving the problem of landfill, energy, especially hydrogen, can also be produced during the waste treatment. Further, to enhance the hydrogen yield and reduce the tar formation during the process, catalyst can also be added into the gasifier.

4.5. Photoelectrochemical/photocatalytic decomposition of water

Photo-electrochemical water splitting involves production of hydrogen from two most abundant renewable sources as water and sunlight. Generally, a two-electrode setup is used where one electrode acts as anode to yield oxygen, and the other electrode as cathode to produce hydrogen. The anode is a semiconducting electrode, which generates electrons when illuminated using solar light. These electrons are capable of producing hydrogen from water. Such cells used for hydrogen production are known as photo-electrochemical cells. This technology is still at its infancy with respect to its commercial viability. Thus a focussed research is required on finding most suited semiconductor, which has ideal band edge positions as well as has very good stability in electrolyte. Another important aspect is reactor designing, which needs directional attention from researchers and engineers to resolve various problems occurring in fabrication and utilization of an ideal configuration. Fig. 7 shows schematic of a laboratory scale

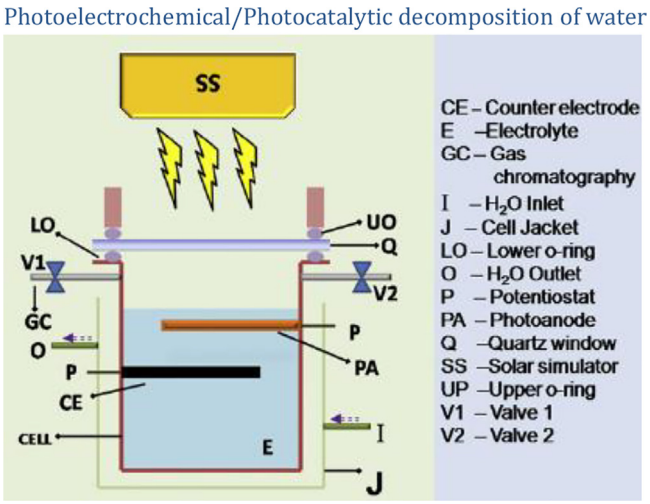

Fig. 7. Schematic shows working of photoelectrochemical cells [Adapted from Ref. [26] with permission].

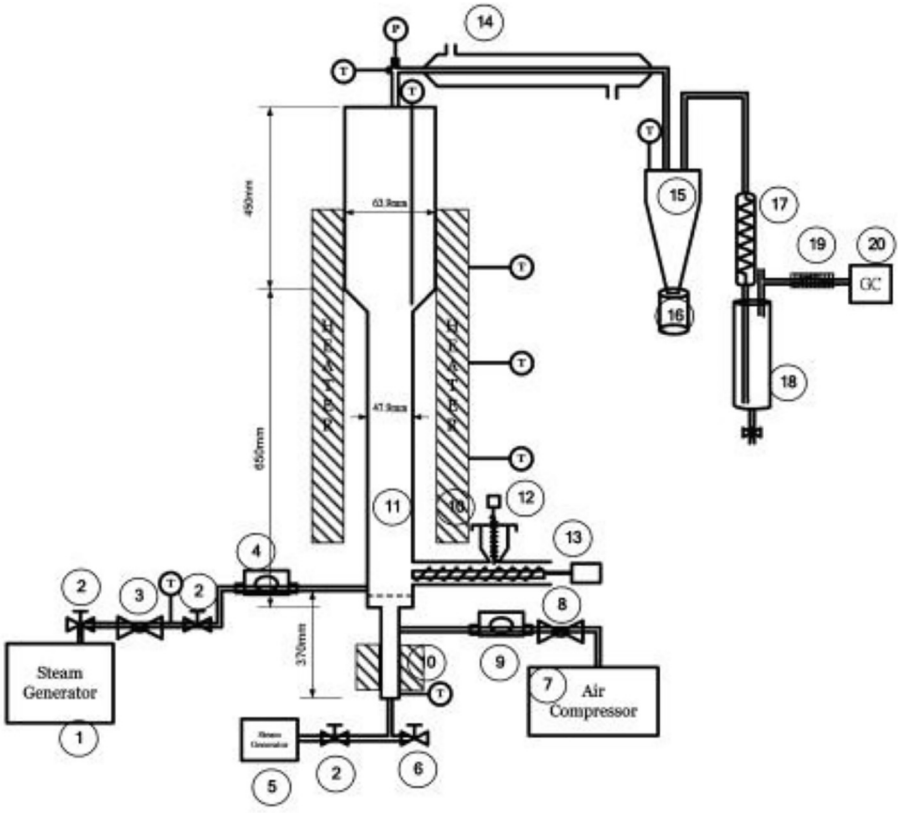

Fig. 6. Schematic showing hydrogen production *via.* biomass gasification [Adapted from Ref. [25] with permission].

photo electrochemical cell that is capable of performing PEC studies under simulated solar radiation [27]. Photocatalytic hydrogen production involves use of semiconducting powder for the production of hydrogen. This kind of reactions doesn't need any external biasing.

4.6. Thermochemical water splitting

Thermochemical processes involve chemical reaction that produces hydrogen derived by high temperature heat (500–2000 °C). The source of heat could be nuclear reactor or solar concentrators. Chemicals are reused within each cycle to create a closed loop chemical reaction with only consumption of water for hydrogen production as shown in Fig. 8.

In thermochemical water splitting, series of chemical reactions are carried out at high temperature to split water into hydrogen and oxygen. This technology produces hydrogen at low cost and high efficiency. But still it couldn't reach commercial stage. The following reactions are followed in Sulphur/Iodine cycle [28].

$$H_2SO_4(850\ ^\circ C) \rightarrow SO_2 + H_2O + 1/2O_2$$

$$I_2(120\ ^\circ C) + SO_2 + 2H_2O \rightarrow H_2SO_4 + 2HI$$

$$2HI(450\ ^\circ C) \rightarrow H_2 + I_2$$

This technology is suitable for large scale and centralized hydrogen production. The advantage of use of above method involves clean and pure hydrogen production with zero greenhouse gas emissions. This technology faces the challenges of reducing the cost of solar concentrators and heat transfer medium and also development of nuclear reactor technology to provide required heat at low temperature.

4.7. Bio-hydrogen production

Bio-hydrogen method of hydrogen production has gained tremendous momentum since last two decades in view of rising fraction of waste-materials and thereby need of their minimization. Biological processes are catalysed by microorganisms those exist in aqueous environment, atmospheric pressure and under ambient temperature [29–33]. Such processes can be exploited in the localities where sources of biomass or bio-waste materials are well-accessible. Natural availability of these precursors thus reduce the energy costs and the transport-cost of the initial raw material. It is imperative that the low cost of raw material, content of carbohydrate, their bio-degradability and availability enables one to select these materials for generating useful hydrogen energy. In general, biological processes occur over various types of anaerobic bacteria or algae. Microorganisms participate in different manner wrt. the type of substrate and the process conditions.

Unlike various other methods bio-hydrogen is interesting renewable methodology, that needs a technology development *wrt.* efficient hydrogen production by an economic way. Biologically produced hydrogen is a *by-product* of various metabolic processes of microorganisms. There are various newly developed technologies those can be explained in following section.

Biological hydrogen production methods can be classified as follows:

- Direct bio-photolysis
- Indirect bio-photolysis
- Photo fermentation
- Dark fermentation
- Two stage process (integration of dark and photo fermentation)
- Bio-catalyzed electrolysis

We briefly explain each of the methods in following sections below:

4.7.1. Direct bio-photolysis

Direct photolysis is one where water molecule is split over biological system under the irradiation of photons, such processes are found in plants and algal photosynthesis. Fig. 9 shows a schematic of one such process. The figure clearly shows that how solar energy is directly converted to hydrogen *via.* photosynthetic reactions.

$$2H_2O + \text{'light energy'} \rightarrow 2H_2 + O_2$$

Algae splits water molecules to H^+ and oxygen *via.* photosynthesis process. The generated H^+ are converted into hydrogen gas by "*hydrogenase enzyme*". Chlamydomonas reinhardtii is one of the *well-known* hydrogen producing algae. Activity of hydrogenase has also been observed in other *green algae* like *Scenedesmus obliquus*, *Chlorococcum littorale*, *Platymonas subcordiformis* and *Chlorella fusca*. The advantage of the present method is utilization of water as an inexpensive and abundant reactant. There are quite a few reports on improvement of bio-hydrogen production efficiency using micro algae [34].

Direct bio-photolysis method occurs at a partial pressure of nearly one atmosphere of O_2, which is a 1000-fold higher than its maximum tolerance. Thus, the O_2 sensitivity of the *hydrogenase enzyme reaction* and supporting reductant generating pathway remains the key problem for more than 3 decades.

Hydrogen production by green algae based direct photolysis is currently limited by three issues: (i) solar conversion efficiency of the photosynthetic reactor; (ii) H_2 synthesis processes (*i.e. the need to separate the processes of H_2O oxidation from H_2 synthesis*); and (iii) Bio-reactor design and economy. There are number of

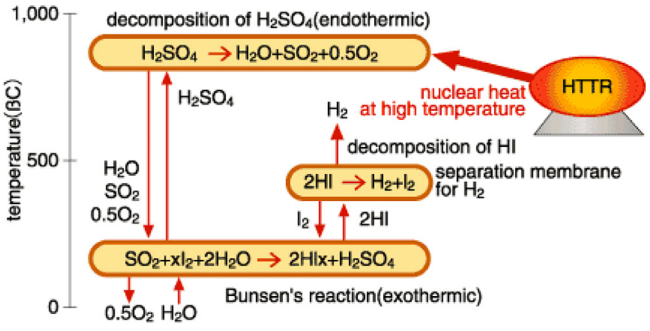

Fig. 8. Schematic shows hydrogen production via thermochemical water splitting [Based on Ref. [28]].

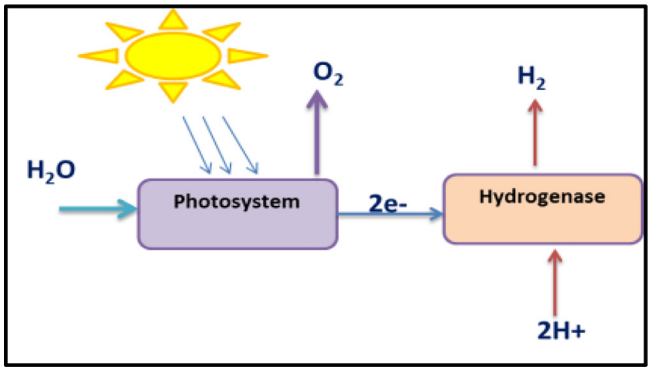

Fig. 9. Schematic of direct bio-photolysis method under the bio-hydrogen production category.

approaches to improve H_2 production by green algae. They include -Genetic engineering of light gathering antennae, Optimization of light input into photo-bioreactors, and Improvement to the *two-phase* H_2 production systems used with green algae. In direct bio-photolysis, hydrogen production rates of the order of 0.07 mmol/h per liter have been reported in the literature.

4.7.2. Indirect bio-photolysis

In indirect bio-photolysis, problems of sensitivity of the hydrogen evolving process are potentially circumvented by separating temporally and/or spatially oxygen evolution and hydrogen evolution. Thus indirect bio-photolysis processes involve separation of the H_2 and O_2 evolution reactions into separate stages, coupled through CO_2 fixation/evolution. The schematic for the indirect bio-photolysis is shown in Fig. 10. Cyanobacteria have the unique characteristics of using CO_2 in the air as a carbon source and solar energy as an energy source. The cells take up CO_2 first to produce cellular substances, which are subsequently used for hydrogen production. The overall mechanism of hydrogen production in cyanobacteria can be represented by the following reactions [29]:

$$12H_2O+6CO_2+\text{`lightenergy'}\rightarrow C_6H_{12}O_6+6O_2$$

$$C_6H_{12}O_6+12H_2O+\text{`light energy'}\rightarrow 12H_2+6CO_2$$

Cyanobacteria possess key enzymes (*nitrogenase and hydrogenase*) those carry out the metabolic functions facilitate the hydrogen generation. Anabaena species and strains have been subject of intense study due to their higher rates of H_2 production. In indirect bio-photolysis mutant strains of A. variabilis have demonstrated hydrogen production rate of the order of 0.355 mmol/h per liter.

4.7.3. Photo fermentation

H_2 production by purple non-sulfur bacteria is mainly due to the presence of nitrogenase under nitrogen-deficient conditions using light energy and reduced compounds (organic acids). The reaction is as follows:

$$CH_3COOH+2H_2O+\text{`light energy'}\rightarrow 4H_2+2CO_2$$

Photosynthetic bacteria have long been studied for their capacity to produce significant amounts of hydrogen. The advantage of this method are that oxygen does not inhibit the process. These photoheterotrophic bacteria have been found suitable to convert light energy into H_2 using organic wastes as substrate in batch processes, continuous cultures, or immobilized whole cell system using different solid matrices like carrageenan, agar gel, porous glass, and polyurethane foam. The disadvantages are the limited availability of organic acids, the nitrogenase enzyme is slow, the process requires a relatively high amount of energy, and hydrogen re-oxidation. To increase the nitrogenase activity and decrease the energy requirements, the proper ratio of carbon to nitrogen nutrients must be maintained. Another major factor affecting the photo-fermentation process is light intensity. Although an increase in light intensity has shown some stimulatory effect on the overall hydrogen production rate of photosynthetic micro-organisms, an adverse effect was also reported on their light conversion efficiency at high light intensities. However, the light conversion efficiency can be improved by genetic manipulation of the light-harvesting antennae, thereby reducing the saturation effect of light. Hydrogen production rates of the order of 145–160 mmol/h per liter by this methods have been reported. Certain photo-heterotrophic bacteria within the superfamily Rhodospirillaceae can grow in the dark using CO as the sole carbon source to generate ATP with the simultaneous release of H_2 and CO_2. The oxidation of CO to CO_2 with the release of H_2 occurs via a water gas shift reaction as shown below:

$$CO+H_2O\rightarrow CO_2+H_2$$

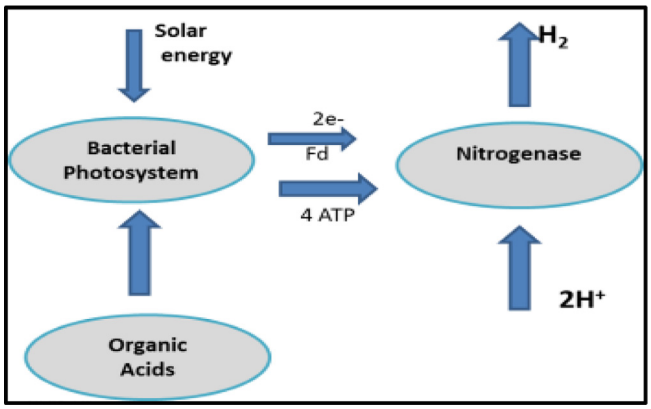

Fig. 10. Schematic of indirect bio-photolysis of bio-hydrogen production.

4.7.4. Dark fermentation

Hydrogen can be produced by anaerobic bacteria, grown in the dark on carbohydrate-rich substrates. Bacteria known to produce hydrogen include species of Enterobacter, Bacillus, and Clostridium. Carbohydrates, mainly glucose, are the preferred carbon sources for fermentation processes, which predominantly give rise to acetic and butyric acids together with hydrogen gas. Theoretically bioconversion of 1 mol of glucose yields 12 mol of hydrogen gas (H_2). According to reaction stoichiometry, bioconversion of 1 mol of glucose into acetate yields 4 mol H_2/mol glucose, but only 2 molH2/mol glucose is formed when butyrate is the end product. The equations below explain the stoichiometry.

$$C_6H_{12}O_6+2H_2O\rightarrow 2CH_3COOH+2CO_2+4H_2$$

$$C_6H_{12}O_6+2H_2O\rightarrow 2CH_3CH_2COOH+2CO_2+2H_2$$

While direct and indirect photolysis systems produce pure H_2, dark fermentation processes produce a mixed biogas containing primarily H_2 and carbon dioxide (CO_2), but which may also contain lesser amounts of methane (CH_4), CO, and/or hydrogen sulfide (H_2S). Dark-fermentation proves to be superior over photo-fermentation as this requires no light and the energy produced is relatively higher, due to the fermentation of sugar and carbohydrates.

The process is initiated by the hydrolysis of organic polymers to monomers, thereafter acetogenic conversion of monomers to organic acids, alcohols, and release of hydrogen. Although bio-hydrogen production by dark fermentation is promising and advantageous over photo-fermentation. However, the requirement of organic biomass as a feedstock makes this process quite expensive. Hydrogen production by these bacteria is highly dependent on the process conditions such as pH, hydraulic retention time (HRT), and gas partial pressure, which affect metabolic balance. The partial pressure of H_2 (pH_2) is an extremely important factor for continuous H_2 synthesis. Hydrogen synthesis pathways are sensitive to H_2 concentrations and are subject to end-product inhibition. As H_2 concentrations increase, H_2 synthesis decreases. Sugars and carbohydrate rich biomass are reported to be the most suitable feedstock for the formation of bio-hydrogen from dark fermentation.

Two stage process with integration of dark and photo fermentation

In fermentation, complete oxidation of 1 mol of glucose yields 12 mol of hydrogen. However, complete oxidation of glucose into

Table 1
The cost and other parameters is summarised in the table below.

Process	Energy required (kWh/Nm^3)	Status of technology	Efficiency (%)	Cost relative to SMR
Steam Methane Reforming (SMR)	2–2.5	Mature	70–80	1
Coal gasification	8.6	Mature	60	1.4–2.6
Electrolysis	3.54	Mature	27	3–10
Biomass gasification		R&D	45–50	2.0–2.4
Photoelectrochemical water splitting		Early R & D		
Photocatalytic		Early R &D		
Photobiological		Early R & D	<1	
Thermochemical cycles		Early R & D	35–45	6

This table was originally published in Ref. [35].

hydrogen and carbon dioxide is not possible as the corresponding reaction is not feasible thermodynamically as can be understood from the following equation.

$$C_6H_{12}O_6+6H_2O\rightarrow 12H_2+6CO_2$$

With external energy supply (*photon-energy in photo-fermentation*) theoretically 12 mol of hydrogen per mole of glucose can be produced. However, this process cannot be operated in the absence of light. On the other hand, in the absence of external energy (*in the case of dark fermentation*), oxidation of glucose by fermentative bacteria results in other by-products also and maximum 4 mol of hydrogen are produced per mole of glucose consumption with acetate as the sole by-product as given by the equation below.

$$C_6H_{12}O_6+2H_2O\rightarrow 4H_2+2CO_2+2CH_3COOH$$

Acetate produced in the dark-fermentation stage can be oxidized by photosynthetic bacteria to produce hydrogen as follows:

$$CH_3COOH+2H_2O+\text{'light energy'}\rightarrow 4H_2+2CO_2$$

Hence continuous production of hydrogen at maximum yield can be achieved by integrating dark- and photo-fermentation methods [30].

4.7.5. Bio-catalyzed electrolysis

Another way of oxidizing the acetate (or the effluent of dark fermentation process) to produce hydrogen is to provide external energy in the form of electrical energy instead of solar energy. In this approach, the bioreactor containing acetate forms the anodic compartment of an electrolyzer cell and protons and electrons produced by bacteria are collected at cathode (a platinum electrode catalysing hydrogen evolution reaction). Anodic and cathodic reactions are as follows:

$$\text{Anodic:}2CH_3COOH+2H_2O\rightarrow 2CO_2+8H^++8e^-$$

$$\text{Cathodic:}8H^++8e^-\rightarrow 4H_2$$

This section distinctly validates that there is tremendous potential in Bio-hydrogen methodology as an eco-friendly and renewable option. The ongoing developments are thus expected to yield a technology that would generate hydrogen in a more rapid manner. Such developments would facilitate the promotion of hydrogen as fuel of the future [35].

5. Summary

Hydrogen production using natural gas and fossil fuels covers major part of industrial hydrogen production at present time. It is predicted to continue in future also at rather large scale of production with this technology. However, generation of greenhouse gases is a major drawback of these reactions, in addition the dwindling stocks of fossil fuels is a topic of concern. The 95% of today's hydrogen demands are fulfilled by natural gas as it proves to be promising technique relative to present scenario of all other hydrogen production techniques. Another useful method, which involves hydrogen production at feasible stage, is electrolysis. There are tremendous attempts to use other renewable sources instead of electricity as; it makes this hydrogen technology a comparatively a costly method. Distributed hydrogen production can be possible by making use of electrolysis process which can also be utilized in small scale industries. But predicted higher infrastructure cost is seen as a financial burden for small capacity plants. Hydrogen production using coal gasification and biomass gasification are simpler to utilize for hydrogen generation but they still need solution with respect to minimization of heavy carbon dioxide production produced during these gasification reactions. In other words carbon capture and sequestration must be more effective. Photo-electrochemical and Bio hydrogen production involves clean and pure hydrogen production *via.* most abundant renewable sources like water and sunlight. But these technologies are still in infancy and thus need significant research and commercialization steps. Nonetheless, the cost of hydrogen (summarized in Table 1) remains an important issue to be considered. SMR costs 18 dollar/million BTU, which is 3 times more than natural gas (6 dollar/million BTU). Electrolysis produces pure hydrogen at the cost of 28 dollar/million BTU. Thus, till today natural gas is the most favoured option for hydrogen generation and utilization in industries. In order to have a competing renewable energy option, though bio-hydrogen seems to be most relevant but it needs lot of efforts for cost reduction. At the extreme end hydrogen generation using renewable sources as water and solar light, it would need some important achievement with respect to photocatalytic and photoelectron chemical hydrogen generation.

CRediT authorship contribution statement

Alka Pareek: Conceptualization, Visualization, Validation, Writing - review & editing. **Rekha Dom:** Writing - original draft, Methodology, Investigation. **Jyoti Gupta:** Writing - review & editing, Software, Formal analysis. **Jyothi Chandran:** Data curation, Software. **V. Adepu:** Formal analysis, Software. **Pramod H. Borse:** Supervision, Conceptualization, Project administration.

Acknowledgement

The authors thank the support of the Director, ARCI, India.

Declaration of Competing Interest

None.

References

[1] C.A. Grimes, O.K. Varghese, S. Ranjan, Light, water, hydrogen: the solar generation of hydrogen by water photoelectrolysis, 2008. doi:10.1007/978-0-387-68238-9.

[2] G. Karlsson, S. Oparaocha, The road to Johannesburg and beyond: networking for gender and energy, Energy Sustain. Dev. (2009), https://doi.org/10.1016/s0973-0826(08)60366-x.

[3] K. Rajeshwar, R. McConnell, S. Licht, Solar Hydrogen Generation: Towards Renewable Energy Future, 2008th ed., Springer, 2008, doi:10.1007/978-0-387-72810-0.

[4] M. Dresselhaus, G. Crabtree, M. Buchanan, T. Mallouk, L. Mets, K. Taylor, P. Jena, F. DiSalvo, T. Zawodzinski, H. Kung, I. Anderson, P. Britt, Basic Research Needs for the Hydrogen Economy. Report of the Basic Energy Sciences Workshop on Hydrogen Production, Storage and Use, May 13–15, 2003, (2004). doi:10.2172/899224.

[5] R.D. Shrestha, Energy For Development The Potential Role of Renewable Energy in Meeting the Millennium Development Goals, in: 2005.

[6] WEC, Global Energy Scenarios Comparison Review About the World Energy Council, (2019) 35.

[7] I. Yüksel, Hydropower for sustainable water and energy development, Renew. Sustain. Energy Rev. (2010), https://doi.org/10.1016/j.rser.2009.07.025.

[8] C. Bueno, J.A. Carta, Technical-economic analysis of wind-powered pumped hydrostorage systems. Part II: Model application to the island of El Hierro, Sol. Energy 78 (2005) 396–405, https://doi.org/10.1016/j.solener.2004.08.007.

[9] W.T. Xie, Y.J. Dai, R.Z. Wang, K. Sumathy, Concentrated solar energy applications using Fresnel lenses: a review, Renew. Sustain. Energy Rev. (2011), https://doi.org/10.1016/j.rser.2011.03.031.

[10] E. Barbier, Geothermal energy technology and current status: An overview, Renew. Sustain. Energy Rev. 6 (2002) 3–65, https://doi.org/10.1016/S1364-0321(02)00002-3.

[11] M. Balat, Potential importance of hydrogen as a future solution to environmental and transportation problems, Int. J. Hydrogen Energy. 33 (2008) 4013–4029, https://doi.org/10.1016/j.ijhydene.2008.05.047.

[12] F. Gutiérrez-Martín, J.M. De María, A. Baïri, N. Laraqi, Management strategies for surplus electricity loads using electrolytic hydrogen, Int. J. Hydrog. Energy 34 (2009) 8468–8475, https://doi.org/10.1016/j.ijhydene.2009.08.018.

[13] A. Ursúa, L.M. Gandía, P. Sanchis, Hydrogen production from water electrolysis: current status and future trends, Proc. IEEE 100 (2012) 410–426, https://doi.org/10.1109/JPROC.2011.2156750.

[14] M. Balat, Possible methods for hydrogen production, energy sources. Part A recover, Util. Environ. Eff. 31 (2008) 39–50, https://doi.org/10.1080/15567030701468068.

[15] K. Mazloomi, N. Sulaiman, H. Moayedi, Electrical efficiency of electrolytic hydrogen production, Int. J. Electrochem. Sci. 7 (2012) 3314–3326.

[16] H. Power, A. Milbrandt, M. Mann, Hydrogen Resource Assessment Hydrogen Potential from Coal, Natural Hydrogen Resource Assessment Hydrogen Potential from Coal , Natural Gas , Nuclear , and Hydro Power, Contract. (2009).

[17] M. [National R.E.L. (NREL) Melaina Golden, CO (United States)], M. [National R. E.L. (NREL) Penev Golden, CO (United States)], D. [National R.E.L. (NREL) Heimiller Golden, CO (United States)], Resource Assessment for Hydrogen Production: Hydrogen Production Potential from Fossil and Renewable Energy Resources, United States, 2013. doi:10.2172/1260322.

[18] C. Acar, I. Dincer, A review and evaluation of photoelectrode coating materials and methods for photoelectrochemical hydrogen production, Int. J. Hydrogen Energy 41 (2016) 7950–7959, https://doi.org/10.1016/j.ijhydene.2015.11.160.

[19] C. Acar, I. Dincer, Comparative assessment of hydrogen production methods from renewable and non-renewable sources, Int. J. Hydrogen Energy. 39 (2014) 1–12, https://doi.org/10.1016/j.ijhydene.2013.10.060.

[20] C. Song, Q. Liu, N. Ji, Y. Kansha, A. Tsutsumi, Optimization of steam methane reforming coupled with pressure swing adsorption hydrogen production process by heat integration, Appl. Energy 154 (2015) 392–401, https://doi.org/10.1016/j.apenergy.2015.05.038.

[21] K. Yamashita, L. Barreto, Energyplexes for the 21st century: coal gasification for co-producing hydrogen, electricity and liquid fuels, Energy 30 (2005) 2453–2473, https://doi.org/10.1016/j.energy.2004.12.002.

[22] N. Howaniec, A. Smoliński, Effect of fuel blend composition on the efficiency of hydrogen-rich gas production in co-gasification of coal and biomass, Fuel 128 (2014) 442–450, https://doi.org/10.1016/j.fuel.2014.03.036.

[23] A.L. Yuvaraj, S. Daniel, A systematic study on electrolytic production of hydrogen gas by using graphite as electrode, Mater. Res. 17 (2014) 83–87, https://doi.org/10.1590/S1516-14392013005000153.

[24] S.S. Kumar, V. Himabindu, Hydrogen production by PEM water electrolysis – a review, Mater. Sci. Energy Technol. 2 (2019) 442–454, https://doi.org/10.1016/j.mset.2019.03.002.

[25] A.C.C. Chang, H.F. Chang, F.J. Lin, K.H. Lin, C.H. Chen, Biomass gasification for hydrogen production, Int. J. Hydrogen Energy. 36 (2011) 14252–14260, https://doi.org/10.1016/j.ijhydene.2011.05.105.

[26] A. Pareek, R. Dom, P.H. Borse, Fabrication of large area nanorod like structured CdS photoanode for solar H2 generation using spray pyrolysis technique, Int. J. Hydrogen Energy 38 (2013) 36–44, https://doi.org/10.1016/j.ijhydene.2012.10.057.

[27] J.H. Kim, D. Hansora, P. Sharma, J.-W. Jang, J.S. Lee, Toward practical solar hydrogen production – an artificial photosynthetic leaf-to-farm challenge, Chem. Soc. Rev. 48 (2019) 1908–1971, https://doi.org/10.1039/C8CS00699G.

[28] K. Onuki, S. Kubo, A. Terada, N. Sakaba, R. Hino, Thermochemical water-splitting cycle using iodine and sulfur, Energy Environ. Sci. 2 (2009) 491–497, https://doi.org/10.1039/b821113m.

[29] O. Bičáková, P. Straka, Production of hydrogen from renewable resources and its effectiveness, Int. J. Hydrogen Energy (2012) 11563–11578, https://doi.org/10.1016/j.ijhydene.2012.05.047.

[30] S.M. Kotay, D. Das, Biohydrogen as a renewable energy resource—Prospects and potentials, Int. J. Hydrogen Energy 33 (2008) 258–263, https://doi.org/10.1016/j.ijhydene.2007.07.031.

[31] K. Nath, D. Das, Amelioration of biohydrogen production by a two-stage fermentation process, Ind. Biotechnol. 2 (2006) 44–47, https://doi.org/10.1089/ind.2006.2.44.

[32] D. Das, A road map on biohydrogen production from organic wastes, Ina. Lett. 2 (2017) 153–160, https://doi.org/10.1007/s41403-017-0031-y.

[33] H. Singh, D. Das, Biofuels from Microalgae: Biohydrogen, in: E. Jacob-Lopes, L. Queiroz Zepka, M.I. Queiroz (Eds.), Energy from Microalgae, Springer International Publishing, Cham, 2018, pp. 201–228, https://doi.org/10.1007/978-3-319-69093-3_10.

[34] N. Fakhimi, O. Tavakoli, Improving hydrogen production using co-cultivation of bacteria with Chlamydomonas reinhardtii microalga, Mater. Sci. Energy Technol. 2 (2019) 1–7, https://doi.org/10.1016/j.mset.2018.09.003.

[35] A.T. Raissi, D.L. Block, Hydrogen: automotive fuel of the future, IEEE Power Energy Mag. 2 (2004) 40–45, https://doi.org/10.1109/MPAE.2004.1359020.

Dr. Dibakar Das
Professor,
School of Engineering Sciences and Technology (SEST),
University of Hyderabad,
Hyderabad-500046, INDIA,
E-mail: ***ddse@uohyd.ernet.in*** or ***dibakar1871@gmail.com***
Tel: 91 – 040 23134454 (Office), 91 – 958104879 (Mobile)

Date: 16th June, 2023

To
The Controller of Examination (CE),
University of Hyderabad,
Hyderabad – 500046.

Through
Supervisor, SEST,
University of Hyderabad.

Subject – Ph.D. thesis submission of Jyoti Gupta (Reg. No. 18ENPH03) reg.

Dear Sir,

Please find the enclosed Ph.D. thesis titled "Investigation of efficient and stable nanostructured Mo based chalcogenides electrocatalysts for Hydrogen Evolution Reaction" by Jyoti Gupta (Reg. No. 18ENPH03). The thesis has been checked for plagiarism from the central library of University of Hyderabad and the report shows the similarity index of 9%, out of which 2-3% is from our own work. So, an effective similarity index of 7-6% (9-2/3) has been found for the thesis, which is within the acceptable limit. Hope you will find everything in order.

Please let me know if you need anything else in this regard.

Thanking you in anticipation.

Sincerely yours,

19/6/23

(Prof. Dibakar Das, Supervisor)

DIBAKAR DAS, Ph.D., FIIC
Professor
School of Engineering Sciences and Technology
University of Hyderabad, Prof. C. R. Rao Road,
Gachibowli, Hyderabad 500 046, INDIA

Investigation of efficient and stable nanostructured Mo based chalcogenides electrocatalysts for Hydrogen Evolution Reaction

by Jyoti Gupta

Submission date: 09-May-2023 10:02AM (UTC+0530)
Submission ID: 2088268247
File name: 20230504_Ph.D._Thesis_Jyoti_Gupta_18ENPH03.pdf (1.74M)
Word count: 31405
Character count: 166728

Investigation of efficient and stable nanostructured Mo based chalcogenides electrocatalysts for Hydrogen Evolution Reaction

ORIGINALITY REPORT

9%	6%	9%	3%
SIMILARITY INDEX	INTERNET SOURCES	PUBLICATIONS	STUDENT PAPERS

PRIMARY SOURCES

1	Pramod H Borse, Jyoti Gupta, Dibakar Dibakar Das, Anirudha Karati, Joydip Joardar, Pramod H Borse. " Nanostructure MoS electrocatalyst modified large area carbon electrode for efficient hydrogen evolution ", Physica Scripta, 2022 Publication	2%
2	www.researchgate.net Internet Source	1%
3	pubs.rsc.org Internet Source	1%
4	Submitted to University of Hyderabad, Hyderabad Student Paper	<1%
5	Submitted to University of Ulsan Student Paper	<1%
6	purehost.bath.ac.uk Internet Source	<1%

DIBAKAR DAS, Ph.D., FIIC
Professor
School of Engineering Sciences and Technology
University of Hyderabad, Prof. C. R. Rao Road,
Gachibowli, Hyderabad 500 046, INDIA

7	www.science.gov Internet Source	<1 %
8	www.mdpi.com Internet Source	<1 %
9	Jyoti Gupta, Dibakar Das, Anirudha Karati, Joydip Joardar, Pramod H Borse. " Nanostructure MoS electrocatalyst modified large area carbon electrode for efficient hydrogen evolution ", Physica Scripta, 2022 Publication	<1 %
10	assets.researchsquare.com Internet Source	<1 %
11	"Atomic and Nano Scale Materials for Advanced Energy Conversion", Wiley, 2022 Publication	<1 %
12	dr.ntu.edu.sg Internet Source	<1 %
13	Yingying Xiao, Mingyue Tan, Zongnan Li, Liwen He, Bifen Gao, Yilin Chen, Yun Zheng, Bizhou Lin. "Ethylenediamine-assisted phase engineering of 1T/2H–MoS2/graphene for efficient and stable electrocatalytic hydrogen evolution", International Journal of Hydrogen Energy, 2021 Publication	<1 %

DIBAKAR DAS, Ph.D., FIIC
Professor
School of Engineering Sciences and Technology
University of Hyderabad, Prof. C. R. Rao Road,
Gachibowli, Hyderabad 500 046, INDIA

14	Congli Zhen, Bin Zhang, Yuhong Zhou, Yunchen Du, Ping Xu. "Hydrothermal synthesis of ternary MoS2xSe2(1-x) nanosheets for electrocatalytic hydrogen evolution", Inorganic Chemistry Frontiers, 2018 Publication	<1 %
15	Jun Wan, Jiabin Wu, Xiang Gao, Tianqi Li, Zhimi Hu, Huimin Yu, Liang Huang. " Structure Confined Porous Mo C for Efficient Hydrogen Evolution ", Advanced Functional Materials, 2017 Publication	<1 %
16	Qing Zhu, Yuanju Qu, Detao Liu, Kar Wei Ng, Hui Pan. "Two-Dimensional Layered Materials: High-Efficient Electrocatalysts for Hydrogen Evolution Reaction", ACS Applied Nano Materials, 2020 Publication	<1 %
17	www.frontiersin.org Internet Source	<1 %
18	Kaiwen Wang, Zhipeng Liu, Qian Gao, Nan Li, Kaifeng Yu. "Ni(OH)2 Nanoparticles Decorated on 1T Phase MoS2 Basal Plane for Efficient Water Splitting", Applied Surface Science, 2022 Publication	<1 %

19	Xiaobei Zang, Yijiang Qin, Teng Wang, Fashun Li, Qingguo Shao, Ning Cao. " 1T/2H Mixed Phase MoS Nanosheets Integrated by a 3D Nitrogen-Doped Graphene Derivative for Enhanced Electrocatalytic Hydrogen Evolution ", ACS Applied Materials & Interfaces, 2020 Publication	<1 %
20	Aida Contreras-Ramirez, Bryan E. Tomlin, Gregory S. Day, Abraham Clearfield, Hong-Cai Zhou. "Solvent Free Synthesis of Nano Zirconium Phenylphosphonates with Molten Phenylphosphonic Acid", Chemistry – A European Journal, 2020 Publication	<1 %
21	liu.diva-portal.org Internet Source	<1 %
22	Hailing Guo, Nuerguli Youliwasi, Lei Zhao, Yongming Chai, Chenguang Liu. "Carbon-encapsulated nickel-cobalt alloys nanoparticles fabricated via new post-treatment strategy for hydrogen evolution in alkaline media", Applied Surface Science, 2018 Publication	<1 %
23	d-nb.info Internet Source	<1 %
24	Wen Qiao, Wei Xu, Xiaoyong Xu, Liqian Wu, Shiming Yan, Dunhui Wang. " Construction of	<1 %

	Active Orbital via Single-Atom Cobalt Anchoring on the Surface of 1T-MoS Basal Plane toward Efficient Hydrogen Evolution ", ACS Applied Energy Materials, 2020 Publication	
25	Submitted to University of Lincoln Student Paper	<1 %
26	unsworks.unsw.edu.au Internet Source	<1 %
27	Photoelectrochemical Solar Fuel Production, 2016. Publication	<1 %
28	Sweety Sarma, Barun Ghosh, Sekhar Chandra Ray, Hsiaotsu Wang, Tebogo Sfiso Mahule, Way-Faung Pong. "Electronic structure and magnetic behaviors of exfoliated MoS_2 nanosheets", Journal of Physics: Condensed Matter, 2019 Publication	<1 %
29	etd.auburn.edu Internet Source	<1 %
30	Varun Vij, Siraj Sultan, Ahmad M. Harzandi, Abhishek Meena, Jitendra N. Tiwari, Wang-Geun Lee, Taeseung Yoon, Kwang S. Kim. "Nickel-Based Electrocatalysts for Energy-Related Applications: Oxygen Reduction,	<1 %

Oxygen Evolution, and Hydrogen Evolution Reactions", ACS Catalysis, 2017
Publication

---

31 Duan, Jingjing, Sheng Chen, Mietek Jaroniec, and Shi-Zhang Qiao. "Heteroatom-doped Graphene-based Materials for Energy-relevant Electrocatalytic Processes", ACS Catalysis
Publication

<1 %

---

32 Ting Zhang, Jing Du, Pinxian Xi, Cailing Xu. "Hybrids of Cobalt/Iron Phosphides Derived from Bimetal–Organic Frameworks as Highly Efficient Electrocatalysts for Oxygen Evolution Reaction", ACS Applied Materials & Interfaces, 2017
Publication

<1 %

---

33 Wee-Jun Ong, Lling-Lling Tan, Yun Hau Ng, Siek-Ting Yong, Siang-Piao Chai. " Graphitic Carbon Nitride (g-C N)-Based Photocatalysts for Artificial Photosynthesis and Environmental Remediation: Are We a Step Closer To Achieving Sustainability? ", Chemical Reviews, 2016
Publication

<1 %

---

34 K. N. Brinda, Jan Grzegorz Małecki, Zhoveta Yhobu, D. H. Nagaraju, Srinivasa Budagumpi, E. S. Erakulan, Ranjit Thapa. "Novel Carbene Anchored Molecular Catalysts for Hydrogen

<1 %

Evolution Reactions", The Journal of Physical Chemistry C, 2021
Publication

35 Bishnupad Mohanty, Piyali Bhanja, Bikash Kumar Jena. "An overview on advances in design and development of materials for electrochemical generation of hydrogen and oxygen", Materials Today Energy, 2022 <1 %
Publication

36 dspace.ncl.res.in:8080 <1 %
Internet Source

37 Jie Xu, Ying Hong, Ming-Jie Cheng, Bing Xue, Yong-Xin Li. "Vanadyl acetylacetonate grafted on ordered mesoporous silica KIT-6 and its enhanced catalytic performance for direct hydroxylation of benzene to phenol", Microporous and Mesoporous Materials, 2019 <1 %
Publication

38 Kowsalya Devi Rasamani, Farbod Alimohammadi, Yugang Sun. "Interlayer-expanded MoS 2", Materials Today, 2017 <1 %
Publication

39 S. Gupta, N. Patel, R. Fernandes, R. Kadrekar, Alpa Dashora, A.K. Yadav, D. Bhattacharyya, S.N. Jha, A. Miotello, D.C. Kothari. "Co–Ni–B nanocatalyst for efficient hydrogen evolution reaction in wide pH range", Applied Catalysis B: Environmental, 2016 <1 %

Publication

40	scholarsmine.mst.edu Internet Source	<1 %
41	Huiru Yang, Yang Liu, Chenshan Gao, Lei Meng, Yufei Liu, Xiaosheng Tang, Huaiyu Ye. " Adsorption Behavior of Nucleobases on Doped MoS Monolayer: A DFT Study ", The Journal of Physical Chemistry C, 2019 Publication	<1 %
42	Qi Wang, Didier Astruc. "State of the Art and Prospects in Metal–Organic Framework (MOF)-Based and MOF-Derived Nanocatalysis", Chemical Reviews, 2019 Publication	<1 %
43	Shuo Geng, Hu Liu, Weiwei Yang, Yongsheng Yu. "Activating MoS2 Basal Plane by Controllable Fabricating Pores for Enhanced Hydrogen Evolution Reaction", Chemistry - A European Journal, 2018 Publication	<1 %
44	digital.lib.washington.edu Internet Source	<1 %
45	www.intechopen.com Internet Source	<1 %
46	Xin Wang, Yuwei Zhang, Haonan Si, Qinghua Zhang et al. " Single-Atom Vacancy Defect to Trigger High-Efficiency Hydrogen Evolution of	<1 %

MoS ", Journal of the American Chemical Society, 2020
Publication

47	iopscience.iop.org Internet Source	<1 %
48	Hongwei Cao, Zhe Bai, Yueting Li, Zhourong Xiao, Xiangwen Zhang, Guozhu Li. " Solvothermal Synthesis of Defect-Rich Mixed 1T-2H MoS Nanoflowers for Enhanced Hydrodesulfurization ", ACS Sustainable Chemistry & Engineering, 2020 Publication	<1 %
49	Lina Wang, Xia Zhang, Ying Ma, Min Yang, Yanxing Qi. " Supercapacitor Performances of the MoS /CoS Nanotube Arrays in Situ Grown on Ti Plate ", The Journal of Physical Chemistry C, 2017 Publication	<1 %
50	Xiaoru Liang, Yajing Han, Shengli Zhu, Zhaoyang Li, Shuilin Wu, Lan Ling, Yanqin Liang. "Activity descriptor identification for hydrogen evolution reaction on well-dispersed few layer MoS2(O) nanosheets over the mesoporous carbonic arrays", Journal of Alloys and Compounds, 2020 Publication	<1 %
51	Xiujun Fan, Haiqing Zhou, Xia Guo. "WC Nanocrystals Grown on Vertically Aligned	<1 %

	Carbon Nanotubes: An Efficient and Stable Electrocatalyst for Hydrogen Evolution Reaction", ACS Nano, 2015 Publication	
52	core.ac.uk Internet Source	<1 %
53	etheses.whiterose.ac.uk Internet Source	<1 %
54	idr.nitk.ac.in Internet Source	<1 %
55	Submitted to Indian Institute of Science Education and Research Student Paper	<1 %
56	Khine Yi Mya. "Photocurable epoxy/cubic silsesquioxane hybrid materials for polythiourethane: Failure mechanism of adhesion under weathering", Journal of Applied Polymer Science, 04/05/2008 Publication	<1 %
57	Lei Deng, Dongxu Yu, Ge Sun, Xinyuan Zhang, Chunzhong Wang, Ruiyuan Tian, Fei Du. "In-situ electrochemical synthesis of high-performance S/VOx composite for aqueous zinc ion battery", Journal of Physics D: Applied Physics, 2022 Publication	<1 %

58	Prasad Prakash Patel, Prashanth Jampani Hanumantha, Moni Kanchan Datta, Oleg I. Velikokhatnyi et al. "Cobalt based nanostructured alloys: Versatile high performance robust hydrogen evolution reaction electro-catalysts for electrolytic and photo-electrochemical water splitting", International Journal of Hydrogen Energy, 2017 Publication	<1 %
59	Submitted to Skolkovo Institute of Science and Technology (Skoltech) Student Paper	<1 %
60	Huiqiao Guo, Lei Wang, Wenbin You, Liting Yang, Xiao Li, Guanyu Chen, Zhengchen Wu, Xiang Qian, Min Wang, Renchao Che. " Engineering Phase Transformation of MoS /RGO by N-doping as an Excellent Microwave Absorber ", ACS Applied Materials & Interfaces, 2020 Publication	<1 %
61	Jian Gao, Zhihua Cheng, Changxiang Shao, Yang Zhao, Zhipan Zhang, Liangti Qu. "A 2D free-standing film-inspired electrocatalyst for highly efficient hydrogen production", Journal of Materials Chemistry A, 2017 Publication	<1 %

62	Submitted to Pusan National University Library Student Paper	<1%
63	Submitted to The Robert Gordon University Student Paper	<1%
64	mdpi-res.com Internet Source	<1%

Exclude quotes	On	Exclude matches	< 14 words
Exclude bibliography	On		

School of Engineering Sciences and Technology

University of Hyderabad
2023